EUROPEAN ORGANISATION FOR NUCLEAR RESEARCH

CERN-EP-2000-148
OPAL PR 328
30 November 2000

Precise Determination of the Z Resonance Parameters at LEP: "Zedometry"

The OPAL Collaboration

Abstract

This final analysis of hadronic and leptonic cross-sections and of leptonic forward-backward asymmetries in e^+e^- collisions with the OPAL detector makes use of the full LEP 1 data sample comprising 161 pb^{-1} of integrated luminosity and 4.5×10^6 selected Z decays. An interpretation of the data in terms of contributions from pure Z exchange and from γ/Z interference allows the parameters of the Z resonance to be determined in a model-independent way. Our results are in good agreement with lepton universality and consistent with the vector and axial-vector couplings predicted in the Standard Model. A fit to the complete dataset yields the fundamental Z resonance parameters: $m_Z = (91.1852 \pm 0.0030)\,\mathrm{GeV}$, $\Gamma_Z = (2.4948 \pm 0.0041)\,\mathrm{GeV}$, $\sigma^0_h = (41.501 \pm 0.055)\,\mathrm{nb}$, $R_\ell = 20.823 \pm 0.044$, and $A^{0,\ell}_{FB} = 0.0145 \pm 0.0017$. Transforming these parameters gives a measurement of the ratio between the decay width into invisible particles and the width to a single species of charged lepton, $\Gamma_{inv}/\Gamma_{\ell\ell} = 5.942 \pm 0.027$. Attributing the entire invisible width to neutrino decays and assuming the Standard Model couplings for neutrinos, this translates into a measurement of the effective number of light neutrino species, $N_\nu = 2.984 \pm 0.013$. Interpreting the data within the context of the Standard Model allows the mass of the top quark, $m_t = (162^{+29}_{-16})\,\mathrm{GeV}$, to be determined through its influence on radiative corrections. Alternatively, utilising the direct external measurement of m_t as an additional constraint leads to a measurement of the strong coupling constant and the mass of the Higgs boson: $\alpha_s(m_Z) = 0.127 \pm 0.005$ and $m_H = (390^{+750}_{-280})$ GeV.

To be submitted to Eur. Phys. J. C

The OPAL Collaboration

G. Abbiendi[2], C. Ainsley[5], P.F. Åkesson[3], G. Alexander[22], J. Allison[16], G. Anagnostou[1], K.J. Anderson[9], S. Arcelli[17], S. Asai[23], S.F. Ashby[1], D. Axen[27], G. Azuelos[18,a], I. Bailey[26], A.H. Ball[8], E. Barberio[8], R.J. Barlow[16], T. Behnke[25], K.W. Bell[20], G. Bella[22], A. Bellerive[9], G. Benelli[2], S. Bentvelsen[8], C. Beeston[16], S. Bethke[32], O. Biebel[32], I.J. Bloodworth[1], O. Boeriu[10], P. Bock[11], J. Böhme[14,g], D. Bonacorsi[2], M. Boutemeur[31], S. Braibant[8], P. Bright-Thomas[1], L. Brigliadori[2], R.M. Brown[20], H.J. Burckhart[8], J. Cammin[3], P. Capiluppi[2], R.K. Carnegie[6], B. Caron[28], A.A. Carter[13], J.R. Carter[5], C.Y. Chang[17], D.G. Charlton[1,b], P.E.L. Clarke[15], E. Clay[15], I. Cohen[22], J.E. Conboy[15], O.C. Cooke[8], J. Couchman[15], R.L. Coxe[9], A. Csilling[15,i], M. Cuffiani[2], S. Dado[21], G.M. Dallavalle[2], S. Dallison[16], C. Darling[34] A. De Roeck[8], E.A. De Wolf[8], P. Dervan[15], K. Desch[25], B. Dienes[30,f], M.S. Dixit[7], M. Donkers[6], J. Dubbert[31], E. Duchovni[24], G. Duckeck[31], I.P. Duerdoth[16], P.G. Estabrooks[6], E. Etzion[22], F. Fabbri[2], M. Fanti[2], L. Feld[10], P. Ferrari[12], F. Fiedler[8], I. Fleck[10], M. Ford[5], M. Foucher[17], A. Frey[8], A. Fürtjes[8], D.I. Futyan[16], P. Gagnon[12], J. Gascon[18], S.M. Gascon-Shotkin[17], J.W. Gary[4], G. Gaycken[25], C. Geich-Gimbel[3], G. Giacomelli[2], P. Giacomelli[8], R. Giacomelli[2], D. Glenzinski[9], J. Goldberg[21], C. Grandi[2], K. Graham[26], E. Gross[24], J. Grunhaus[22], M. Gruwé[25], P.O. Günther[3], C. Hajdu[29], G.G. Hanson[12], K. Harder[25], A. Harel[21], M. Harin-Dirac[4], P.A. Hart[9], M. Hauschild[8], C.M. Hawkes[1], R. Hawkings[8], R.J. Hemingway[6], C. Hensel[25], G. Herten[10], R.D. Heuer[25], M.D. Hildreth[8], J.C. Hill[5], S.J. Hillier[1], A. Hocker[9], K. Hoffman[8], R.J. Homer[1], A.K. Honma[8], D. Horváth[29,c], K.R. Hossain[28], R. Howard[27], P. Hüntemeyer[25], P. Igo-Kemenes[11], K. Ishii[23], F.R. Jacob[20], A. Jawahery[17], H. Jeremie[18], C.R. Jones[5], P. Jovanovic[1], T.R. Junk[6], N. Kanaya[23], J. Kanzaki[23], G. Karapetian[18], D. Karlen[6], V. Kartvelishvili[16], K. Kawagoe[23], T. Kawamoto[23], R.K. Keeler[26], R.G. Kellogg[17], B.W. Kennedy[20], D.H. Kim[19], J. Kirk[8], K. Klein[11], A. Klier[24], S. Kluth[32], T. Kobayashi[23], M. Kobel[3], T.P. Kokott[3], S. Komamiya[23], R.V. Kowalewski[26], T. Kress[4], P. Krieger[6], J. von Krogh[11], D. Krop[12], T. Kuhl[3], M. Kupper[24], P. Kyberd[13], G.D. Lafferty[16], R. Lahmann[17], W.P. Lai[19], H. Landsman[21], D. Lanske[14], J. Lauber[15] I. Lawson[26], J.G. Layter[4], A.M. Lee[34], A. Leins[31], D. Lellouch[24], J. Letts[12], L. Levinson[24], R. Liebisch[11], J. Lillich[10], C. Littlewood[5], A.W. Lloyd[1], S.L. Lloyd[13], F.K. Loebinger[16], G.D. Long[26], M.J. Losty[7], J. Lu[27], J. Ludwig[10], A. Macchiolo[18], A. Macpherson[28,l], W. Mader[3], M. Mannelli[8], S. Marcellini[2], T.E. Marchant[16], A.J. Martin[13], J.P. Martin[18], G. Martinez[17], T. Mashimo[23], P. Mättig[24], W.J. McDonald[28], J. McKenna[27], T.J. McMahon[1], R.A. McPherson[26], F. Meijers[8], P. Mendez-Lorenzo[31], W. Menges[25], S. Menke[3] F.S. Merritt[9], H. Mes[7], A. Michelini[2], S. Mihara[23], G. Mikenberg[24], D.J. Miller[15], W. Mohr[10], A. Montanari[2], T. Mori[23], U. Müller[3], K. Nagai[13], I. Nakamura[23], H.A. Neal[33], R. Nisius[8], S.W. O'Neale[1], F.G. Oakham[7], F. Odorici[2], A. Oh[8], A. Okpara[11], N.J. Oldershaw[16], M.J. Oreglia[9], S. Orito[23,n], F. Palmonari[2], G. Pásztor[8,i], J.R. Pater[16], G.N. Patrick[20], P. Pfeifenschneider[14,h], J.E. Pilcher[9], J. Pinfold[28], D.E. Plane[8], B. Poli[2], J. Polok[8], O. Pooth[8], M. Przybycień[8,d], A. Quadt[8], G. Quast[8]. K. Rabbertz[8], B. Raith[3], C. Rembser[8], P. Renkel[24], H. Rick[4], N. Rodning[28], J.M. Roney[26], S. Rosati[3], K. Roscoe[16], A.M. Rossi[2], Y. Rozen[21], K. Runge[10], O. Runolfsson[8], D.R. Rust[12], K. Sachs[6], T. Saeki[23], O. Sahr[31], E.K.G. Sarkisyan[8,m], C. Sbarra[26], A.D. Schaile[31], O. Schaile[31], P. Scharff-Hansen[8], B. Schmitt[8], M. Schröder[8], M. Schumacher[25], C. Schwick[8], W.G. Scott[20], R. Seuster[14,g], T.G. Shears[8,j], B.C. Shen[4], C.H. Shepherd-Themistocleous[5], P. Sherwood[15], G.P. Siroli[2], A. Skuja[17], A.M. Smith[8], T.J. Smith[26] G.A. Snow[17,n], R. Sobie[26], S. Söldner-Rembold[10,e], S. Spagnolo[20], R.W. Springer[17], M. Sproston[20], A. Stahl[3], K. Stephens[16], K. Stoll[10], D. Strom[19], R. Ströhmer[31], L. Stumpf[26], B. Surrow[8], S.D. Talbot[1], S. Tarem[21], R.J. Taylor[15], R. Teuscher[9], M. Tecchio[9], J. Thomas[15], M.A. Thomson[8], S. Towers[6], D. Toya[23], T. Trefzger[31], I. Trigger[8], Z. Trócsányi[30,f], T. Tsukamoto[23] E. Tsur[22], M.F. Turner-Watson[1], I. Ueda[23], B. Vachon[26], P. Vannerem[10], M. Verzocchi[8], E.H. Vokurka[16], H. Voss[8], J. Vossebeld[8], A. Wagner[25], D.L. Wagner[9], D. Waller[6], C.P. Ward[5], D.R. Ward[5], P.M. Watkins[1], A.T. Watson[1], N.K. Watson[1], P.S. Wells[8], T. Wengler[8], N. Wermes[3], D. Wetterling[11] J.S. White[6], G.W. Wilson[16], J.A. Wilson[1], T.R. Wyatt[16], S. Yamashita[23], V. Zacek[18], D. Zer-Zion[8,k]

[1]School of Physics and Astronomy, University of Birmingham, Birmingham B15 2TT, UK
[2]Dipartimento di Fisica dell' Università di Bologna and INFN, I-40126 Bologna, Italy
[3]Physikalisches Institut, Universität Bonn, D-53115 Bonn, Germany
[4]Department of Physics, University of California, Riverside CA 92521, USA
[5]Cavendish Laboratory, Cambridge CB3 0HE, UK
[6]Ottawa-Carleton Institute for Physics, Department of Physics, Carleton University, Ottawa, Ontario K1S 5B6, Canada
[7]Centre for Research in Particle Physics, Carleton University, Ottawa, Ontario K1S 5B6, Canada
[8]CERN, European Organisation for Nuclear Research, CH-1211 Geneva 23, Switzerland
[9]Enrico Fermi Institute and Department of Physics, University of Chicago, Chicago IL 60637, USA
[10]Fakultät für Physik, Albert Ludwigs Universität, D-79104 Freiburg, Germany
[11]Physikalisches Institut, Universität Heidelberg, D-69120 Heidelberg, Germany
[12]Indiana University, Department of Physics, Swain Hall West 117, Bloomington IN 47405, USA
[13]Queen Mary and Westfield College, University of London, London E1 4NS, UK
[14]Technische Hochschule Aachen, III Physikalisches Institut, Sommerfeldstrasse 26-28, D-52056 Aachen, Germany
[15]University College London, London WC1E 6BT, UK
[16]Department of Physics, Schuster Laboratory, The University, Manchester M13 9PL, UK
[17]Department of Physics, University of Maryland, College Park, MD 20742, USA
[18]Laboratoire de Physique Nucléaire, Université de Montréal, Montréal, Quebec H3C 3J7, Canada
[19]University of Oregon, Department of Physics, Eugene OR 97403, USA
[20]CLRC Rutherford Appleton Laboratory, Chilton, Didcot, Oxfordshire OX11 0QX, UK
[21]Department of Physics, Technion-Israel Institute of Technology, Haifa 32000, Israel
[22]Department of Physics and Astronomy, Tel Aviv University, Tel Aviv 69978, Israel
[23]International Centre for Elementary Particle Physics and Department of Physics, University of Tokyo, Tokyo 113-0033, and Kobe University, Kobe 657-8501, Japan
[24]Particle Physics Department, Weizmann Institute of Science, Rehovot 76100, Israel
[25]Universität Hamburg/DESY, II Institut für Experimental Physik, Notkestrasse 85, D-22607 Hamburg, Germany
[26]University of Victoria, Department of Physics, P O Box 3055, Victoria BC V8W 3P6, Canada
[27]University of British Columbia, Department of Physics, Vancouver BC V6T 1Z1, Canada
[28]University of Alberta, Department of Physics, Edmonton AB T6G 2J1, Canada
[29]Research Institute for Particle and Nuclear Physics, H-1525 Budapest, P O Box 49, Hungary
[30]Institute of Nuclear Research, H-4001 Debrecen, P O Box 51, Hungary
[31]Ludwigs-Maximilians-Universität München, Sektion Physik, Am Coulombwall 1, D-85748 Garching, Germany
[32]Max-Planck-Institute für Physik, Föhring Ring 6, 80805 München, Germany
[33]Yale University, Department of Physics, New Haven, CT 06520, USA
[34]Duke University, Department of Physics, Durham, NC 27708-0305, USA

[a] and at TRIUMF, Vancouver, Canada V6T 2A3
[b] and Royal Society University Research Fellow
[c] and Institute of Nuclear Research, Debrecen, Hungary
[d] and University of Mining and Metallurgy, Cracow
[e] and Heisenberg Fellow
[f] and Department of Experimental Physics, Lajos Kossuth University, Debrecen, Hungary
[g] and MPI München
[h] now at MPI für Physik, 80805 München
[i] and Research Institute for Particle and Nuclear Physics, Budapest, Hungary
[j] now at University of Liverpool, Dept of Physics, Liverpool L69 3BX, UK
[k] and University of California, Riverside, High Energy Physics Group, CA 92521, USA

[l] and CERN, EP Div, 1211 Geneva 23
[m] and Tel Aviv University, School of Physics and Astronomy, Tel Aviv 69978, Israel.
[n] deceased

Contents

List of Tables

List of Figures

1 Introduction

One of the principal goals of the Large Electron-Positron (LEP) collider project [?] at CERN is to make precise measurements of the properties of the Z gauge boson, which are basic parameters of nature. These include the Z mass and its total decay width, as well as the composition and angular distributions of Z decay products. In combination with other precise measurements [?, ?], these physical observables provide the most stringent tests of the Standard Model (SM) of electroweak interactions [?] yet possible, allowing it to be investigated at the level of higher-order electroweak corrections [?]. These tests represent a unique probe of the underlying gauge structure of electroweak physics. Possible new physics or new particles beyond those of the SM might be revealed through the subtle changes which they would induce in the precise results reported here.

From 1989 to 1995 LEP produced e^+e^- collisions with centre-of-mass energies, $\sqrt{s}$, close to the Z mass, m_Z. This is referred to as the LEP 1 programme. For much of this period $\sqrt{s}$ was chosen to be within about 200 MeV of m_Z, close to the peak of the Z resonance curve, in order to obtain the maximum number of Z decay events. These "on-peak" data provide high-statistics samples for measurements of production cross-sections and Z decay properties, such as partial decay widths and forward-backward asymmetries. Data were also recorded at several centre-of-mass energy points up to 4 GeV above and below the peak of the Z resonance. These "off-peak" data samples provide sensitivity to the lineshape of the Z resonance and hence to its mass, m_Z, and total decay width, Γ_Z. The OPAL collaboration has previously published measurements of Z properties based on LEP 1 data recorded up to the end of 1992 [?, ?, ?, ?].

In this paper we report new OPAL measurements of hadronic and leptonic cross-sections and leptonic forward-backward asymmetries based on the higher luminosity LEP 1 runs which took place during the years 1993–1995 and resulted in a four-fold increase of our data set. In 1993 and 1995 LEP energy scans were performed with significant luminosity collected at the off-peak points, in order to improve substantially the determination of m_Z and Γ_Z. These off-peak points were chosen to be approximately 1.8 GeV below and above m_Z. In 1994 all data were collected on peak. In the following we will refer to the energy points below, close to and above the Z resonance peak as "peak−2", "peak" and "peak+2", respectively. In parallel to the large increase of the data set, significant progress has been made in each of the many aspects which affect the precision of the results and their interpretation, namely the LEP energy calibration, the luminosity determination, the selection of the Z decay products and the theoretical predictions of observable quantities. The measurements from the 1993–1995 data are combined with those from previous years in order to determine the OPAL values for Z properties based on the full LEP 1 data sample.

We analyse our results by first interpreting the cross-section and forward-backward asymmetry measurements in a model-independent fashion, in which the Z couplings to hadrons and leptons are allowed to vary freely. This provides a useful phenomenological description of observable Z properties and allows basic predictions of the SM, such as lepton universality and the vector and axial-vector structure of the couplings, to be verified. We then go on to make a fit within the full context of the SM, leading to a direct determination of the accessible SM parameters. In a forthcoming publication these OPAL measurements will be combined with similar results from the ALEPH [?], DELPHI [?] and L3 [?] collaborations, in order to determine the final set of LEP results for Z parameters.

The structure of this paper is as follows. Section 2 contains a brief description of the OPAL detector, simulation program and LEP 1 data samples. Section 3 gives an overview of the essential concepts we use to define our measured sample of Z decays. The LEP centre-of-mass energy calibration is outlined in Section 4. The luminosity measurement is reviewed briefly in Section 5, full details being available in [?]. The details of the hadronic and leptonic event selections and analyses are given in Sections 6 and 7. The cross-section and leptonic forward-backward asymmetry measurements are described in Sections 8 and 9. In Section 10 we introduce the basic formalism for the parametrisation of the Z resonance and discuss radiative corrections. The determination of Z properties, their interpretation within the context of the SM and the implications for SM parameters are presented in Section 11. The results are summarised in Section 12.

2 The OPAL detector and its simulation

The OPAL detector is described in detail in [**?**]. Therefore only those aspects which are relevant to the present analysis are mentioned briefly here. In the following, a right-handed coordinate system is used in which the origin is located at the geometrical centre of the tracking chambers, the z-axis is along the electron beam direction, the x-axis points to the centre of the LEP ring, r is the radial coordinate, normal to z, and the angles θ and ϕ are respectively the polar and azimuthal angles with respect to z. The x-axis defines $\phi = 0$. We set $c = \hbar = 1$ throughout.

Charged particle trajectories are reconstructed and their momenta are measured using cylindrical central tracking detectors (CT). These consist of a silicon micro-vertex detector [**?**], a high precision vertex wire chamber, a large volume jet chamber (CJ) and thin z-chambers. The jet chamber is 400 cm in length and 185 cm in radius. Its 24 azimuthal sectors are formed by planes of anode and cathode wires stretched parallel to the z-axis. It provides up to 159 space points per track and also measures the ionisation energy loss of charged particles, $\mathrm{d}E/\mathrm{d}x$ [**?**]. The z-chambers, which improve the track measurements in θ, are situated immediately outside and coaxial with the jet chamber. Quality cuts are made to select well-reconstructed tracks emanating from the interaction point for use in the analysis. In general no track is used which has a momentum component transverse to the beam axis less than 100 MeV. The number of hits associated with the track in the central tracking chambers must be at least 20. The distance of closest approach of the track to the nominal beam crossing point must be less than 2 cm radially and less than 100 cm along the z-axis. Track finding is nearly 100% efficient within the angular region $|\cos\theta| < 0.97$. For the analyses presented here, slightly tighter tracking requirements are imposed which are optimised for each of the Z decay channels. The whole central detector is contained within a pressure vessel which maintains a constant absolute pressure of 4 bar and a solenoid which provides a uniform axial magnetic field of 0.435 T. The solenoid is surrounded by a time-of-flight scintillation counter array.

The electromagnetic calorimeter (ECAL), located outside the CT pressure vessel and the solenoid, measures the energies and positions of showering particles. The barrel consists of a presampler followed by a cylindrical ensemble of 9440 lead glass blocks arranged such that each block points towards the beam collision point, but the inter-block gaps point slightly away from the origin. Mechanically the barrel lead glass calorimeter consists of 10 C-shaped modules. The two endcaps each consist of a presampler followed by 1132 lead glass blocks aligned parallel to the beam axis. The barrel covers the angular region $|\cos\theta| < 0.82$ while the endcaps cover $0.81 < |\cos\theta| < 0.98$. Overall, the electromagnetic calorimeter provides complete coverage for the entire angular range of $|\cos\theta| < 0.98$. Only in the region where the barrel and endcaps overlap, and at the narrow boundaries between the barrel modules, is the uniformity of response slightly degraded. For use in the analysis electromagnetic clusters in the barrel are required to have a minimum energy of 100 MeV, and clusters in the endcaps must consist of energy deposits in at least 2 adjacent lead glass blocks and must have a minimum energy of 200 MeV.

Calorimeters close to the beam axis, and located on both sides of the interaction point, measure the luminosity using small-angle Bhabha scattering events. They complete the geometrical acceptance down to 25 mrad from the beam axis. These include the forward detectors (FD), which are lead-scintillator sandwich calorimeters, and at smaller angles, silicon-tungsten calorimeters [**?**, **?**] (SiW), which were installed in 1993, increasing the precision of the luminosity measurement by an order of magnitude.

The iron return yoke of the magnet lies outside the electromagnetic calorimeter and is instrumented with streamer tubes as a hadronic calorimeter (HCAL). Four layers of muon detectors [**?**] (MU) are situated outside the hadronic calorimeter. Muons with momenta above 3 GeV usually penetrate to the muon detectors. In addition, up to nine hits may be recorded for minimum ionising particles traversing the hadronic calorimeter, further aiding muon identification.

The OPAL data-acquisition system [**?**] reads out and records data associated with particular events which are selected using a three-level system, consisting of a pretrigger [**?**], a trigger [**?**] and an online event filter [**?**]. These make use of a large number of independent signals from a variety of detector

components and have very high efficiency and redundancy for the Z decay events which are of interest for the analyses reported in this paper. The trigger inefficiency for Z events decaying to charged fermions within the geometrical acceptance is less than 0.1% and the trigger redundancy allows all efficiencies to be measured from the data. The online event filter serves primarily for data quality monitoring, but also allows a small number of obvious non-physics events to be identified through software reconstruction and rejected from the data stream. The fact that no good events are rejected by the filter has been carefully tested using the redundancy of selection criteria and also in numerous samples where rejection by the filter was temporarily disabled. Events selected by the filter are fully reconstructed online and written into an offline storage facility for further analyses [**?**].

Unless stated otherwise, all Monte Carlo event samples have been processed using a full simulation of the OPAL detector [**?**] which treats in detail the detector geometry and material as well as the effects of detector resolution and efficiency. The simulated events have been reconstructed using the same procedures that were used for the OPAL data. Monte Carlo event generators are further discussed in Section 3.

2.1 LEP 1 data samples

In Table 1 the integrated luminosities are given for all of the LEP 1 data samples which are used in this analysis. The total integrated luminosity is 161 pb^{-1}, which includes 43 pb^{-1} of data recorded off-peak. The peak data are dominated by the dedicated high-statistics running in 1992 and especially 1994, while most of the off-peak data were collected in the precision scans in 1993 and 1995, when the running was confined to three energies: on-peak and peak$\pm$2 GeV. During the "prescan" periods in 1993 and 1995 running was confined to the peak while all the necessary elements of the LEP beam energy calibration were commissioned. These periods also coincide with the commissioning of the SiW luminometer (1993) or the SiW bunch tagger (1995), described below.

The additional 117 pb^{-1} of luminosity from 1993 to 1995 has warranted a significantly improved analysis of the hadronic decay channel. This has reduced the systematic error in the hadronic acceptance by about a factor of three, which makes it comparable with the much reduced statistical error. In the analysis of the leptonic channels studies of systematic effects have benefited from the greatly increased statistics. Except for the measurement of the $\mu^+\mu^-$ asymmetry in 1992 (see Section 9.1) the data presented in our previous publications has not been reanalysed. However, we have retrospectively applied corrections for a few small effects (see Section 8).

2.1.1 LEP operation

Many aspects of the LEP experimental programme were optimised to reduce potential systematic effects in measuring the parameters of the Z. The off-peak data are essential for the measurements of m_{Z} and Γ_{Z}. For the 1993 and 1995 scans, the choice was made to run at only three points to maximise the statistical precision in the measurement of these quantities: at the peak and approximately $\pm$1.8 GeV from the peak. The exact energies were chosen to allow a precise calibration of the LEP beam energies by resonant depolarisation (see Section 11). In each scan the cross-sections at the two off-peak points were typically measured in adjacent LEP fills, interspersed with fills at the Z peak. This reduces any possible systematic biases resulting from changes in LEP or OPAL operating conditions, and also gives balanced data samples at the off-peak points within each year. For the determination of m_{Z} the crucial experimental measurement is the ratio of the cross-sections above and below the Z peak, and the impact of inter-year systematic effects are minimised by the balance of peak+2 and peak$-$2 measurements within each year. A check of the stability of the LEP energy calibration can also be made by measuring m_{Z} in each scan year (see Section 11).

The determination of Γ_{Z}, however, chiefly depends on the measurement of the ratio of off-peak to on-peak cross-sections. The on-peak cross-sections are essentially determined by the 1992 and especially the 1994 data, while the off-peak cross-sections are determined by the 1993 and 1995 data. The measurement of Γ_{Z} therefore enjoys little inherent protection from time-dependent systematic shifts

in the scale of the cross-section measurements. Control of potential inter-year systematic uncertainties from changes in LEP operation or the OPAL detector configuration are essential.

The operation of the LEP collider has evolved considerably over the years to increase the luminosity delivered to the experiments and to improve the precision with which the centre-of-mass energy could be calibrated (see Section 4). Initially LEP operated in a mode in which four bunches of electrons and four bunches of positrons collided at the four interaction points every 22 μs. From 1992 to 1994 LEP ran in a mode with 8 bunches of electrons and positrons which collide every 11 μs. In 1995 the LEP collider was operated in a new "bunch-train" mode, in which four equally spaced bunch-trains replaced the usual bunches, and crossed at each interaction point every 22 μs. Each train consisted of up to four (typically three) bunchlets, separated from each other by 247 ns. Preparations for the bunch-train mode required a return to 4-bunch running at the end of 1994 (periods peak(c) and (d)). The impact of these changes on the OPAL set up are described below.

2.1.2 OPAL detector stability

The configuration of the OPAL detector has changed slightly over the entire period of these measurements. Of greatest significance was the installation of the precision SiW luminometer before the 1993 run. This yields absolute luminosity measurements for the 1993–1995 data samples which are an order of magnitude more precise than the earlier, systematics-limited measurements using the forward detectors.

A silicon micro-vertex detector was first installed in OPAL before the 1992 running period. The detector was augmented for the 1993 run. It was removed for repairs at the end of 1994 (periods peak(c) and (d)), and replaced with an improved geometry for the 1995 run. Data from the micro-vertex detector are not used directly in the reconstruction of tracks for this analysis. The $\sim 0.015 X_0$ of additional material it introduces affects the conversion of photons into electron pairs, and is adequately reproduced by the detector simulation program.

Halving the interval between bunch crossings from 22 to 11 μsec in 1992 no longer allowed sufficient time to form the full trigger information from the tracking chambers. OPAL adopted a pretrigger scheme [**?**] in which very loose trigger conditions using fast signals identified a small fraction ($\sim 1\%$) of all bunch crossings for which sensitivity to interactions in the next crossing would be lost while waiting for the full track trigger information. The pretrigger inefficiency for all relevant events was determined to be negligible.

The new bunch-train mode of operation in 1995 required several modifications. In particular, the SiW luminometer electronics were considerably modified to operate properly under these conditions [**?**]. In addition, small corrections were applied to the electromagnetic calorimeter energy measurements on the basis of bunchlet timing information obtained from the time-of-flight detectors, or from the tracking chambers. For most events, the tracking detectors are able to determine the bunchlet crossing which produced the visible tracks, since only one potential choice of the origin for the drift times yields good tracks passing through the interaction point. The misassignment of bunchlet number could potentially cause problems in track reconstruction. The influence of such bunchlet effects on the event selection efficiencies has been checked using redundant selections and was found to be negligible.

3 Selection and analysis of Z decay channels

In the SM the Z is expected to decay into a fermion-antifermion pair. With three generations of fermions, there are eleven possible decay channels: five quark flavours (the top quark is too heavy), three neutrino species and three charged leptons. The approximate branching ratios are 70:20:10 to hadrons, neutrinos and charged leptons, respectively. Decays of the Z to neutrinos normally go undetected and are referred to as invisible decays. No attempt is made in this analysis to separate the different quark flavours, with all hadronic Z decays being classified as $e^+e^- \to q\overline{q}$ events. Measurements of Z partial decay widths and forward-backward asymmetries using hadronic Z decays in which the different quark flavours *are* distinguished have been published in [**?**].

The analysis described here is focused on selecting visible Z decay events in just four categories: $e^+e^- \to q\overline{q}$, e^+e^-, $\mu^+\mu^-$ and $\tau^+\tau^-$, where, in each case, initial- and final-state radiation can lead to one or more additional photons in the final state. Also, the classification $e^+e^- \to q\overline{q}$ is inclusive of all final-state QCD interactions, including hard gluon bremsstrahlung. In general, events in these categories can easily be distinguished from each other and from the remaining background, which is very small compared to the Z resonance signal, leading to event selections of high efficiency and purity.

Typical examples of the four event categories as observed in the OPAL detector are shown in Figure 1. Independent of the specific decay channel, the detected particles in Z events generally exhibit momentum balance along the beam direction, in contrast to background events from two-photon interaction processes ($e^+e^- \to e^+e^-f\overline{f}$). Events produced by the passage of cosmic rays through the detector can normally be rejected since they are rarely consistent with the observed origin of true signal events in space and time. The $e^+e^- \to q\overline{q}$ events are characterised by high-multiplicity final states, due to quark fragmentation and hadronisation, in contrast to the low-multiplicity lepton-pair events. The $e^+e^- \to e^+e^-$ events have two high-energy deposits from the final-state electrons in the electromagnetic calorimeter, associated with tracks reconstructed in the central detector. The $e^+e^- \to \mu^+\mu^-$ events typically contain two high-momentum central detector tracks, with little energy deposited in the electromagnetic calorimeter. The tracks are usually associated with track segments in the muon chambers or the hadron calorimeter strips, which provide evidence for penetrating muons. The $e^+e^- \to \tau^+\tau^-$ events are distinguished by two low-multiplicity 'jets', each consistent with the decay of a τ, and typically a lower measured energy than the other lepton-pair final states, due to the undetected neutrinos from the τ decays. The detailed selection criteria for events in each of these four categories are described in Sections 6 and 7. The selections have very little overlap, in particular for the three leptonic selections it is ensured that no event is classified in more than one category (see Section 7.5).

3.1 Experimental acceptance

The limited coverage of the tracking chambers in the forward direction prevents us from detecting leptons close to the beam direction, but the simple topologies of the lepton-pair final states allow a precise experimental acceptance to be defined in a restricted region of $\cos\theta$. In the case of the $e^+e^- \to \mu^+\mu^-$ and $\tau^+\tau^-$ channels the cross-sections in these regions ($|\cos\theta| < 0.95$ and 0.90 respectively) can then be extrapolated to the full angular acceptance.

In addition to the Z s-channel annihilation diagram, the process $e^+e^- \to e^+e^-$ has contributions from t-channel diagrams, dominated by photon exchange, which lead to a divergence of the forward cross-section. This makes a similar extrapolation of the $e^+e^- \to e^+e^-$ cross-sections to the full angular acceptance meaningless. We therefore restrict the $e^+e^- \to e^+e^-$ measurements to a region well within the detector, $|\cos\theta| < 0.70$, which limits the t-channel contributions to a manageable level (15% at the peak), and do not extrapolate them.

For $e^+e^- \to q\overline{q}$ events, the hadronic jets are broad enough to ensure high efficiency even for events with decay axes close to the beam direction. Hence we have almost 100% acceptance for Z events decaying hadronically, and directly measure events produced over essentially the full angular region. The approximately 0.5% inefficiency is dominated by very narrow 2-jet events oriented along the beam line.

3.2 Kinematic acceptance for cross-sections and asymmetries

In order to interpret the measured cross-section and asymmetry for each reaction the limits of kinematic phase space must be specified in a precise manner, which is adapted to available theoretical calculations, in order to take into account properly the effect of initial- and final-state photon radiation. We therefore correct our raw measurements to correspond to simple, ideal, kinematical limits, which are chosen to correspond reasonably closely to the experimental acceptances to reduce the resulting acceptance extrapolations. Table 2 summarises the limits of the ideal kinematic phase space within

which we define our cross-sections and asymmetries for each species. The experimentally observed number of events in each channel is corrected for selection inefficiencies and background to give the total number of events produced within the kinematic acceptance defined by these idealised cuts.

We specify the kinematic phase space for the cross-sections for all species, except electrons, in terms of a lower bound on either s'/s or $m^2_{\mathrm{f\bar{f}}}/s$. Here s' is the squared centre-of-mass energy after initial-state radiation and $m_{\mathrm{f\bar{f}}}$ is the invariant mass of the final-state fermion pair. Both definitions suffer from some degree of ambiguity. In the case of $\mathrm{e^+e^-} \to \mathrm{q\overline{q}}$, QCD effects obscure the precise meaning of $m^2_{\mathrm{f\bar{f}}}$, while s' suffers from the impossibility of distinguishing initial- from final-state radiation. There is, however, little quantitative difference in our regime between $m^2_{\mathrm{f\bar{f}}}$ and s'. Switching between using $m^2_{\mathrm{f\bar{f}}}$ and s' in the acceptance definition changes the hadronic cross-section, for example, by only a few parts in 10^5.

The experimental acceptance becomes very small for events with low s' or $m^2_{\mathrm{f\bar{f}}}$, but the number of produced events in this region is also small. The calculated number of hard radiative events which fall between our ideal and experimental acceptance limits in proportion to all accepted events is about 1.5×10^{-4} for hadrons and 5×10^{-3} for $\mu^+\mu^-$ and $\tau^+\tau^-$. For $\mathrm{e^+e^-} \to \mu^+\mu^-$ and $\tau^+\tau^-$ the dominant acceptance extrapolations (respectively $\sim 7\%$ and 15%) are due to the limited angular region of the experimental event selection.

For the process $\mathrm{e^+e^-} \to \mathrm{e^+e^-}$ the ideal kinematic acceptance is chosen very close to the experimental acceptance, both being defined by the range of polar angles allowed for the final-state $\mathrm{e^-}$ and the maximum $\mathrm{e^+e^-}$ acollinearity. The total acceptance correction required is less than 1%.

For measuring the asymmetries we treat the kinematic acceptance for all the leptons similarly to the electrons, and limit the range of polar angle of the final-state fermions to the nominal experimental acceptance. To reduce effects associated with strong initial-state radiation, we also limit the maximum acollinearity between the pair of leptons to 10° or 15°, as shown in Table 2.

3.3 Four-fermion processes and radiative photon interference

Four-fermion diagrams, as shown in Figure 2, also contribute at a small level to the selected event samples. Some of these, such as the conversion of initial- or final-state photons to fermion pairs (Figure 2(b) and Figure 2(c)) are properly considered as radiative corrections to fermion pair production. We therefore apply corrections to the selection efficiency where necessary to ensure that such events are fully counted as part of the measured signal. Other four-fermion processes, such as multi-peripheral diagrams (two-photon processes, Figure 2(d)) are clearly unrelated to the Z and we therefore subtract them as background. A third class of four-fermion processes (Figure 2(e) and Figure 2(f)) are pair corrections to scattering in the t-channel. Such events are treated as signal only in the $\mathrm{e^+e^-} \to \mathrm{e^+e^-}$ channel. More details concerning the treatment of four-fermion final states are given in Appendix A.1.

Our measured cross-sections and asymmetries include the effects of interference between initial- and final-state photon radiation. Since our primary Monte Carlo programs, JETSET and KORALZ[1] do not include such interference, we adjusted the calculated event selection efficiency for our cross-section measurements by corrections of $\mathcal{O}(10^{-4})$ to account for this deficiency, as described in Appendix A.2. For the asymmetries there is a close correspondence between the experimental and ideal acceptances, and no such acceptance correction is necessary.

3.4 Monte Carlo event generators

The following event generator programs have been used to simulate signal and background processes: $\mathrm{e^+e^-} \to \mathrm{q\overline{q}}$ events have been generated using the programs JETSET, version 7.3 [**?**], and HERWIG, version 5.8 [**?**], with hadronisation parameters tuned using a sample of hadronic events selected from OPAL LEP 1 data [**?**]. Cross checks have been made using version 7.4 of the JETSET program [**?**]

[1]KORALZ can include initial-final-state interference, but only when radiative corrections are treated to $\mathcal{O}(\alpha)$.

with an updated set of parameters [?] tuned using a larger sample of OPAL LEP 1 data. The KORALZ program, version 4.02 [?], has been used for $e^+e^- \to \mu^+\mu^-$ and $e^+e^- \to \tau^+\tau^-$ events and the BHWIDE program, version 1.00 [?], for $e^+e^- \to e^+e^-$ events. Background events produced by two-photon interaction processes, $e^+e^- \to e^+e^-f\overline{f}$, have been studied using the programs PHOJET [?], HERWIG and the program of Vermaseren [?], while those from $e^+e^- \to \gamma\gamma$ have been calculated using the RADCOR program [?]. The four-fermion signal processes in the s-channel have been studied using the FERMISV [?] generator. Background from t-channel four-fermion events has been evaluated using PYTHIA [?] for $e^+e^- \to e^+e^-q\overline{q}$ and grc4f [?] for $e^+e^- \to e^+e^-\ell^+\ell^-$.

4 LEP energy

The LEP energy scale is one of the crucial ingredients in the determination of Z resonance parameters. The initial energy calibration of LEP [?] was performed in 1989 and 1990 by circulating protons in the LEP ring at 20 GeV and using magnetic measurements to obtain the centre-of-mass energy in physics conditions. This resulted in errors on $\sqrt{s}$, and hence m_Z, of 28 MeV and 22 MeV for the 1989 and 1990 data, respectively. Using the technique of resonant depolarisation [?], a precise calibration of the LEP energy scale was achieved in 1991, resulting in a systematic uncertainty of 6 MeV on m_Z and approximately 5 MeV on Γ_Z [?]. The recognition of energy shifts due to the alignment of the copper RF cavities had particular importance at the two interaction points equipped with cavities (OPAL and L3). The calibration of the LEP energy scale in 1992 [?] was performed using a similar procedure. In 1992, however, calibrations with resonant depolarisation were successful only late in the year and showed a large spread. The central value of the energy derived from the polarisation measurements was found to be in good agreement with the one obtained from methods based on measuring the magnetic field in the LEP dipoles. The quoted error of 18 MeV on $\sqrt{s}$ arises predominantly from the scatter of the depolarisation measurements and the extrapolation to the beginning of the year using magnetic measurements. Since the 1992 data have all been collected at the peak of the Z resonance, this larger error has an insignificant impact on the precision of the derived Z resonance parameters.

In 1993 a more complete understanding of the time-dependent parameters that influence the LEP energy, such as tidal deformations of the Earth and changes in magnet temperatures, as well as more frequent polarisation measurements, led to a further increase in the precision of the energy calibration. A concerted effort to ensure the complete logging of all LEP parameters relevant to the energy measurement allowed this inherent precision to be extended to a large fraction of all fills. This resulted in a systematic uncertainty of 1.4 MeV on the absolute centre-of-mass energy of LEP [?], and the point-to-point energy errors, including the error on the centre-of-mass energy spread, contributed an uncertainty of 1.5 MeV on Γ_Z. The quality of measurement was maintained throughout the 1994 running.

In 1995 vertical dispersion of the beam energy at the interaction point was introduced by bunch-train operation, which required frequent vernier scans to control possible shifts in the mean centre-of-mass collision energy [?]. More significantly, additional instrumentation installed in the LEP tunnel allowed the observation of an unexpected change in the beam energy during LEP fills. Leakage currents from the electric railway system in the Geneva area flow through the LEP tunnel and perturb the magnetic field of the LEP dipoles, which causes the bending field (and hence, the beam energy) to rise steadily during a fill. The interplay between the rise introduced by the leakage currents and that due to temperature variations in the dipole magnets necessitated a more detailed study of the temperature-dependence of the bending field, resulting in a much improved model of this behaviour. This knowledge provides the definitive description of the LEP energy calibration for 1993–1995 [?]. In light of this improved understanding, the 1993 energies and their errors, first published in [?], have been revised, and the errors significantly increased. The data needed for updating the less critical calibrations for years earlier than 1993 are unavailable. However, these errors are uncorrelated with the errors for 1993–1995, so the data can easily be combined.

Taking these final calibration results into account, the uncertainties in the LEP energy contribute

errors of 1.8 MeV and 1.3 MeV to the OPAL determination of m_Z and Γ_Z respectively, as described in Section 11.2.1. At a scale a few times larger than the inherent precision of the LEP energy calibration an important and completely independent test of its consistency over time can be made by studying the stability in the value of m_Z measured over the six years of data-taking (see Table 32).

The values for the spread of the centre-of-mass energies, due to the energy spread of the particles in the beams, for the different running periods and energy points are summarised in Tables 20 and 21 of reference [**?**]. For the 1993–1995 data they range between 54.6-56.7 MeV, increasing with $\sqrt{s}$, and with uncertainties of 1.1 MeV in 1993–1994 and 1.3 MeV in 1995. The centre-of-mass energy spreads for data from years before 1993 have been re-evaluated using measurements made in subsequent years. They are between 43-53 MeV, with an error of 3 MeV. We quote our cross-sections and asymmetries both as measured and after correction for the energy spread, as described in Appendix C.

5 The luminosity measurement

All OPAL cross-section measurements rely on normalising the observed number of events in any given final state to the integrated luminosity measured by counting the number of Bhabha scattering events at angles small enough that t-channel photon exchange dominates the cross-section, and the influence of the Z is reduced to a small correction ($\lesssim 1\%$).

The SiW luminometer and the associated luminosity selection, which are fully described in [**?**], have been optimised to exploit the characteristics of Bhabha scattering, $e^+e^- \to e^+e^-$. The small-angle cross-section of $e^+e^- \to e^+e^-$ is dominated by the t-channel exchange of a photon, leading to a $1/\theta^3$ spectrum, where θ is the angle of the out-going electron and positron with respect to the incoming beams. By instrumenting a region at very small angles, the accepted $e^+e^- \to e^+e^-$ cross-section for SiW is approximately 79 nb, sufficiently larger than the total cross-section for Z production to limit the importance of the statistical uncertainty in the luminosity measurement. The forward-peaked $1/\theta^3$ Bhabha spectrum requires that the detector and luminosity analysis define the inner edge of the acceptance with particularly high precision in order to reduce the systematic error. For example, to achieve a precision of 10^{-3}, the inner edge of the acceptance must be known to 10 μrad, corresponding to about 25 μm in the radial coordinate of the showers produced in the calorimeters, which are located at a distance of approximately 2.5 m on each side of the beam crossing point.

For the measurement of the absolute luminosity, the experimental error achieved by the SiW luminometer is 3.4×10^{-4}, which includes all intrinsic and time-dependent sources of experimental uncertainty, such as detector geometry, gain variations, energy and positional biases in the detector response to electromagnetic showers, variations in the LEP beam geometry, backgrounds and other environmental influences. In 1995 the introduction of bunch-trains in LEP led us to install a "wagon tagger" [**?**] which allowed the luminometer to measure Bhabha-scattering events in all bunchlet crossings in each bunch-train with no compromise in performance.

For the first four years of the LEP 1 programme OPAL used the forward detectors [**?**] for measuring the luminosity with a resulting systematic uncertainty of 4.1×10^{-3}. This uncertainty dominates the total uncertainty on the hadronic pole cross-section obtained from the 1990–1992 data. The larger systematic error of the FD measurement leads to a reduced weight from the earlier data ($\sim 4\%$) in determining the hadronic cross-section. Since the SiW luminometer was installed in front of FD, obscuring its inner edge, no direct experimental cross-calibration of the two detectors is possible. A retrospective check of the hadronic peak cross-sections measured from the 1992 and 1994 data shows good agreement $(0.4 \pm 0.5)\%$.

The luminosity measurement requires that the theoretical cross-section for small-angle Bhabha scattering within the experimental acceptance be accurately calculated. At the time of our last Z resonance publication [**?**], techniques based on YFS exponentiation yielded an error of 2.5×10^{-3} [**?**]. These calculations have been extended to include second-order next-to-leading log terms [**?**], and calculations of third-order indicate that the error is 6.1×10^{-4} [**?**]. Improved calculations of light pair corrections within the OPAL SiW acceptance result in a final total theoretical error of 5.4×10^{-4} [**?**].

The scale of our previously published cross-sections, normalised with the FD luminometer, have been corrected in this analysis to incorporate these latest theoretical results in small-angle Bhabha scattering.

6 Measurement of $e^+e^- \to q\overline{q}$ events

In the SM about 87% of visible Z decays are expected to result in quark-antiquark pairs, leading to hadronic final states. These events therefore provide the most accurate determination of m_Z and Γ_Z. In general, hadronic events can be clearly distinguished from leptonic Z decays, or other background processes, due to their high multiplicity and large visible energy of final-state particles and the balance of visible momentum along the beam direction. Problems mainly arise for events consisting of two narrow jets in which most of the final-state particles have trajectories with only a very small angle relative to the beam axis. The geometrical coverage of the detector is incomplete in these regions, because of the beam pipe and associated apparatus, and therefore only a fraction of the particles from such an event are registered. The evaluation of the selection inefficiency which results from the loss of such events depends on the modelling of QCD effects in the process $q\overline{q} \to$ hadrons, which we subsequently refer to as "hadronisation" modelling. Since the treatment of hadronisation in Monte Carlo event generators is limited by phenomenological uncertainties, we have developed a new technique which uses the centre of the barrel region to emulate the setup and response of the detector close to the beam axis. This allows us to estimate the inefficiency using real data events and results in a factor of almost three reduction in the systematic error for the acceptance calculation compared to our previous publications [**?**, **?**].

6.1 Selection criteria

The selection of $e^+e^- \to q\overline{q}$ events uses the information from tracks reconstructed in the central detector (CT) and clusters of energy reconstructed in both the lead glass (ECAL) and the forward detector (FD) electromagnetic calorimeters. Tracks are typically reconstructed with good efficiency down to $\theta = 15^o$, ECAL clusters extend down to $\theta = 11^o$ and the FD covers the range from $3^o < \theta < 9^o$.

The selection is based on the following event parameters. $N_{\rm track}$ is the total number of tracks. $N_{\rm cluster}$ and $N_{\rm FD}$ are the total numbers of ECAL clusters and FD clusters, respectively. $E^i_{\rm cluster}$ is the energy of ECAL cluster i, $(i = 1, N_{\rm cluster})$. $E^j_{\rm FD}$ is the energy of FD cluster j, $(j = 1, N_{\rm FD})$, where a valid FD cluster must have at least 3 GeV. Each event is divided into two hemispheres with respect to the thrust axis of the event, which is determined using all the tracks and clusters in the event. The invariant mass of each hemisphere is calculated from the tracks and clusters which lie within it, assigning the pion mass to tracks and zero mass to clusters. No attempt is made to eliminate the implicit double counting of energy when using both track momenta and calorimeter energy for charged particles, such as electrons. The sum of these two hemisphere invariant masses is $m_{\rm hemi}$.
Five selection criteria are used to define a candidate $e^+e^- \to q\overline{q}$ event:

- Charged multiplicity: $N_{\rm track} \geq 2$.
- Total multiplicity: $N_{\rm all} \equiv N_{\rm track} + N_{\rm cluster} + N_{\rm FD} \geq 11$.
- Sum of the invariant masses of the two hemispheres: $m_{\rm hemi} > 4.5$ GeV.
- Visible energy in ECAL and FD: $E^{\rm mh}_{\rm cal}/\sqrt{s} \equiv \left(\sum_i E^i_{\rm cluster} + (\sum_j E^j_{\rm FD}/3)\right) / \sqrt{s} > 0.1$.
- Energy balance along the beam direction:

$$R^{\rm energy}_{\rm bal} \equiv \frac{\left|\sum_i (E^i_{\rm cluster} \cos\theta_i) + \sum_j (E^j_{\rm FD} \cos\theta_j)\right|}{(\sum_i E^i_{\rm cluster} + \sum_j E^j_{\rm FD})} < 0.75\,,$$

  where θ_i and θ_j are the polar angles of ECAL cluster i and FD cluster j, respectively.

Most Z decays to leptonic final states are rejected by the cuts on $N_{\rm all}$ and $m_{\rm hemi}$. The additional loose cut on $N_{\rm track}$ reduces the background arising from events induced by cosmic ray muons or showers. The requirements on $E_{\rm cal}^{\rm mh}/\sqrt{s}$ and $R_{\rm bal}^{\rm energy}$ suppress contributions from two-photon interaction processes. The factor 1/3, by which the weight of the FD energy is reduced in the construction of $E_{\rm cal}^{\rm mh}/\sqrt{s}$, is chosen to optimise the separation between $\mathrm{e^+e^-} \to \mathrm{q\overline{q}}$ signal events and two-photon background. A comparison of distributions of some of the cut variables between data and Monte Carlo simulation is shown in Figure 3.

The Monte Carlo prediction, based on the JETSET [**?**] event generator, for the $\mathrm{e^+e^-} \to \mathrm{q\overline{q}}$ selection inefficiency on-peak is $\bar{\varepsilon}^{\rm MC} = (48.1 \pm 1.1) \times 10^{-4}$ within $s'/s > 0.01$. The inefficiency of the selection is approximately constant as a function of s' down to $s'/s = 0.25$. For events with still harder initial-state radiation (ISR) it rises rapidly and approaches 100% for $s'/s = 0.01$, most events being rejected by the requirement on $R_{\rm bal}^{\rm energy}$. At the peak energy events with hard radiation ($s'/s < 0.25$) comprise only a small fraction (4×10^{-4}) of the total cross-section and about half of these fail the selection. At centre-of-mass energies away from the Z peak the relative rate of hard-radiation events is higher, which slightly reduces the efficiency compared to the peak. Changes of -4.7×10^{-4} and -1.4×10^{-4} were calculated using dedicated Monte Carlo samples at peak-2 and peak$+2$, respectively. In addition, a small contamination (0.3×10^{-4} at the peak) from selected events with $s'/s < 0.01$ is subtracted. Effects from multiple ISR, which are not simulated in the JETSET Monte Carlo generator, have been checked and were found to be negligible for determining the efficiency.

The total number of $\mathrm{e^+e^-} \to \mathrm{q\overline{q}}$ events selected from the 1993–1995 data samples is 2 908 566, giving a relative statistical error of 6×10^{-4}. In order to reduce the uncertainties on systematic effects to a corresponding level one must carefully disentangle the potential error sources and apply new techniques which base the corrections largely on the observed data properties. In the following subsections we first describe a method to determine the inefficiency due to events lost along the beam axis based on well-measured data events in the barrel region of the detector. We then discuss corrections and systematic errors associated with the selection of $\mathrm{e^+e^-} \to \mathrm{q\overline{q}}$ events and the background estimation. Unless specified otherwise the quoted correction factors and uncertainties refer to the 1994 peak data. Full details for all data periods are given in Table 3. Correlations between energy points and data-taking years are specified in Table 17.

6.2 Acceptance hole emulation

The overall inefficiency of the event selection is approximately 5×10^{-3}. Most events which are lost have narrow, two-jet final states pointing into the very small polar-angle region (large $|\cos\theta|$, close to the beam axis), where there is a "hole" in the acceptance. In contrast, the inefficiency in the entire barrel region is about 1×10^{-4}. One of the principal systematic errors in the Monte Carlo calculation of the selection inefficiency arises from uncertainties in the physics modelling of this class of events and hence in the evaluation of the rate of events lost in the acceptance hole. In order to match the goal of 5×10^{-4} acceptance uncertainty set by the statistical precision, the rate of such lost events must be understood at the 10 % level.

In previous OPAL analyses [**?**, **?**] this hadronisation uncertainty was assessed by comparing the inefficiencies predicted by different Monte Carlo generators, JETSET and HERWIG, and by using different parameter settings within the JETSET program, which led to a systematic error assignment of 0.11% in the cross-section. To reduce substantially this source of uncertainty a new technique was developed, which uses data events collected in the barrel region of the detector as a control sample. In this technique, which we refer to as the "acceptance hole emulation", we modify the response of both the real detector and its Monte Carlo simulation in the region surrounding the x-axis, *i.e.* perpendicular to the beam axis, to correspond closely to the actual gaps and imperfections in detector coverage around the z-axis.

The first step of the acceptance hole emulation is to identify a sample of hadronic Z events whose thrust axes lie within a well-defined cone around the x-axis, chosen to be large enough to safely cover the corresponding problematic region around the z-axis ($|\cos\theta_{\rm thr}| > 0.90$). This sample is complete

and unbiased due to the almost complete detection efficiency in the barrel region. We then emulate the detector response which would have been observed if the defining cone of this sample had been oriented along the z-axis by degrading the actual detector response correspondingly. Since CT plays a minor role in the selection, the edge of the CT acceptance is emulated simply by rejecting tracks which point within the corresponding narrow cone about the x-axis. For the most crucial detector component, ECAL, in addition to using such a geometric rejection, we emulate the position-dependent energy response and cluster separation near the edge of the hole. Similarly, the FD is emulated using the data from the ECAL clusters in the barrel by mapping the appropriate angular range, cluster size and energy threshold. Small adjustments of the selection cuts are made, such that the exclusive inefficiency of each cut[2] due to the emulated hole matches the corresponding inefficiency due to the endcap hole. We then re-apply the event selection criteria[3] to determine the inefficiency of the selection for the emulated, x-axis hole, $\bar{\varepsilon}_x^{\rm data}$.

This entire procedure is repeated with a sample of Monte Carlo events to determine the corresponding inefficiency of the selection in the x-axis hole, $\bar{\varepsilon}_x^{\rm MC}$. To the extent that the emulated holes in the Monte Carlo simulation and in the data are identical, the differences in $\bar{\varepsilon}_x^{\rm data}$ and $\bar{\varepsilon}_x^{\rm MC}$ will be exclusively due to departures in the Monte Carlo model of hadronisation. The ratio between the two emulated inefficiencies, $\bar{\varepsilon}_x^{\rm data}/\bar{\varepsilon}_x^{\rm MC}$, therefore provides a correction factor to the Monte Carlo calculation, which accounts for the imperfections in the hadronisation modelling. The overall corrected $\mathrm{e^+e^-} \to \mathrm{q\overline{q}}$ event selection inefficiency, $\bar{\varepsilon}^{\rm corr}$, is calculated as

$$\bar{\varepsilon}^{\rm corr} = \frac{\bar{\varepsilon}_x^{\rm data}}{\bar{\varepsilon}_x^{\rm MC}}\,\bar{\varepsilon}^{\rm MC}\ , \tag{1}$$

where $\bar{\varepsilon}^{\rm MC}$ is the overall selection inefficiency predicted by the Monte Carlo simulation. We obtain $\bar{\varepsilon}^{\rm corr} = (56.8 \pm 1.3) \times 10^{-4}$, which is 8.7×10^{-4} larger than $\bar{\varepsilon}^{\rm MC}$. Accounting for detector simulation deficiencies in the barrel region, as discussed in Section 6.3.1, reduces this difference to 5.5×10^{-4}. Note that it is sufficient to calibrate the rate of lost events with this method at the level of several per-cent. It is not necessary, or expected, that either $\bar{\varepsilon}_x^{\rm MC}$ or $\bar{\varepsilon}_x^{\rm data}$ gives an accurate estimate of the true inefficiency close to the z-axis. Small differences between the composition of the event samples along the x- and z-axes, such as introduced by initial-state radiation, are completely negligible for this purpose.

6.3 Selection uncertainties for $\mathrm{e^+e^-} \to \mathrm{q\overline{q}}$ events

In this subsection the various sources of systematic uncertainties in the selection of $\mathrm{e^+e^-} \to \mathrm{q\overline{q}}$ events are discussed. The acceptance hole emulation strongly reduces the dependence on the hadronisation modelling. However, it also introduces new systematic errors which are related to the quality of the hole emulation and the detector simulation in the barrel for determining $\bar{\varepsilon}_x^{\rm MC}$. The direct reliance on detector simulation for determining $\bar{\varepsilon}^{\rm MC}$ is the other main source of uncertainty. Here the simulation of the endcap detectors is of particular importance. In our previous analysis [**?**] a detector simulation uncertainty of 0.14% was assigned, based on the global comparison of data and Monte Carlo energy distributions. Such broad checks cannot distinguish between detector simulation problems and deficiencies in the physics modelling of the generator. They are also insensitive to possible local inhomogeneities in detector response. In order to disentangle these effects a new approach has been adopted which investigates in more detail the simulation of individual hadronic and electromagnetic showers in the calorimeters. Finally, the performance of the detector was carefully checked. Each aspect of triggering, data taking and data quality which could bias the selection has been examined.

[2]The inefficiency due to events which fail just the cut under discussion.

[3]In applying this event selection all axis-sensitive quantities, such as $R_{\rm bal}^{\rm energy}$, are transformed from the z-axis to the x-axis.

6.3.1 Systematic errors in the acceptance hole emulation

Three different sources contribute to systematic uncertainties of the acceptance hole emulation: (*i*) the residual hadronisation dependence, (*ii*) limitations of the acceptance hole emulation program, and (*iii*) the quality of the detector simulation in the barrel region for determining $\bar{\varepsilon}_x^{\mathrm{MC}}$. Table 4 summarises the corresponding uncertainties.

Residual hadronisation dependence: The sensitivity of the method to uncertainties in the modelling of hadronisation has been assessed by varying the parameters of the fragmentation model in the JETSET [**?**] Monte Carlo event generator and by employing an alternative Monte Carlo program, HERWIG [**?**], which uses a different fragmentation mechanism. As an example, we changed the JETSET parameter Q_0, the invariant mass cut-off below which gluon radiation stops, from its default value of 1.0 GeV to 1.8 GeV. This change corresponds to one standard deviation as determined from a global tuning of the JETSET parameters to OPAL LEP 1 data [**?**], and shifts $\bar{\varepsilon}^{\mathrm{MC}}$ by $(7 \pm 1) \times 10^{-4}$. Using the acceptance hole emulation, however, the corresponding shift in $\bar{\varepsilon}^{\mathrm{corr}}$ is only $(0.8 \pm 1.1) \times 10^{-4}$, which illustrates the effectiveness of the method. The variation of other fragmentation parameters yielded effects of similar size. The value of $\bar{\varepsilon}^{\mathrm{corr}}$ calculated using the sample of HERWIG Monte Carlo events differs by $(2.3 \pm 2.0) \times 10^{-4}$ compared to the reference value obtained using JETSET Monte Carlo events. We take this difference as the systematic error due to the residual sensitivity to hadronisation. A further uncertainty arises from the small inefficiency in the barrel region which is not addressed by the hole extrapolation. From similar Monte Carlo studies of the hadronisation dependence, *i.e.*, variation of fragmentation parameters and comparison of models, the largest change in this inefficiency is found to be $(2.2 \pm 0.5) \times 10^{-4}$, which is taken as an additional systematic error. The total direct hadronisation uncertainty is 3.2×10^{-4}.

Limitations of the acceptance hole emulation procedure: The detector setup and response differs substantially between barrel and endcap, therefore the emulation of the endcap hole in the barrel is only approximate. As discussed above the selection cuts for the barrel hole are adjusted to match the exclusive inefficiency in the endcap hole. This scaling of the cuts changes $\bar{\varepsilon}^{\mathrm{corr}}$ by 1.5×10^{-4} which we take as a systematic error. Furthermore, the radius defining the edge of the ECAL acceptance in the hole emulation program was varied over the full size of an ECAL block, which leads to an additional uncertainty of 0.4×10^{-4}.

Detector simulation in the barrel region: The acceptance hole emulation procedure relies on the quality of the barrel detector simulation for determining $\bar{\varepsilon}_x^{\mathrm{MC}}$. Figure 4 shows distributions of the emulated variables used in the cuts for events close to the x-axis. There are small offsets between the data and Monte Carlo prediction for the energy and multiplicity distributions, although the shapes of the distributions are well simulated. Rescaling the Monte Carlo energy and multiplicity distributions in order to correct for these differences changes the value of $\bar{\varepsilon}^{\mathrm{corr}}$ by 3.3×10^{-4}. Switching on and off the correction methods described in Section 6.3.2, which are independent of assumptions about hadronisation, gives a consistent difference in $\bar{\varepsilon}^{\mathrm{corr}}$. We take this value as a correction and assign to it a 100 % uncertainty.

In summary, the acceptance hole emulation leads to an efficiency correction of $(5.5 \pm 4.8) \times 10^{-4}$.

6.3.2 Detector simulation uncertainties

In addition to hadronisation uncertainties, which are reduced by the hole emulation study, the event selection efficiency also relies directly on the accuracy of the detector simulation for determining $\bar{\varepsilon}^{\mathrm{MC}}$. Since the main source of selection inefficiency occurs for events with jets close to the beam axis, the simulation of the detector response in the endcap region is more critical than that in the barrel region. The cut on $E_{\mathrm{cal}}^{\mathrm{mh}}/\sqrt{s}$ causes the largest inefficiency and consequently the most important issue is the simulation of the energy response in the ECAL and the FD.

The electromagnetic response of these calorimeters has been examined using lepton-pair events with an identified low-energy radiated photon. The measured photon energy is compared to the energy predicted from the momenta of the two leptons, assuming a three-particle final state. Checks are

made for global differences between data and Monte Carlo distributions and for local inhomogeneities. Most crucial for the $e^+e^- \to q\overline{q}$ event selection inefficiency are the regions just inside the edges of the acceptance, at small angles to the beam axis. The stability of the energy response of the ECAL endcap inner rings has been found to be good and the simulation is accurate to the 5% level. This corresponds to an uncertainty of 2.0×10^{-4} on the overall inefficiency. There are further small differences between the data and detector simulation for the remainder of the ECAL endcaps, leading to a further correction to the inefficiency of $(2.0 \pm 2.0) \times 10^{-4}$. A similar check for the FD electromagnetic response shows good consistency between data and Monte Carlo simulation. The statistical precision of this check translates into an uncertainty of 2.0×10^{-4} on the overall inefficiency.

The studies described above provide verification of the ECAL response to electromagnetic showers. Also important is the ECAL response to hadrons. The energy spectra of single ECAL clusters associated with isolated tracks in hadronic events were studied in narrow bins of track momentum in both data and Monte Carlo simulation. The simulation did not reproduce the response spectra exactly, although the mean detector behaviour was modelled adequately. The barrel, endcap, and overlap regions of the ECAL were studied separately. In each momentum bin and detector region a correction function depending on energy was then constructed to adjust the detailed shape of the simulated calorimeter response to match that observed in the data. When this correction is applied in the Monte Carlo event simulation to all ECAL energy deposits which arise from charged or neutral hadrons (using the measured and true particle momentum, respectively), the overall selection efficiency shifts by $(2.0 \pm 2.0) \times 10^{-4}$, which we take as a correction. The effect of the correction on the barrel ECAL response is used in deriving the hole emulation systematic uncertainty. Figure 5 shows the distribution of ECAL cluster energies for all tracks summed over all momenta from the data and from the Monte Carlo simulation before and after correction. The response of FD to hadrons plays a minor role for the selection since most hadronic showers remain below the threshold of 3 GeV required for a valid FD cluster. Therefore no additional uncertainty is assigned.

Overall, general improvements in the Monte Carlo simulation and detailed studies of the calorimeter response to electromagnetic and hadronic showers have reduced the direct detector simulation uncertainty, and result in an efficiency correction of $(4.0 \pm 4.0) \times 10^{-4}$.

6.3.3 Detector performance

The OPAL trigger system [**?**] uses a large number of independent signals from a variety of detector components. This information is combined to form many different event selection criteria, any one of which is sufficient to trigger the OPAL detector to be read out. The relatively low beam-induced background conditions of LEP 1 permit the choice of very loose settings for these trigger conditions. In general, $e^+e^- \to q\overline{q}$ events satisfy many independent trigger criteria. This redundancy allows the trigger inefficiency to be determined directly from the data. It is found to be less than 10^{-5}. Each subsequent step in the data-recording chain, from data acquisition, through online reconstruction, to the final writing of the data samples into the offline storage facility, was investigated. Possible effects, such as incorrect logging of detector status, bookkeeping discrepancies at various stages or failures of the event reconstruction have been examined. Only one problem has been found: very rarely, individual events suffer from high electronic noise levels in the central tracking detector, which causes the track reconstruction to fail. These events are not classified as $e^+e^- \to q\overline{q}$ candidates, which causes an inefficiency of about 0.8×10^{-4}. Both the short-term and long-term stability of each of the detector components used for the selection of $e^+e^- \to q\overline{q}$ events have been examined, as have distributions of the cut variables themselves. Only one significant effect has been found: for the FD small offsets in the energy distribution of the 1995 data give rise to an additional inefficiency of $(5 \pm 3) \times 10^{-4}$. The stability of the selection was checked by using alternative selection criteria, each based on data from only a single detector component. No notable effect is seen. In total an uncertainty of 2×10^{-4} is assigned due to irregularities in the detector performance during the 1993 and 1994 data-taking.

For the 1995 data further studies were performed to search for possible effects on the $e^+e^- \to q\overline{q}$ selection inefficiency due to the bunch-train mode of operation of LEP. As discussed in Section 2.1 the

bunch-train mode could potentially affect the CT reconstruction and the ECAL response. In order to check for such problems a tracking-independent selection has been developed, which is designed to overlap as much as possible with the standard selection. Within statistics no bunchlet-dependent effects are observed. The 3×10^{-4} precision of the check is assigned as a systematic uncertainty. Together with the FD energy offset discussed above and the general 2×10^{-4} data-taking uncertainty, the overall detector performance error for 1995 is 4.7×10^{-4}.

6.4 Background in the $e^+e^- \to q\overline{q}$ channel

The largest backgrounds to the $e^+e^- \to q\overline{q}$ event selection arise from $e^+e^- \to \tau^+\tau^-$ events and from two-photon interaction processes, $e^+e^- \to e^+e^-q\overline{q}$. The background fraction from $e^+e^- \to \tau^+\tau^-$ events is estimated to be 14.1×10^{-4} using the KORALZ Monte Carlo event generator [**?**]. Detailed studies of variables sensitive to $e^+e^- \to \tau^+\tau^-$ events indicate that the Monte Carlo simulation underestimates this background by 13%. Part of this underestimate is caused by deficiencies in the simulation of the conversion of radiated photons into electron-positron pairs. Taking this into account results in a corrected background estimate of $(15.9 \pm 2.0) \times 10^{-4}$, where the assigned systematic error is based on the observed discrepancy.

The background from two-photon interaction processes has been estimated directly from the data by making use of the characteristics of two-photon events. In general they have low visible energy, $E_{\rm cal}^{\rm mh}/\sqrt{s}$, and large energy imbalance along the beam-axis, $R_{\rm bal}^{\rm energy}$ (see Figure 3). The cross-section for two-photon processes is proportional to $\log s$ and therefore the cross-section changes by less than 1 % in the energy range between peak−2 and peak+2. Figure 6 shows, for the three energy points, the cross-sections for low $E_{\rm cal}^{\rm mh}/\sqrt{s}$ (0.10–0.18) or high $R_{\rm bal}^{\rm energy}$ (0.50–0.75) events versus the cross-section for events with high $E_{\rm cal}^{\rm mh}/\sqrt{s}$ (> 0.18) and low $R_{\rm bal}^{\rm energy}$ (< 0.50). Most events from two-photon processes fall into the former category, whereas the latter is completely dominated by hadronic Z decays. The constant cross-section from non-resonant background sources, mainly two-photon events, is obtained from the intercept of a straight-line fit to these data, which yields 0.051 ± 0.006 nb. The error is dominated by the data statistics available.

This estimate is corrected for the small fraction, $(7 \pm 5)\%$, of accepted two-photon events which fall outside the defined region of low $E_{\rm cal}^{\rm mh}/\sqrt{s}$ or high $R_{\rm bal}^{\rm energy}$ using the Monte Carlo generators PHOJET [**?**] and HERWIG [**?**], which simulate two-photon interactions. Furthermore, the estimate based on the data contains a small bias due to the larger fraction of events with high-energy initial-state radiation photons at the off-peak energy points. These events tend to have a high value of $R_{\rm bal}^{\rm energy}$ and therefore give a small contribution from signal events to the fitted non-resonant background. This bias is estimated using Monte Carlo simulation to be 0.004 ± 0.002 nb. Overall, the non-resonant background is 0.051 ± 0.007 nb, which amounts to $(16.7 \pm 2.3) \times 10^{-4}$ at the peak energy point.

The background from four-fermion processes other than two-photon interactions is evaluated using four-fermion event generators, FERMISV [**?**] for s-channel $\ell^+\ell^-\,f\overline{f}$ and PYTHIA [**?**] for t-channel $e^+e^-\,f\overline{f}$. Part of the t-channel four-fermion events are implicitly included in the two-photon subtraction. Adding the residual fraction and the s-channel four-fermion events results in a small contamination at the 0.4×10^{-4} level which is subtracted.

Other background sources are even lower; contributions from $e^+e^- \to e^+e^-$ and cosmic-ray induced events are estimated to be 0.2×10^{-4} each. There is no indication of any backgrounds induced by beam interactions with the residual gas in the LEP vacuum or the wall of the beam pipe.

7 Measurement of leptonic events

The branching fraction of the Z boson to charged leptons is approximately 10%. Consequently the leptonic decays provide less information on $m_{\rm Z}$ and $\Gamma_{\rm Z}$ than the hadronic decays of the Z. Since the Z bosons we observe at LEP are all produced through their coupling to electrons in the initial state, however, the measurement of the leptonic decay channels is of particular interest. By measuring the cross-sections for all visible Z decays, including electrons, the absolute branching fraction to invisible

final states can be determined. Assuming these states are exclusively neutrinos coupling to the Z according to the SM then allows the effective number of such light neutrino species to be determined.

In contrast to the quarks in hadronic events, the charge of the leptons can be determined almost unambiguously, thereby allowing the forward-backward charge asymmetry, $A_{\rm FB}$, to be measured. Measurements of $A_{\rm FB}$ determine the relative strengths of the vector and axial-vector couplings of the Z to each of the three charged lepton species, $g_{{\rm V}\ell}/g_{{\rm A}\ell}$. In the SM, this ratio is related to the weak mixing angle, $\sin^2\theta_{\rm W}$. When combined with the $\ell^+\ell^-$ cross-sections, which are proportional to $g^2_{{\rm V}\ell} + g^2_{{\rm A}\ell}$, the couplings $g_{{\rm A}\ell}$ and $g_{{\rm V}\ell}$ are determined. In addition, comparisons among the partial Z decay widths to the three charged lepton species and the respective forward-backward asymmetries provide a precise test of the lepton universality of the neutral current.

7.1 Introduction

Leptonic decays of the Z boson, $\mathrm{e^+e^-} \to \ell^+\ell^-$, result in low multiplicity events. The different leptonic species are distinguished from each other mainly using the sum of the track momenta, $p_{\rm total}$, and the energy deposited in the electromagnetic calorimeter, $E_{\rm total}$. The total momentum is calculated as a scalar sum over the individual track momenta, $p_{\rm total} = \sum p^i_{\rm track}$. Similarly the total energy is the sum of the energies of the individual clusters in the electromagnetic calorimeter, $E_{\rm total} = \sum E^i_{\rm cluster}$. Figure 7 shows the distribution of $(p_{\rm total}, E_{\rm total})$ for a small sample of Monte Carlo $\mathrm{e^+e^-} \to \ell^+\ell^-$ events. The $\mathrm{e^+e^-} \to \mathrm{e^+e^-}$ events have both $E_{\rm total}$ and $p_{\rm total}$ concentrated around the centre-of-mass energy, $\sqrt{s}$. However, due to final-state and Bremsstrahlung photons the distribution of $p_{\rm total}$ extends to lower values. The $\mathrm{e^+e^-} \to \mu^+\mu^-$ events are concentrated around $p_{\rm total} = \sqrt{s}$ and have low values of $E_{\rm total}$. Final-state radiation has the effect of producing a small tail of events at higher values of $E_{\rm total}$ and correspondingly lower values of $p_{\rm total}$. Due to the undetected neutrinos from τ decays in $\mathrm{e^+e^-} \to \tau^+\tau^-$ events the distributions of both $E_{\rm total}$ and $p_{\rm total}$ are broad but well separated from the other leptonic decays of the Z, with only a few events with $E_{\rm total}$ or $p_{\rm total}$ close to $\sqrt{s}$. Cuts on the global quantities $E_{\rm total}$ and $p_{\rm total}$ provide the basis for separating the different leptonic decay modes.

Detailed descriptions of the selection criteria for the three different $\mathrm{e^+e^-} \to \ell^+\ell^-$ categories are described in Sections 7.2-7.4. The event selections use a series of cuts to reject background. The selections are exclusive, with no event allowed to be classified in more than one category. The largest backgrounds in the selected $\mathrm{e^+e^-} \to \mathrm{e^+e^-}$, $\mu^+\mu^-$ and $\tau^+\tau^-$ event samples arise from cross-contamination between the three lepton species. The treatment of four-fermion final states is discussed in Appendix A.1. Backgrounds from the processes, $\mathrm{e^+e^-} \to \mathrm{q\overline{q}}$, $\mathrm{e^+e^-} \to \mathrm{e^+e^-}\ell^+\ell^-$, $\mathrm{e^+e^-} \to \gamma\gamma$ and cosmic ray events, are all relatively small. The background from $\mathrm{e^+e^-} \to \mathrm{q\overline{q}}$ is rejected by cuts on the number of observed tracks and the number of clusters in the electromagnetic calorimeter. In two-photon processes, $\mathrm{e^+e^-} \to \mathrm{e^+e^-}\ell^+\ell^-$, the scattering angles of the incident electron and positron tend to be close to the beam direction, beyond the experimental acceptance. This source of background is rejected by lower bounds on variables such as $E_{\rm total}$ or $p_{\rm total}$. Background from cosmic rays is removed by requiring the event to originate from the $\mathrm{e^+e^-}$ interaction region and to be in time with the $\mathrm{e^+e^-}$ beam crossing.

7.1.1 Corrections and systematic uncertainties

Estimates of selection efficiencies and accepted background cross-sections are obtained from Monte Carlo samples generated at peak and off-peak centre-of-mass energies. These efficiencies are corrected to the s' acceptance specified in Section 3 and are also corrected to account for interference between initial- and final-state radiation diagrams (see Appendix A.2). Data and Monte Carlo distributions are compared to assess the quality of the simulation for each cut used in the event selection and where necessary, corrections are derived. Depending on the exact nature of the systematic check, a single correction factor is often adequate to describe all 1993–1995 data. Otherwise, where the effect under consideration is related to the performance of the detector, independent corrections are determined for each year. Similarly, when the effect depends on the centre-of-mass energy, different corrections are derived for each of the different centre-of-mass energy points. The derived corrections greatly reduce

the dependence on the accuracy of the Monte Carlo simulation.

There are two important sources of detector-related systematic uncertainty which affect each of the three lepton channels. The largest potential source of systematic bias arises from imperfect simulation of the detector response to charged particles whose paths lie near one of the wire planes of the jet chamber. The wire planes, which create the drift field, are situated at 7.5° intervals in azimuth around the chamber, alternating between the anode and cathode planes which form the 24 sectors of the jet chamber. The reconstruction of tracks within ±0.5° of an anode wire plane can be problematic due to field distortions. This does not cause problems for low momentum tracks, which bend significantly in the axial magnetic field, since only a small fraction of the trajectory will be close to a wire plane. For high momentum particles with relatively straight trajectories, such as muons and electrons from $e^+e^- \to \ell^+\ell^-$, a serious degradation of track quality can occur in a small fraction of the events where most of the track lies near an anode wire plane. This can result in a degraded momentum measurement, single tracks being reconstructed as two tracks (split across a wire plane) or, in the worst instance, failure to reconstruct the track at all, resulting in 'lost' tracks. Field distortions close to the wire planes are simulated in the Monte Carlo but the numbers of tracks affected is significantly underestimated. These effects are particularly important in the selection of $e^+e^- \to \mu^+\mu^-$. Events where the measured momentum of one of the muons is anomalously low, due to wire plane effects, result in the Monte Carlo prediction of 0.3% for the selection inefficiency being under-estimated by approximately 0.4% compared to the true value. Significant corrections to the Monte Carlo selection efficiencies, relating to these tracking problems, are therefore obtained from the data. Since $e^+e^- \to \mu^+\mu^-$ events measured to have anomalously low total momenta are classified as $e^+e^- \to \tau^+\tau^-$, the uncertainties in these corrections lead to anti-correlated errors in the $\mu^+\mu^-$ and $\tau^+\tau^-$ selections. Details are given in Sections 7.3.2 and 7.5.

The measurement of energy in the electromagnetic calorimeter plays the primary role in the selection of $e^+e^- \to e^+e^-$ events and in discriminating them from $e^+e^- \to \tau^+\tau^-$. An uncertainty in the energy scale or in the response of the ECAL can therefore introduce correlated uncertainties in the e^+e^- and $\tau^+\tau^-$ cross-section measurements. The Monte Carlo simulation underestimates the fraction of e^+e^- events which fail the selection due to imperfect Monte Carlo modelling of the response of the electromagnetic calorimeter near the mechanical boundaries between calorimeter modules, at $\phi = \pm 90°$ and $|\cos\theta| = 0.22$ and 0.60. In addition, there is an unsimulated problem in the electronic gain calibration for two out of the 9440 barrel lead glass blocks for the 1994 and 1995 data samples. As a result the Monte Carlo estimates of the $e^+e^- \to e^+e^-$ selection efficiency need to be corrected by $0.1 - 0.2\%$. Details are given in Sections 7.2.3 and 7.5.

7.1.2 Trigger efficiency for $e^+e^- \to \ell^+\ell^-$ events

Low multiplicity events from $e^+e^- \to \ell^+\ell^-$ produce relatively few energy deposits in the detector. As a result, there is the potential that events are lost due to trigger inefficiency. The trigger efficiency for $e^+e^- \to \ell^+\ell^-$ events is determined using independent sets of trigger signals [**?**] from the electromagnetic calorimeters, from the tracking chambers, from the muon chambers and from the time-of-flight counters. The efficiencies are determined in bins of polar and azimuthal angle and then combined into an overall efficiency. When averaged over the three years of data analysed here, the trigger efficiencies for the $e^+e^- \to e^+e^-$, $\mu^+\mu^-$ and $\tau^+\tau^-$ selections are $(> 99.99)\%$, $(99.96 \pm 0.01)\%$ and $(99.98 \pm 0.01)\%$ respectively. The online event filter [**?**] is found to be 100% efficient for $e^+e^- \to \ell^+\ell^-$ events and no systematic error is assigned.

7.2 Selection of $e^+e^- \to e^+e^-$ events

The selection of $e^+e^- \to e^+e^-$ events is accomplished with high efficiency and purity by requiring low-multiplicity events with large total electromagnetic energy and by requiring at least two electron[4]

[4]Throughout this section the word "electron" should be understood to imply "electron or positron". Where a distinction is required, the symbols e^- and e^+ are used.

candidates. In order to maintain high efficiency, an electron is identified simply as a high energy deposit in the electromagnetic calorimeter which is associated with a track in the central detector. The main experimental systematic uncertainties are from the energy response of the calorimeter, the edge of the polar angle acceptance, the track reconstruction quality and the background from $e^+e^- \to \tau^+\tau^-$ events.

7.2.1 *t*-channel contribution to $e^+e^- \to e^+e^-$

The analysis of *s*-channel Z decays into e^+e^- pairs is complicated by indistinguishable contributions from *t*-channel scattering processes, and interference between *s*- and *t*-channels. The *t*-channel amplitude is non-resonant and is dominated by photon-exchange. These contributions are accounted for when fitting the $e^+e^- \to e^+e^-$ data (see Appendix B), but statistical and systematic uncertainties on the magnitude of the *t*-channel contribution result in an overall reduction of the sensitivity of the $e^+e^- \to e^+e^-$ analysis to the Z properties. The relative size of the *t*-channel amplitude depends on the scattering angle (polar angle) of the electron, θ_{e^-}, and becomes the major component at high values of $\cos\theta_{e^-}$. In order to enhance the *s*-channel component of the selected data sample, a cut is made, for the $e^+e^- \to e^+e^-$ analysis only, constraining the polar angle to lie well within the barrel region of the detector ($|\cos\theta_{e^-}| < 0.70$, see Section 7.2.2). The relative size of the *t*-channel component is larger for the off-peak data samples than the $\sim 15\%$ it represents on-peak, due to the reduction of the *s*-channel contribution from the Z resonance. This results in small differences in efficiencies, backgrounds and systematic uncertainties amongst the $e^+e^- \to e^+e^-$ data samples at different energy points. Because of the *t*-channel diagram the differential cross-section rises steeply in the forward direction, resulting in an increased sensitivity to the precise definition of the edge of the acceptance in $\cos\theta_{e^-}$.

7.2.2 Selection criteria for $e^+e^- \to e^+e^-$

The selection criteria for $e^+e^- \to e^+e^-$ events make use of information from the electromagnetic calorimeter and the central tracking detectors by requiring:

- Low multiplicity:

  $2 \le N_{\rm track} \le 8$ and $2 \le N_{\rm cluster} \le 8$,

  where $N_{\rm track}$ is the number of tracks and $N_{\rm cluster}$ is the number of clusters.

- High energy clusters:
  The energies of the highest energy, E_1, and second highest energy, E_2, clusters must satisfy

  $E_1 > 0.2\sqrt{s}$ and $E_2 > 0.1\sqrt{s}$.

- Total electromagnetic energy:

  $E_{\rm total} \equiv \sum E^i_{\rm cluster} > 0.80\sqrt{s}$.

- Two electrons:
  At least two of the three highest energy clusters of energy above 2 GeV must be associated with a track, which is required to point to the cluster position to within $\Delta\phi < 5^\circ$ in azimuth and to within $\Delta\theta < 10^\circ$ in polar angle. These clusters are identified as electron candidates.

- Geometrical and kinematic acceptance:

  $|\cos\theta_{e^-}| < 0.70$ and $\theta_{\rm acol} < 10^\circ$,

  where $\theta_{\rm acol}$ is the acollinearity angle of the e^+e^- pair, defined as $180^\circ - \alpha$, where α is the opening angle between the directions of the two tracks.

These criteria select 96 669 events from the 1993–1995 data sample. The efficiency and background are first estimated using a sample of Monte Carlo events. Corrections to these estimates are obtained by studying the data. The correction factors and their associated systematic errors are summarised

in Table 5 for the seven data samples recorded during 1993–1995 at the three energy points. The systematic errors for the seven data samples are strongly correlated, as shown in Table 18. The main corrections and systematic uncertainties are described below.

7.2.3 Selection efficiency for $e^+e^- \to e^+e^-$

The Monte Carlo prediction for the $e^+e^- \to e^+e^-$ selection efficiency within the geometrical acceptance of $|\cos\theta_{e^-}| < 0.70$ is $(99.44 \pm 0.02)\%$ for peak data. The main corrections to this efficiency and related systematic errors are described below.

Electromagnetic energy cuts: The main effect of the cut on $E_{\rm total} > 0.8\sqrt{s}$, shown in Figure 8(a), is to remove background from $e^+e^- \to \tau^+\tau^-$. From the Monte Carlo simulation only 11×10^{-4} of $e^+e^- \to e^+e^-$ events are rejected by this cut. There is a discrepancy between data and Monte Carlo in the vicinity of the cut, due to imperfect Monte Carlo modelling of the electromagnetic calorimeter response near the mechanical boundaries between calorimeter modules and a problem with the electronic gain calibration for two lead glass blocks in 1994 and 1995. These two effects introduce additional inefficiencies for the data, estimated to be $(9 \pm 10) \times 10^{-4}$, $(22 \pm 7) \times 10^{-4}$ and $(17 \pm 8) \times 10^{-4}$ for 1993, 1994 and 1995, respectively. These efficiency corrections are obtained from a detailed study of events which fail only the cut on electromagnetic energy. For these events, the acoplanarity, $\phi_{\rm acop} \equiv ||\phi_{e^-} - \phi_{e^+}| - 180^\circ|$, and the sum of the track momenta, $p_{\rm total}$, are used to discriminate $e^+e^- \to e^+e^-$ events from the dominant $e^+e^- \to \tau^+\tau^-$ background. The distribution of $\phi_{\rm acop}$ for events which fail only the cut on electromagnetic energy is shown in Figure 8(b). The $\phi_{\rm acop}$ distribution for $e^+e^- \to e^+e^-$ events is strongly peaked at 0°. The distribution for $e^+e^- \to \tau^+\tau^-$ events is broader due to the momentum transverse to the tracks which is carried away by the unobserved neutrinos from the τ decays. The excess of data events compared to Monte Carlo near $\phi_{\rm acop} = 0^\circ$ indicates that the excess of events in the region of the cut arises from $e^+e^- \to e^+e^-$. This interpretation is corroborated by the distribution of $p_{\rm total}/\sqrt{s}$ for events in the region of small $\phi_{\rm acop}$, shown in Figure 8(c), where the excess of data over Monte Carlo events is clustered near $p_{\rm total}/\sqrt{s} = 1.0$. The efficiency corrections are derived from the distributions of $\phi_{\rm acop}$ and $p_{\rm total}$ in the region $0.6\sqrt{s} < E_{\rm total} < 0.8\sqrt{s}$.

Electron identification: Electron candidates are defined as electromagnetic clusters of energy greater than 2 GeV which are associated with a track. An electron can fail these requirements if the track associated with the cluster is of very low momentum, due to hard bremsstrahlung in the material in front of the tracking detectors. It can also fail due to the emission of a hard final state photon or if, due to poor track reconstruction, the track fails the geometrical matching conditions or the track quality requirements.

The inefficiency arising from the demand for at least two electron candidates is estimated from Monte Carlo simulation to be $(39 \pm 2) \times 10^{-4}$ for $e^+e^- \to e^+e^-$. The inefficiency in the data is assessed from a sample of events where only one electron candidate is found. This control sample is obtained by assuming the electrons in the event correspond to the two highest energy clusters, only one of which is identified as an electron candidate on the basis of the tracking requirements. The background from the non-resonant QED process $e^+e^- \to \gamma\gamma$ where one of the photons has converted to an e^+e^- pair is reduced by removing events where two tracks are associated to the same cluster. Within this sample there are more events in the data than the Monte Carlo predicts. The excess is concentrated in the regions of ϕ near the wire planes of the jet chamber. In this region the polar angle resolution for reconstructed tracks can be degraded sufficiently such that the track no longer points to the cluster. The excess of data over the Monte Carlo prediction is used to evaluate a correction to the Monte Carlo estimate for these inefficiencies. The size of the correction differs for each year of data-taking. For example in the 1994 data an efficiency correction of $(26 \pm 5) \times 10^{-4}$ is derived.

Acceptance definition: The geometrical and kinematic acceptance for $e^+e^- \to e^+e^-$ events is defined by cuts on $|\cos\theta_{e^-}|$ and on $\theta_{\rm acol}$, shown in Figure 9. The polar angle cut is made with respect to θ_{e^-}, the direction of the negatively charged lepton as measured in the electromagnetic calorimeter.

This is determined from an energy-weighted average of the positions of the lead glass blocks which form the cluster, which is then corrected for biases caused by showering in the material in front of the calorimeter. The existence of any systematic offset between the reconstructed cluster position and the actual trajectory of the electron was studied by measuring the displacement between well measured electron tracks and their associated clusters near the critical $\cos\theta$ boundaries. These studies indicated that the effective edge of the acceptance is offset symmetrically from the nominal cut value towards $\cos\theta_{\mathrm{e}^-} = 0$ by 0.0004 ± 0.0006 at $\cos\theta_{\mathrm{e}^-} = \pm 0.70$. Consistent displacements were obtained in both the data and Monte Carlo simulation. The central value of the offset is obtained from the high-statistics Monte Carlo samples and the uncertainty is taken as the statistical precision of the study based on data. For the peak data the uncertainty in the location of the $\cos\theta_{\mathrm{e}^-} = \pm 0.70$ boundary results in an uncertainty of $\pm 9 \times 10^{-4}$ in the measured cross-section.

Further corrections and uncertainties: The inefficiency arising from the multiplicity cuts is estimated to be $(1 \pm 1) \times 10^{-4}$. This estimate is obtained from the simulation and checked by examining the electromagnetic calorimeter energy distribution for the events which fail only the multiplicity cuts. The trigger inefficiency is determined to be less than 5×10^{-5} and no correction is applied. Corrections related to four-fermion events, determined as described in Appendix A.1, are negligible and a 2×10^{-4} uncertainty is assigned.

7.2.4 Background in the $\mathrm{e^+e^-} \to \mathrm{e^+e^-}$ channel

The expected background in the peak data samples is $(34 \pm 6) \times 10^{-4}$, dominated by $\mathrm{e^+e^-} \to \tau^+\tau^-$. The energy-dependence of the $\mathrm{e^+e^-} \to \mathrm{e^+e^-}$ cross-section is different from the other s-channel fermion-pair production processes due to the t-channel photon exchange contributions. Consequently the background fraction is dependent on centre-of-mass energy.

Background from $\mathrm{e^+e^-} \to \tau^+\tau^-$: The Monte Carlo estimate of this background for the peak energy point is $(32 \pm 1) \times 10^{-4}$. The majority of the $\mathrm{e^+e^-} \to \tau^+\tau^-$ background is rejected by the cut $E_{\mathrm{total}} > 0.8\sqrt{s}$, shown in Figure 8(a). The distribution of $E_{\mathrm{total}}/\sqrt{s}$ is well reproduced by the Monte Carlo simulation in the region dominated by the $\mathrm{e^+e^-} \to \tau^+\tau^-$ background, $E_{\mathrm{total}} < 0.70\sqrt{s}$. To investigate the level of the background within the $\mathrm{e^+e^-} \to \mathrm{e^+e^-}$ sample, events just above the energy cut are selected, $0.8 < E_{\mathrm{total}}/\sqrt{s} < 0.9$. For these events the data and Monte Carlo distributions of p_{total} and ϕ_{acop} are again used to distinguish $\mathrm{e^+e^-} \to \mathrm{e^+e^-}$ events from $\mathrm{e^+e^-} \to \tau^+\tau^-$. The Monte Carlo estimate of the $\mathrm{e^+e^-} \to \tau^+\tau^-$ background has been found to be consistent with the observations from the data, to within the statistical errors of the comparisons made. The systematic uncertainty on the $\mathrm{e^+e^-} \to \tau^+\tau^-$ background for the peak energy point is estimated to be 6×10^{-4}.

Other backgrounds: The energy deposits in the electromagnetic calorimeter from $\mathrm{e^+e^-} \to \gamma\gamma$ events are similar to those from $\mathrm{e^+e^-} \to \mathrm{e^+e^-}$ events. However, for $\mathrm{e^+e^-} \to \gamma\gamma$ events to pass the electron identification requirements the two electromagnetic calorimeter clusters both must have associated tracks. The probability that both the photons convert is about 1% and the $\mathrm{e^+e^-} \to \gamma\gamma$ cross-section is relatively small. Consequently, the background fraction in the $\mathrm{e^+e^-} \to \mathrm{e^+e^-}$ sample is small ($\sim 1 \times 10^{-4}$). The background from hadronic events is estimated to be about the same size. A 100% relative uncertainty is assigned to the background from hadronic events and to that from $\mathrm{e^+e^-} \to \gamma\gamma$ events. Backgrounds from two-photon interaction processes, $\mathrm{e^+e^-} \to \mathrm{e^+e^-f\bar{f}}$, and from cosmic ray events are less than 1×10^{-4}. No correction is applied, and this estimate is taken as a systematic error.

7.3 Selection of $\mathrm{e^+e^-} \to \mu^+\mu^-$ events

Of the three $\mathrm{e^+e^-} \to \ell^+\ell^-$ channels, the $\mu^+\mu^-$ final state provides the cleanest environment for precise measurements of the $\ell^+\ell^-$ cross-sections and asymmetries. The $\mu^+\mu^-$ channel does not suffer from the theoretical uncertainties associated with t-channel corrections in the $\mathrm{e^+e^-}$ final state nor

the systematic uncertainties arising from the less well defined experimental signature of the $\tau^+\tau^-$ final state. However, of the three lepton channels, $\mu^+\mu^-$ events are the most sensitive to systematic uncertainties arising from track reconstruction. The $e^+e^- \to \mu^+\mu^-$ events are separated from other Z decays and background processes by requiring exactly two tracks to be reconstructed in the central detector both of which are identified as muons. The cross-sections are measured within the phase space region defined by $m^2_{\mu\mu}/s > 0.01$. The selection criteria are summarised below.

7.3.1 Selection criteria for $e^+e^- \to \mu^+\mu^-$

The selection criteria for $e^+e^- \to \mu^+\mu^-$ events are:

- Two tracks:
  Exactly two tracks are required each of which satisfies

  $$p_{\rm track} > 6 \text{ GeV}, \quad |\cos\theta| < 0.95,$$

  where $p_{\rm track}$ is the track momentum and θ is the reconstructed polar angle. Tracks identified as coming from photon conversions are not counted.

- Azimuthal separation:
  The azimuthal angular separation between the two tracks must satisfy $\cos(\Delta\phi) < 0.95$, *i.e.* $\Delta\phi > 18°$, to avoid difficulties in the muon identification of two closely separated tracks.

- Muon identification:
  Both tracks must satisfy at least one of the following three muon identification criteria:

  (a) At least two muon chamber hits are associated with the track.

  (b) At least four hadronic calorimeter strips are associated with the track. The average number of strips in layers containing hits has to be less than two, in order to reject hadronic showers. For $|\cos\theta| < 0.65$, where tracks traverse all nine layers of strips in the barrel calorimeter, at least one hit in the last three layers of strips is required.

  (c) The track has $p_{\rm track} > 15$ GeV and the sum of the energy deposited in the electromagnetic calorimeter within a cone of half-angle 63 mrad about the track is less than 3 GeV.

- Visible energy:
  Backgrounds from $e^+e^- \to \tau^+\tau^-$ and two-photon interaction events are reduced by requiring

  $$E^{\mu}_{\rm vis} > 0.6\sqrt{s},$$

  where the visible energy, $E^{\mu}_{\rm vis}$, is the scalar sum of the two track momenta and the energy of the highest energy cluster found in the electromagnetic calorimeter.

- Despite the fact that the OPAL detector is situated in a cavern 100 m underground there is still a large flux of cosmic ray particles. The majority of these are muons which traverse the detector volume. Those which happen to pass close to the beam interaction point and which are synchronous with a bunch crossing can resemble $e^+e^- \to \mu^+\mu^-$ events. Cosmic ray background is rejected by requiring that the selected events originate from the average e^+e^- interaction point and are coincident in time with the beam crossing.

These criteria select 128 682 events which enter the cross-section analysis from the 1993–1995 data sample. Control samples from the data are used to check and, where necessary, correct the Monte Carlo estimates. The dominant corrections are due to tracking losses and the residual background from $e^+e^- \to \tau^+\tau^-$ events. The resulting correction factors and their systematic errors are summarised in Table 6 for the seven data samples recorded during 1993–1995 at the three energy points. The systematic errors of the seven data samples are strongly correlated as shown in Table 19. Unless otherwise specified, the illustrative errors quoted in the following text refer to the 1994 sample.

7.3.2 Selection efficiency for $e^+e^- \to \mu^+\mu^-$

The Monte Carlo prediction for the $e^+e^- \to \mu^+\mu^-$ selection efficiency is $(91.34 \pm 0.05)\%$. This corresponds to a selection efficiency of $(98.40 \pm 0.03)\%$ within the geometric acceptance of $|\cos\theta_{\mu^-}| < 0.95$. Small corrections are then applied to account for the Monte Carlo events generated below the ideal kinematic acceptance limit of $m^2_{\bar{f}f}/s > 0.01$, and for interference between photons radiated in the initial and final states, as described in Appendix A.2. Using the 1994 data as an example, the selection efficiency from the Monte Carlo simulation is then corrected by $(-76 \pm 8) \times 10^{-4}$ through comparisons with the data. The main efficiency corrections and systematic errors are described below.

Tracking losses: The selection of $e^+e^- \to \mu^+\mu^-$ events relies heavily on track reconstruction in the central detector, which is required to measure $E^{\mu}_{\rm vis}$ and to associate tracks with activity in the outer detectors used for muon identification. As discussed in Section 7.1.1, of particular concern are tracks whose paths lie within $\pm 0.5^\circ$ of an anode wire plane of the jet chamber. Figure 10(a) shows the distribution of $E^{\mu}_{\rm vis}$ for events passing all other selection cuts. There is a clear discrepancy between data and Monte Carlo. The origin of this discrepancy is the imperfect Monte Carlo simulation of tracking in the region close to the jet chamber wire planes. The discrepancy becomes more apparent in Figure 10(b) which shows the corresponding $E^{\mu}_{\rm vis}$ distribution for tracks within 0.5° of the anode wire planes.

The wire plane effect was investigated using an alternative $e^+e^- \to \mu^+\mu^-$ selection procedure. This selection is independent of the central detector, relying instead on back-to-back signals in the muon chambers (within 30 mrad) and electromagnetic calorimeters (within 50 mrad). By using relatively tight cuts on the acollinearity measured in the outer detectors the background from $e^+e^- \to \tau^+\tau^-$ events is strongly suppressed. This is mainly due to the greater deflection in the magnetic field experienced by the lower momentum charged particles from τ decays. Background is suppressed further by requiring at least one identified muon in the event. The efficiency of the tracking-independent selection is approximately 79%.

The events which are selected by the tracking-independent selection but fail the default $\mu^+\mu^-$ selection are concentrated in regions where one of the muons passes near a jet-chamber wire plane. The numbers of "lost" $e^+e^- \to \mu^+\mu^-$ events, selected by these cuts, are corrected for the inefficiency of the tracking-independent selection. The corrected numbers are compared between data and Monte Carlo simulation in bins of $\cos\theta$ for each year of data taking. There is an excess of lost events in the data, indicating that the Monte Carlo estimate of 30×10^{-4} for the inefficiency due to tracking problems is too low. The difference is $(42 \pm 4) \times 10^{-4}$ for the 1994 data. The uncertainties are the combined statistical errors of the data and Monte Carlo control samples. The correction factors obtained in this manner are applied to the Monte Carlo inefficiency estimates.

Track multiplicity cuts: In addition to the tracking losses discussed above, 0.5% of $e^+e^- \to \mu^+\mu^-$ events are rejected by the requirement of exactly two tracks due to additional tracks from converted final-state photons which have failed to be classified as such, or if a track is poorly reconstructed and split into two tracks. A correction to the Monte Carlo prediction for the inefficiency due to this cut is made on the basis of a visual scan of both data and Monte Carlo events containing three, four or five tracks, but which otherwise pass the $e^+e^- \to \mu^+\mu^-$ selection. The resulting corrections, typically less than 10^{-3}, are listed in Table 6, with the errors reflecting the data and Monte Carlo statistics and the uncertainty of the scanning procedure.

Muon identification: Both tracks in a selected $e^+e^- \to \mu^+\mu^-$ event are required to be identified as muons using data from at least one of three independent detector subsystems; the muon chambers, the hadronic calorimeter and the electromagnetic calorimeter. The Monte Carlo estimate of the inefficiency introduced by the muon identification requirement is $(79 \pm 5) \times 10^{-4}$. Most of this inefficiency occurs in geometrical regions where either the muon chamber coverage or the hadronic calorimeter coverage are incomplete. In particular, for one sixth of the total azimuth in the polar angle range $0.65 < |\cos\theta| < 0.85$ these gaps overlap due to support structures, leaving coverage only from the

electromagnetic calorimeter. For collinear $e^+e^- \to \mu^+\mu^-$ events there is a high degree of correlation between the muon identification inefficiencies of the two tracks due to the symmetry of the detectors.

The redundancy of the three muon identification requirements is used to determine the single track muon identification efficiency in bins of azimuthal and polar angle. For each muon identification criterion, the muon identification criteria from the other two outer detectors are used to define a control sample of tagged muons. The single track efficiencies, determined in bins of $(\cos\theta, \phi)$, are used to calculate overall muon identification inefficiencies for $e^+e^- \to \mu^+\mu^-$ events accounting for expected angular distributions. The total inefficiency determined in this way is compared between data and Monte Carlo prediction separately for each year of data. There is good agreement for the 1993 and 1995 data, and no correction is applied. For the 1994 data, it is found that the inefficiency from the corresponding Monte Carlo sample needs to be corrected by $(15 \pm 4) \times 10^{-4}$ where the errors reflect the statistical power of the checks. The correction arises due to inadequate simulation of the response of the hadron calorimeter in the Monte Carlo sample used to simulate data from the 1994 operation of the OPAL detector.

Acceptance definition: Both muon tracks are required to lie within the geometrical acceptance $|\cos\theta| < 0.95$. The measurement of $\cos\theta$ in this region therefore affects the overall event selection inefficiency and any discrepancy between data and Monte Carlo simulation must be corrected. A 1 mrad bias in angle at $|\cos\theta| = 0.95$ corresponds to a bias in the acceptance of 5×10^{-4}.

For muon tracks there are generally three separate detector components which can be used to measure $\cos\theta$; the track reconstructed in the central detector, the energy cluster in the electromagnetic calorimeter and the track found in the muon chambers. For muons close to $|\cos\theta| = 0.95$ the end-cap muon chambers have the best polar angle resolution, approximately 1 mrad, and this measurement is used when available, otherwise the angle from the reconstructed central detector track is used (about 10% of cases). The changes to the numbers of $e^+e^- \to \mu^+\mu^-$ events selected when using alternative measurements of the polar angle are investigated and compared between data and Monte Carlo simulated events, separately for each year of data. Based on the scatter of these comparisons a systematic error of 10×10^{-4} is assigned for the 1993 data sample, and 5×10^{-4} for the 1994 and 1995 data samples.

Further efficiency corrections: The trigger inefficiency for $e^+e^- \to \mu^+\mu^-$ events is estimated to be $(6 \pm 2) \times 10^{-4}$, $(5 \pm 2) \times 10^{-4}$ and $(2 \pm 2) \times 10^{-4}$ for the 1993, 1994 and 1995 data, respectively. Corrections to the selection efficiency related to four-fermion events are determined as described in Appendix A.1. Finally, the inefficiency associated with the cosmic ray veto is found to be less than 1×10^{-4}.

7.3.3 Background in the $e^+e^- \to \mu^+\mu^-$ channel

The background in the $e^+e^- \to \mu^+\mu^-$ event selection is approximately 1%, dominated by misclassified $e^+e^- \to \tau^+\tau^-$ events. The backgrounds from two-photon interaction processes, such as $e^+e^- \to e^+e^-\mu^+\mu^-$, and from events induced by the passage of cosmic ray muons through the detector are small. The Monte Carlo background estimates are corrected for discrepancies between simulated and real data. These corrections are described below and the resulting background estimates are summarised in Table 6.

$e^+e^- \to \tau^+\tau^-$ background: The lifetime of the τ lepton is sufficiently short that only the decay products of the τ are registered in the detector. For $e^+e^- \to \tau^+\tau^-$ events to be selected as $e^+e^- \to \mu^+\mu^-$ both tau decays must result in an identified muon and the visible energy requirement must be satisfied, $E^{\mu}_{\rm vis} > 0.6\sqrt{s}$. Approximately 17% of τ leptons decay into a muon and neutrinos, consequently about 3% of $e^+e^- \to \tau^+\tau^-$ events result in a visible $\mu^+\mu^-$ final state. In addition, other decays of the τ to single charged particles, in particular $\tau \to \pi\nu$, can be misidentified as muons.

Two control samples are selected from the data to check the simulation of the $\tau^+\tau^-$ background. The first is sensitive to problems with the visible energy distribution and the second is sensitive to

possible problems with muon identification. For the first control sample the $E^{\mu}_{\rm vis}$ cut in the $\mu^+\mu^-$ selection is relaxed to $E^{\mu}_{\rm vis} > 0.5\sqrt{s}$ and the low visible energy region considered, $E^{\mu}_{\rm vis} < 0.8\sqrt{s}$. Events with tracks within 0.5° in azimuth of a wire plane are rejected to remove poorly measured $e^+e^- \to \mu^+\mu^-$ events. The $\tau^+\tau^-$ background is further enhanced by rejecting events, predominantly $\mu^+\mu^-$, which have low acoplanarity < 20 mrad. A loose cut is also made to eliminate events with high energy radiated photons by requiring the acollinearity to be less than 150 mrad. This selected control sample is predicted by Monte Carlo simulation to be made up of approximately 97% $e^+e^- \to \tau^+\tau^-$ events with the remainder being $e^+e^- \to \mu^+\mu^-$ events. The data are in good agreement with the Monte Carlo prediction.

A second, higher statistics control sample is selected by relaxing the $E^{\mu}_{\rm vis}$ requirement of the $e^+e^- \to \mu^+\mu^-$ selection to $0.5 < E^{\mu}_{\rm vis} < 0.8$, and requiring exactly one of the tracks to be identified as a muon. Approximately 99.2% of Monte Carlo generated events selected in this way are $e^+e^- \to \tau^+\tau^-$ events, in the majority of which one τ decays to a muon and the other τ decays to a single charged particle which is not a muon. From the 1993 and 1995 samples there is good agreement between the numbers of events selected in the data and the Monte Carlo expectation. In the 1994 samples an excess of about 4% of Monte Carlo over data events is observed. On the basis of these two studies the Monte Carlo prediction for the $e^+e^- \to \tau^+\tau^-$ background of 1.00% for the 1994 $e^+e^- \to \mu^+\mu^-$ data sample is corrected to (0.97 ± 0.04)%. No corrections are made for the 1993 or 1995 samples, and a systematic uncertainty of 2×10^{-4} is assigned.

Other background: Most events from the two-photon process $e^+e^- \to e^+e^-\mu^+\mu^-$ are rejected by the cut on visible energy, $E^{\mu}_{\rm vis} > 0.6\sqrt{s}$. The Monte Carlo predicts the remaining background to be approximately 0.05% on-peak and 0.1% off-peak, at which energies the resonant Z production is less dominant. The two-photon background is evaluated separately for each year and systematic errors of 1×10^{-4} are assigned to these calculations. The backgrounds from cosmic ray events, estimated from time-of-flight and vertex information, were $(2 \pm 2) \times 10^{-4}$ in 1993 and 1994 and $(3 \pm 2) \times 10^{-4}$ in 1995.

7.4 Selection of $e^+e^- \to \tau^+\tau^-$ events

Tau leptons produced in the process $e^+e^- \to \tau^+\tau^-$ decay before entering the sensitive volume of the detector. The branching ratio for the decay $\tau^- \to \ell^-\nu_\tau\overline{\nu}_\ell$ is about 35%, and the resulting electron or muon has, in general, less momentum than a directly produced fermion from $Z \to \ell^+\ell^-$ due to the two associated neutrinos. In τ decays to hadrons the associated single neutrino also reduces the total visible energy of the final state. The τ-decay branching ratio to three or more charged hadrons is about 15%, and electrons from the conversion of photons from π^0 decays further increase the average charged multiplicity of the final state. The experimental signature for $e^+e^- \to \tau^+\tau^-$ events is therefore less well defined than that for either $e^+e^- \to e^+e^-$ or $e^+e^- \to \mu^+\mu^-$ events. Consequently, the cuts used to select $e^+e^- \to \tau^+\tau^-$ events are relatively involved.

7.4.1 Selection criteria for $e^+e^- \to \tau^+\tau^-$

The selection criteria used to identify $e^+e^- \to \tau^+\tau^-$ events remain unchanged with respect to our previous publications where a more detailed description is provided [**?**, **?**, **?**]. The selection is summarised below:

- Multiplicity cuts, shown in Figures 11(a) and 11(b), to reject hadronic Z decays:

  $2 \le N_{\rm track} \le 6$ and $N_{\rm track} + N_{\rm cluster} \le 15$.

- $e^+e^- \to \tau^+\tau^-$ event topology:

  Events are reconstructed using a cone jet-finding algorithm [**?**] with a cone half-angle of 35°. The sum of the electromagnetic calorimeter energy and scalar sum of track momenta in each cone has to be more than 1% of the beam energy. Exactly two cones containing tracks are

required, not counting cones which contain only tracks associated with photon conversions. The direction of each τ candidate is taken to be the total momentum vector reconstructed from the tracks and electromagnetic clusters in its cone.

- $e^+e^- \to \tau^+\tau^-$ event acollinearity:

  $\theta_{\rm acol} < 15^\circ$

  where the acollinearity angle, $\theta_{\rm acol}$, is 180° minus the angle between the directions of the two τ candidates.

- Geometrical acceptance:

  $|\cos\theta_\tau| < 0.9.$

  where θ_τ is the polar angle of the event axis, defined using the vectorial difference between the momenta of the two τ candidates.

- Rejection of $e^+e^- \to \mu^+\mu^-$ events:

  Events selected as $e^+e^- \to \mu^+\mu^-$ by the criteria described in Section 7.3.1 are rejected.

- Rejection of $e^+e^- \to e^+e^-$ events:

  $E_{\rm total} \equiv \sum E^i_{\rm cluster} < 0.8\sqrt{s}$, shown in Figure 11(c). For the region $|\cos\theta_\tau| > 0.7$, where there is additional material in front of the electromagnetic calorimeter, it is also required that:

  $$E^\tau_{\rm vis} < 1.05\sqrt{s} \quad \text{or} \quad E_{\rm total} < 0.25\sqrt{s}, \quad (\text{for } |\cos\theta_\tau| > 0.7),$$

  where $E^\tau_{\rm vis}$ is the total visible energy, $E^\tau_{\rm vis} = E_{\rm total} + p_{\rm total}$.

- Rejection of non-resonant $e^+e^- \to e^+e^-\ell^+\ell^-$ events, see Figure 11(d):

  $E^\tau_{\rm vis} > 0.18\sqrt{s}$.

- Cosmic ray background is rejected by requiring that the selected events originate from the average e^+e^- interaction point and are coincident in time with the beam crossing.

These criteria select 107 340 events from the 1993–1995 data sample. The selection efficiency and background contributions from processes other than $e^+e^- \to \tau^+\tau^-$ are estimated using Monte Carlo events. These efficiencies and backgrounds are corrected for the observed differences between data and Monte Carlo. The corrections and systematic errors are summarised in Table 7 and are described below. The systematic errors of the seven data samples are strongly correlated, as shown in Table 20. Unless otherwise specified, the numbers quoted in the text correspond to the 1994 data.

7.4.2 Selection efficiency for $e^+e^- \to \tau^+\tau^-$

The Monte Carlo prediction for the $e^+e^- \to \tau^+\tau^-$ selection efficiency is $(75.18 \pm 0.07)\%$. This corresponds to a selection efficiency of $(87.70 \pm 0.05)\%$ within the geometric acceptance of $|\cos\theta_\tau| < 0.90$. Small corrections are then applied to account for the Monte Carlo events generated below the ideal kinematic acceptance limit of $m^2_{\rm f\bar{f}}/s > 0.01$, and for interference between photons radiated in the initial and final states, as described in Appendix A.2 and listed in Table 7. Within the angular acceptance, the largest source of inefficiency arises from the cuts used to reject background from $e^+e^- \to e^+e^-$. To estimate the efficiency for data, the inefficiency introduced by each cut exclusively is first estimated from the Monte Carlo simulation. These estimates are corrected by comparing the data and Monte Carlo. The decomposition into exclusive inefficiencies is appropriate since only 0.6% of events fail more than one of the classes of selection cuts. Using the 1994 data as an example, the selection efficiency from the Monte Carlo simulation is corrected by $(-1.30 \pm 0.28)\%$ to give an estimated selection efficiency of $(73.88 \pm 0.29)\%$. Details of the main corrections to the efficiency and the main sources of systematic uncertainty are given below.

Multiplicity cuts: The multiplicity requirements exclusively reject $(1.32 \pm 0.02)\%$ of Monte Carlo $e^+e^- \to \tau^+\tau^-$ events. However, a number of effects which can influence multiplicity are not perfectly modelled, such as the simulation of the material of the detector which affects the rate of photon conversions and the two-track resolution. To assess the effect using the data, the multiplicity cuts are removed from the $e^+e^- \to \tau^+\tau^-$ selection yielding a sample dominated by $e^+e^- \to \tau^+\tau^-$ and $e^+e^- \to q\overline{q}$. In this sample, $e^+e^- \to \tau^+\tau^-$ events are identified by requiring that one of the two τ cones is consistent with being a $\tau \to \mu\nu_\mu\nu_\tau$ decay. This requirement removes essentially all $e^+e^- \to q\overline{q}$ events. Backgrounds from $e^+e^- \to \mu^+\mu^-$ and $e^+e^- \to e^+e^-\mu^+\mu^-$ are rejected using cuts on acoplanarity and momentum. In this way a sample of $e^+e^- \to \tau^+\tau^-$ events is isolated using only the multiplicity information from a single τ cone. The other τ cone is used to provide an unbiased estimator for the multiplicity distribution for a single τ cone. By convolving this measured single cone multiplicity distribution with itself, the $e^+e^- \to \tau^+\tau^-$ multiplicity distribution is estimated using data alone. The convolution is performed in two dimensions, track and total multiplicity. The multiplicity cuts are applied to the convolved distribution to determine the exclusive inefficiency of $(1.69 \pm 0.11)\%$ for the 1994 data sample[5]. The validity of the procedure is verified using different Monte Carlo samples.

Acollinearity and cone cuts: The acollinearity cut and the requirement that there be exactly two charged τ cones in the event reject $(3.29 \pm 0.03)\%$ of Monte Carlo $e^+e^- \to \tau^+\tau^-$ events. These cuts reject background from $e^+e^- \to e^+e^-$ and $e^+e^- \to q\overline{q}$. To study the effect of these cuts, the acollinearity and cone requirements are replaced by cuts using particle identification information such as dE/dx. Relatively hard cuts are necessary to be able to study the acollinearity distribution for $e^+e^- \to \tau^+\tau^-$ events since, in the region of the cut, the background from $e^+e^- \to e^+e^-$ dominates. Figure 12(a) shows the acollinearity distribution for this alternative selection which has an efficiency for $e^+e^- \to \tau^+\tau^-$ of approximately 33% but has little background (less than 0.5%). For Monte Carlo $e^+e^- \to \tau^+\tau^-$ events it is verified that the alternative selection does not significantly bias the acollinearity distribution. In the region $\theta_{\rm acol} < 15^\circ$ the good agreement between data and Monte Carlo indicates that the modelling of the efficiency of the particle identification cuts is reasonable. The relative normalisations of the data and Monte Carlo in the region $15^\circ < \theta_{\rm acol} < 45^\circ$ are used to determine corrections to the Monte Carlo efficiencies for the different centre-of-mass energies. A similar check of the inefficiency related to the cone requirements is made. The corrected inefficiency due to the acollinearity and cone cuts is $(3.55 \pm 0.14)\%$.

Definition of $|\cos\theta_\tau|$: A systematic uncertainty on the selection efficiency of 0.1% is assigned due to the uncertainty in the definition of the geometrical acceptance, $|\cos\theta_\tau| < 0.9$. This estimate is obtained by comparing relative numbers of selected events in data and Monte Carlo using various definitions of $|\cos\theta_\tau|$, *e.g.* calculated using tracks, using clusters in the electromagnetic calorimeter or using both tracks and clusters.

$e^+e^- \to e^+e^-$ rejection cuts: The Monte Carlo simulation predicts an exclusive inefficiency due to the $e^+e^- \to e^+e^-$ rejection cuts of $(3.40 \pm 0.03)\%$. To investigate potential biases, the energy-based $e^+e^- \to e^+e^-$ rejection is replaced by cuts using electron identification information. Imperfect modelling of the detector response in the region $|\cos\theta_\tau| > 0.7$, shown in Figure 12(b), results in the Monte Carlo underestimating the true inefficiency. The inefficiency for the data is estimated to be $(3.92 \pm 0.17)\%$.

Further corrections and uncertainties : By using lepton identification information the effect of the cuts used to reject $e^+e^- \to \mu^+\mu^-$ and $e^+e^- \to e^+e^-\ell^+\ell^-$ events are found to be adequately modelled by the Monte Carlo, however corrections, consistent with unity, and corresponding uncertainties are obtained from the data. The trigger efficiency for $e^+e^- \to \tau^+\tau^-$ events is estimated to be

[5] We give here, by way of example for all these corrections, the correspondence between this correction to the exclusive inefficiency and the multiplicity correction factor, f, in Table 7. $f = 1.0 + (0.0169 - 0.0132)/(0.7388 + 0.0169)$, where 0.7388 is the overall corrected efficiency, *i.e.* 1.3536^{-1}.

$(99.98 \pm 0.02)\%$. During 1995, when LEP operated in bunch-train mode, no discernible effect on the $e^+e^- \to \tau^+\tau^-$ selection is observed and no systematic error is assigned. Uncertainties in the branching ratios of the τ lepton result in a 0.05% uncertainty in the $e^+e^- \to \tau^+\tau^-$ selection efficiency. The uncertainty on the mean τ polarisation [**?**] has a negligible effect on the $e^+e^- \to \tau^+\tau^-$ selection efficiency ($< 0.01\%$). Corrections to the selection efficiency related to four-fermion events are determined as described in Appendix A.1. A 10% uncertainty is assigned to the Monte Carlo expectation that 0.6% of events fail more than one of the classes of selection cuts.

7.4.3 Background in the $e^+e^- \to \tau^+\tau^-$ channel

For peak data approximately 2.6% of the events passing the $e^+e^- \to \tau^+\tau^-$ selection come from background processes. This is significantly larger than the corresponding backgrounds in the $e^+e^- \to e^+e^-$ and $e^+e^- \to \mu^+\mu^-$ selections. The main backgrounds are from $e^+e^- \to e^+e^-$ (0.4%), $e^+e^- \to \mu^+\mu^-$ (1.1%), $e^+e^- \to q\overline{q}$ (0.4%) and $e^+e^- \to e^+e^-\ell^+\ell^-$ (0.6%). The background fractions from $e^+e^- \to e^+e^-$ and $e^+e^- \to e^+e^-\ell^+\ell^-$ are higher for the off-peak samples. To estimate the size of the background contributions using the data, cuts are applied to the selected $e^+e^- \to \tau^+\tau^-$ sample to enhance the various background sources. The resulting background estimations and systematic uncertainties are given in Table 7 and are summarised below (for peak data).

Background from $e^+e^- \to e^+e^-$: The Monte Carlo expectation for the $e^+e^- \to e^+e^-$ background fraction is $(0.26 \pm 0.02)\%$. For the reasons discussed in Section 7.2.3, the Monte Carlo underestimates the $e^+e^- \to e^+e^-$ background in the barrel region of the detector. The techniques described in Section 7.2.3 are used to estimate the effect on the background level in the $e^+e^- \to \tau^+\tau^-$ selection. Similar studies indicate that the $e^+e^- \to e^+e^-$ background in the end-cap region, ($|\cos\theta_\tau| > 0.7$), is well modelled. The corrected total background from $e^+e^- \to e^+e^-$ is then $(0.47 \pm 0.07)\%$

Background from $e^+e^- \to \mu^+\mu^-$: The $e^+e^- \to \mu^+\mu^-$ background is estimated from Monte Carlo simulation to be $(0.98 \pm 0.02)\%$. For $e^+e^- \to \mu^+\mu^-$ events to enter the $e^+e^- \to \tau^+\tau^-$ sample either one of the tracks must fail the muon identification criteria of Section 7.3 or $E^{\mu}_{\rm vis}$ must be less than $0.6\sqrt{s}$. The $e^+e^- \to \mu^+\mu^-$ background in the $e^+e^- \to \tau^+\tau^-$ sample is enhanced by requiring at least one identified muon and by imposing loose momentum and electromagnetic energy cuts. The acoplanarity distribution of the surviving events is used to estimate corrections to the Monte Carlo expectation for the $e^+e^- \to \mu^+\mu^-$ background. Discrepancies between data and Monte Carlo are observed for tracks near the anode planes of the central jet chamber as indicated in Figure 12(c). As a result of these comparisons, the Monte Carlo background estimate for the 1994 data is corrected to $(1.17 \pm 0.09)\%$.

Background from $e^+e^- \to q\overline{q}$: The Lund string model as implemented in the JETSET program is used to describe the hadronisation process for the generated Monte Carlo samples. The parameters within JETSET are tuned to describe the properties of OPAL $e^+e^- \to q\overline{q}$ events [**?**,**?**]. Although these Monte Carlo samples provide a good description of the global properties of $e^+e^- \to q\overline{q}$, *e.g.* event shape variables, there is no guarantee that they adequately describe the low multiplicity region. This is illustrated by the comparison of the $e^+e^- \to q\overline{q}$ background expectations obtained from Monte Carlo samples using two different JETSET tunes, [**?**] and [**?**], which give respective background estimates of $(0.40 \pm 0.02)\%$ and $(0.88 \pm 0.02)\%$.

To assess the $e^+e^- \to q\overline{q}$ background fraction from the data, the multiplicity cuts of the $e^+e^- \to \tau^+\tau^-$ selection are relaxed and events where one of the τ cones is consistent with a leptonic τ decay are removed from the selected $e^+e^- \to \tau^+\tau^-$ sample. Events in the predominant $\tau^+\tau^-$ track multiplicity topologies, $1-1$, $1-3$ and $3-3$, are also rejected. In this way $e^+e^- \to \tau^+\tau^-$ events are removed whilst retaining a large fraction of the $e^+e^- \to q\overline{q}$ background. For example, Figure 12(d) shows the distribution of track multiplicity after the $e^+e^- \to q\overline{q}$ enhancement. The resulting background enriched sample allows the $e^+e^- \to q\overline{q}$ background fraction to be estimated from the data by fitting the track and total multiplicity distributions with contributions from $e^+e^- \to \tau^+\tau^-$ and $e^+e^- \to q\overline{q}$ where the shapes are taken from Monte Carlo and the normalisations left free. In this manner the

$e^+e^- \to q\overline{q}$ background is estimated to be $(0.41 \pm 0.11)\%$. The systematic error reflects the sensitivity to the Monte Carlo model used to describe the shape of the multiplicity distributions.

Background from $e^+e^- \to e^+e^-\ell^+\ell^-$: At the Z peak, the Monte Carlo prediction of the background from $e^+e^- \to e^+e^-\ell^+\ell^-$ two-photon processes is $(0.53 \pm 0.02)\%$. The Monte Carlo predictions for the background from $e^+e^- \to e^+e^-e^+e^-$ and $e^+e^- \to e^+e^-\mu^+\mu^-$ backgrounds are checked by requiring both cones in selected $e^+e^- \to \tau^+\tau^-$ events to be consistent with being electrons and muons respectively. Distributions of $E^\tau_{\rm vis}/\sqrt{s}$ and missing transverse momentum are used to estimate the background directly from data. No deviations from the Monte Carlo expectation are found. The statistical precision of the check is taken as the systematic error. A 100% systematic uncertainty is assigned to the background from $e^+e^- \to e^+e^-\tau^+\tau^-$. The resulting estimate of the background from two-photon processes for the 1994 data is $(0.58 \pm 0.07)\%$.

Other backgrounds: The background from four-fermion processes (see Appendix A.1) is estimated to be $(4 \pm 1) \times 10^{-4}$ for the peak data. The cosmic ray background is estimated from the data and found to be small, $(2 \pm 2) \times 10^{-4}$ for the 1994 data.

7.5 Correlations among lepton species

Although the cross-sections for each lepton species are measured independently, the requirement that there is no overlap in the selections leads to anti-correlations between the systematic errors for each species. These anti-correlations reduce the precision with which the inter-species ratios can be measured. However, components of the total systematic uncertainties which are anti-correlated between lepton species do not contribute significantly to the uncertainty on the leptonic cross-section from all species taken together.

The separation of $e^+e^- \to e^+e^-$ and $e^+e^- \to \tau^+\tau^-$ events is made primarily on the basis of the cut on the total deposited electromagnetic energy, $E_{\rm total}$. Almost all e^+e^- events failing this cut are accepted by the $\tau^+\tau^-$ selection, while $\tau^+\tau^-$ events which exceed this cut appear as background in the e^+e^- sample. Consequently, the covariance between e^+e^- and $\tau^+\tau^-$ cross-section measurements is taken as the product of the systematic uncertainty in e^+e^- efficiency due to the electromagnetic energy cut and the uncertainty of $\tau^+\tau^-$ background in the e^+e^- sample. A second source of anti-correlation arises from $e^+e^- \to \mu^+\mu^-$ events being explicitly excluded from the $e^+e^- \to \tau^+\tau^-$ sample. The covariance is taken as the product of the uncertainty in the estimated $\mu^+\mu^-$ background in the $\tau^+\tau^-$ sample and the uncertainty in the loss of $\tau^+\tau^-$ events improperly identified as $\mu^+\mu^-$. The covariance between the $\mu^+\mu^-$ and $\tau^+\tau^-$ selections and between the $\tau^+\tau^-$ and e^+e^- selections are of similar size, with the exact values listed in Table 21. Due to their very different experimental signatures, there is no cross-talk between the $e^+e^- \to e^+e^-$ and $e^+e^- \to \mu^+\mu^-$ selections.

8 Cross-section measurements

Table 1 gives the number of selected events in each channel used in the cross-section analysis of the entire OPAL LEP 1 data sample. For measuring the cross-section of a particular final state both the detector sub-systems relevant for the selection and the luminosity detector are required to be fully operational. Since the detector sub-systems used in the different event selections are not identical, the luminosity and mean beam energy differ slightly for each final state. Within these 'detector status' requirements, the number of selected final state events, the number of luminosity events, the luminosity weighted beam energy and the beam-energy spread are calculated for each data sample. The cross-sections in the idealised phase space described in Section 3 are then calculated by multiplying the number of selected events by the correction factors given in Tables 3, 5, 6 and 7, and dividing by the integrated luminosity. Details of the luminosity calculation entering these tables can be found in [**?**].

Tables 8, 9, 10, and 11 give the measured fermion-pair cross-sections within the kinematic cuts described in Section 3, for hadrons, electrons, muons, and taus respectively. The "measured" cross-

sections have been corrected for all effects except the spread of collision energies. The "corrected" cross-sections have been corrected for this spread according to the expected curvature of the cross-section as a function of energy, and correspond to the true cross-section at the central beam energy, as described in Appendix C. The cross-section measurements from 1990–1992 correspond to the results published in [?, ?, ?], except for two corrections. The small effect of initial-final state interference (see Appendix A) has been applied retrospectively to the lepton cross-sections. In addition, the improved theoretical calculations (see Section 5) of the small-angle Bhabha scattering cross-section causes a slight change of the FD luminosity used for the 1990–1992 cross-sections.

The SiW luminosity detector was fully operational for 94% of the 1994 peak running and the energy scans in 1993 and 1995 (but not during the 1993 and 1995 prescan periods). During the periods when the SiW luminosity detector was not fully functional, the data are used to measure ratios of cross-sections. For these measurements the integrated luminosity is determined from the number of selected $e^+e^- \to q\overline{q}$ events using the expected cross-section. A common 10 % normalisation uncertainty is assigned to these "pseudo-cross-sections". This arbitrary large uncertainty ensures that these pseudo-cross-section measurements only contribute to the measurement of R_ℓ, but do not affect the determination of m_Z, Γ_Z or σ^0_h (see Section 11). Table 12 gives the pseudo-cross-sections, where the errors given are statistical only. The systematic errors, and their correlations, are taken to be the same as those for the peak cross-sections measured in the same year, except for the correlated normalisation scale error.

For the 1990 data the systematic uncertainties on the absolute luminosity and centre-of-mass energy scales are significantly larger than in subsequent years (see Section 4). For this reason the 1990 cross-section measurements are treated as pseudo-cross-sections with a common luminosity as well as LEP energy scale error imposed across all decay channels and energy points. Since the 1990 data includes off-peak as well as on-peak points, it contributes to the measurement of R_ℓ and Γ_Z, but not to m_Z or σ^0_h.

The quoted errors on the measured cross-sections listed in Tables 8–11 are the statistical errors from the counting of signal and luminosity events. Systematic errors, which arise from uncertainties of the LEP centre-of-mass energy, the luminosity measurement and the event selections, have varying degrees of correlation between the different final-state species and the various data-taking periods. Tables 13–15 give the covariance matrices for the LEP energy and its spread. The covariance matrix for the luminosity is specified in Table 16 and Tables 17–21 show the covariance matrices for the hadron and lepton event selections. Appendix C describes in detail how the full covariance matrix for the cross-sections (and asymmetries) is constructed.

Many checks were made to ensure the consistency of the event sample over widely varying time scales. One example is shown in Figure 13, which shows the distributions of the number of luminosity events observed between consecutive $e^+e^- \to q\overline{q}$ events and *vice versa*. If OPAL had temporarily lost sensitivity to small angle Bhabha scattering events in the SiW detector or $e^+e^- \to q\overline{q}$ decays (but not both) for a continuous period of a few minutes in the approximately six months of OPAL live time spent running at the peak during 1993–1995, the failure would be visible as a tail in one of these distributions. Similar tests involving the lepton species also revealed no such problems. Other checks probing the constancy of event type ratios at time scales varying from hours to months revealed no statistically significant effect. For the 1995 data, the cross-section for each final state was determined, specific to each bunchlet in the bunch-train. No significant variation was observed.

9 The asymmetry measurements

The forward-backward asymmetry $A^{\ell\ell}_{FB}$ is defined as

$$A^{\ell\ell}_{FB} = \frac{\sigma_F - \sigma_B}{\sigma_F + \sigma_B}, \tag{2}$$

where σ_F and σ_B are the cross-sections integrated over the forward ($0 < \cos\theta_{\ell^-} < 1$) and backward ($-1 < \cos\theta_{\ell^-} < 0$) hemispheres respectively, and θ_{ℓ^-} is the angle between the final state ℓ^- and the e^-

beam direction.

In the SM the s-channel contribution to the differential cross-section for the reaction $e^+e^- \to \ell^+\ell^-$ with unpolarised beams is expected to have an approximately quadratic dependence on the cosine of the lepton scattering angle:

$$\frac{d\sigma}{d(\cos\theta_{\ell^-})} \quad \propto \quad 1 + \frac{8}{3} A_{FB}^{\ell\ell} \cos\theta_{\ell^-} + \cos^2\theta_{\ell^-} \ . \tag{3}$$

For $e^+e^- \to e^+e^-$ events, the angular dependence is more complex due to the large contributions from the t-channel and interference between s- and t-channels, discussed in Appendix B. The magnitude and energy-dependence of $A_{FB}^{\ell\ell}$ are sensitive to the vector and axial-vector couplings between leptons and the Z (see Section 11). Within the SM, the asymmetry is predicted to be about 0.01 at $\sqrt{s} = m_Z$ (after unfolding initial-state radiation) and to increase with $\sqrt{s}$.

In principle the measurement of $A_{FB}^{\ell\ell}$ is simple and suffers from few systematic uncertainties. The statistically most powerful method of extracting a measurement of the forward-backward asymmetry is to perform an unbinned maximum likelihood fit of the differential cross-section with $A_{FB}^{\ell\ell}$ as the only free parameter using the logarithm of the product of the event weights, w_i :

$$w_i \quad = \quad \frac{3}{8}(1 + (\cos\theta_{\ell^-}^i)^2) + A_{FB}^{\ell\ell} \cos\theta_{\ell^-}^i, \tag{4}$$

where $\theta_{\ell^-}^i$ is the polar angle of the negatively charged lepton in the ith event. This method, which is used for the $e^+e^- \to \mu^+\mu^-$ and $e^+e^- \to \tau^+\tau^-$ channels, has the advantage of being insensitive to any event selection inefficiencies, or any variation of the efficiency with $\cos\theta_{\ell^-}$, provided there is no forward-backward charge asymmetry in the efficiency function itself. Technically, the inclusion of a selection efficiency term in the event weights results in an additive constant when taking the logarithm of the likelihood function provided the efficiency can be expressed in terms of $|\cos\theta_{\ell^-}^i|$. This is in contrast to the event-counting method (see below) which must be corrected for selection inefficiencies. The fit yields a value for $A_{FB}^{\ell\ell}$ over the full polar angle range. This can be corrected to a restricted range $|\cos\theta| < k$ using a simple geometrical factor

$$A_{FB}^{\ell\ell}(|\cos\theta| < k) \quad = \quad A_{FB}^{\ell\ell}(|\cos\theta| < 1)\frac{4k}{3+k^2}. \tag{5}$$

This region corresponds to the ideal acceptance definition of Table 2 and is chosen to correspond closely to the geometric acceptance of the event selection. In addition, small corrections to the measured asymmetry are required to take account of background and other biases.

The measurement of the forward-backward asymmetry in the $e^+e^- \to e^+e^-$ channel is more complicated. Due to the t-channel contributions, the angular distribution in $e^+e^- \to e^+e^-$ events can not be parametrised as a simple function of the forward-backward asymmetry, A_{FB}^{ee}. For this reason A_{FB}^{ee} is measured from the observed numbers of events in the forward and backward hemispheres, N_F and N_B:

$$A_{FB}^{ee} = \frac{N_F - N_B}{N_F + N_B}. \tag{6}$$

This counting method is also used as a cross check of the unbinned maximum likelihood method in the $e^+e^- \to \mu^+\mu^-$ and $e^+e^- \to \tau^+\tau^-$ channels and yields consistent results.

In each of the three leptonic channels the choice of which particle (ℓ^+ or ℓ^-) is used to define the polar angle of the event is varied at random from event to event. This reduces many possible geometrical biases to the asymmetry measurement arising from an asymmetry in the detector. In the cases where the ℓ^+ track is used, the angle θ is measured relative to the e^+ beam direction. The measured asymmetries are corrected for the energy spread of the colliding beams as described in Appendix C. Corrections are required to account for charge misassignment and for differences between the experimental acceptance and the ideal acceptance of Table 2. Details of these corrections

and the main systematic uncertainties are given below. Note that our measured asymmetries implicitly include the effects of initial-final-state interference. We make no correction to remove these effects from our measurements, but calculate the predicted asymmetries accounting for this interference using ZFITTER. The asymmetry measurements are dominated by statistical rather than systematic uncertainties even when all data sets are combined.

9.1 $e^+e^- \to \mu^+\mu^-$ forward-backward asymmetry

The forward-backward asymmetry of muon pairs, $A_{\rm FB}^{\mu\mu}$, is a conceptually simple measurement. Muon pair events are selected with high efficiency and the asymmetry measurement itself is robust against many systematic effects. Compared to our previous publication [**?**] the analysis presented here represents a significant improvement in the understanding of the experimental biases. To benefit from the resulting reduction in systematic uncertainties, the asymmetry in the 1992 data sample has been re-evaluated.

In addition to the $e^+e^- \to \mu^+\mu^-$ selection cuts of Section 7.3.1, the acollinearity angle between the directions of the two muon tracks is required to be less than 15°. This removes about 1.3% of the total sample by rejecting events with high-energy radiated photons. Such events distort the angular distribution and bias the asymmetry measurement due to the lower value of the effective centre-of-mass energy, $\sqrt{s'}$. Equivalent acceptance cuts are made inside the ZFITTER program [**?**] when evaluating the theoretical predictions used to fit the data, as discussed in Section 11.

About 1.2% of the selected $e^+e^- \to \mu^+\mu^-$ events have the same sign assigned to both candidate muon tracks. These events are concentrated in the region where the tracks are close to the jet chamber wire planes or are in the forward region, $|\cos\theta| > 0.90$. The probability that a track is assigned the incorrect charge is found to be dependent both on the polar angle of the track and on its direction of curvature. Both positive tracks with $\cos\theta < 0$ and negative tracks with $\cos\theta > 0$ are more likely to be assigned the wrong charge. Rejection of same-sign events would therefore lead to a selection inefficiency which is both asymmetric and charge-dependent, removing more events in the backward hemisphere than in the forward hemisphere and producing a positive bias in $A_{\rm FB}^{\mu\mu}$. The origin of this effect is not understood. The size of this bias is found to be 0.0010. These "like-charge" events are recovered by determining which track was the most likely to have been assigned the wrong charge, based on numbers of assigned track hits, measured momentum and its uncertainty and the acoplanarity angle for tracks close to the anode wire planes of the central detector. The efficiency of this procedure is determined using the sample of events where the charge can be almost unambiguously determined from the acoplanarity as measured in the muon chambers. The resulting charge measurement is estimated to be correct for 93% of like-charge events. A small correction is made for the 7% of like-charge events where the assignment is incorrect. The fraction of events where both muons are assigned the wrong charge is small, 2×10^{-4}, and has negligible impact on the measurement.

For Monte Carlo events the cut on $E_{\rm vis}^{\mu}$ introduces a small additional bias, approximately 1×10^{-4}, in the measured asymmetry with respect to the asymmetry within the ideal acceptance of Table 2. However there is an additional bias for the data, related to the detector response, from events which fail the $E_{\rm vis}^{\mu}$ cut due to being mismeasured. These events are concentrated in two regions either $|\cos\theta| > 0.90$ or within 0.5° of an anode wire plane. Additional selection criteria were applied to recover these mismeasured events. The main background in the region $E_{\rm vis}^{\mu} < 0.6$ arises from $e^+e^- \to \tau^+\tau^-$. Cuts based on acoplanarity and the reconstructed momenta of the two muon tracks reduced this background to a manageable level. The inclusion of the recovered events in the event sample changes the measured value of $A_{\rm FB}^{\mu\mu}$ by $(6 \pm 2) \times 10^{-4}$.

Figure 15 shows the observed angular distribution of $e^+e^- \to \mu^+\mu^-$ events from the 1993–1995 data samples, after applying small corrections for inefficiency and background. The asymmetries are obtained from unbinned maximum likelihood fits to the observed distributions of $\cos\theta_{\mu^-}$ and corrected to the restricted acceptance of $|\cos\theta| < 0.95$ using Equation 5. In the event selection both reconstructed muons are required to be within $|\cos\theta| < 0.95$. In contrast, the acceptance for the muon pair asymmetry is defined constraining only $|\cos\theta_{\mu^-}| < 0.95$, thus including a larger fraction

of events with significant initial state radiation. The measured asymmetries are therefore corrected for the resulting bias of about 0.0003, which was estimated using KORALZ Monte Carlo events. The forward-backward asymmetry measurements for the $e^+e^- \to \mu^+\mu^-$ channel, fully corrected to the acceptance definition of Table 2, are summarised in Table 22.

For each of the data sets the systematic errors are less than 10% of the statistical uncertainties. The total systematic uncertainty on the measured asymmetry for the highest statistics data sample is estimated to be 0.0004. The largest uncertainty is related to charge misassigned events, described above, varying between ± 0.0002 and ± 0.0010 depending on the data sample. The second largest systematic error, ± 0.0002, comes from limits on the possible inadequacies of the fitting function in the maximum likelihood fit. In addition, small systematic uncertainties, each less than 0.0002, are assigned due to the definition of the angular acceptance, the residual tau pair background and biases from the event selection. The systematic errors for the different data samples and their correlations are given in Table 25.

9.2 $e^+e^- \to \tau^+\tau^-$ forward-backward asymmetry

Measurement of $A_{\rm FB}^{\tau\tau}$ begins with the definition of a suitable event sample. In addition to the $e^+e^- \to \tau^+\tau^-$ selection cuts of Section 7.4.1, events in which the sums of the charges in both τ cones have the same sign are rejected and the sum of the charges of the tracks in at least one of the tau cones must be either ± 1. These additional requirements reject approximately 2% of the selected $e^+e^- \to \tau^+\tau^-$ events. Unlike in the muon-pair asymmetry measurement, the softer momentum spectrum of charged particles from tau decays allows like-charged events to be rejected without introducing a significant bias. The charge misassignment in $e^+e^- \to \tau^+\tau^-$ events mainly arises from track reconstruction ambiguities for tau decays producing three or more closely separated tracks. Another difference with respect to the muon-pair asymmetry measurement is that the tau-pair asymmetry is subject to a potentially important background from electron-pair events. Due to the t-channel contribution, $e^+e^- \to e^+e^-$ background events have a large forward-backward asymmetry. To reduce the sensitivity of the $A_{\rm FB}^{\tau\tau}$ measurement to uncertainties in the $e^+e^- \to e^+e^-$ background, additional cuts are applied. These cuts, based on dE/dx, acoplanarity and $E_{\rm total}$, reduce the $e^+e^- \to e^+e^-$ background by over 90% and remove only 1.5% of $e^+e^- \to \tau^+\tau^-$ events. Figure 14 shows the angular distributions of the events selected for the $e^+e^- \to \tau^+\tau^-$ asymmetry measurement. Figure 16 shows the corresponding distributions after corrections for background and selection efficiency are applied. Unbinned maximum likelihood fits to the uncorrected observed data distributions are used to measure $A_{\rm FB}^{\tau\tau}$. The measured asymmetries are then corrected for the presence of background

$$\Delta A_{\rm FB} = (A_{\rm FB}^{\tau\tau} - A_{\rm FB}^{\rm bkg}) f_{\rm bkg},$$

where $f_{\rm bkg}$ is the background fraction and $A_{\rm FB}^{\rm bkg}$ is the asymmetry of the background. The resulting corrections are small, corresponding to less than 10% of the statistical error.

The measured values of $A_{\rm FB}^{\tau\tau}$ correspond to the asymmetry in the selected sample extrapolated to the full $\cos\theta$ acceptance. These are corrected to the acceptance definition $|\cos\theta_{\tau^-}| < 0.9$ and $\theta_{\rm acol} < 15^\circ$ given in Table 2. The corrections are obtained using Monte Carlo $e^+e^- \to \tau^+\tau^-$ events which are treated in the same manner as data. The corrections also take into account other biases such as the effect of the non-zero average polarisation of the τ lepton. The visible energy spectra from decays of positive and negative helicity τ leptons are different. The $e^+e^- \to \tau^+\tau^-$ event selection is approximately 1.5% more efficient for the negative helicity final states than for positive helicity final states and a bias arises since the forward-backward asymmetries for the two helicity states are different. For each energy point, the measured asymmetry from the Monte Carlo sample is compared with the true asymmetry within the acceptance $|\cos\theta_{\tau^-}| < 0.9$ and $\theta_{\rm acol} < 15^\circ$ obtained from the Monte Carlo generator information. The differences are used to obtain corrections to the measured asymmetries of -0.0027 ± 0.0017, -0.0014 ± 0.0011 and -0.0013 ± 0.0015 for the peak-2, peak and peak$+2$ data samples, respectively, where the errors include statistical and systematic components. These correc-

tions and uncertainties implicitly include effects due to possible inadequacies of the function used in the maximum likelihood fit.

The corrected forward-backward asymmetry measurements for the $e^+e^- \to \tau^+\tau^-$ channel are summarised in Table 23. The overall systematic uncertainties on $A_{FB}^{\tau\tau}$ are 0.0018, 0.0012 and 0.0016 for the peak−2, peak and peak+2 data points, respectively. The errors for the different data sets and their correlations are listed in Table 25. The systematic errors are dominated by the uncertainties on the Monte Carlo correction from the measured asymmetries to the asymmetry definition of Table 2. The systematic error associated with the measurement of $\cos\theta$ is studied by using 12 different definitions of this angle, *e.g.* using tracks and clusters, using tracks alone, taking the average value from the two tau cones. The shifts in the measured asymmetries compared to the default result are reasonably well reproduced by the Monte Carlo and a systematic error of 0.0005 is assigned. The knowledge of the absolute angular scale, or length-width ratio of the detector, has negligible impact on these measurements. As a consequence of the additional $e^+e^- \to e^+e^-$ rejection cuts, the systematic errors arising from the uncertainties in the background fractions are small (typically 0.0002).

9.3 $e^+e^- \to e^+e^-$ forward-backward asymmetry

A_{FB}^{ee} is measured from the observed numbers of events in the forward and backward hemispheres:

$$A_{FB}^{ee} = \frac{N_F - N_B}{N_F + N_B}. \tag{7}$$

Here N_F and N_B are the numbers of events within $0.00 < \cos\theta_{e^-} < 0.70$ and $-0.70 < \cos\theta_{e^-} < 0.00$, respectively, and θ_{e^-} is the e^- scattering angle. In 1.5% of the selected $e^+e^- \to e^+e^-$ events the signs of reconstructed charges of the tracks are the same. These events are retained for the asymmetry measurement by using the acoplanarity angle between the electromagnetic calorimeter clusters associated with the two electron candidates to distinguish their charges. This method is limited by the experimental resolution of the acoplanarity measurement giving the correct assignment in about 92% of events. This performance is studied in both data and Monte Carlo by applying the cluster-based acoplanarity method to selected events in which the two tracks have been assigned opposite charges. We therefore correct the measured asymmetry for residual bias due to the fact that we make the wrong charge assignment for an estimated 1.2×10^{-3} of all events when we recover the like-sign events using the acoplanarity method. The resulting corrections to A_{FB}^{ee} are 0.0010 ± 0.0005, 0.0004 ± 0.0003 and 0.0004 ± 0.0006 for the peak−2, peak and peak+2 energy points, respectively.

In the process $e^+e^- \to e^+e^-$, there is a small difference in the event selection efficiency for forward and backward events due mainly to the cut on the electromagnetic energy. This is caused by the softer energy spectra of ISR photons from s-channel Z than from t-channel photon exchange processes. ISR photons tend to be produced along the beam direction and are therefore likely to remain undetected. Consequently, events with harder ISR are more likely to be rejected by the cut on the total visible electromagnetic energy in the event, $E_{total} > 0.80\sqrt{s}$. The t-channel contribution is relatively more important in the forward direction while the contribution from the Z dominates in the backward direction. As a result a small forward-backward asymmetry in the $e^+e^- \to e^+e^-$ event selection efficiency arises. The resulting $\sqrt{s}$-dependent effect on A_{FB}^{ee} is evaluated using the Monte Carlo simulation to be -0.0002 ± 0.0004, -0.0003 ± 0.0003 and -0.0007 ± 0.0008 for the peak−2, peak and peak+2 energy points, respectively.

Unlike the unbinned maximum likelihood fit, the counting method used to obtain A_{FB}^{ee} is sensitive to variations in the selection efficiency as a function of $|\cos\theta|$. The efficiency variations for $e^+e^- \to e^+e^-$, however, are small enough to have negligible impact on the asymmetry measurement. The background in the $e^+e^- \to e^+e^-$ sample is dominated by $e^+e^- \to \tau^+\tau^-$ events for which the expected asymmetry is different from that of $e^+e^- \to e^+e^-$ events. Small corrections for background are obtained in the same manner as used for $A_{FB}^{\tau\tau}$. The corresponding systematic uncertainties are negligible.

The offset of 0.0004 ± 0.0005 in the effective edge of the acceptance in polar angle relative to the nominal value (see Section 7.2.3) causes a small bias in the measured asymmetry. The size of this

effect has been evaluated numerically, using the SM prediction for the differential cross-section at the acceptance edges. Corrections of 0.0003 ± 0.0009, 0.0002 ± 0.0004 and 0.0002 ± 0.0005 are obtained for the peak-2, peak and peak$+2$ energy points, respectively. The systematic errors correspond to the uncertainty on the edge of the acceptance. The accuracy of the definition of the boundary at $\cos\theta = 0.0$ is also important for the asymmetry measurement, since this is used to separate forward events from backward events. However, by randomly choosing either the e^- or the e^+ to classify each event, the effect of any possible small bias is largely cancelled and is reduced to a negligible level. As a check of the asymmetry measurement, $A_{\rm FB}^{\rm ee}$ has also been evaluated using several different methods to classify events as forward or backward: using only e^- clusters and tracks; using only e^+ clusters and tracks; using only θ measurements from tracks rather than from clusters when a high quality track is found; and using only events in which the two tracks have been assigned opposite charges. There are no significant differences between these results, beyond what is expected from statistical fluctuations.

The forward-backward asymmetry measurements for the $e^+e^- \to e^+e^-$ channel are summarised in Table 24. The systematic errors for the different data samples and their correlations are given in Table 25. Figure 17 shows the electron differential cross-sections at the three main energy points, fully corrected for the effects discussed above.

10 Parametrisation of the Z resonance

Before proceeding to interpret the measurements we first discuss the basic formalism used to describe cross-sections and asymmetries at the Z resonance. Then we give a brief overview of radiative corrections and the programs which we use for their calculation. Finally, we describe the t-channel corrections which need to be accounted for in e^+e^- final states.

10.1 Lowest order formulae

The process $e^+e^- \to f\bar{f}$ can be mediated in the s-channel by two spin-1 bosons, a massless photon and a massive Z boson. In lowest order and neglecting fermion masses the differential cross-section for this reaction can be written as:

$$\begin{aligned}\frac{2s}{\pi N_{\rm c}}\frac{{\rm d}\sigma_{f\bar{f}}}{{\rm d}\cos\theta} &= \alpha^2 Q_{\rm f}^2 (1+\cos^2\theta) \\ &+ 8\,{\rm Re}\left\{\alpha\, Q_{\rm f}\, \chi^*(s)\ [\ C_{\gamma Z}^{\rm s}(1+\cos^2\theta) + 2C_{\gamma Z}^{\rm a}\cos\theta\ ]\right\} \\ &+ 16\,|\chi(s)|^2\ [\ C_{ZZ}^{\rm s}(1+\cos^2\theta) + 8C_{ZZ}^{\rm a}\cos\theta\ ]\end{aligned} \tag{8}$$

with

$$\chi(s) = \frac{G_{\rm F}\overline{m}_{\rm Z}^2}{8\pi\sqrt{2}}\frac{s}{s-\overline{m}_{\rm Z}^2 + i\,\overline{m}_{\rm Z}\overline{\Gamma}_{\rm Z}} \tag{9}$$

and

$$C_{\gamma Z}^{\rm s} = \hat{g}_{\rm Ve}\hat{g}_{\rm Vf} \quad , \quad C_{\gamma Z}^{\rm a} = \hat{g}_{\rm Ae}\hat{g}_{\rm Af}\ , \tag{10}$$

$$C_{ZZ}^{\rm s} = (\hat{g}_{\rm Ve}^2+\hat{g}_{\rm Ae}^2)(\hat{g}_{\rm Vf}^2+\hat{g}_{\rm Af}^2) \quad , \quad C_{ZZ}^{\rm a} = \hat{g}_{\rm Ve}\hat{g}_{\rm Ae}\hat{g}_{\rm Vf}\hat{g}_{\rm Af}\ . \tag{11}$$

Here α is the electromagnetic coupling constant, $G_{\rm F}$ is the Fermi constant and $Q_{\rm f}$ is the electric charge of the final state fermion f. The colour factor $N_{\rm c}$ is 1 for leptons and 3 for quarks, $\overline{m}_{\rm Z}$ is the mass of the Z boson and $\overline{\Gamma}_{\rm Z}$ its total decay width.[6] $\hat{g}_{\rm Af}$ and $\hat{g}_{\rm Vf}$ are the axial-vector and vector couplings between the participating fermions and the Z boson.

The first term in Equation 8 accounts for pure photon exchange, the second term for γ/Z interference and the third for pure Z exchange. The four coefficients $C_{\gamma Z}^{\rm s}$, $C_{\gamma Z}^{\rm a}$, $C_{ZZ}^{\rm s}$ and $C_{ZZ}^{\rm a}$ parametrise the

[6] The bars on $\overline{m}_{\rm Z}$ and $\overline{\Gamma}_{\rm Z}$ distinguish quantities defined in terms of the Breit-Wigner parametrisation with an s–independent total width from $m_{\rm Z}$ and $\Gamma_{\rm Z}$ which are defined in terms of an s–dependent total width, as discussed in connection with Equation 21.

terms symmetric ('s') and antisymmetric ('a') in $\cos\theta$. The relative size and the energy dependence of the five components of the differential cross-section (three symmetric terms for γ, γ/Z and Z, and two anti-symmetric terms for γ/Z and Z) as expected in the SM are shown in Figure 18. The symmetric terms are clearly dominated by pure Z exchange. In contrast, the antisymmetric pure Z term is much smaller in magnitude than the corresponding contribution from γ/Z interference, except very close to the pole of the Z resonance, where the latter crosses zero.

Integrated over the full angular phase space, the Z exchange term can be further expressed as a Breit-Wigner resonance:

$$\sigma^{\mathrm{Z}}_{\mathrm{f\bar{f}}}(s) = \sigma^0_{\mathrm{f}} \frac{s\overline{\Gamma}^2_{\mathrm{Z}}}{(s-\overline{m}^2_{\mathrm{Z}})^2 + \overline{m}^2_{\mathrm{Z}}\overline{\Gamma}^2_{\mathrm{Z}}} \quad , \tag{12}$$

where σ^0_{f} is the "pole cross-section", *i.e.* the total cross-section at $s = \overline{m}^2_{\mathrm{Z}}$. It is given in terms of the partial widths or the $C^{\mathrm{s}}_{\mathrm{ZZ}}$ parameter:

$$\sigma^0_{\mathrm{f}} = \frac{12\pi}{\overline{m}^2_{\mathrm{Z}}} \frac{\Gamma_{\mathrm{ee}}\Gamma_{\mathrm{ff}}}{\overline{\Gamma}^2_{\mathrm{Z}}} = \frac{C^{\mathrm{s}}_{\mathrm{ZZ}}\, N_{\mathrm{c}}}{6\pi} \left(\frac{\overline{m}^2_{\mathrm{Z}} G_{\mathrm{F}}}{\overline{\Gamma}_{\mathrm{Z}}} \right)^2 \quad , \tag{13}$$

where Γ_{ee} and Γ_{ff} are the partial decay widths of the Z to electron pairs and the fermion pair $\mathrm{f\bar{f}}$, respectively. In terms of couplings the partial width is given by:

$$\Gamma_{\mathrm{ff}} = \frac{G_{\mathrm{F}} N_{\mathrm{c}} \overline{m}^3_{\mathrm{Z}}}{6\pi\sqrt{2}} \left(\hat{g}^2_{\mathrm{Vf}} + \hat{g}^2_{\mathrm{Af}} \right) \quad . \tag{14}$$

The anti-symmetric terms in Equation 8 give rise to the forward-backward asymmetry A_{FB} defined in Equation 2. At centre-of-mass energies close to m_{Z} it can be approximated by:

$$A_{\mathrm{FB}}(s) = -\frac{3\pi\sqrt{2}\alpha Q_{\mathrm{f}}}{G_{\mathrm{F}}\overline{m}^2_{\mathrm{Z}}} \frac{C^{\mathrm{a}}_{\gamma\mathrm{Z}}}{C^{\mathrm{s}}_{\mathrm{ZZ}}} \frac{s-\overline{m}^2_{\mathrm{Z}}}{s} + \frac{3C^{\mathrm{a}}_{\mathrm{ZZ}}}{C^{\mathrm{s}}_{\mathrm{ZZ}}} \, . \tag{15}$$

The first term arises from the γ/Z interference and the second from pure Z exchange. The former gives the dominant contribution to A_{FB} except very close to the pole and causes a strong $\sqrt{s}$ dependence, as illustrated in Figure 18 (b). The latter is termed the "pole forward-backward asymmetry", $A^{0,\mathrm{f}}_{\mathrm{FB}}$, and can be conveniently expressed in terms of the coupling parameters $\mathcal{A}_{\mathrm{f}}$

$$A^{0,\mathrm{f}}_{\mathrm{FB}} = \frac{3}{4}\mathcal{A}_{\mathrm{e}}\mathcal{A}_{\mathrm{f}} \quad \text{with} \quad \mathcal{A}_{\mathrm{f}} = 2\frac{\hat{g}_{\mathrm{Vf}}\hat{g}_{\mathrm{Af}}}{\hat{g}^2_{\mathrm{Vf}} + \hat{g}^2_{\mathrm{Af}}} \, . \tag{16}$$

One should note that the relations presented so far are generally valid for the exchange of a massive spin-1 boson, independent of the specific form or size of the couplings between the heavy boson and the fermions. Only the well-tested prediction of QED for the strength of the vector-type coupling between photon and fermions is assumed. Within the SM, however, $\hat{g}_{\mathrm{Af}}$ and $\hat{g}_{\mathrm{Vf}}$ are given at tree level by the third component of the weak isospin I^3_{f}, the electric charge Q_{f} and the universal electroweak mixing angle, $\sin^2\theta_{\mathrm{W}}$:

$$\hat{g}_{\mathrm{Af}} = I^3_{\mathrm{f}} \quad , \quad \hat{g}_{\mathrm{Vf}} = I^3_{\mathrm{f}} - 2Q_{\mathrm{f}}\sin^2\theta_{\mathrm{W}} \, . \tag{17}$$

10.2 Radiative corrections

Radiative corrections significantly modify the $\mathrm{e^+e^-} \to \mathrm{f\bar{f}}$ cross-sections and forward-backward asymmetries with respect to the tree level calculation. One can distinguish four main categories:

- **Photon vacuum polarisation:** Vacuum polarisation leads to a scale dependence of the electromagnetic coupling constant α:

$$\alpha(0) \longrightarrow \alpha(s) = \frac{\alpha(0)}{1 - \Delta\alpha(s)} \, . \tag{18}$$

Due to uncertainties in the hadronic contribution to $\Delta\alpha(s)$ the value of α at $s = m_{\mathrm{Z}}^2$ has a considerable uncertainty ($\alpha(m_{\mathrm{Z}}^2)^{-1} = 128.886 \pm 0.090$ [**?**]), despite the high precision of α at $s = 0$ (0.04 ppm). There is also a small imaginary component of $\Delta\alpha(s)$ which leads to an additional contribution to the γ/Z interference in conjunction with the imaginary part of the Z propagator in Equation 9.

- **Initial-state radiation:** Photonic radiation in the initial state has a profound effect on the Z lineshape. It reduces the peak height by about 25%, shifts the peak upward by about 100 MeV and increases the apparent (FWHM) width by about 500 MeV, as illustrated in Figure 18 (e). Initial-state radiative corrections can be implemented in terms of a radiator function, $H(s, s')$, which relates the electroweak cross-section, $\sigma_{\mathrm{f\bar{f}}}$, to the observable cross-section, $\sigma_{\mathrm{f\bar{f}}}^{\mathrm{obs}}$, in terms of an integral over s', the squared invariant mass available to the hard electroweak interaction

$$\sigma_{\mathrm{f\bar{f}}}^{\mathrm{obs}}(s) = \int_{s_{\mathrm{min}}}^{s} \sigma_{\mathrm{f\bar{f}}}(s') H(s, s')\, \mathrm{d}s' \quad , \tag{19}$$

  where s_{min} is the minimum invariant mass squared of the system after initial state radiation.

- **Final-state radiation:** The radiation of photons or gluons (only for $\mathrm{q\overline{q}}$) in the final state increases the partial widths in first order by factors

$$\delta_{\mathrm{QED}} = 1 + \frac{3}{4}\frac{Q_f^2\,\alpha(m_{\mathrm{Z}}^2)}{\pi} \quad , \quad \delta_{\mathrm{QCD}} \simeq 1 + \frac{\alpha_{\mathrm{s}}(m_{\mathrm{Z}}^2)}{\pi} \, , \tag{20}$$

  where α_{s} is the strong coupling constant. For hadronic final states δ_{QCD} causes a sizeable correction which allows a precise determination of $\alpha_{\mathrm{s}}(m_{\mathrm{Z}}^2)$ from the inclusive hadronic width, Γ_{had}.

- **Electroweak corrections:** Quantum-loop effects in the Z propagator and vertex corrections involving the Higgs and the top quark give rise to radiative corrections, which in leading order depend quadratically on the mass of the top quark, m_{t}, and logarithmically on the Higgs boson mass, m_{H}. These effects give sensitivity to physics at much larger scales than m_{Z}^2.

When higher order corrections are considered mixed corrections arise; in particular QED/QCD and QCD/electroweak corrections are significant. In addition to γ and Z exchange, box diagrams also make small contributions to the process $\mathrm{e^+e^-} \to \mathrm{f\bar{f}}$, with a relative size $\leq 10^{-4}$ close to the Z resonance.

After unfolding the effects of initial and final-state radiation one can still retain the form of the differential cross-section expressed in Equation 8 with a few modifications:

- $\alpha(0)$ must be replaced by the (complex) $\alpha(m_{\mathrm{Z}}^2)$.

- Electroweak corrections can be absorbed by replacing the tree-level axial-vector and vector couplings, $\hat{g}_{\mathrm{Af}}$ and $\hat{g}_{\mathrm{Vf}}$, by the corresponding effective couplings $\mathcal{G}_{A\mathrm{f}}$ and $\mathcal{G}_{V\mathrm{f}}$, which are complex numbers with small imaginary components. In general, the effect of these imaginary components, termed "remnants", on the different terms of the differential cross-section is small. Most notable is their contribution to the symmetric part of the γ/Z interference, as shown in Figure 18 (c).

- Loop corrections to the Z propagator lead to an s–dependent decay width [**?**]. This can be accounted for by replacing ($\overline{\Gamma}_{\mathrm{Z}} \to \Gamma_{\mathrm{Z}}(s) \equiv s\Gamma_{\mathrm{Z}}/m_{\mathrm{Z}}^2$) in Equation 9, resulting in:

$$\chi(s) = \frac{G_{\mathrm{F}} m_{\mathrm{Z}}^2}{8\pi\sqrt{2}} \frac{s}{s - m_{\mathrm{Z}}^2 + i\,\frac{s}{m_{\mathrm{Z}}}\Gamma_{\mathrm{Z}}} \quad . \tag{21}$$

  One should note that this does not alter the form of the resonance curve but corresponds to a transformation which redefines both the Z mass, $m_{\mathrm{Z}} = \overline{m}_{\mathrm{Z}}\sqrt{1 + \overline{\Gamma}_{\mathrm{Z}}/\overline{m}_{\mathrm{Z}}}$, and width, $\Gamma_{\mathrm{Z}} = \overline{\Gamma}_{\mathrm{Z}}\sqrt{1 + \overline{\Gamma}_{\mathrm{Z}}/\overline{m}_{\mathrm{Z}}}$. Numerically, m_{Z} is shifted by about +34 MeV and Γ_{Z} by +1 MeV.

The Z resonance measurements are conveniently interpreted in terms of "model-independent" parameters, such as mass, total width, partial widths or pole cross-section, and pole asymmetry. In the presence of radiative corrections these parameters are no longer direct observables but depend on the specific choice of which radiative corrections to unfold or include and are therefore termed "pseudo-observables". In this paper we define the Z mass and width, m_{Z} and Γ_{Z}, in terms of the s–dependent Breit-Wigner of Equation 21. Following the standard convention adopted by the LEP experiments, the partial decay widths absorb all final-state and electroweak corrections, such that their sum equals the total decay width:

$$\Gamma_{\mathrm{ff}} = \frac{G_{\mathrm{F}} N_{\mathrm{c}} m_{\mathrm{Z}}^3}{6\pi\sqrt{2}} \left(|\mathcal{G}_{\mathrm{V}}^{\mathrm{f}}|^2 R_{\mathrm{V}}^{\mathrm{f}} + |\mathcal{G}_{\mathrm{A}}^{\mathrm{f}}|^2 R_{\mathrm{A}}^{\mathrm{f}} \right) + \Delta_{\mathrm{ew/QCD}} \, . \tag{22}$$

Here, $R_{\mathrm{V}}^{\mathrm{f}}$ and $R_{\mathrm{A}}^{\mathrm{f}}$ account for final-state corrections and fermion masses and $\Delta_{\mathrm{ew/QCD}}$ accounts for non-factorisable mixed electroweak/QCD contributions. After unfolding initial-state radiation the total cross-section from Z exchange can then be written as:

$$\sigma_{\mathrm{ff}}^{\mathrm{Z}}(s) = \frac{\sigma_{\mathrm{f}}^0}{\delta_{\mathrm{QED}}} \frac{s\Gamma_{\mathrm{Z}}^2}{(s-m_{\mathrm{Z}}^2)^2 + \frac{s^2}{m_{\mathrm{Z}}^2}\Gamma_{\mathrm{Z}}^2} \quad \text{with} \quad \sigma_{\mathrm{f}}^0 = \frac{12\pi}{m_{\mathrm{Z}}^2} \frac{\Gamma_{\mathrm{ee}}\Gamma_{\mathrm{ff}}}{\Gamma_{\mathrm{Z}}^2} \quad . \tag{23}$$

The factor $1/\delta_{\mathrm{QED}}$ (Equation 20) is needed to cancel the final-state radiative corrections in Γ_{ee} when used to describe the couplings to the initial state.

In contrast, for the pole asymmetries (Equation 16), the effects of final-state radiation and imaginary remnants are excluded; they are interpreted in terms of the real parts of the effective couplings:

$$A_{\mathrm{FB}}^{0,\mathrm{f}} = \frac{3}{4}\mathcal{A}_{\mathrm{e}}\mathcal{A}_{\mathrm{f}} \quad , \quad \mathcal{A}_{\mathrm{f}} = 2\,\frac{g_{\mathrm{Vf}}g_{\mathrm{Af}}}{g_{\mathrm{Vf}}^2 + g_{\mathrm{Af}}^2} \quad \text{with} \quad g_{\mathrm{Vf}} \equiv \mathrm{Re}(\mathcal{G}_{\mathrm{V}}^{\mathrm{f}}) \, , \; g_{\mathrm{Af}} \equiv \mathrm{Re}(\mathcal{G}_{\mathrm{A}}^{\mathrm{f}}) \, . \tag{24}$$

The imaginary remnants ($\mathrm{Im}(\mathcal{G}_{\mathrm{A}}^{\mathrm{f}})$, $\mathrm{Im}(\mathcal{G}_{\mathrm{V}}^{\mathrm{f}})$) are evaluated in the SM and the corresponding corrections are applied.

For the calculation of radiative corrections we used the programs ZFITTER [**?**] and TOPAZ0 [**?**]. Initial-state radiation is implemented completely to $\mathcal{O}(\alpha^2)$ [**?**] with leading $\mathcal{O}(\alpha^3)$ corrections [**?**]. The radiation of fermion pairs in the initial state is also included to $\mathcal{O}(\alpha^3)$ [**?**]. Photon radiation in the final state as well as initial and final state interference is treated to $\mathcal{O}(\alpha)$. The calculation of final-state radiation deserves a further comment. For the asymmetries and $\mathrm{e^+e^-} \to \mathrm{e^+e^-}$ cross-section, which are measured within tight kinematic cuts, we use $\alpha(0)$ as recommended in [**?**]. In contrast, for the other cross-sections, which are measured within inclusive cuts, we use $\alpha(m_{\mathrm{Z}}^2)$, which implicitly covers the dominant part of small effects from final-state pair production.

In addition to the one-loop level electroweak corrections, TOPAZ0 and ZFITTER include the leading ($\mathcal{O}(m_{\mathrm{t}}^4)$) and sub-leading ($\mathcal{O}(m_{\mathrm{t}}^2 m_{\mathrm{Z}}^2)$) two-loop corrections [**?**]. QCD corrections are calculated to $\mathcal{O}(\alpha_{\mathrm{s}}^3)$ [**?**], with mixed terms included to $\mathcal{O}(\alpha\alpha_{\mathrm{s}})$ and the leading $\mathcal{O}(m_{\mathrm{t}}^2\alpha_{\mathrm{s}})$ terms [**?**, **?**].

10.3 *t*-channel contributions to $\mathrm{e^+e^-} \to \mathrm{e^+e^-}$

For $\mathrm{e^+e^-} \to \mathrm{e^+e^-}$ events not only s-channel annihilation contributes but also the exchange of γ and Z in the t-channel. Since t-channel exchange is not included in our main fitting program, ZFITTER, an external treatment is needed to account for it. We use the program ALIBABA [**?**] to calculate the expected contribution from t-channel and s-t interference and add them to the pure s channel contributions calculated with ZFITTER. The details of how we treat these contributions in the fit and the associated uncertainties are described in Appendix B. The uncertainties on the fitted $\mathrm{e^+e^-}$ partial width, Γ_{ee}, and pole asymmetry, $A_{\mathrm{FB}}^{0,\mathrm{e}}$, due to the t-channel are 0.11 MeV and 0.0015, respectively, with a correlation coefficient of 0.85.

11 Determination of electroweak and Standard Model parameters

The 211 measurements of cross-sections and asymmetries listed in Tables 8 – 12 and Tables 22 – 24 form the basis of our tests of SM expectations, and our determination of electroweak parameters. The cross-section measurements at the three energy points of the precision scan determine the basic parameters of the Z resonance, its mass, m_{Z}, width, Γ_{Z}, and its pole production cross-sections, σ^0_{f}, for each of the four final states. By combining the measured pole cross-sections one can determine directly the absolute branching ratios ($\Gamma_{\mathrm{ff}}/\Gamma_{\mathrm{Z}}$) to hadrons and leptons, as can be seen from Equation 23. The branching ratio to invisible states, such as neutrinos, can be inferred from the difference between unity and the sum of the visible branching ratios. Combining the branching ratios with the total width yields the decay widths to each species. For leptons these widths provide a precise check of SM predictions for the leptonic couplings. The hadronic width, through QCD effects, provides a measurement of α_{s}. In contrast to almost all other measurements of this quantity, no hadronisation corrections are needed to compare with QCD calculations, which are available in $\mathcal{O}(\alpha_{\mathrm{s}}^3)$. Therefore QCD uncertainties are small. The charge asymmetries of the leptons produced at the peak allow the ratios of the leptonic vector and axial-vector couplings to be determined. Finally, through radiative effects on the effective couplings, limits can be placed on the mass of the Higgs boson.

The interpretation of our measured cross-sections and asymmetries in terms of electroweak parameters proceeds in three stages. First, we use a parametrisation based on Equation 8, where the C coefficients are treated as independent parameters, not imposing the constraints of Equations 10 and 11. Secondly, we perform the analysis in terms of the "model-independent Z parameters", which are based on mass, total width, pole cross-sections and pole asymmetries of the Z. The main difference with respect to the first approach is that in deriving the model-independent Z parameters the γ/Z interference is constrained to the theoretical prediction. Finally, we compare our measured cross-sections and asymmetries directly with calculations made in the context of the SM. This allows us to test the consistency of our measurements with the theoretical prediction and also to determine the SM parameters, m_{Z}, m_{t}, m_{H} and α_{s}.

For all our fits we use ZFITTER, version 6.21, with the default settings[7] to calculate the cross-sections and asymmetries within our ideal kinematic acceptance as functions of the fit parameters. The fit parameters are obtained from a χ^2 minimisation based on MINUIT [**?**], which takes into account the full covariance matrix of our data. In Appendix C we describe how the various sources of uncertainty are combined to construct the covariance matrix.

The SM calculations require the full specification of the fundamental SM parameters. The main parameters are the masses of the Z boson (m_{Z}), the top quark (m_{t}) and the Higgs boson (m_{H}), and the strong and electromagnetic coupling constants, α_{s} and α. Unless explicitly specified otherwise, we use for the calculation of imaginary remnants ($\mathrm{Im}(\mathcal{G}^{\mathrm{f}}_{\mathrm{A}})$, $\mathrm{Im}(\mathcal{G}^{\mathrm{f}}_{\mathrm{V}})$), non-factorisable corrections and for comparison with the SM predictions the following values and ranges:

$$\begin{aligned} m_{\mathrm{Z}} &= 91.1856 \pm 0.0030 \text{ GeV} \quad , \quad m_{\mathrm{t}} = 175 \pm 5 \text{ GeV} \, , \\ m_{\mathrm{H}} &= 150^{+850}_{-60} \text{ GeV} \quad , \quad \alpha_{\mathrm{s}} = 0.119 \pm 0.002 \text{ [?]} \, , \\ \Delta\alpha^{(5)}_{\mathrm{had}} &= 0.02804 \pm 0.00065 \quad . \end{aligned} \tag{25}$$

The values and ranges of m_{t} and α_{s} differ slightly from the most recent evaluations [**?**, **?**]. They were chosen for consistency with the corresponding publications of the other LEP experiments; the small differences are completely negligible for the results presented here. The range of m_{H} corresponds approximately to the lower limit from direct searches [**?**] and the upper limit from theoretical considerations [**?**]. The electromagnetic coupling α is expressed here in terms of $\Delta\alpha^{(5)}_{\mathrm{had}}$, the contribution of the five light quark flavours to the running of α at $s = m^2_{\mathrm{Z}}$ as described in Equation 18. The quoted value for $\Delta\alpha^{(5)}_{\mathrm{had}}$ corresponds to $\alpha(m^2_{\mathrm{Z}})^{-1} = 128.886 \pm 0.090$ [**?**] when the contributions

[7] Except for $\Delta\alpha^{(5)}_{\mathrm{had}}$, which we specify directly (flag ALEM = 2), and the correction of [**?**], which is used only for the SM fits in Section 11.4 (flag CZAK) as recommended by the authors of ZFITTER.

from the top quark and the leptons are also included. A further crucial parameter is the Fermi constant G_F, which can be determined precisely from the muon lifetime. We use the most recent value, $G_F = (1.16637 \pm 0.00001) \times 10^{-5}\,\mathrm{GeV}^{-2}$ [**?**], which includes two-loop QED corrections. Other input parameters of the SM, such as the masses of the five light quarks[8] and the leptons, are fixed to their present values [**?**].

11.1 *C*-Parameter fits

Our first analysis is based on a parametrisation according to Equation 8, treating the C-coefficients as independent fit parameters. In this ansatz, which we first introduced in the analyses of our 1990/1991 data samples [**?**, **?**], the differential cross-section is described in terms of four independent parameters, $C^{s}_{\gamma Z}$, $C^{a}_{\gamma Z}$, C^{s}_{ZZ} and C^{a}_{ZZ}, which express the symmetric and anti-symmetric contributions from γ/Z interference and pure Z exchange, respectively. Specifically we do not impose the constraints expressed in Equations 10 and Equations 11, which are in principle generally valid for the exchange of a massive vector boson with arbitrary axial-vector and vector couplings interfering with the photon. Contributions from new physics, however, such as an additional heavy vector boson, would lead to additional terms in Equation 8. In particular one would expect contributions from the interference between the Z and the extra boson, which would have the same form as the γ/Z interference. In the case of leptonic final states, the measurements of cross-sections and asymmetries are sensitive to all four parameters independently. Fitting the data with independent interference terms retains the sensitivity to such new physics effects. In addition, from the independent determination of $C^{s}_{\gamma Z}$ and $C^{a}_{\gamma Z}$ one can distinguish g_{Vf} and g_{Af} and determine the relative signs of the couplings, as discussed below in Section 11.3.3. This is not possible from the pure Z terms C^{s}_{ZZ} and C^{a}_{ZZ} alone, which are symmetric in g_{Vf} and g_{Af}.

In this analysis we do not include any hadronic forward-backward asymmetry data and hence only the terms symmetric in $\cos\theta$, $C^{s}_{\gamma Z}$ and C^{s}_{ZZ}, are accessible. However, the sensitivity to the γ/Z interference ($C^{s}_{\gamma Z}$) is small at centre-of-mass energies close to m_Z, since a shift of the interference term is essentially equivalent to a shift in m_Z. The fact that high statistics measurements of the cross-section are available only for three different centre-of-mass energies further aggravates the lack of discrimination between shifts in m_Z and the interference term. In the following analysis we therefore use the C-parametrisation only for leptons. The hadrons are parametrised in terms of an s–dependent Breit-Wigner resonance (Equation 23) with m_Z, Γ_Z and σ^0_h as fit parameters. The hadronic γ/Z interference term is fixed to the SM prediction. This constraint allows a precise determination of m_Z. With the leptonic γ/Z interference terms left free in the fit, m_Z is determined from the hadronic data and the $C^{s}_{\gamma Z}$ parameters for leptons therefore depend on the assumed interference term for hadrons.

For the precise definition of the C-parameters several choices could be made. We employ a definition such that the parameters can be interpreted directly in terms of the real parts of the effective couplings, *i.e.* the meaning of the C-parameters in the SM corresponds to Equations 10 and 11 with $\hat{g}_{Af}$ and $\hat{g}_{Vf}$ replaced by g_{Af} and g_{Vf} as in Equation 24. We use ZFITTER to correct for initial and final-state radiation and the running of α and to calculate the imaginary remnants of the couplings. Since these remnants are small and essentially independent of the centre-of-mass energy in the LEP 1 region, this SM correction does not compromise the independence of the parametrisation from theoretical assumptions, but it preserves a transparent interpretation of the C-parameters in terms of SM couplings.

If lepton universality is not assumed, there are a total of 15 parameters: $m_Z, \Gamma_Z, \sigma^0_h$ and four C-parameters – $C^{s}_{\gamma Z}$, $C^{a}_{\gamma Z}$, C^{s}_{ZZ}, C^{a}_{ZZ} – for each lepton species. These fitted parameters are shown in column two of Table 26. The values obtained from the different lepton species for the C-parameters are consistent with one another, compatible with lepton universality. Column three of Table 26 gives the results for a 7 parameter fit when lepton universality is imposed by requiring each of the four C-parameters to be equal across the three lepton species. The SM predictions are shown in the last

[8] See [**?**] for details on the treatment of quark masses.

column. The error correlation matrices are given in Tables 27 and 28.

Figure 19 compares the parameters measured assuming lepton universality with the SM predictions as a function of $m_{\rm H}$. We see agreement for all parameters. The largest discrepancy, of about two standard deviations, occurs in the parameter $C^{\rm a}_{\gamma{\rm Z}}$. The same tendency was observed in our previous analysis using only the data collected from 1990 to 1992 [**?**]. This parameter corresponds to the energy dependence of the leptonic forward-backward asymmetry.

As a check we also performed a fit releasing the SM constraint for the hadronic $\gamma/{\rm Z}$ interference by introducing a scale factor for the $\gamma/{\rm Z}$ interference contribution ($f_{\gamma/{\rm Z}} = 1$ in the SM) which was treated as an additional free parameter. The fit resulted in $m_{\rm Z} = 91.190 \pm 0.011$ GeV and $f_{\gamma/{\rm Z}} = 0.0 \pm 3.0$, with a correlation coefficient of -0.96. This is in good agreement with the $m_{\rm Z}$ result in Table 26 and with $f_{\gamma/{\rm Z}} = 1$. The large increase of the $m_{\rm Z}$ uncertainty and the high anti-correlation with $f_{\gamma/{\rm Z}}$ illustrates the fact that LEP 1 measurements alone give marginal discrimination between hadronic $\gamma/{\rm Z}$ interference effects and $m_{\rm Z}$ shifts. In combination with measurements at energies further away from the Z resonance, *e.g.*, the fermion-pair cross-sections at LEP 2, this problem can be resolved [**?**].

An alternative model-independent parametrisation of the Z resonance is the S-Matrix formalism [**?**]. In practice this approach is equivalent to the C-parameters. Since the S-Matrix parametrisation is the standard framework for combined LEP 1 and LEP 2 cross-section and asymmetry measurements we also give the S-Matrix results in Appendix D.

11.2 Results of the model-independent Z parameter fits

Our second fit is based on the model-independent Z parameters, which consist of $m_{\rm Z}$, $\Gamma_{\rm Z}$, $\sigma^0_{\rm h}$, and $A^{0,\ell}_{\rm FB}$ as given in Equations 23 and 24, as well as the ratios of hadronic to leptonic widths:

$$R_\ell \equiv \frac{\Gamma_{\rm had}}{\Gamma_{\ell\ell}} \quad (\ell = {\rm e}, \mu, \tau) \quad . \tag{26}$$

The partial widths include final-state and electroweak corrections as defined in Equation 22. This set of pseudo-observables is closely related to the experimental measurements and sufficient to parametrise the Z properties; correlations between the parameters are small. For this reason it has been adopted by the four LEP collaborations to facilitate the comparisons and averaging of the Z resonance measurements.

The essential difference between this fit and the C-parameter fit above is that now, in addition to the hadronic interference term, the leptonic $\gamma/{\rm Z}$ interference terms ($C^{\rm s}_{\gamma{\rm Z}}$ and $C^{\rm a}_{\gamma{\rm Z}}$) are also constrained to the SM prediction. The expression of resonant lepton production in terms of R_ℓ, $\sigma^0_{\rm h}$ and $A^{0,\ell}_{\rm FB}$ is equivalent to the $C^{\rm s}_{\rm ZZ}$ and $C^{\rm a}_{\rm ZZ}$ formulation.

The results of the 9 parameter fit (without lepton universality) and the 5 parameter fit (assuming lepton universality) are shown in Table 29, together with the SM predictions in the last column. The error correlations are given in Tables 30 and 31. For the fits where lepton universality is not imposed the large mass of the τ is expected to reduce $\Gamma_{\tau\tau}$ by about 0.2%. Lepton universality would therefore be reflected in R_τ being 0.047 larger than $R_{\rm e}$ and R_μ. In the 5 parameter fit, where lepton universality *is* imposed, the τ mass effect is corrected; $\Gamma_{\ell\ell}$ refers to the partial decay width of the Z into massless charged leptons. Figure 20 compares the parameters fit assuming lepton universality with the SM prediction as a function of the Higgs mass. The agreement for all parameters is good.

In the context of this parameter set, we also make a test of the consistency of the LEP energy calibration. To make this test, we replace the single parameter $m_{\rm Z}$ with three independent parameters for the three periods which distinguish the stages in the evolution of the LEP calibration; these are 1990–92, 1993–94 and 1995. The results are given in Table 32. The errors of the three $m_{\rm Z}$ values are largely uncorrelated, and the stability of the LEP energy calibration is verified within the precision of our measurements.

The value of $m_{\rm Z}$ we obtain in the fit to the model-independent Z parameters is about 1 MeV smaller than the value we obtain in the fit to the C-parameters. This difference is due to the fact that in the C-parameter fit the leptons contribute much less to the $m_{\rm Z}$ measurement, since the leptonic $\gamma/{\rm Z}$

interference terms are allowed to vary freely. One should also note that m_Z shifts by -0.5 MeV when lepton universality is imposed, in both the fit with C-parameters and the fit with model-independent Z parameters. This is due to a subtle effect in the $e^+e^- \to e^+e^-$ t-channel correction, which gives an additional weak constraint on m_Z (see Appendix B).

Figures 21 and 22 compare the cross-section and asymmetry measurements with the results of the 9-parameter model-independent fit. Figure 23 shows the contours in the $A_{FB}^{0,\ell}$ – R_ℓ plane, separately for the three lepton species as well as for a universal charged lepton. There is a large anti-correlation between $A_{FB}^{0,e}$ and R_e, due to the appreciable non-s-channel contributions, as discussed in Appendix B.

11.2.1 Error composition and χ^2

Table 33 shows the approximate error composition for the model-independent Z parameters and for the derived parameters which are discussed below. Only in the case of σ_h^0 and R_τ do systematic uncertainties exceed the statistical errors. For Γ_Z and the asymmetries the statistical errors are still much larger than the systematics. This parameter set also benefits from a division of the major systematic uncertainties. The LEP energy mainly affects m_Z and Γ_Z, the luminosity uncertainty enters nearly exclusively in σ_h^0, and t-channel uncertainties are isolated in R_e and $A_{FB}^{0,e}$. Such a separation of effects greatly facilitates the combination of the results with the other LEP experiments, since these are the uncertainties which are common to all experiments. For other possible parametrisations, *e.g.*, in terms of partial widths, C-parameters or the S-matrix, the systematic effects on the parameters are much more poorly separated.

The χ^2 values of our fits are somewhat lower than expected, for example in the 9-parameter model-independent fit $\chi^2 = 155.6$ with 194 degrees of freedom.[9] The probability to obtain $\chi^2 \leq 155.6$ is 2%. The low value of χ^2 can be attributed predominantly to anomalously low statistical fluctuations in the data with lower precision taken in the early phase of LEP running (1990–1992). It was already present in our earlier publications [?, ?, ?]. A fit to the 1993–1995 data alone results in χ^2/d.o.f. $= 34.2/40$, where the probability to obtain a lower χ^2 is 27%.

11.2.2 Theoretical uncertainties

The relatively large effects from theoretical uncertainties in the luminosity determination and the $e^+e^- \to e^+e^-$ t-channel correction are discussed elsewhere in this paper; these are already treated in the fit procedure and included in the quoted parameter errors. Additional uncertainties arise from the deconvolution of initial-state radiation (ISR), possible ambiguities in the precise definition of the pseudo-observables and residual dependence on the values of the SM parameters which we have assumed.

ISR corrections substantially affect the Z lineshape. In the fitting programs ZFITTER and TOPAZ0, their implementation is complete to $\mathcal{O}(\alpha^2)$ and includes the leading $\mathcal{O}(\alpha^3)$ terms. In a recent evaluation [?] different schemes have been compared and the effect of missing higher order terms estimated; the residual uncertainties are limited to 0.004 nb for σ_h^0, 0.1 MeV for m_Z and Γ_Z, and are negligible for other parameters. A related effect is the correction for fermion-pair radiation in the initial state. Although this correction is about two orders of magnitude smaller than the ISR correction it gives rise to somewhat larger uncertainties. Comparing different schemes and implementations[10] leads to uncertainties of 0.3 MeV for m_Z, 0.2 MeV for Γ_Z and 0.006 nb for σ_h^0.

We further investigated possible differences in the definition of pseudo-observables or their implementation by comparing the programs ZFITTER and TOPAZ0. In a very detailed comparison [?] the authors of the two packages demonstrated the good overall consistency in their implementations of radiative corrections and SM calculations. In addition, we evaluated differences between the two

[9] For determining the number of degrees of freedom one needs to account for the six sets of "pseudo-cross-sections" (Section 8) and for the fact that we allow the absolute normalisation of the cross-sections and the energy scale to float in the 1990 data. Therefore the number of effective measurements is reduced from 211 to 203.

[10] We repeated the fits varying the ZFITTER flags ISPP=2,3,4 which select the parametrisations of [?] and two variants of [?]. The maximal difference is taken as the error.

programs by using one to calculate a set of cross-sections and asymmetries and using the other to re-fit this set. The effective differences in terms of pseudo-observables are 0.2 MeV for $m_{\rm Z}$, 0.1 MeV for $\Gamma_{\rm Z}$, 0.003 nb for $\sigma^0_{\rm h}$, 0.004 for R_ℓ, and 0.0001 for $A^{0,\ell}_{\rm FB}$. The difference in R_ℓ is the only notable effect; it corresponds to 10% of the experimental error. Further effects from missing higher order electroweak corrections have also been studied. Such corrections are small and affect the pseudo-observables only through the tiny SM remnants. Numerically, the changes are found to be negligible.

Finally, we evaluated the dependence of the fitted pseudo-observables on the SM parameters $\alpha(m^2_{\rm Z})$, $\alpha_{\rm s}(m^2_{\rm Z})$, $m_{\rm t}$ and $m_{\rm H}$. The values assumed for these parameters affect the fitted pseudo-observables mainly through the γ/Z interference which is taken from the SM. The effects, however, are small; the only notable impact is on $m_{\rm Z}$, which changes by 0.2 MeV when varying $m_{\rm H}$ from 90 to 1000 GeV.

The overall theoretical uncertainties for the Z resonance parameters from all these sources are given in the last column of Table 33. These have a negligible effect on our results, since in all cases the theoretical error is much less than the total uncertainty; the largest effects are for $\sigma^0_{\rm h}$ with 15% and $m_{\rm Z}$ and R_ℓ with 10% of the total error.

11.3 Interpretation

The model-independent Z parameters were chosen to be closely related to the measured quantities and have minimal correlations with each other. These parameters can easily be transformed to other equivalent sets of physical quantities for the interpretation of our results.

11.3.1 Z decay widths

From the model-independent Z parameters $\Gamma_{\rm Z}$, $\sigma^0_{\rm h}$, $R_{\rm e}$, R_μ, and R_τ the partial Z decay widths $\Gamma_{\rm inv}$, $\Gamma_{\rm ee}$, $\Gamma_{\mu\mu}$, $\Gamma_{\tau\tau}$, and $\Gamma_{\rm had}$ can be derived, and are shown in Table 34. Here $\Gamma_{\rm inv}$ is the width of the Z to final states not accounted for in the analysis of $\rm e^+e^- \to e^+e^-$, $\mu^+\mu^-$, $\tau^+\tau^-$ and $\rm q\overline{q}$ processes discussed in the previous sections

$$\Gamma_{\rm inv} \equiv \Gamma_{\rm Z} - \Gamma_{\rm ee} - \Gamma_{\mu\mu} - \Gamma_{\tau\tau} - \Gamma_{\rm had} \; . \tag{27}$$

The correlations between the partial widths are large and are given in Tables 35 and 36. In Table 34 good agreement is seen among the measured lepton partial widths and with the SM expectations. By assuming lepton universality, our measurement of $\Gamma_{\rm inv}$ becomes more precise.

A quantity sensitive to a possible deviation of the data from the SM prediction for the invisible width is the ratio

$$R_{\rm inv} \equiv \frac{\Gamma_{\rm inv}}{\Gamma_{\ell\ell}} \; . \tag{28}$$

In this ratio experimental errors partially cancel and theoretical uncertainties due to the assumed values of $m_{\rm t}$ and $m_{\rm H}$ are strongly reduced. In the SM only neutrinos contribute to $\Gamma_{\rm inv}$. The first Z resonance measurements at SLC and LEP in 1989 [**?**] demonstrated the existence of three generations of light neutrinos. For three generations one expects

$$R^{\rm SM}_{\rm inv} = 3\frac{\Gamma_{\nu\nu}}{\Gamma_{\ell\ell}} = 5.974 \pm 0.004 \; ,$$

where the uncertainty corresponds to variations of $m_{\rm t} = 175 \pm 5$ GeV and $90 < m_{\rm H} < 1000$ GeV. Taking into account the correlation between $\Gamma_{\rm inv}$ and $\Gamma_{\ell\ell}$ our measured value is

$$R_{\rm inv} = 5.942 \pm 0.027 \; .$$

Dividing $R_{\rm inv}$ by the SM expectation for a single generation, $\Gamma_{\nu\nu}/\Gamma_{\ell\ell}$, gives

$$N_\nu = 2.984 \pm 0.013 \; .$$

The measurements of the total and partial Z decay widths give important constraints for extensions of the SM which predict additional decay modes of the Z into new particles. From the difference

between measured widths and the SM predictions (assuming three neutrino species) one can derive upper limits for such contributions from new physics. New particles could contribute either to one of the visible decay channels in the partial widths or to the invisible width, depending on their specific properties. In order to calculate the upper limits for such extra contributions to the widths we added the experimental and theoretical errors in quadrature. For the latter we evaluated the change of the predicted widths when varying the SM input parameters, m_{Z}, m_{t}, $\alpha_{\mathrm{s}}(m_{\mathrm{Z}}^2)$ and $\alpha(m_{\mathrm{Z}}^2)$, within their experimental precision (Equation 25). For the mass of the Higgs boson we used 1000 GeV. This results in the smallest theoretical predictions for the widths and therefore in the most conservative limits. We obtain

$$\Gamma_{\mathrm{Z}}^{\mathrm{new}} < 14.8\,\mathrm{MeV} \quad \text{and} \quad \Gamma_{\mathrm{inv}}^{\mathrm{new}} < 3.7\,\mathrm{MeV} \tag{29}$$

as one-sided upper limits at 95% confidence level for additional contributions to the total ($\Gamma_{\mathrm{Z}}^{\mathrm{new}}$) and the invisible width ($\Gamma_{\mathrm{inv}}^{\mathrm{new}}$). The limits for $m_{\mathrm{H}} = 150$ GeV and for the visible partial widths are given in Table 37. All limits are Bayesian with a prior probability which is uniform for positive $\Gamma_{\mathrm{x}}^{\mathrm{new}}$.

11.3.2 Coupling parameters and the effective mixing angle

From the measured pole asymmetries $A_{\mathrm{FB}}^{0,\ell}$ it is straightforward (Equation 24) to determine the coupling parameters $\mathcal{A}_\ell$, which quantify the asymmetry of the Z–lepton coupling for each lepton species. The results for the three lepton species are consistent with each other and agree well with the SM predictions, as shown in Table 38. However, since the measured $A_{\mathrm{FB}}^{0,\mu}$ and $A_{\mathrm{FB}}^{0,\tau}$ are products of $\mathcal{A}_{\mathrm{e}}$ with either $\mathcal{A}_\mu$ or $\mathcal{A}_\tau$, large anti-correlations (Table 39) arise between $\mathcal{A}_{\mathrm{e}}$ and $\mathcal{A}_\mu$, $\mathcal{A}_\tau$.

An equivalent formulation of the coupling asymmetries can be made in terms of the effective weak mixing angle $\sin^2\theta_{\mathrm{eff}}^{\mathrm{lept}}$. Assuming lepton universality we obtain

$$\sin^2\theta_{\mathrm{eff}}^{\mathrm{lept}} \equiv \frac{1}{4}\left(1 - \frac{g_{\mathrm{V}\ell}}{g_{\mathrm{A}\ell}}\right) = 0.2325 \pm 0.0010\ , \tag{30}$$

which is in good agreement with the world average of 0.23151 ± 0.00017 [**?**].

11.3.3 Vector and axial-vector couplings

Using the set of the model-independent Z parameters one can determine the leptonic vector and axial-vector couplings $g_{\mathrm{V}\ell}$ and $g_{\mathrm{A}\ell}$ for the neutral currents. The results are given in Table 40. There are strong anti-correlations between the $\mathrm{e^+e^-}$ couplings on one side and the $\mu^+\mu^-$ and $\tau^+\tau^-$ couplings on the other, and also between vector and axial-vector couplings for each lepton species. This is shown in Table 41 and illustrated in Figure 24. When lepton universality is imposed the anti-correlation between $g_{\mathrm{V}\ell}$ and $g_{\mathrm{A}\ell}$ is reduced to -29%. Good agreement is found with the prediction of the SM. Being determined primarily from the lepton cross-sections, $g_{\mathrm{A}\ell}$ has a small relative error. Ratios of couplings provide a powerful test of lepton universality for the axial-vector couplings at the 0.5% level:

$$\frac{g_{\mathrm{A}\mu}}{g_{\mathrm{Ae}}} = 0.9989^{+0.0033}_{-0.0058}\ , \quad \frac{g_{\mathrm{A}\tau}}{g_{\mathrm{Ae}}} = 1.0003^{+0.0037}_{-0.0055}\ , \quad \frac{g_{\mathrm{A}\tau}}{g_{\mathrm{A}\mu}} = 1.0014^{+0.0036}_{-0.0034}\ . \tag{31}$$

For the vector couplings the relative uncertainties are much larger. They are also very asymmetric and strongly correlated between lepton species. Because the observables $A_{\mathrm{FB}}^{0,\mu}$ or $A_{\mathrm{FB}}^{0,\tau}$ are each products of $g_{\mathrm{V}\mu}$ or $g_{\mathrm{V}\tau}$ and g_{Ve}, the derived values of $g_{\mathrm{V}\mu}$ and $g_{\mathrm{V}\tau}$ diverge if g_{Ve} approaches zero. This pathology is visible in the strongly asymmetric errors in $g_{\mathrm{V}\mu}$ and $g_{\mathrm{V}\tau}$ and the corresponding tails in Figure 24. When we form the vector coupling ratios the non-Gaussian behaviour of the uncertainties is further enhanced for $g_{\mathrm{V}\mu}/g_{\mathrm{Ve}}$ and $g_{\mathrm{V}\tau}/g_{\mathrm{Ve}}$, while $g_{\mathrm{V}\tau}/g_{\mathrm{V}\mu}$ has much smaller and rather symmetric errors:

$$\frac{g_{\mathrm{V}\mu}}{g_{\mathrm{Ve}}} = 1.79^{+1.84}_{-0.64}\ , \quad \frac{g_{\mathrm{V}\tau}}{g_{\mathrm{Ve}}} = 1.63^{+1.72}_{-0.61}\ , \quad \frac{g_{\mathrm{V}\tau}}{g_{\mathrm{V}\mu}} = 0.91^{+0.25}_{-0.21}\ . \tag{32}$$

One should emphasise that the non-linearities in the determination of $g_{\mathrm{V}\ell}$ are driven by the observed, statistically limited, measurement of $A_{\mathrm{FB}}^{0,\mathrm{e}}$. Our value of $A_{\mathrm{FB}}^{0,\mathrm{e}}$ is small and only two standard deviations

above zero, although compatible with the SM prediction. The problem is less apparent and the propagated errors in the vector couplings are significantly reduced when $A_{\rm FB}^{0,\rm e}$ happens to be large, as is the case for example in [**?**].

The pure Z pseudo-observables R_ℓ and $A_{\rm FB}^{0,\ell}$ are symmetric in $g_{\rm V\ell}$ and $g_{\rm A\ell}$, as can be seen from Equations 14 and 16. The results would not change if the values of $g_{\rm V\ell}$ and $g_{\rm A\ell}$ were interchanged. Our measurements of the C-parameters describing the γ/Z interference (Equation 10) can be used to resolve this ambiguity. $C_{\gamma\rm Z}^{\rm s}$ parametrises the interference contribution symmetric in $\cos\theta$ and $C_{\gamma\rm Z}^{\rm a}$ the strong $\sqrt{s}$ dependence of the asymmetries (Equation 15). The results of the fit, as given in Table 26, distinguish $g_{\rm V\ell}$ and $g_{\rm A\ell}$ unambiguously. $C_{\gamma\rm Z}^{\rm a}$ and $C_{\rm ZZ}^{\rm a}$ also determine the signs of $g_{\rm A\mu}$ and $g_{\rm A\tau}$ relative to $g_{\rm Ae}$ (and the signs of $g_{\rm V\mu}$ and $g_{\rm V\tau}$ relative to $g_{\rm Ve}$). The last remaining ambiguity, which the lineshape and asymmetry data alone cannot resolve, is the relative sign[11] of $g_{\rm V\ell}$ and $g_{\rm A\ell}$. This can be determined by measurements of the τ *polarisation* asymmetries [**?**] or the *left-right* asymmetry [**?**], which determine directly the ratio $g_{\rm V\ell}/g_{\rm A\ell}$ for a specific flavour.

11.3.4 $\alpha_{\rm s}$ from the Z resonance parameters

As discussed in Section 10.2 the hadronic partial decay width, $\Gamma_{\rm had}$, is increased by final state QCD corrections, in first order by a factor $1+\frac{\alpha_{\rm s}}{\pi}$. In ZFITTER corrections up to $\mathcal{O}(\alpha_{\rm s}^3)$ are included.

The largest contribution to $\Gamma_{\rm Z}$ is from $\Gamma_{\rm had}$. As a result several Z resonance parameters are sensitive to $\alpha_{\rm s}$, namely the total width $\Gamma_{\rm Z}$ directly, the ratio of hadronic to leptonic partial width R_ℓ, the hadronic pole cross-section $\sigma_{\rm h}^0$ and finally the leptonic pole cross-section σ_ℓ^0 (obtained by transforming the results in Table 29, $\sigma_\ell^0 = 1.9932 \pm 0.0043\,$nb). From the three observables R_ℓ, $\sigma_{\rm h}^0$, σ_ℓ^0 only two are independent and the best constraint on $\alpha_{\rm s}$ is obtained in a simultaneous fit to all parameters. This is discussed in Section 11.4. However, from the experimental point of view rather different effects dominate the uncertainty of each of these observables, and it is therefore instructive to examine the value of $\alpha_{\rm s}$ derived from each individual observable. The measurement via $\Gamma_{\rm Z}$ is statistics limited and free of normalisation errors, that via R_ℓ is independent of the luminosity and limited by lepton statistics and systematics, while for the measurement via $\sigma_{\rm h}^0$ statistics, selection systematics and luminosity uncertainties contribute about equally, and finally, the measurement via σ_ℓ^0 is free of any hadronisation uncertainties.

Figure 25 shows these observables and the SM prediction as implemented in ZFITTER as a function of $\alpha_{\rm s}$. Also shown are the effects of varying the parameters $m_{\rm t}$, $m_{\rm H}$ and $\alpha(m_{\rm Z}^2)$. The resulting values for $\alpha_{\rm s}$ are listed in Table 42. They are in good agreement within the experimental errors.

Since σ_ℓ^0, $\sigma_{\rm h}^0$ and R_ℓ are ratios of partial or total widths, the values of $\alpha_{\rm s}$ derived through these parameters are rather insensitive to variations of the SM parameters, which affect $\Gamma_{\ell\ell}$, $\Gamma_{\rm had}$ and $\Gamma_{\rm Z}$ similarly, while the value derived through $\Gamma_{\rm Z}$ depends more strongly on $m_{\rm t}$ and $m_{\rm H}$. It is interesting to note that $\alpha_{\rm s}$ from σ_ℓ^0, a measurement relying entirely on leptonic final states, has by far the smallest uncertainty. This somewhat counter-intuitive result is due to the fact that σ_ℓ^0 depends quadratically on $\Gamma_{\rm Z}$ and is therefore most sensitive to the effect of $\alpha_{\rm s}$ on $\Gamma_{\rm had}$, through the dominant contribution of the latter to $\Gamma_{\rm Z}$.

QCD uncertainties on the determination of $\alpha_{\rm s}(m_{\rm Z}^2)$ from the Z resonance parameters are small. The dominant effect comes from the unknown terms of $\mathcal{O}(\alpha_{\rm s}^4)$ and higher. However, several evaluations exist in the literature, which result in rather different error estimates. In Reference [**?**], which is the basis of the ZFITTER QCD corrections, the renormalisation scale dependence ($1/4 < \mu^2/m_{\rm Z}^2 < 4$) of the massless non-singlet terms entering $\Gamma_{\rm had}$ translates into $-0.0002 < \delta\alpha_{\rm s} < +0.0013$ for $\alpha_{\rm s} = 0.125$. Other contributions, such as the renormalisation scheme or the uncertainty of the b quark mass, are below ± 0.0005. In Reference [**?**] the renormalisation scale dependence of R_ℓ is evaluated based on an effective parametrisation of R_ℓ as function of $\alpha_{\rm s}$. Using a wider range ($1/16 < \mu^2/m_{\rm Z}^2 < 16$) results in $-0.0004 < \delta\alpha_{\rm s} < +0.0028$. In Reference [**?**] a similar scale dependence of $\alpha_{\rm s}(m_{\rm Z}^2)$ from R_ℓ is found. However, the authors then resum additional terms ("π^2 terms") in the perturbative expansion of R_ℓ,

[11] The absolute sign of one of the axial-vector or vector couplings needs to be defined. By convention one takes $g_{\rm Ae}$ as negative.

which leads to a slight correction of +0.6% for the resulting $\alpha_s(m_Z^2)$ and reduces the renormalisation scale uncertainty to ± 0.0005.

Given the small size of this correction, and to remain consistent with the other LEP collaborations, we do not correct our result obtained from ZFITTER and assign a conservative systematic error of ± 0.002 as the QCD uncertainty for α_s derived from the Z resonance parameters, which is still significantly smaller than the experimental precision. In principle, α_s dependent propagator corrections enter differently in the various Z resonance observables.[12] However, since these corrections are much smaller than the dominating α_s correction to Γ_{had}, these differences can be safely neglected for the overall QCD uncertainty.

11.4 Standard Model fits

As a last step we compare our measured cross-sections and asymmetries directly with the full SM calculations implemented in ZFITTER, using as fit parameters m_Z, α_s, m_t and m_H. In addition, the electromagnetic coupling constant is constrained by $\Delta\alpha^{(5)}_{had} = 0.02804 \pm 0.00065$ [**?**]. The lineshape and asymmetry measurements alone are not sufficient to determine simultaneously m_t, m_H and α_s. The leading electroweak radiative corrections in terms of m_t^2 and $-\log(m_H)$ have the same form for all fermion partial widths and lepton asymmetries. The only exception is the b-quark partial width, which has unique m_t dependent vertex corrections. This leads to a somewhat different m_t dependence for the inclusive hadronic width, Γ_{had}. However, this potential discrimination power is absorbed by α_s when it can vary freely in the fit. Therefore additional constraints on these parameters or supplementary electroweak precision measurements are needed for a simultaneous fit to m_t, m_H and α_s.

We choose to restrict ourselves to three scenarios: *(i)* determination of α_s and m_t from the lineshape and asymmetry measurements alone, restricting m_H to the range 90–1000 GeV, with a central value of 150 GeV; *(ii)* determination of m_H and α_s, using the direct Tevatron measurement of the top quark mass, $m_t = 174.3 \pm 5.1$ GeV [**?**], as an external constraint; and *(iii)* determination of m_H alone, using in addition to the m_t constraint also the recent world average of $\alpha_s = 0.1184 \pm 0.0031$ [**?**].

The results of these fits are shown in Table 43. Our measured cross-sections and asymmetries are consistent with the SM predictions as indicated both by the absolute χ^2/d.o.f. and by its small change with respect to the model-independent fits. In fit *(i)* we determine a value of $m_t = 162 \pm 15^{+25}_{-5}\,(m_H)$ GeV through the indirect effect of radiative corrections, which agrees well with the direct measurement. This agreement is a sensitive validation of the electroweak loop corrections. In fit *(ii)* we obtain

$$\alpha_s(m_Z^2) = 0.127 \pm 0.005 \pm 0.002\,(\,\mathrm{QCD}) \tag{33}$$

for the strong coupling constant, which is consistent within about 1.5 standard deviations with the world average. Also in fit *(ii)* we find $m_H = 390^{+750}_{-280}$ GeV as the mass of the Higgs boson. In fit *(iii)*, when we further use the external value of α_s, the fitted result for the Higgs mass moves lower, to $m_H = 190^{+335}_{-165}$ GeV, due to the correlation between α_s and m_H. The correlation is illustrated in Figure 26 which shows the 68% C.L. contour of α_s and m_H for fit *(ii)*. Since the leading radiative corrections depend logarithmically on m_H the uncertainty of m_H is very asymmetric. But even in terms of $\log m_H$ the error is asymmetric. This is due to the fact that the fit allows a wide range for m_H but only for $m_H \gg m_W$ is the logarithmic dependence a good approximation.

It is important to verify that performing a SM fit on the level of pseudo-observables is equivalent to fitting the cross-sections and asymmetries directly. Using the results of the 9-parameter model-independent fit (Tables 29 and 31) as input to the SM fit yields consistent results: the central values for the SM parameters agree within 10% of the error; uncertainties and correlations are indistinguishable within the quoted precision. This is illustrated in Figure 26 which also shows the 68% contour from

[12] The residual differences are caused by QCD effects in terms involving the top-quark mass which almost completely cancel in quantities that depend on the ratio of widths. At present, uncertainties in these effects [**?**] are equivalent to an error ~ 1 GeV in m_t, and are much smaller than the uncertainty on the measured top mass.

the pseudo-observable fit. When these results are combined with other electroweak measurements [?] to determine SM parameters, the fits are performed at the level of pseudo-observables.

12 Summary and conclusions

We present here the OPAL analysis of the Z cross-section and lepton forward-backward asymmetry measurements. This analysis includes the entirety of the OPAL data sample taken near the Z resonance from 1990 to 1995. In addition to the nearly four-fold increase in statistics since our last publication [?] many improvements have been made in the experimental and theoretical systematic uncertainties of the measurements. One important contribution is the reduction of the experimental error of the luminosity determination [?] by more than a factor of ten. New techniques to evaluate systematic effects of the event selections more than halved this source of uncertainty for the hadronic cross-section. Similar progress has been made in the precision of the external inputs to our measurements, namely the precise determination of the LEP centre-of-mass energy [?] and the theoretical calculation of the luminosity cross-section [?, ?], as well as in the theoretical tools and programs used to evaluate and interpret our results [?, ?, ?]. Overall, these coherent efforts allowed us to exploit most of the inherent statistical precision of our 4.5×10^6 measurable Z decays.

In a model-independent ansatz we parametrise independently the contributions from pure Z exchange and from γ/Z interference. Our results are in good agreement with lepton universality and consistent with the vector and axial-vector couplings between the Z and fermions as predicted in the SM. Our main results in terms of Z resonance parameters, assuming lepton universality, can be summarised as:

$$\begin{aligned} m_{\mathrm{Z}} &= 91.1852 \pm 0.0030\,\mathrm{GeV}\ , \\ \Gamma_{\mathrm{Z}} &= 2.4948 \pm 0.0041\,\mathrm{GeV}\ , \\ \sigma^0_{\mathrm{h}} &= 41.501 \pm 0.055\,\mathrm{nb}\ , \\ R_\ell &= 20.823 \pm 0.044\ , \\ A^{0,\ell}_{\mathrm{FB}} &= 0.0145 \pm 0.0017\ . \end{aligned}$$

Transforming these parameters yields the ratio of invisible to leptonic decay width,

$$\Gamma_{\mathrm{inv}}/\Gamma_{\ell\ell} = 5.942 \pm 0.027\ .$$

Assuming the SM couplings for leptons this can be converted into a measurement of the effective number of light neutrino species

$$N_\nu = 2.984 \pm 0.013\ .$$

Alternatively, one can use the SM prediction of Γ_{inv} for three neutrino generations and derive an upper limit for additional contributions from new physics to the invisible or the total Z width:

$$\Gamma^{\mathrm{new}}_{\mathrm{inv}} < 3.7\,\mathrm{MeV} \quad \text{or} \quad \Gamma^{\mathrm{new}}_{\mathrm{Z}} < 14.8\,\mathrm{MeV} \quad \text{at } 95\,\%\ \text{C.L.}$$

Finally, we compare our measured cross-sections and asymmetries with the full SM calculations. Radiative corrections are sensitive to the parameters m_{t}, m_{H} and $\alpha_{\mathrm{s}}(m^2_{\mathrm{Z}})$, allowing our measurements to determine:

$$\begin{aligned} m_{\mathrm{t}} &= 162 \pm 15^{+25}_{-5}\,(m_{\mathrm{H}})\ \mathrm{GeV}\ , \\ \alpha_{\mathrm{s}}(m^2_{\mathrm{Z}}) &= 0.125 \pm 0.005^{+0.004}_{-0.001}\,(m_{\mathrm{H}}) \pm 0.002\,(\,\mathrm{QCD})\ , \end{aligned}$$

where we fixed $m_{\mathrm{H}} = 150^{+850}_{-60}$ GeV. Including the direct measurement of the top quark mass ($m_{\mathrm{t}} = 174.3 \pm 5.1$ GeV [?]) as an additional constraint we obtain results for $\alpha_{\mathrm{s}}(m^2_{\mathrm{Z}})$ and the mass of the Higgs boson:

$$\begin{aligned} \alpha_{\mathrm{s}}(m^2_{\mathrm{Z}}) &= 0.127 \pm 0.005 \pm 0.002\,(\,\mathrm{QCD}) \\ m_{\mathrm{H}} &= 390^{+750}_{-280}\ \mathrm{GeV}\,. \end{aligned}$$

These Z lineshape and asymmetry measurements test and confirm the SM at the level of quantum loop corrections and set tight constraints on new physics.

Acknowledgements

We particularly wish to thank the SL Division for the efficient operation of the LEP accelerator, for the painstaking calibration of the beam energy and for their continuing close cooperation with our experimental group. We would also like to extend special thanks to the community of theorists whose contributions to precise electroweak calculations we cite, and whose efforts have made our own meaningful. We thank our colleagues from CEA, DAPNIA/SPP, CE-Saclay for their efforts over the years on the time-of-flight and trigger systems which we continue to use. In addition to the support staff at our own institutions we are pleased to acknowledge the
Department of Energy, USA,
National Science Foundation, USA,
Particle Physics and Astronomy Research Council, UK,
Natural Sciences and Engineering Research Council, Canada,
Israel Science Foundation, administered by the Israel Academy of Science and Humanities,
Minerva Gesellschaft,
Benoziyo Center for High Energy Physics,
Japanese Ministry of Education, Science and Culture (the Monbusho) and a grant under the Monbusho International Science Research Program,
Japanese Society for the Promotion of Science (JSPS),
German Israeli Bi-national Science Foundation (GIF),
Bundesministerium für Bildung und Forschung, Germany,
National Research Council of Canada,
Research Corporation, USA,
Hungarian Foundation for Scientific Research, OTKA T-029328, T023793 and OTKA F-023259.

A Four-fermion processes and radiative photon interference

Small radiative corrections to fermion-pair production due to four-fermion final states and the interference between initial- and final-state photon radiation are not treated by the fermion-pair Monte Carlo generators, JETSET and KORALZ, which we used in determining our event selection efficiencies. We describe here, in some technical detail, how we derived the small acceptance corrections arising from these effects.

A.1 Treatment of four-fermion final states

The selection criteria for hadronic and lepton-pair events define samples which are primarily the result of fermion-pair production processes $e^+e^- \to f\bar{f}$. Studies have been made of the much smaller contributions arising from four-fermion final states $e^+e^- \to f\bar{f}F\bar{F}$, as shown in Figure 2. Some classes of four-fermion events have little connection to Z production, and can properly be considered as background, for example multi-peripheral (d) or pair corrections to t-channel scattering (e,f). Other four-fermion events (b,c) however, must be considered as radiative corrections to the fermion-pair production (a) which interests us. In the following we use the designation $f\bar{f}$ to refer to the primary fermion pair of interest and $F\bar{F}$ to refer to the radiated pair, although a rigid distinction between the pairs cannot always be made.

From the theoretical point-of-view it is desirable to design the selection of fermion pairs in such a way that no stringent cuts are imposed on events with photon radiation and pair production. One then benefits from cancellations between real and virtual corrections leading to smaller uncertainties in the theoretical calculations. In practice, however, the event selection efficiency for events with radiated pairs can be expected to be different from the efficiency for events without such radiation, and this efficiency cannot be evaluated using the standard Monte Carlo event generators for fermion-pair production since they do not in general include such four-fermion final states. Studies have been made following the approach described in [**?**] using a specially generated sample of Monte Carlo four-fermion events.

An unambiguous separation of signal and background four-fermion events is not possible due to the interference of amplitudes which lead to the same final states. We therefore adopt a practical signal definition based on kinematics. Typically the fermion pair ($f\bar{f}$) from Z decay is of high invariant mass and the radiated pair ($F\bar{F}$) is of low mass. Four-fermion final states from t-channel and multi-peripheral diagrams tend to occupy a region of phase space well separated from the signal events of interest. We ignore the interference between s-channel and t-channel diagrams and generate separate four-fermion Monte Carlo samples: four-fermion events from s-channel diagrams are generated using the FERMISV program, while those from the t-channel diagrams are generated using the grc4f (version 1.11) and Pythia programs.

For channels other than $e^+e^- \to e^+e^-$, ($e^+e^- \to f\bar{f}$, with $f \neq e$), we identify four-fermion events from s-channel diagrams as part of the fermion-pair signal if they satisfy $m_{f\bar{f}} > m_{F\bar{F}}$ and $m^2_{f\bar{f}}/s > 0.01$. The second requirement is common to our definition of the fermion-pair signal phase space. All other four-fermion events arising from s-channel diagrams failing these requirements, as well as those from t-channel diagrams and the two photon process, are regarded as background.

In case of $e^+e^- \to e^+e^-$, four-fermion final states are considered as signal if the final-state electron-pair meets the normal requirements for the $e^+e^- \to e^+e^-$ signal in terms of electron energy, acollinearity and electron polar angle. Here, four-fermion events from t-channel diagrams are treated as signal. In principle even contributions from Figure 2(e) where the lower boson is a virtual Z are considered as signal. The number of such events falling within our ideal acceptance, however, is negligible.

Including four-fermion events leads to a correction of the effective signal efficiency of

$$\Delta_\varepsilon = -\frac{\sigma_{f\bar{f}F\bar{F}}}{\sigma}(\varepsilon_{f\bar{f}} - \varepsilon_{f\bar{f}F\bar{F}}) \,, \tag{34}$$

where σ is the total cross-section for $f\bar{f}$ production including the effects of pair-production, and $\sigma_{f\bar{f}F\bar{F}}$ is the cross-section for four-fermion events $f\bar{f}F\bar{F}$ defined as signal. The selection efficiency calculated

using the fermion-pair Monte Carlo is denoted by $\varepsilon_{f\bar{f}}$, and the selection efficiency calculated for the four-fermion signal contributions is $\varepsilon_{f\bar{f}F\bar{F}}$.

We expect the largest effect in the case of the $e^+e^- \to \mu^+\mu^-$ selection, where the requirement that the number of tracks be exactly two explicitly excludes all the visible four-fermion final states, even those which need to be counted as part of the signal. Here we find that the efficiency for signal four-fermion final states is typically 20–30% for $e^+e^- \to \mu^+\mu^-\mu^+\mu^-$, $\mu^+\mu^-q\overline{q}$, $\mu^+\mu^-\tau^+\tau^-$, and about 80% for $e^+e^- \to \mu^+\mu^-e^+e^-$, but the resulting correction to the $e^+e^- \to \mu^+\mu^-$ efficiency is only about 0.1%. Background from the t-channel diagrams gives a very small contribution of 2×10^{-5}, and background four-fermion events from s-channel diagrams give an even smaller contribution. We find a correction of similar size for the $e^+e^- \to \tau^+\tau^-$ selection.

In the $e^+e^- \to e^+e^-$ selection no tight multiplicity requirement is made. The efficiency for signal four-fermion events is found to be high (over 90%). As a result, the efficiency correction is nearly cancelled by the small background contributions, and no overall correction due to four-fermion final states is necessary. In the case of $e^+e^- \to q\overline{q}$ the event selection is very inclusive so that there is no notable effect on the efficiency. We subtract a very small four-fermion background contribution of 0.4×10^{-4}.

The theoretical programs ZFITTER and TOPAZ0 which we use to compute expected cross-sections and asymmetries treat pair radiation inclusively in the pair mass and do not include contributions from virtual Z bosons. Therefore the four-fermion signal definition as described here cannot be exactly mapped to these calculations, e.g. the separation between signal and background based on the mass of the pairs is not made in these programs. However the differences are quantitatively negligible [**?**].

A.2 Initial-final state interference

The effect of interference between initial and final state photon radiation is in general strongly suppressed at the Z resonance. In view of the high precision measurements presented here, however, we studied several possible effects. The main effect of initial-final state interference is a change in the angular distribution, proportional to the value of the differential cross-section, but of opposite sign in the forward and backward hemispheres, giving an increasing effect towards $\cos\theta = \pm1$. The size of the effect depends on the cuts, mainly on s' or $m_{\ell\ell}$: in general the tighter the cut on the energy of radiated photon, the larger the effect.

Initial-final state interference is not included in the Monte Carlo event samples used to calculate the event selection efficiency for the $e^+e^- \to q\overline{q}$, $\mu^+\mu^-$, or $\tau^+\tau^-$ processes, while it *is* included in our use of ZFITTER. We therefore do not remove its effects in our measured cross-sections and asymmetries but need to make small corrections to our calculated selection efficiencies to account for its absence in the Monte Carlo samples. Since the major source of the event selection inefficiency is due to limited angular acceptance near $|\cos\theta| = 1$ and reduced acceptance at small $s'(m_{\ell\ell})$, the missing initial-final state interference in these Monte Carlo samples can cause some bias in the acceptance extrapolation.

The effect of this missing initial-final state interference was evaluated using the program ZFITTER, for which this effect can be switched on and off. To incorporate the event selection efficiency in the calculation, a matrix of efficiency resolved in bins of $\cos\theta$ and the invariant mass of the final state lepton pair, $m^2_{\ell\ell}$, was calculated using the KORALZ Monte Carlo sample. The expected observed cross-section was obtained by multiplying the efficiency in each bin by the corresponding differential cross-section calculated using ZFITTER, and then summing over the full phase space. The overall efficiency was calculated as the ratio of the observed to the total cross-section. Two calculations were performed, one with and one without initial-final state interference, and the two results compared.

For both $e^+e^- \to \mu^+\mu^-$ and $e^+e^- \to \tau^+\tau^-$ the effect of missing initial-final state interference is found to be small (at 10^{-4} level) as a result of the large acceptance (in both $\cos\theta$ and $m^2_{\ell\ell}$) of both these selections. For $e^+e^- \to q\overline{q}$, the effect of initial-final state interference is more complicated to calculate due to the presence of a mixed QED and QCD parton shower in the final state. The size of the effect is strongly suppressed, however, by the almost complete acceptance of the $e^+e^- \to q\overline{q}$ event selection in both $\cos\theta$ and s' (the selection inefficiency is only 0.5%), as well as the smaller size of the

quark charges. Without considering the effect of the parton shower, we evaluated the effect to be less than 10^{-5}, which we neglect.

In the $e^+e^- \to e^+e^-$ selection, the experimental acceptance and ideal kinematical acceptance are very close. No appreciable phase-space extrapolation which could introduce a significant correction for the effect of initial-final state interference is needed. Therefore no correction is applied to the $e^+e^- \to e^+e^-$ selection efficiency.

B *t*-channel contributions to $e^+e^- \to e^+e^-$

For the reaction $e^+e^- \to e^+e^-$ not only s-channel annihilation but also the t-channel exchange of γ and Z contribute. Since our primary fitting program (ZFITTER) includes only s-channel processes an external correction is needed to account for the contributions from t-channel exchange diagrams and their interference with the s-channel. To ensure a consistent treatment of the s-channel in all final states we continue to calculate the $e^+e^- \to e^+e^-$ s-channel terms using ZFITTER, but proceed as follows. We use the program ALIBABA [**?**] to calculate the SM prediction for both the pure s-channel and the full s+t channel, separately for forward and backward cross-sections. The contributions from t-channel and s-t interference are obtained by subtracting the ALIBABA s-channel cross-section from the full ALIBABA s+t cross-section, $\sigma^{\mathrm{AL},t}_{\mathrm{F(B)}} = \sigma^{\mathrm{AL},s+t}_{\mathrm{F(B)}} - \sigma^{\mathrm{AL},s}_{\mathrm{F(B)}}$. To these t and s-t contributions we then add the s-channel cross-sections calculated with ZFITTER ($\sigma^{\mathrm{ZF},s}_{\mathrm{F}},\ \sigma^{\mathrm{ZF},s}_{\mathrm{B}}$) to obtain the predictions for the total cross-section and asymmetry:

$$\begin{aligned} \sigma_{\mathrm{ee}} &= \sigma^{\mathrm{ZF},s}_{\mathrm{F}} + \sigma^{\mathrm{AL},t}_{\mathrm{F}} + \sigma^{\mathrm{ZF},s}_{\mathrm{B}} + \sigma^{\mathrm{AL},t}_{\mathrm{B}} \\ A^{\mathrm{ee}}_{\mathrm{FB}} &= \frac{(\sigma^{\mathrm{ZF},s}_{\mathrm{F}} + \sigma^{\mathrm{AL},t}_{\mathrm{F}}) - (\sigma^{\mathrm{ZF},s}_{\mathrm{B}} + \sigma^{\mathrm{AL},t}_{\mathrm{B}})}{(\sigma^{\mathrm{ZF},s}_{\mathrm{F}} + \sigma^{\mathrm{AL},t}_{\mathrm{F}}) + (\sigma^{\mathrm{ZF},s}_{\mathrm{B}} + \sigma^{\mathrm{AL},t}_{\mathrm{B}})} \ . \end{aligned} \tag{35}$$

The separation into forward and backward cross-sections ensures a correct propagation of errors to the fitted s-channel observables R_{e} and $A^{0,\mathrm{e}}_{\mathrm{FB}}$. The non s-channel contributions lead to a statistical correlation of $-11\,\%$ between R_{e} and $A^{0,\mathrm{e}}_{\mathrm{FB}}$.

The size of the t-channel corrections changes rapidly as a function of centre-of-mass energy, since the s-t interference is proportional to $\sqrt{s} - m_{\mathrm{Z}}$ in the vicinity of the Z pole. We therefore parametrise the corrections $\sigma^{\mathrm{AL},t}_{\mathrm{F}}$ and $\sigma^{\mathrm{AL},t}_{\mathrm{B}}$ as a function of $(\sqrt{s} - m_{\mathrm{Z}})$ in order to account for their variation as m_{Z} converges in the fit. In this way our results for R_{e} and $A^{0,\mathrm{e}}_{\mathrm{FB}}$ properly respect the uncertainty of our fitted m_{Z} and the corresponding correlations. However, one should note a subtle side effect of this treatment. When lepton universality is assumed in the fit the measurement of σ_{ee} at the peak contributes to the determination of m_{Z}. The imposition of lepton universality introduces a tension in the fit since fluctuations induce discrepancies between the measured and predicted cross-sections for each lepton species at the peak point. This tension can be relaxed in the case of the electron cross-section by shifting m_{Z} since the non-s contributions in the electron channel have a non-zero slope with energy at the pole. This effect is responsible for the shift of 0.5 MeV of m_{Z} between the fits with and without lepton universality (Section 11.2).

Theoretical uncertainties of the t-channel correction have been estimated in [**?**] and the uncertainties in the forward and backward cross-section have also been determined separately [**?**]. Adjusting these estimates to the smaller angular acceptance used in our e^+e^- selection results in the uncertainties listed in Table 44 which are separated into three classes according to the centre-of-mass energy (below, at and above the peak). For the fit these uncertainties are translated into the corresponding uncertainties of the measured σ_{ee} and $A^{\mathrm{ee}}_{\mathrm{FB}}$ and included in the covariance matrix. It is not known to what extent the errors between the energy points and the forward-backward regions are correlated. We tested several possibilities – uncorrelated, fully correlated and fully anti-correlated – and found that our fitted parameters are insensitive within the effective t-channel errors to the scenario chosen. For the results presented here we assumed no correlation between forward and backward regions, full correlation between data points within each centre-of-mass energy class and no correlation between

data points of different classes. The effective t-channel theory uncertainties on $R_{\rm e}$ and $A_{\rm FB}^{0,{\rm e}}$ amount to 0.027 and 0.0015, respectively, with a correlation of -0.85. Overall, statistical errors and the theoretical t-channel uncertainties lead to a correlation of -0.20 between $R_{\rm e}$ and $A_{\rm FB}^{0,{\rm e}}$.

C Fit covariance matrix and energy spread corrections

For all our fits we perform a χ^2 minimisation using the MINUIT [**?**] package. The χ^2 is defined as

$$\chi^2 = \Delta^{\rm T}\, C^{-1}\, \Delta \;, \tag{36}$$

where Δ is the vector of residuals between the measured and predicted cross-sections and asymmetries and C is the covariance matrix describing the statistical and systematic uncertainties of the measurements and their correlations. In total we have 211 measured points, 124 cross-sections and 87 asymmetries. Therefore 22366 components C_{ij} need to be determined to specify the full matrix C. Due to the large variety of error sources entering the measurements and non-trivial correlations, the construction of the covariance matrix is a rather complex task. In general, each C_{ij} is composed of

$$C_{ij} = C_{ij}^{\rm sel,stat} + C_{ij}^{\rm lumi,stat} + C_{ij}^{\rm sel,syst} + C_{ij}^{\rm lumi,syst} + C_{ij}^{\rm t-chan} + C_{ij}^{E_{\rm cm}} + C_{ij}^{\delta_E} \;. \tag{37}$$

The elements $C_{ij}^{\rm XX}$ are in general constructed from 'small' covariance matrices $V^{\rm XX}$, which describe the year, energy point and final state dependencies. In the following we give a brief overview of how each uncertainty is treated. The indices i and j refer to the 211 measured points; k and l to the specific element in the V matrices. So the notation σ_i^k refers to the i-th cross-section which is related to the row or column k in the matrix V.

Statistical errors of the cross-sections (σ_i) are determined by the number of selected events, $N_{\rm sel}$, and corrected for estimated background, $N_{\rm bg}$. They enter only the diagonal elements

$$C_{ii}^{\rm sel,stat} = \left(\frac{\sqrt{N_{\rm sel}}}{N_{\rm sel} - N_{\rm bg}}\, \sigma_i \right)^2 \;. \tag{38}$$

Luminosity statistical errors are common to all cross-sections for a specific running period. They are calculated as

$$C_{ij}^{\rm lumi,stat} = (\delta_k^{\rm lumi,stat})^2\, \sigma_i^k\, \sigma_j^k \;, \tag{39}$$

where $\delta_k^{\rm lumi,stat}$ is the relative statistical luminosity error and $\sigma_{i,j}^k$ refers to the four cross-sections in each running period k.

Systematic errors from the event selection affect mostly a specific final state. A large fraction of this error is fully correlated but there are also components which are independent or only partially correlated for different running periods or energy points. Therefore these errors are themselves specified in a covariance matrix of relative errors, $V^{\rm sel}$. We use three such matrices, one for the hadron cross-sections (Table 17), one for the three leptonic cross-sections (Tables 18–21), and one for the three lepton asymmetries (Table 25). In this way correlations among the three lepton species are accounted for. $C_{ij}^{\rm sel,syst}$ is given by

$$C_{ij}^{\rm sel,syst} = V_{k,l}^{{\rm sel},\sigma}\, \sigma_i^k\, \sigma_j^l \quad \text{or} \quad C_{ij}^{\rm sel,syst} = V_{k,l}^{{\rm sel},A_{\rm FB}} \;. \tag{40}$$

There is no correlation between the experimental errors for the cross-sections and those for the asymmetries.

Luminosity errors include the experimental systematics and the theoretical uncertainties of the luminosity measurement. They affect all cross-section measurements, but similar to the selection errors there are components which are only partially correlated between running periods or energy points. Therefore a covariance matrix of relative luminosity errors, $V^{\rm lumi}$, is also used (Table 16):

$$C_{ij}^{\rm lumi,syst} = V_{k,l}^{\rm lumi}\, \sigma_i^k\, \sigma_j^l \;.$$

***t*-channel errors** refer to the theoretical uncertainty in the t-channel correction for e^+e^- cross-sections and asymmetries. These are specified in terms of forward and backward cross-sections, $\Delta\sigma_F$ and $\Delta\sigma_B$ (Table 44). Different data points are only correlated if both energies are either below, at, or above the peak (Appendix B). Then C_{ij}^{t-chan} is given by:

$$\begin{aligned}
\sigma_{ee}^i \leftrightarrow \sigma_{ee}^j \;:\quad C_{ij}^{t-chan} &= (\Delta\sigma_F^k)^2 + (\Delta\sigma_B^k)^2 \\
A_{FB}^{ee,i} \leftrightarrow A_{FB}^{ee,j} \;:\quad C_{ij}^{t-chan} &= \frac{1-A_{FB}^{ee,i}}{\sigma_{ee}^i}\,\frac{1-A_{FB}^{ee,j}}{\sigma_{ee}^j}\,(\Delta\sigma_F^k)^2 + \frac{1+A_{FB}^{ee,i}}{\sigma_{ee}^i}\,\frac{1+A_{FB}^{ee,j}}{\sigma_{ee}^j}\,(\Delta\sigma_B^k)^2 \\
\sigma_{ee}^i \leftrightarrow A_{FB}^{ee,j} \;:\quad C_{ij}^{t-chan} &= \frac{1-A_{FB}^{ee,j}}{\sigma_{ee}^j}\,(\Delta\sigma_F^k)^2 - \frac{1+A_{FB}^{ee,j}}{\sigma_{ee}^j}\,(\Delta\sigma_B^k)^2
\end{aligned} \tag{41}$$

Centre-of-mass energy errors have been determined in [**?**] and are specified as a covariance matrix $V^{E_{cm}}$ (see Tables 13 and 14). They are transformed into the corresponding cross-section or asymmetry errors using the derivatives

$$C_{ij}^{E_{cm}} = V_{kl}^{E_{cm}}\,\frac{d\,O_i^k}{d\,E}\,\frac{d\,O_j^l}{d\,E} \quad (O = \sigma \text{ or } A_{FB}). \tag{42}$$

The slopes $d\sigma/dE$ and dA_{FB}/dE are determined numerically using ZFITTER (σ^{ZF}) in an iteration during the fit. For cross-sections the dependence of the luminosity on the centre-of-mass energy must also be taken into account. Since this is a tiny effect it is sufficient to consider only the dominant $1/E^2$ dependence of the low-angle Bhabha cross-section, neglecting small distortions due to the γ/Z interference. Combining the predicted slope and the luminosity dependence yields

$$\frac{d\,\sigma_i}{d\,E} = \frac{d\,\sigma_i^{ZF}}{d\,E} + 2\,\frac{\sigma_i}{E_i}\,. \tag{43}$$

Beam-energy spread of the electrons and positrons in LEP leads to a dispersion of the centre-of-mass energy with a width $\delta_{E_{cm}} \approx 50$ MeV. Therefore the measured cross-sections and asymmetries do not correspond to a sharp energy, E_i, but form a weighted average around $E_i \pm \delta_{E_{cm}}$ which can be shifted from the value exactly at E_i. A similar effect is caused by the fact that many LEP fills are combined for each data point. These fills are not at precisely the same energy but scatter by typically 10 MeV around the average. Moreover, within a fill the energy also varies by several MeV. These two effects need to be added in quadrature with the intrinsic LEP $\delta_{E_{cm}}$. Correction terms are determined according to

$$\begin{aligned}
\Delta_{\sigma_i}^{spr} &= -\frac{1}{2}\left[\frac{d^2\,\sigma}{d\,E^2}\right]_i \delta_{E_{cm}}^2 \\
\Delta_{A_{FB}^i}^{spr} &= -\left[\frac{1}{2}\frac{d^2\,A_{FB}}{d\,E^2} + \frac{1}{\sigma}\,\frac{d\,\sigma}{d\,E}\,\frac{d\,A_{FB}}{d\,E}\right]_i \delta_{E_{cm}}^2
\end{aligned} \tag{44}$$

and added to the measured σ_i and A_{FB}^i. The first and second derivatives of σ and A_{FB} are again determined numerically with ZFITTER during the fit.

The spread $\delta_{E_{cm}}$ has typically an uncertainty of about 1.2 MeV, which is largely correlated between years and energy points and specified in detail in the energy spread covariance matrix V^{δ_E} (Table 15). It enters the fit covariance matrix as

$$C_{ij}^{\delta_E} = 4\,\Delta_i^{spr}\,\Delta_j^{spr}\,\frac{V_{kl}^{\delta_E}}{\delta_{E_{cm}}^k\,\delta_{E_{cm}}^l}\,. \tag{45}$$

Δ_i^{spr} refers to the corrections $\Delta_{\sigma_i}^{spr}$ and $\Delta_{A_{FB}^i}^{spr}$ in Equation 44.

D S-Matrix results

The S-Matrix formalism [**?**] is an alternative phenomenological approach to describe the s-channel reaction $e^+e^- \to f\bar{f}$ by the exchange of two spin-1 bosons, a massless photon and a massive Z boson. The lowest-order total cross-section, $\sigma^0_{\rm tot}$, and forward-backward asymmetry, $A^0_{\rm fb}$, are given as:

$$\sigma^0_a(s) = \frac{4}{3}\pi\alpha^2\left[\frac{g^a_f}{s} + \frac{j^a_f(s-\overline{m}_Z^2) + r^a_f\, s}{(s-\overline{m}_Z^2)^2 + \overline{m}_Z^2\overline{\Gamma}_Z^2}\right] \qquad \text{for } a = \text{tot, fb} \tag{46}$$

$$A^0_{\rm fb}(s) = \frac{3}{4}\frac{\sigma^0_{\rm fb}(s)}{\sigma^0_{\rm tot}(s)}\,, \tag{47}$$

where $\sqrt{s}$ is the centre-of-mass energy. The S-Matrix ansatz uses a Breit-Wigner denominator with s–*in*dependent width for the Z resonance, $s - \overline{m}_Z^2 + i\overline{m}_Z\overline{\Gamma}_Z$. As discussed in Section 10.2 the two Breit-Wigner forms with s–independent width and s–dependent width, respectively, are equivalent. They differ only in that the definition of the mass and width, $\overline{m}_Z$ and $\overline{\Gamma}_Z$ are shifted with respect to m_Z and Γ_Z. Note that in order to avoid confusion with different definitions we quote values for m_Z and Γ_Z, rather than $\overline{m}_Z$ and $\overline{\Gamma}_Z$, by applying the respective transformations.

The S-Matrix parameters r_f, j_f and g_f, which are real numbers, describe the Z exchange, γZ interference and photon exchange contributions, respectively. For the latter (g_f) the QED prediction is in general used. The parameters r_f and j_f are identical at tree-level to the C-parameters introduced in Section 10.1, apart from constant factors:

$$\begin{array}{rclcrcl} r_f^{\rm tot} &=& \kappa^2\, C^{\rm s}_{\rm ZZ} & , & r_f^{\rm fb} &=& 4\kappa^2\, C^{\rm a}_{\rm ZZ} \\ j_f^{\rm tot} &=& 2\kappa\, C^{\rm s}_{\gamma{\rm Z}} & , & j_f^{\rm fb} &=& 2\kappa\, C^{\rm a}_{\gamma{\rm Z}}\,, \end{array} \tag{48}$$

where $\kappa = \frac{G_F m_Z^2}{2\sqrt{2}\pi\alpha} \approx 1.50$. When radiative corrections are considered the relation is less direct; the S-Matrix parameters absorb by definition all electroweak and final state corrections. Further differences are caused by the treatment of the imaginary components in $\alpha(m_Z^2)$ and the couplings $\mathcal{G}_{Af}$ and $\mathcal{G}_{Vf}$.

In the S-Matrix approach the $q\bar{q}$ final states are also parametrised in terms of r_q and j_q. For the inclusive hadronic final state these are summed over all colours and open quark flavours to yield the corresponding parameters $r_{\rm had}$ and $j_{\rm had}$. The results of the full fit with 16 parameters are given in Table 45. The 12 parameters describing the three lepton flavours are consistent with lepton universality and we find overall good agreement with the SM expectations. The interpretation suffers, however, from the large correlations between the fitted parameters (Table 46). As discussed in Section 11.1 the precision of the fitted m_Z is much reduced when the hadronic interference, $j_{\rm had}$, is treated as a fit parameter; the correlation coefficient between m_Z and $j_{\rm had}$ is -0.96. For comparison, we performed a fit with the hadronic interference fixed to the SM prediction. The results are shown in Table 45. This parametrisation is in practice equivalent to the C-parameters (Table 26); we transformed the C-parameters into S-Matrix parameters, accounting for the differences in the treatment of radiative corrections, and obtained consistent results at the level of $1-2\,\%$ of the errors.

Year	Data sample	$\sqrt{s}$ (GeV)	$\int \mathcal{L}\,\mathrm{d}t$ (pb^{-1})	N_{had}	N_{ee}	$N_{\mu\mu}$	$N_{\tau\tau}$
	peak−3	88.22	0.5	2229	169	109	81
	peak−2	89.23	0.6	5322	306	231	214
	peak−1	90.23	0.4	7045	320	316	221
1990	peak	91.22	3.5	103664	3363	4834	3563
	peak+1	92.21	0.5	10412	271	527	364
	peak+2	93.22	0.6	6848	203	308	260
	peak+3	94.22	0.6	4373	128	202	161
	prescan	91.25	5.1	156592	5624	7563	6059
	peak−3	88.48	0.7	3646	297	176	166
	peak−2	89.47	0.8	7991	451	363	289
	peak−1	90.23	0.9	16011	683	744	569
1991	peak	91.22	3.0	92025	3365	4422	3603
	peak+1	91.97	0.8	20353	566	916	734
	peak+2	92.97	0.6	8356	325	478	436
	peak+3	93.72	0.9	9404	284	404	359
1992	peak	91.30	24.9	733059	23998	32492	27036
1990–1992	Total		44.4	1187330	40353	54085	44115
	prescan(a)	91.14	0.3	9905	345	454	370
	prescan(b)	91.32	5.3	162218	5256	7139	6002
1993	peak−2	89.45	8.5	85727	4595	3884	3336
	peak	91.21	8.8	265494	8766	10871	9712
	peak+2	93.04	9.0	125320	3549	5521	4612
	peak(ab)	91.22	50.1	1520277	49142	67791	55886
1994	peak(c)	91.43	0.4	11255	345	500	381
	peak(d)	91.22	2.3	69062	2170	3060	2478
	prescan(a)	91.80	0.2	5941	178	259	191
	prescan(b)	91.30	9.9	300676	9642	13401	11049
1995	peak−2	89.44	8.4	84236	4407	3768	3185
	peak	91.28	4.6	140749	4623	6338	5262
	peak+2	92.97	8.9	127707	3651	5696	4876
1993–1995	Total		116.7	2908566	96669	128682	107340
Grand	Total		161.1	4095896	137022	182767	151455

Table 1: Summary of the data samples used for the cross-section measurements, showing the numbers of selected events for each final state at each energy point and the integrated luminosities ($\int \mathcal{L}\,\mathrm{d}t$) for the $\mathrm{e^+e^-} \to \mathrm{q\overline{q}}$ analyses. The integrated luminosities for the other final states vary within about 1% due to different requirements on the status of the detector performance for the various event selections. For the leptonic forward-backward asymmetry measurements the data samples available for analysis are generally larger since there is no reliance on the operation of the luminometers. The peak data from 1994, and from the 1993 and 1995 prescan data samples, have been divided into subsets corresponding to data-taking periods characterised by significantly different mean values of $\sqrt{s}$.

Measurement	process	$E_{\min}$(GeV)	$\theta_{\rm acol}^{\max}$	$\lvert\cos\theta_{\ell^-}\rvert_{\max}$	$(s'/s)_{\min}$	$(m^2_{\rm f\overline{f}}/s)_{\min}$
cross-sections	$e^+e^- \to q\overline{q}$	–	–	1.00	0.01	–
	$e^+e^- \to \mu^+\mu^-$	–	–	1.00	–	0.01
	$e^+e^- \to \tau^+\tau^-$	–	–	1.00	–	0.01
	$e^+e^- \to e^+e^-$	0.2	10°	0.70	–	–
asymmetries	$e^+e^- \to e^+e^-$	0.2	10°	0.70	–	–
	$e^+e^- \to \mu^+\mu^-$	6.0	15°	0.95	–	–
	$e^+e^- \to \tau^+\tau^-$	6.0	15°	0.90	–	–

Table 2: The measured cross-sections and asymmetries are corrected to correspond to ideal regions of phase-space adapted to theoretical calculations. The phase-space is defined by the maximum $|\cos\theta_{\ell^-}|$ in which the fermion must fall, and, either the minimum final-state energy fraction, or a combined requirement on the minimum fermion energy, $E_{\min}$(GeV), and $\theta_{\rm acol}^{\max}$ where $\theta_{\rm acol}$ is the acollinearity angle of the fermion pair, defined as $180^\circ - \alpha$, where α is the opening angle between the directions of the two fermions. The final-state energy fraction is defined in terms of either the squared centre-of-mass energy available after initial-state radiation, (s'/s), or the final-state fermion pair mass squared, $(m^2_{\rm f\overline{f}}/s)$. The symbol $(-)$ indicates that no requirements are made on the indicated quantity.

	1993						1994		1995					
	peak−2		peak		peak+2		peak		peak−2		peak		peak+2	
	f	$\Delta f/f$ (%)	f	$\Delta f/f$ (%)	f	$\Delta f/f$ (%)	f	$\Delta f/f$ (%)	f	$\Delta f/f$ (%)	f	$\Delta f/f$ (%)	f	$\Delta f/f$ (%)
$e^+e^- \to q\overline{q}$ Monte Carlo	1.00481	0.011	1.00481	0.011	1.00481	0.011	1.00481	0.011	1.00481	0.011	1.00481	0.011	1.00481	0.011
ISR effects	1.00037	0.030	0.99997	0.003	1.00007	0.010	0.99997	0.003	1.00037	0.030	0.99997	0.003	1.00007	0.010
Acceptance														
Hadronisation	1.00055	0.048	1.00055	0.048	1.00055	0.048	1.00055	0.048	1.00055	0.048	1.00055	0.048	1.00055	0.048
Detector simulation	0.99960	0.040	0.99960	0.040	0.99960	0.040	0.99960	0.040	0.99960	0.040	0.99960	0.040	0.99960	0.040
Detector performance	1.00008	0.020	1.00008	0.020	1.00008	0.020	1.00008	0.020	1.00058	0.047	1.00058	0.047	1.00058	0.047
Corrected Acceptance	1.00542	0.071	1.00501	0.066	1.00511	0.067	1.00501	0.066	1.00593	0.083	1.00551	0.079	1.00561	0.079
Backgrounds														
$e^+e^- \to \tau^+\tau^-$	0.99841	0.020	0.99841	0.020	0.99841	0.020	0.99841	0.020	0.99841	0.020	0.99841	0.020	0.99841	0.020
Non-resonant														
(0.051 ± 0.007 nb)	0.99490	0.070	0.99833	0.023	0.99637	0.050	0.99833	0.023	0.99490	0.070	0.99833	0.023	0.99637	0.050
Four fermion	0.99994	0.004	0.99996	0.003	0.99992	0.006	0.99996	0.003	0.99994	0.004	0.99996	0.003	0.99992	0.006
$e^+e^- \to e^+e^-$ plus														
Cosmics	0.99988	0.009	0.99996	0.003	0.99992	0.006	0.99996	0.003	0.99988	0.009	0.99996	0.003	0.99992	0.006
Background Sum	0.99314	0.073	0.99666	0.031	0.99463	0.055	0.99666	0.031	0.99314	0.073	0.99666	0.031	0.99463	0.055
Total Correction	0.99852	0.102	1.00166	0.073	0.99971	0.086	1.00166	0.073	0.99902	0.111	1.00216	0.085	1.00021	0.096

Table 3: Summary of the correction factors, f, and their relative systematic errors, $\Delta f/f$, for the $e^+e^- \to q\overline{q}$ cross-section measurements. These numbers, when multiplied by the number of events actually selected, give the number of signal events which would have been observed in the ideal acceptance described in Table 2. ISR effects encompass the off-peak acceptance change due to initial-state radiation and the contamination from events with $s'/s < 0.01$. Hadronisation refers to the full correction and uncertainty resulting from the acceptance hole emulation (Table 4). The error correlation between the energy points and data-taking years is specified in Table 17.

	Uncertainty ($\times 10^{-4}$)
Residual hadronisation model dependence:	
Inefficiency correction	2.3
Inefficiency from barrel region	2.2
Adjustment of cut variables	1.5
Change of ECAL acceptance radius	0.4
Barrel detector simulation	3.3
Total	**4.8**

Table 4: Systematic errors on the selection inefficiency for $e^+e^- \to q\overline{q}$ events arising from uncertainties of the acceptance hole emulation.

	1993						1994		1995					
	peak−2		peak		peak+2		peak		peak−2		peak		peak+2	
	f	$\Delta f/f$ (%)	f	$\Delta f/f$ (%)	f	$\Delta f/f$ (%)	f	$\Delta f/f$ (%)	f	$\Delta f/f$ (%)	f	$\Delta f/f$ (%)	f	$\Delta f/f$ (%)
Monte Carlo														
$e^+e^- \to e^+e^-$ Monte Carlo	1.0063	0.06	1.0056	0.02	1.0061	0.04	1.0056	0.02	1.0063	0.06	1.0056	0.02	1.0061	0.04
Acceptance Correction														
Electromagnetic energy	1.0009	0.10	1.0009	0.10	1.0009	0.10	1.0022	0.07	1.0017	0.09	1.0017	0.08	1.0017	0.09
Electron identification	1.0025	0.08	1.0025	0.08	1.0025	0.08	1.0026	0.05	1.0031	0.08	1.0031	0.08	1.0031	0.08
Acceptance definition	1.0000	0.14	1.0000	0.09	1.0000	0.10	1.0000	0.09	1.0000	0.14	1.0000	0.09	1.0000	0.10
Low multiplicity	1.0001	0.01	1.0001	0.01	1.0001	0.01	1.0001	0.01	1.0001	0.01	1.0001	0.01	1.0001	0.01
Other Corrections														
Four-fermion events	1.0000	0.03	1.0000	0.02	1.0000	0.03	1.0000	0.02	1.0000	0.03	1.0000	0.02	1.0000	0.03
Signal Correction	1.0098	0.20	1.0091	0.16	1.0096	0.17	1.0105	0.13	1.0112	0.20	1.0105	0.15	1.0110	0.17
Backgrounds														
$e^+e^- \to \tau^+\tau^-$	0.9982	0.04	0.9968	0.06	0.9965	0.07	0.9968	0.06	0.9982	0.04	0.9968	0.06	0.9965	0.07
$e^+e^- \to \gamma\gamma$	0.9999	0.01	0.9999	0.01	0.9999	0.02	0.9999	0.01	0.9999	0.01	0.9999	0.01	0.9999	0.02
$e^+e^- \to q\overline{q}$	0.9999	0.01	0.9999	0.02	0.9998	0.02	0.9999	0.02	0.9999	0.01	0.9999	0.02	0.9998	0.02
$e^+e^- \to e^+e^-\ell^+\ell^-$	1.0000	0.01	1.0000	0.01	1.0000	0.01	1.0000	0.01	1.0000	0.01	1.0000	0.01	1.0000	0.01
Background Correction	0.9979	0.04	0.9966	0.06	0.9961	0.08	0.9966	0.06	0.9979	0.04	0.9966	0.06	0.9961	0.08
Total Correction Factor	1.0078	0.21	1.0057	0.17	1.0057	0.19	1.0071	0.14	1.0091	0.20	1.0070	0.16	1.0070	0.18

Table 5: Summary of the correction factors, f, and their relative systematic errors, $\Delta f/f$, for the $e^+e^- \to e^+e^-$ cross-section measurements. The Monte Carlo correction factor corresponds to the efficiency for events within the ideal phase space definition. The factors listed under acceptance corrections take into account the observed discrepancies between the data and Monte Carlo. The total correction factor, when multiplied by the number of events actually selected, gives the number of signal events which would have been observed in the ideal acceptance described in Table 2. The error correlation matrix is given in Table 18.

	1993						1994		1995					
	peak−2		peak		peak+2		peak		peak−2		peak		peak+2	
	f	$\Delta f/f$ (%)	f	$\Delta f/f$ (%)	f	$\Delta f/f$ (%)	f	$\Delta f/f$ (%)	f	$\Delta f/f$ (%)	f	$\Delta f/f$ (%)	f	$\Delta f/f$ (%)
Monte Carlo														
$e^+e^- \to \mu^+\mu^-$ Monte Carlo	1.0995	0.10	1.0955	0.07	1.0986	0.10	1.0948	0.04	1.1032	0.12	1.0970	0.05	1.1001	0.10
s' cut correction	0.9971	–	0.9990	–	0.9980	–	0.9990	–	0.9971	–	0.9990	–	0.9980	–
Initial/final state interference	1.0003	–	1.0002	–	1.0001	–	1.0002	–	1.0003	–	1.0002	–	1.0001	–
Acceptance Correction														
Tracking losses	1.0046	0.06	1.0046	0.06	1.0046	0.06	1.0042	0.04	1.0043	0.06	1.0043	0.06	1.0043	0.06
Track multiplicity cuts	0.9999	0.05	1.0007	0.04	1.0000	0.04	1.0004	0.02	1.0007	0.09	1.0010	0.04	1.0013	0.08
Muon identification	1.0000	0.05	1.0000	0.05	1.0000	0.05	1.0015	0.04	1.0000	0.06	1.0000	0.06	1.0000	0.06
Acceptance definition	1.0000	0.10	1.0000	0.10	1.0000	0.10	1.0000	0.05	1.0000	0.05	1.0000	0.05	1.0000	0.05
Other Corrections														
Trigger efficiency	1.0006	0.02	1.0006	0.02	1.0006	0.02	1.0005	0.02	1.0002	0.02	1.0002	0.02	1.0002	0.02
Four-fermion events	1.0009	0.01	1.0011	0.01	1.0011	0.01	1.0011	0.01	1.0009	0.01	1.0011	0.01	1.0011	0.01
Signal Correction	1.1032	0.17	1.1022	0.15	1.1034	0.17	1.1024	0.09	1.1071	0.18	1.1034	0.12	1.1056	0.16
Backgrounds														
$e^+e^- \to \tau^+\tau^-$	0.9914	0.02	0.9914	0.02	0.9914	0.02	0.9903	0.04	0.9905	0.02	0.9905	0.02	0.9905	0.02
$e^+e^- \to e^+e^-\mu^+\mu^-$	0.9988	0.01	0.9995	0.01	0.9991	0.01	0.9996	0.01	0.9987	0.01	0.9995	0.01	0.9990	0.01
Cosmic rays	0.9998	0.02	0.9998	0.02	0.9998	0.02	0.9998	0.02	0.9997	0.02	0.9997	0.02	0.9997	0.02
Background Correction	0.9900	0.03	0.9907	0.03	0.9903	0.03	0.9897	0.05	0.9889	0.03	0.9897	0.03	0.9892	0.03
Total Correction Factor	1.0922	0.17	1.0920	0.16	1.0927	0.17	1.0910	0.10	1.0948	0.18	1.0920	0.12	1.0937	0.17

Table 6: Summary of the correction factors, f, and their relative systematic errors, $\Delta f/f$, for the $e^+e^- \to \mu^+\mu^-$ cross-section measurements. These numbers, when multiplied by the number of events actually selected, give the number of signal events which would have been observed in the ideal acceptance described in Table 2. The effects tracking losses, track multiplicity cuts and muon identification were, in principle, simulated by the Monte Carlo. The quoted corrections were introduced to take into account the observed discrepancies between the data and Monte Carlo for these effects. The error correlation matrix is given in Table 19.

	1993						1994		1995					
	peak−2		peak		peak+2		peak		peak−2		peak		peak+2	
	f	$\Delta f/f$ (%)	f	$\Delta f/f$ (%)	f	$\Delta f/f$ (%)	f	$\Delta f/f$ (%)	f	$\Delta f/f$ (%)	f	$\Delta f/f$ (%)	f	$\Delta f/f$ (%)
Monte Carlo														
$e^+e^- \to \tau^+\tau^-$ Monte Carlo	1.3384	0.22	1.3302	0.09	1.3388	0.19	1.3302	0.09	1.3384	0.22	1.3302	0.09	1.3388	0.19
s' cut correction	0.9976	–	0.9992	–	0.9984	–	0.9992	–	0.9976	–	0.9992	–	0.9984	–
Initial/final state interference	1.0005	–	1.0004	–	1.0001	–	1.0004	–	1.0005	–	1.0004	–	1.0001	–
Acceptance Correction														
Multiplicity cuts	1.0018	0.16	1.0017	0.16	1.0019	0.17	1.0049	0.14	1.0021	0.16	1.0021	0.16	1.0022	0.17
Acollinearity and cone cuts	0.9999	0.25	1.0002	0.23	1.0007	0.28	1.0034	0.19	1.0008	0.25	1.0008	0.23	1.0012	0.28
Definition of $\lvert\cos\theta_\tau\rvert$	1.0000	0.10	1.0000	0.10	1.0000	0.10	1.0000	0.10	1.0000	0.10	1.0000	0.10	1.0000	0.10
$e^+e^- \to e^+e^-$ rejection	1.0037	0.25	1.0038	0.26	1.0037	0.25	1.0068	0.23	1.0044	0.25	1.0045	0.26	1.0043	0.25
$e^+e^- \to \mu^+\mu^-$ rejection	0.9997	0.08	0.9997	0.08	0.9997	0.08	0.9998	0.05	0.9993	0.08	0.9994	0.08	0.9993	0.08
$e^+e^- \to e^+e^-\ell^+\ell^-$ rejection	1.0019	0.12	1.0018	0.11	1.0019	0.12	1.0014	0.07	1.0000	0.10	1.0000	0.10	1.0000	0.10
Cosmic ray cuts	1.0001	0.01	1.0001	0.01	1.0001	0.01	1.0001	0.01	1.0001	0.01	1.0001	0.01	1.0001	0.01
Combinations of cuts	1.0000	0.09	1.0000	0.08	1.0000	0.10	1.0000	0.08	1.0000	0.09	1.0000	0.08	1.0000	0.10
Other Corrections														
Trigger efficiency	1.0002	0.01	1.0002	0.01	1.0002	0.01	1.0002	0.01	1.0002	0.01	1.0002	0.01	1.0002	0.01
Tau branching ratios	1.0000	0.05	1.0000	0.05	1.0000	0.05	1.0000	0.05	1.0000	0.05	1.0000	0.05	1.0000	0.05
Four-fermion events	1.0012	0.04	1.0013	0.04	1.0018	0.04	1.0013	0.04	1.0012	0.04	1.0013	0.04	1.0018	0.04
Signal Correction	1.3473	0.50	1.3414	0.45	1.3502	0.51	1.3536	0.39	1.3467	0.50	1.3409	0.44	1.3490	0.50
Backgrounds														
$e^+e^- \to e^+e^-$	0.9921	0.16	0.9966	0.07	0.9963	0.08	0.9953	0.07	0.9906	0.16	0.9959	0.07	0.9957	0.08
$e^+e^- \to \mu^+\mu^-$	0.9900	0.12	0.9902	0.11	0.9902	0.11	0.9886	0.09	0.9892	0.13	0.9893	0.12	0.9894	0.13
$e^+e^- \to q\overline{q}$	0.9961	0.10	0.9960	0.11	0.9961	0.10	0.9960	0.11	0.9961	0.10	0.9960	0.11	0.9961	0.10
$e^+e^- \to e^+e^-\ell^+\ell^-$	0.9848	0.22	0.9948	0.07	0.9893	0.16	0.9943	0.07	0.9838	0.22	0.9947	0.07	0.9887	0.16
Four-fermion	0.9991	0.02	0.9994	0.02	0.9993	0.02	0.9994	0.02	0.9991	0.02	0.9994	0.02	0.9993	0.02
Cosmic rays	0.9991	0.05	0.9997	0.02	0.9994	0.04	0.9996	0.02	0.9993	0.06	0.9998	0.02	0.9996	0.04
Background Correction	0.9618	0.32	0.9768	0.19	0.9708	0.24	0.9733	0.18	0.9587	0.32	0.9752	0.19	0.9690	0.25
Total Correction Factor	1.2960	0.59	1.3105	0.48	1.3108	0.56	1.3178	0.42	1.2913	0.59	1.3077	0.48	1.3074	0.56

Table 7: Summary of the correction factors, f, and their relative systematic errors, $\Delta f/f$, for the $e^+e^- \to \tau^+\tau^-$ cross-section measurements. These numbers, when multiplied by the number of events actually selected, give the number of signal events which would have been observed in the ideal acceptance described in Table 2. The error correlation matrix is given in Table 21.

Sample		$\sqrt{s}$(GeV)		$e^+e^- \to q\overline{q}$ cross-section (nb)		
		mean	rms	measured	corrected	fit
	peak-3	88.2510	0.0481	4.669 ± 0.110	4.667	4.605
	peak-2	89.2510	0.0490	8.501 ± 0.130	8.494	8.687
	peak-1	90.2490	0.0500	18.899 ± 0.281	18.890	18.713
1990	peak	91.2440	0.0510	30.445 ± 0.130	30.488	30.500
	peak+1	92.2350	0.0520	21.400 ± 0.271	21.394	21.529
	peak+2	93.2380	0.0529	12.434 ± 0.180	12.427	12.450
	peak+3	94.2350	0.0539	7.947 ± 0.130	7.944	8.045
	prescan	91.2540	0.0471	30.355 ± 0.099	30.391	30.510
	peak-3	88.4810	0.0441	5.326 ± 0.095	5.323	5.258
	peak-2	89.4720	0.0451	10.087 ± 0.126	10.080	10.210
	peak-1	90.2270	0.0461	18.243 ± 0.171	18.234	18.398
1991	peak	91.2230	0.0471	30.370 ± 0.129	30.407	30.469
	peak+1	91.9690	0.0481	24.603 ± 0.215	24.605	24.836
	peak+2	92.9680	0.0490	14.058 ± 0.178	14.051	14.304
	peak+3	93.7170	0.0500	9.916 ± 0.115	9.912	9.949
1992	peak	91.2990	0.0520	30.566 ± 0.045	30.609	30.514
	peak-2	89.4505	0.0564	10.053 ± 0.037	10.042	10.048
1993	peak	91.2063	0.0570	30.352 ± 0.070	30.407	30.433
	peak+2	93.0351	0.0570	13.856 ± 0.043	13.847	13.808
	peak(ab)	91.2199	0.0565	30.379 ± 0.029	30.433	30.463
1994	peak(c)	91.4287	0.0562	30.308 ± 0.339	30.353	30.163
	peak(d)	91.2195	0.0557	30.598 ± 0.138	30.650	30.462
	peak-2	89.4415	0.0568	9.989 ± 0.037	9.978	9.981
1995	peak	91.2829	0.0578	30.559 ± 0.097	30.614	30.520
	peak+2	92.9715	0.0581	14.282 ± 0.044	14.272	14.278

Table 8: The $e^+e^- \to q\overline{q}$ production cross-section near the Z resonance. The cross-section is corrected to the simple kinematic acceptance region defined by $s'/s > 0.01$. For each data sample, we list here the mean $\sqrt{s}$ of the colliding beams, its root-mean-square (rms) spread, and the observed $e^+e^- \to q\overline{q}$ cross-section. The errors shown are statistical only. The cross-section measurements are also shown after being corrected for the beam energy spread to correspond to the physical cross-section at the central value of $\sqrt{s}$. The fit values are the result of the 9-parameter model-independent fit.

Sample		$\sqrt{s}$(GeV)		$e^+e^- \to e^+e^-$ cross-section (nb)		
		mean	rms	measured	corrected	fit
	peak-3	88.2510	0.0481	0.3520 ± 0.0281	0.3519	0.3403
	peak-2	89.2510	0.0490	0.4850 ± 0.0281	0.4848	0.4795
	peak-1	90.2490	0.0500	0.8110 ± 0.0451	0.8109	0.7762
1990	peak	91.2420	0.0510	1.0120 ± 0.0180	1.0132	1.0054
	peak+1	92.2350	0.0520	0.6010 ± 0.0371	0.6007	0.6307
	peak+2	93.2380	0.0529	0.3650 ± 0.0261	0.3648	0.3594
	peak+3	94.2350	0.0539	0.2310 ± 0.0210	0.2309	0.2429
	prescan	91.2540	0.0471	0.9875 ± 0.0140	0.9886	1.0036
	peak-3	88.4810	0.0441	0.3623 ± 0.0239	0.3622	0.3636
	peak-2	89.4720	0.0451	0.5628 ± 0.0280	0.5626	0.5282
	peak-1	90.2270	0.0461	0.7617 ± 0.0299	0.7616	0.7677
1991	peak	91.2230	0.0471	1.0093 ± 0.0190	1.0104	1.0079
	peak+1	91.9690	0.0481	0.6885 ± 0.0300	0.6884	0.7422
	peak+2	92.9680	0.0490	0.4165 ± 0.0270	0.4163	0.4114
	peak+3	93.7170	0.0500	0.3020 ± 0.0180	0.3019	0.2920
1992	peak	91.2990	0.0520	1.0062 ± 0.0065	1.0074	0.9958
	peak-2	89.4505	0.0564	0.5414 ± 0.0080	0.5411	0.5231
1993	peak	91.2063	0.0570	1.0064 ± 0.0109	1.0080	1.0098
	peak+2	93.0351	0.0570	0.3945 ± 0.0067	0.3942	0.3973
	peak(ab)	91.2197	0.0565	1.0047 ± 0.0046	1.0063	1.0083
1994	peak(c)	91.4286	0.0562	0.9422 ± 0.0512	0.9434	0.9635
	peak(d)	91.2195	0.0557	0.9676 ± 0.0210	0.9691	1.0083
	peak-2	89.4415	0.0568	0.5260 ± 0.0080	0.5257	0.5209
1995	peak	91.2829	0.0578	1.0074 ± 0.0150	1.0089	0.9988
	peak+2	92.9715	0.0581	0.4088 ± 0.0068	0.4085	0.4107

Table 9: The $e^+e^- \to e^+e^-$ production cross-section near the Z resonance. The cross-section is corrected to the simple kinematic acceptance region defined by $|\cos\theta_{e^-}| < 0.70$ and $\theta_{acol} < 10^\circ$.
For each data sample, we list here the mean $\sqrt{s}$ of the colliding beams, its root-mean-square (rms) spread, and the observed $e^+e^- \to e^+e^-$ cross-section. The errors shown are statistical only. The cross-section measurements are also shown after being corrected for the beam energy spread to correspond to the physical cross-section at the central value of $\sqrt{s}$. The fit values are the result of the 9-parameter model-independent fit.

Sample		$\sqrt{s}$(GeV)		$e^+e^- \to \mu^+\mu^-$ cross-section (nb)		
		mean	rms	measured	corrected	fit
	peak-3	88.2510	0.0481	0.2450 ± 0.0243	0.2449	0.2345
	peak-2	89.2510	0.0490	0.4181 ± 0.0284	0.4178	0.4302
	peak-1	90.2490	0.0500	0.8432 ± 0.0477	0.8427	0.9116
1990	peak	91.2440	0.0510	1.4833 ± 0.0221	1.4854	1.4779
	peak+1	92.2350	0.0520	1.0841 ± 0.0477	1.0838	1.0467
	peak+2	93.2380	0.0529	0.5961 ± 0.0345	0.5958	0.6102
	peak+3	94.2350	0.0539	0.3970 ± 0.0284	0.3969	0.3983
	prescan	91.2540	0.0471	1.4851 ± 0.0182	1.4869	1.4784
	peak-3	88.4810	0.0441	0.2319 ± 0.0202	0.2318	0.2657
	peak-2	89.4720	0.0451	0.5171 ± 0.0273	0.5167	0.5034
	peak-1	90.2270	0.0461	0.9082 ± 0.0353	0.9078	0.8965
1991	peak	91.2230	0.0471	1.4859 ± 0.0232	1.4877	1.4764
	peak+1	91.9690	0.0481	1.2447 ± 0.0424	1.2448	1.2057
	peak+2	92.9680	0.0490	0.6836 ± 0.0354	0.6833	0.6994
	peak+3	93.7170	0.0500	0.4794 ± 0.0242	0.4792	0.4899
1992	peak	91.2990	0.0520	1.4781 ± 0.0083	1.4802	1.4785
	peak-2	89.4505	0.0564	0.4964 ± 0.0081	0.4959	0.4956
1993	peak	91.2072	0.0568	1.4563 ± 0.0142	1.4589	1.4748
	peak+2	93.0351	0.0570	0.6681 ± 0.0091	0.6677	0.6755
	peak(ab)	91.2200	0.0565	1.4752 ± 0.0058	1.4778	1.4761
1994	peak(c)	91.4286	0.0562	1.4786 ± 0.0674	1.4808	1.4617
	peak(d)	91.2195	0.0557	1.4762 ± 0.0272	1.4787	1.4761
	peak-2	89.4415	0.0568	0.4912 ± 0.0081	0.4907	0.4923
1995	peak	91.2827	0.0578	1.5085 ± 0.0193	1.5111	1.4789
	peak+2	92.9715	0.0581	0.6894 ± 0.0093	0.6889	0.6981

Table 10: The $e^+e^- \to \mu^+\mu^-$ production cross-section near the Z resonance. The cross-section is corrected to the simple kinematic acceptance region defined by $m^2_{f\bar{f}}/s > 0.01$. For each data sample, we list here the mean $\sqrt{s}$ of the colliding beams, its root-mean-square (rms) spread, and the observed $e^+e^- \to \mu^+\mu^-$ cross-section. The errors shown are statistical only. The cross-section measurements are also shown after being corrected for the beam energy spread to correspond to the physical cross-section at the central value of $\sqrt{s}$. The fit values are the result of the 9-parameter model-independent fit.

Sample		$\sqrt{s}$(GeV)		$e^+e^- \to \tau^+\tau^-$ cross-section (nb)		
		mean	rms	measured	corrected	fit
	peak-3	88.2510	0.0481	0.2152 ± 0.0245	0.2151	0.2343
	peak-2	89.2510	0.0490	0.4304 ± 0.0296	0.4301	0.4299
	peak-1	90.2490	0.0500	0.9328 ± 0.0633	0.9323	0.9109
1990	peak	91.2440	0.0510	1.4566 ± 0.0245	1.4587	1.4767
	peak+1	92.2350	0.0520	1.0292 ± 0.0552	1.0289	1.0459
	peak+2	93.2380	0.0529	0.6518 ± 0.0409	0.6515	0.6097
	peak+3	94.2350	0.0539	0.4095 ± 0.0327	0.4094	0.3980
	prescan	91.2540	0.0471	1.4325 ± 0.0194	1.4343	1.4771
	peak-3	88.4810	0.0441	0.2769 ± 0.0235	0.2768	0.2655
	peak-2	89.4720	0.0451	0.4845 ± 0.0297	0.4841	0.5029
	peak-1	90.2270	0.0461	0.8331 ± 0.0368	0.8327	0.8957
1991	peak	91.2230	0.0471	1.4384 ± 0.0256	1.4402	1.4751
	peak+1	91.9690	0.0481	1.1892 ± 0.0450	1.1893	1.2047
	peak+2	92.9680	0.0490	0.6953 ± 0.0409	0.6950	0.6988
	peak+3	93.7170	0.0500	0.4989 ± 0.0276	0.4987	0.4895
1992	peak	91.2990	0.0520	1.4734 ± 0.0092	1.4755	1.4773
	peak-2	89.4505	0.0564	0.5074 ± 0.0092	0.5069	0.4951
1993	peak	91.2060	0.0570	1.5048 ± 0.0158	1.5074	1.4734
	peak+2	93.0351	0.0570	0.6660 ± 0.0102	0.6656	0.6750
	peak(ab)	91.2198	0.0565	1.4812 ± 0.0065	1.4838	1.4749
1994	peak(c)	91.4286	0.0562	1.3708 ± 0.0724	1.3730	1.4605
	peak(d)	91.2195	0.0557	1.4477 ± 0.0301	1.4502	1.4748
	peak-2	89.4415	0.0568	0.4892 ± 0.0091	0.4887	0.4919
1995	peak	91.2827	0.0578	1.4988 ± 0.0213	1.5014	1.4776
	peak+2	92.9715	0.0581	0.7089 ± 0.0105	0.7084	0.6976

Table 11: The $e^+e^- \to \tau^+\tau^-$ production cross-section near the Z resonance. The cross-section is corrected to the simple kinematic acceptance region defined by $m^2_{f\bar{f}}/s > 0.01$. For each data sample, we list here the mean $\sqrt{s}$ of the colliding beams, its root-mean-square (rms) spread, and the observed $e^+e^- \to \tau^+\tau^-$ cross-section. The errors shown are statistical only. The cross-section measurements are also shown after being corrected for the beam energy spread to correspond to the physical cross-section at the central value of $\sqrt{s}$. The fit values are the result of the 9-parameter model-independent fit.

Sample	$\sqrt{s}$ (GeV)		input (nb)	pseudo-cross-sections (nb)		
	mean	rms	$e^+e^- \to q\overline{q}$	$e^+e^- \to e^+e^-$	$e^+e^- \to \mu^+\mu^-$	$e^+e^- \to \tau^+\tau^-$
1993						
prescan(a)	91.1386	0.0867	30.176 ± 0.306	1.056 ± 0.057	1.499 ± 0.071	1.444 ± 0.078
prescan(b)	91.3211	0.0566	30.479 ± 0.076	0.988 ± 0.014	1.461 ± 0.018	1.471 ± 0.020
peak	91.1964	0.0576	30.383 ± 0.198	1.024 ± 0.036	1.420 ± 0.045	1.435 ± 0.050
1994						
peak(ab)	91.2183	0.0568	30.437 ± 0.122	1.051 ± 0.023	1.469 ± 0.028	1.426 ± 0.031
1995						
prescan(a)	91.7990	0.0568	26.910 ± 0.352	0.810 ± 0.061	1.278 ± 0.080	1.129 ± 0.084
prescan(b)	91.3030	0.0576	30.501 ± 0.056	0.983 ± 0.010	1.481 ± 0.013	1.463 ± 0.014

Table 12: For some periods of running at the Z peak a precise luminosity measurement is not available. We nevertheless use this data to measure inter-species cross-section ratios. To make these data compatible with other cross-section measurements, we fix each $e^+e^- \to q\overline{q}$ cross-section to its expected value, and normalise the cross-sections for the three lepton species measured in the same period to this arbitrary hadron cross-section. We term such measurements pseudo-cross-sections, and allow the absolute scale of each set of four to float by 10% in the fit using appropriate error matrices. For each data sample we list here the mean $\sqrt{s}$ of the colliding beams, its rms spread, and the observed pseudo-cross-sections. The errors shown are statistical only.

Centre-of-mass energy errors															
		1990							1991						
		−3	−2	−1	0	+1	+2	+3	0	−3	−2	−1	0	+1	+2	+3
	−3	193	194	195	196	197	198	199	6.1	7.4	7.0	6.6	6.1	5.7	5.1	4.7
	−2	194	195	196	197	198	199	200	5.8	6.7	6.4	6.1	5.8	5.5	5.2	4.9
	−1	195	196	197	198	199	200	201	5.5	5.9	5.8	5.6	5.5	5.4	5.2	5.0
1990	0	196	197	198	199	200	202	203	5.1	5.0	5.1	5.1	5.1	5.2	5.2	5.2
	+1	197	198	199	200	202	203	204	4.8	4.0	4.3	4.5	4.8	5.0	5.2	5.4
	+2	198	199	200	202	203	204	205	4.4	2.4	3.3	3.8	4.4	4.8	5.2	5.6
	+3	199	200	201	203	204	205	206	4.0	−1.9	1.8	2.9	3.9	4.6	5.3	5.8
	pre	6.1	5.8	5.5	5.1	4.8	4.4	4.0	20.3	6.6	6.3	6.1	5.8	5.6	5.2	5.0
	−3	7.4	6.7	5.9	5.0	4.0	2.4	−1.9	6.6	9.7	7.8	7.3	6.6	6.0	5.2	4.4
	−2	7.0	6.4	5.8	5.1	4.3	3.3	1.8	6.3	7.8	8.8	6.9	6.3	5.9	5.2	4.6
	−1	6.6	6.1	5.6	5.1	4.5	3.8	2.9	6.1	7.3	6.9	8.2	6.1	5.7	5.2	4.8
1991	0	6.1	5.8	5.5	5.1	4.8	4.4	3.9	5.8	6.6	6.3	6.1	7.6	5.6	5.2	4.9
	+1	5.7	5.5	5.4	5.2	5.0	4.8	4.6	5.6	6.0	5.9	5.7	5.6	7.3	5.2	5.1
	+2	5.1	5.2	5.2	5.2	5.2	5.2	5.3	5.2	5.2	5.2	5.2	5.2	5.2	7.3	5.3
	+3	4.7	4.9	5.0	5.2	5.4	5.6	5.8	5.0	4.4	4.6	4.8	4.9	5.1	5.3	7.4

Table 13: The signed square-root of the covariance matrix elements for systematic errors in the LEP centre-of-mass energy calibration for 1990–1991. The column and row headings label the centre-of-mass energies relative to the peak in GeV. The entries are the absolute errors in units of MeV. The energy measurement in 1992 is uncorrelated with other years. Its error is 18.0 MeV.

Centre-of-mass energy errors							
	1993 pk−2	1993 peak	1993 pk+2	1994 peak	1995 pk−2	1995 peak	1995 pk+2
1993 pk−2	3.55	2.88	2.73	2.36	1.31	1.21	1.22
1993 peak	2.88	6.76	2.77	2.49	1.16	1.22	1.17
1993 pk+2	2.73	2.77	3.09	2.28	1.25	1.27	1.35
1994 peak	2.36	2.49	2.28	3.78	1.25	1.32	1.26
1995 pk−2	1.31	1.16	1.25	1.25	1.83	1.28	1.26
1995 peak	1.21	1.22	1.27	1.32	1.28	5.41	1.38
1995 pk+2	1.22	1.17	1.35	1.26	1.26	1.38	1.74

Table 14: The signed square-root of the covariance matrix elements for systematic errors in the LEP centre-of-mass energy in 1993 – 1995. These errors are specific to the OPAL interaction point. The entries are the absolute errors in units of MeV.

Centre-of-mass energy spread errors										
	1990	1991	1992	1993 pk−2	1993 peak	1993 pk+2	1994 peak	1995 pk−2	1995 peak	1995 pk+2
1990	3.0	3.0	0.0	0.0	0.0	0.0	0.0	0.0	0.0	0.0
1991	3.0	3.0	0.0	0.0	0.0	0.0	0.0	0.0	0.0	0.0
1992	0.0	0.0	3.0	1.8	1.8	1.8	1.8	1.8	1.8	1.8
1993 pk−2	0.0	0.0	1.8	1.1	1.1	1.1	1.1	1.1	1.1	1.1
1993 peak	0.0	0.0	1.8	1.1	1.1	1.1	1.1	1.1	1.1	1.1
1993 pk+2	0.0	0.0	1.8	1.1	1.1	1.1	1.1	1.1	1.1	1.1
1994 peak	0.0	0.0	1.8	1.1	1.1	1.1	1.1	1.1	1.1	1.1
1995 pk−2	0.0	0.0	1.8	1.1	1.1	1.1	1.1	1.3	1.3	1.3
1995 peak	0.0	0.0	1.8	1.1	1.1	1.1	1.1	1.3	1.3	1.3
1995 pk+2	0.0	0.0	1.8	1.1	1.1	1.1	1.1	1.3	1.3	1.3

Table 15: The signed square-root of the covariance matrix elements for systematic errors in the LEP centre-of-mass energy spread. The entries are the absolute errors in units of MeV.

Luminosity errors										
	1990	1991	1992	1993 pk−2	1993 peak	1993 pk+2	1994 peak	1995 pk−2	1995 peak	1995 pk+2
1990	3000.00	30.91	30.91	5.40	5.40	5.40	5.40	5.40	5.40	5.40
1991	30.91	60.25	30.91	5.40	5.40	5.40	5.40	5.40	5.40	5.40
1992	30.91	30.91	41.82	5.40	5.40	5.40	5.40	5.40	5.40	5.40
1993 pk−2	5.40	5.40	5.40	6.52	6.27	6.09	6.26	6.44	6.26	6.08
1993 peak	5.40	5.40	5.40	6.27	6.52	6.27	6.44	6.26	6.44	6.26
1993 pk+2	5.40	5.40	5.40	6.09	6.27	6.52	6.26	6.08	6.26	6.44
1994 peak	5.40	5.40	5.40	6.26	6.44	6.26	6.49	6.26	6.44	6.26
1995 pk−2	5.40	5.40	5.40	6.44	6.26	6.08	6.26	6.59	6.33	6.15
1995 peak	5.40	5.40	5.40	6.26	6.44	6.26	6.44	6.33	6.58	6.33
1995 pk+2	5.40	5.40	5.40	6.08	6.26	6.44	6.26	6.15	6.33	6.58

Table 16: The signed square-root of the covariance matrix elements for systematic errors in the luminosity measurement. The entries are the relative errors in units of 10^{-4}. The theoretical error in the calculated luminometer acceptance is included. The large error for the 1990 luminosity has been artificially inflated, as explained in the text.

$e^+e^- \to q\overline{q}$ cross-section errors										
	1990	1991	1992	1993 pk−2	1993 peak	1993 pk+2	1994 peak	1995 pk−2	1995 peak	1995 pk+2
1990	40.00	19.00	19.00	10.51	10.51	10.51	10.51	10.51	10.51	10.51
1991	19.00	19.00	19.00	7.27	7.27	7.27	7.27	7.27	7.27	7.27
1992	19.00	19.00	19.00	7.27	7.27	7.27	7.27	7.27	7.27	7.27
1993 pk−2	10.51	7.27	7.27	10.24	8.05	9.28	7.80	10.04	7.80	9.07
1993 peak	10.51	7.27	7.27	8.05	7.32	7.75	7.04	7.80	7.04	7.49
1993 pk+2	10.51	7.27	7.27	9.28	7.75	8.65	7.49	9.07	7.49	8.41
1994 peak	10.51	7.27	7.27	7.80	7.04	7.49	7.32	7.80	7.04	7.49
1995 pk−2	10.51	7.27	7.27	10.04	7.80	9.07	7.80	11.08	9.10	10.21
1995 peak	10.51	7.27	7.27	7.80	7.04	7.49	7.04	9.10	8.46	8.84
1995 pk+2	10.51	7.27	7.27	9.07	7.49	8.41	7.49	10.21	8.84	9.63

Table 17: The signed square-root of the covariance matrix elements for systematic errors in the measurement of the $e^+e^- \to q\overline{q}$ cross-section. The hadrons are not appreciably correlated with any of the leptons. The entries are the relative errors in units of 10^{-4}. They do not include errors in the luminosity measurement, which are specified separately in Table 16.

$e^+e^- \to e^+e^-$ cross-section errors										
	1990	1991	1992	1993 pk−2	1993 peak	1993 pk+2	1994 peak	1995 pk−2	1995 peak	1995 pk+2
1990	70.0	22.0	22.0	14.0	14.0	14.0	14.0	14.0	14.0	14.0
1991	22.0	22.0	22.0	14.0	14.0	14.0	14.0	14.0	14.0	14.0
1992	22.0	22.0	23.0	14.0	14.0	14.0	14.0	14.0	14.0	14.0
1993 pk−2	14.0	14.0	14.0	20.0	17.0	18.0	15.0	18.0	15.0	16.0
1993 peak	14.0	14.0	14.0	17.0	17.0	17.0	14.0	15.0	14.0	15.0
1993 pk+2	14.0	14.0	14.0	18.0	17.0	19.0	15.0	16.0	15.0	17.0
1994 peak	14.0	14.0	14.0	15.0	14.0	15.0	14.0	15.0	14.0	15.0
1995 pk−2	14.0	14.0	14.0	18.0	15.0	16.0	15.0	19.0	17.0	17.0
1995 peak	14.0	14.0	14.0	15.0	14.0	15.0	14.0	17.0	16.0	16.0
1995 pk+2	14.0	14.0	14.0	16.0	15.0	17.0	15.0	17.0	16.0	18.0

Table 18: The signed square-root of the covariance matrix elements for systematic errors in the measurement of the $e^+e^- \to e^+e^-$ cross-section. Additional terms arise between electrons and taus, which are given in Table 21. The entries are the relative errors in units of 10^{-4}. They do not include errors in the luminosity measurement, which are specified separately in Table 16.

$e^+e^- \to \mu^+\mu^-$ cross-section errors										
	1990	1991	1992	1993 pk−2	1993 peak	1993 pk+2	1994 peak	1995 pk−2	1995 peak	1995 pk+2
1990	50.0	16.0	16.0	9.0	9.0	9.0	9.0	9.0	9.0	9.0
1991	16.0	25.0	16.0	9.0	9.0	9.0	9.0	9.0	9.0	9.0
1992	16.0	16.0	16.0	9.0	9.0	9.0	9.0	9.0	9.0	9.0
1993 pk−2	9.0	9.0	9.0	17.0	13.3	13.3	8.4	9.8	9.8	9.8
1993 peak	9.0	9.0	9.0	13.3	16.0	13.3	8.4	9.8	9.8	9.8
1993 pk+2	9.0	9.0	9.0	13.3	13.3	17.0	8.4	9.8	9.8	9.8
1994 peak	9.0	9.0	9.0	8.4	8.4	8.4	10.0	8.5	8.5	8.5
1995 pk−2	9.0	9.0	9.0	9.8	9.8	9.8	8.5	18.0	10.6	10.6
1995 peak	9.0	9.0	9.0	9.8	9.8	9.8	8.5	10.6	12.0	10.6
1995 pk+2	9.0	9.0	9.0	9.8	9.8	9.8	8.5	10.6	10.6	17.0

Table 19: The signed square-root of the covariance matrix elements for systematic errors in the measurement of the $e^+e^- \to \mu^+\mu^-$ cross-section. Additional terms arise between muons and taus, which are given in Table 21. The entries are the relative errors in units of 10^{-4}. They do not include errors in the luminosity measurement, which are specified separately in Table 16.

$e^+e^- \to \tau^+\tau^-$ cross-section errors										
	1990	1991	1992	1993 pk−2	1993 peak	1993 pk+2	1994 peak	1995 pk−2	1995 peak	1995 pk+2
1990	130.	40.	40.	20.	20.	20.	20.	20.	20.	20.
1991	40.	76.	40.	20.	20.	20.	20.	20.	20.	20.
1992	40.	40.	43.	20.	20.	20.	20.	20.	20.	20.
1993 pk−2	20.	20.	20.	60.	48.	54.	33.	45.	34.	34.
1993 peak	20.	20.	20.	48.	49.	47.	35.	34.	37.	34.
1993 pk+2	20.	20.	20.	54.	47.	57.	32.	34.	33.	43.
1994 peak	20.	20.	20.	33.	35.	32.	42.	33.	35.	33.
1995 pk−2	20.	20.	20.	45.	34.	34.	33.	60.	47.	55.
1995 peak	20.	20.	20.	34.	37.	33.	35.	47.	48.	47.
1995 pk+2	20.	20.	20.	34.	34.	43.	33.	55.	47.	58.

Table 20: The signed square-root of the covariance matrix elements for systematic errors in the measurement of the $e^+e^- \to \tau^+\tau^-$ cross-sections. The $\tau\tau-$ee terms and $\tau\tau - \mu\mu$ terms are given in Table 21. The entries are the relative errors in units of 10^{-4}. They do not include errors in the luminosity measurement, which are specified separately in Table 16.

inter-species cross-section errors											
		1990	1991	1992	1993 pk−2	1993 peak	1993 pk+2	1994 peak	1995 pk−2	1995 peak	1995 pk+2
		$\tau\tau$	$\tau\tau$	$\tau\tau$	$\tau\tau$	$\tau\tau$	$\tau\tau$	$\tau\tau$	$\tau\tau$	$\tau\tau$	$\tau\tau$
1990	ee	−20.0	−4.8	−4.4	0.0	0.0	0.0	0.0	0.0	0.0	0.0
1991	ee	−4.8	−18.0	−4.1	0.0	0.0	0.0	0.0	0.0	0.0	0.0
1992	ee	−4.4	−4.1	−15.0	0.0	0.0	0.0	0.0	0.0	0.0	0.0
1993 pk−2	ee	0.0	0.0	0.0	−14.0	−9.0	−9.4	−2.9	−3.1	−2.9	−3.0
1993 peak	ee	0.0	0.0	0.0	−9.0	−10.0	−7.9	−2.4	−2.6	−2.4	−2.5
1993 pk+2	ee	0.0	0.0	0.0	−9.4	−7.9	−11.0	−2.5	−2.8	−2.5	−2.6
1994 peak	ee	0.0	0.0	0.0	−2.9	−2.4	−2.5	−9.0	−2.5	−2.3	−2.4
1995 pk−2	ee	0.0	0.0	0.0	−3.1	−2.6	−2.8	−2.5	−11.0	−7.5	−7.9
1995 peak	ee	0.0	0.0	0.0	−2.9	−2.4	−2.5	−2.3	−7.5	−9.0	−7.1
1995 pk+2	ee	0.0	0.0	0.0	−3.0	−2.5	−2.6	−2.4	−7.9	−7.1	−10.0
1990	$\mu\mu$	−40.0	−8.0	−7.3	0.0	0.0	0.0	0.0	0.0	0.0	0.0
1991	$\mu\mu$	−8.0	−24.0	−5.3	0.0	0.0	0.0	0.0	0.0	0.0	0.0
1992	$\mu\mu$	−7.3	−5.3	−18.0	0.0	0.0	0.0	0.0	0.0	0.0	0.0
1993 pk−2	$\mu\mu$	0.0	0.0	0.0	−11.0	−8.3	−8.3	−2.4	−3.1	−2.9	−3.0
1993 peak	$\mu\mu$	0.0	0.0	0.0	−8.3	−11.0	−8.3	−2.4	−3.1	−2.9	−3.0
1993 pk+2	$\mu\mu$	0.0	0.0	0.0	−8.3	−8.3	−11.0	−2.4	−3.1	−2.9	−3.0
1994 peak	$\mu\mu$	0.0	0.0	0.0	−2.4	−2.4	−2.4	−8.0	−2.8	−2.5	−2.6
1995 pk−2	$\mu\mu$	0.0	0.0	0.0	−3.1	−3.1	−3.1	−2.8	−14.0	−9.8	−10.1
1995 peak	$\mu\mu$	0.0	0.0	0.0	−2.9	−2.9	−2.9	−2.5	−9.8	−12.0	−9.4
1995 pk+2	$\mu\mu$	0.0	0.0	0.0	−3.0	−3.0	−3.0	−2.6	−10.1	−9.4	−13.0

Table 21: The signed square-root of the covariance matrix elements for systematic errors correlated between species in the measurement of the lepton cross-sections. The entries are the relative errors in units of 10^{-4}. They do not include errors in the luminosity measurement, which are specified separately in Table 16.

Sample		$\sqrt{s}$(GeV) mean	$\sqrt{s}$(GeV) rms	$N_{\mu\mu}$	$e^+e^- \to \mu^+\mu^-$ asymmetry measured	corrected	fit
	peak-3	88.2600	0.0481	130	-0.1590 ± 0.0830	-0.1591	-0.2720
	peak-2	89.2550	0.0490	258	-0.2780 ± 0.0570	-0.2782	-0.1781
	peak-1	90.2570	0.0500	391	-0.0770 ± 0.0480	-0.0772	-0.0825
1990	peak	91.2430	0.0510	4963	0.0100 ± 0.0130	0.0100	0.0047
	peak+1	92.2420	0.0520	576	0.0490 ± 0.0400	0.0491	0.0735
	peak+2	93.2450	0.0529	354	0.0940 ± 0.0510	0.0941	0.1218
	peak+3	94.2420	0.0539	231	0.0830 ± 0.0610	0.0830	0.1561
	prescan	91.2540	0.0471	7563	0.0020 ± 0.0110	0.0020	0.0056
	peak-3	88.4800	0.0441	176	-0.2280 ± 0.0700	-0.2281	-0.2515
	peak-2	89.4720	0.0451	363	-0.1060 ± 0.0500	-0.1061	-0.1573
	peak-1	90.2270	0.0461	744	-0.0690 ± 0.0340	-0.0691	-0.0853
1991	peak	91.2240	0.0471	4422	-0.0220 ± 0.0140	-0.0220	0.0032
	peak+1	91.9690	0.0481	916	0.0020 ± 0.0310	0.0021	0.0571
	peak+2	92.9680	0.0490	478	0.1520 ± 0.0420	0.1521	0.1101
	peak+3	93.7170	0.0500	404	0.0850 ± 0.0460	0.0851	0.1393
1992	peak	91.2989	0.0520	33733	0.0088 ± 0.0051	0.0088	0.0092
	prescan(a)	91.1354	0.0868	449	-0.0439 ± 0.0442	-0.0439	-0.0041
	prescan(b)	91.3209	0.0566	7325	0.0081 ± 0.0109	0.0081	0.0109
1993	peak-2	89.4502	0.0564	3937	-0.1503 ± 0.0146	-0.1505	-0.1594
	peak	91.2063	0.0570	12066	-0.0020 ± 0.0085	-0.0020	0.0018
	peak+2	93.0348	0.0570	5628	0.1001 ± 0.0124	0.1002	0.1130
	peak(ab)	91.2198	0.0565	70493	0.0040 ± 0.0035	0.0040	0.0028
1994	peak(c)	91.4285	0.0561	637	0.0182 ± 0.0371	0.0183	0.0193
	peak(d)	91.2194	0.0558	3157	0.0096 ± 0.0166	0.0096	0.0028
	prescan(a)	91.7994	0.0568	256	0.0523 ± 0.0585	0.0524	0.0460
	prescan(b)	91.3032	0.0575	14619	0.0094 ± 0.0077	0.0094	0.0095
1995	peak-2	89.4414	0.0568	3739	-0.1414 ± 0.0151	-0.1416	-0.1603
	peak	91.2826	0.0578	6510	0.0198 ± 0.0115	0.0198	0.0079
	peak+2	92.9716	0.0581	5688	0.1170 ± 0.0123	0.1171	0.1103

Table 22: The $e^+e^- \to \mu^+\mu^-$ forward–backward charge asymmetry near the Z resonance. The measured asymmetry is corrected to the simple kinematic acceptance region defined by $|\cos\theta_{\ell^-}| < 0.95$ and $\theta_{\rm acol} < 15^\circ$, with the energy of each fermion required to be greater than 6.0 GeV. For each data sample we list here the mean $\sqrt{s}$ of the colliding beams, its root-mean-square (rms) spread, and the observed $e^+e^- \to \mu^+\mu^-$ asymmetry. The errors shown are statistical only. The asymmetries are also shown after being corrected for the beam energy spread to correspond to the physical asymmetry at the central value of $\sqrt{s}$. The fit values are the result of the 9-parameter model-independent fit.

Sample		$\sqrt{s}$(GeV) mean	$\sqrt{s}$(GeV) rms	$N_{\tau\tau}$	$e^+e^- \to \tau^+\tau^-$ asymmetry measured	corrected	fit
	peak-3	88.2610	0.0481	102	-0.3467 ± 0.0800	-0.3468	-0.2651
	peak-2	89.2540	0.0490	224	-0.0667 ± 0.0620	-0.0669	-0.1743
	peak-1	90.2630	0.0500	281	-0.0954 ± 0.0550	-0.0956	-0.0810
1990	peak	91.2460	0.0510	3722	-0.0084 ± 0.0150	-0.0084	0.0034
	peak+1	92.2420	0.0520	416	0.0686 ± 0.0460	0.0687	0.0700
	peak+2	93.2480	0.0529	302	0.1277 ± 0.0550	0.1278	0.1171
	peak+3	94.2400	0.0539	183	0.0887 ± 0.0720	0.0887	0.1503
	prescan	91.2540	0.0471	6059	0.0146 ± 0.0120	0.0146	0.0040
	peak-3	88.4800	0.0441	166	-0.2547 ± 0.0680	-0.2548	-0.2454
	peak-2	89.4720	0.0451	289	-0.1017 ± 0.0540	-0.1018	-0.1541
	peak-1	90.2270	0.0461	569	-0.0714 ± 0.0390	-0.0715	-0.0843
1991	peak	91.2240	0.0471	3603	-0.0004 ± 0.0160	-0.0004	0.0017
	peak+1	91.9690	0.0481	734	0.0386 ± 0.0350	0.0387	0.0540
	peak+2	92.9680	0.0490	436	0.0947 ± 0.0440	0.0948	0.1056
	peak+3	93.7170	0.0500	359	0.1697 ± 0.0480	0.1697	0.1340
1992	peak	91.2990	0.0520	28037	0.0152 ± 0.0056	0.0152	0.0075
	prescan(a)	91.1361	0.0867	347	-0.0191 ± 0.0508	-0.0191	-0.0053
	prescan(b)	91.3211	0.0566	5745	-0.0084 ± 0.0136	-0.0084	0.0092
1993	peak-2	89.4504	0.0564	3255	-0.1497 ± 0.0167	-0.1499	-0.1561
	peak	91.2052	0.0570	10374	-0.0060 ± 0.0094	-0.0060	0.0002
	peak+2	93.0348	0.0570	4551	0.1106 ± 0.0142	0.1107	0.1085
	peak(ab)	91.2196	0.0565	56230	0.0008 ± 0.0040	0.0008	0.0013
1994	peak(c)	91.4277	0.0561	451	-0.0926 ± 0.0438	-0.0925	0.0172
	peak(d)	91.2194	0.0558	2471	-0.0193 ± 0.0189	-0.0193	0.0013
	prescan(a)	91.7987	0.0568	195	0.1095 ± 0.0673	0.1096	0.0432
	prescan(b)	91.3032	0.0575	11765	0.0006 ± 0.0088	0.0006	0.0078
1995	peak-2	89.4413	0.0568	3060	-0.1334 ± 0.0171	-0.1336	-0.1569
	peak	91.2823	0.0578	5242	0.0227 ± 0.0132	0.0227	0.0062
	peak+2	92.9715	0.0581	4711	0.0938 ± 0.0139	0.0939	0.1058

Table 23: The $e^+e^- \to \tau^+\tau^-$ forward–backward charge asymmetry near the Z resonance. The measured asymmetry is corrected to the simple kinematic acceptance region defined by $|\cos\theta_{\ell^-}| < 0.90$ and $\theta_{\rm acol} < 15^\circ$, with the energy of each fermion required to be greater than 6.0 GeV. For each data sample we list here the mean $\sqrt{s}$ of the colliding beams, its root-mean-square (rms) spread, and the observed $e^+e^- \to \tau^+\tau^-$ asymmetry. The errors shown are statistical only. The asymmetries are also shown after being corrected for the beam energy spread to correspond to the physical asymmetry at the central value of $\sqrt{s}$. The fit values are the result of the 9-parameter model-independent fit.

Sample		$\sqrt{s}$(GeV) mean	rms	N_{ee}	$e^+e^- \to e^+e^-$ asymmetry measured	corrected	fit
	peak-3	88.2610	0.0481	194	0.3730 ± 0.0670	0.3731	0.3877
	peak-2	89.2550	0.0490	321	0.3290 ± 0.0530	0.3291	0.2977
	peak-1	90.2610	0.0500	384	0.2260 ± 0.0500	0.2261	0.1911
1990	peak	91.2460	0.0510	3719	0.0850 ± 0.0160	0.0849	0.1004
	peak+1	92.2450	0.0520	308	0.0790 ± 0.0570	0.0789	0.0691
	peak+2	93.2470	0.0529	236	-0.0070 ± 0.0650	-0.0070	0.0994
	peak+3	94.2420	0.0539	160	0.2180 ± 0.0780	0.2181	0.1588
	prescan	91.2540	0.0471	5624	0.0900 ± 0.0130	0.0899	0.0999
	peak-3	88.4790	0.0441	297	0.4700 ± 0.0510	0.4701	0.3697
	peak-2	89.4690	0.0451	451	0.2750 ± 0.0450	0.2751	0.2759
	peak-1	90.2270	0.0461	683	0.1820 ± 0.0380	0.1821	0.1948
1991	peak	91.2200	0.0471	3365	0.1070 ± 0.0170	0.1069	0.1022
	peak+1	91.9690	0.0481	566	0.1180 ± 0.0420	0.1179	0.0705
	peak+2	92.9680	0.0490	325	0.0780 ± 0.0550	0.0780	0.0866
	peak+3	93.7170	0.0500	284	0.0580 ± 0.0590	0.0580	0.1256
1992	peak	91.2990	0.0520	25280	0.0996 ± 0.0063	0.0995	0.0969
	prescan(a)	91.1447	0.0857	343	0.2141 ± 0.0528	0.2139	0.1076
	prescan(b)	91.3213	0.0566	5254	0.0930 ± 0.0137	0.0928	0.0955
1993	peak-2	89.4502	0.0565	4750	0.2619 ± 0.0140	0.2621	0.2778
	peak	91.2055	0.0571	9628	0.1052 ± 0.0101	0.1051	0.1032
	peak+2	93.0346	0.0570	3664	0.0958 ± 0.0164	0.0958	0.0894
	peak(ab)	91.2196	0.0565	51939	0.1046 ± 0.0044	0.1045	0.1022
1994	peak(c)	91.4282	0.0562	462	0.1312 ± 0.0461	0.1310	0.0893
	peak(d)	91.2195	0.0558	2281	0.0999 ± 0.0208	0.0998	0.1022
	prescan(a)	91.7987	0.0567	261	0.0894 ± 0.0617	0.0892	0.0740
	prescan(b)	91.3032	0.0575	10741	0.0943 ± 0.0096	0.0941	0.0967
1995	peak-2	89.4417	0.0568	4451	0.2840 ± 0.0144	0.2842	0.2787
	peak	91.2823	0.0578	4812	0.0736 ± 0.0144	0.0735	0.0980
	peak+2	92.9715	0.0581	3706	0.0878 ± 0.0164	0.0878	0.0867

Table 24: The $e^+e^- \to e^+e^-$ forward–backward charge asymmetry near the Z resonance. The measured asymmetry is corrected to the simple kinematic acceptance region defined by $|\cos\theta_{\ell^-}| < 0.70$ and $\theta_{\rm acol} < 10^\circ$, with the energy of each fermion required to be greater than 0.2 GeV. For each data sample we list here the mean $\sqrt{s}$ of the colliding beams, its root-mean-square (rms) spread, and the observed $e^+e^- \to e^+e^-$ asymmetry. The errors shown are statistical only. The asymmetries are also shown after being corrected for the beam energy spread to correspond to the physical asymmetry at the central value of $\sqrt{s}$. The fit values are the result of the 9-parameter model-independent fit.

lepton asymmetry errors											
		1990	1991	1992	1993 pk−2	1993 peak	1993 pk+2	1994 peak	1995 pk−2	1995 peak	1995 pk+2
		ee	ee	ee	ee	ee	ee	ee	ee	ee	ee
1990	ee	5.0	1.0	1.0	1.0	1.0	1.0	1.0	1.0	1.0	1.0
1991	ee	1.0	3.0	1.0	1.0	1.0	1.0	1.0	1.0	1.0	1.0
1992	ee	1.0	1.0	2.0	1.0	1.0	1.0	1.0	1.0	1.0	1.0
1993 pk−2	ee	1.0	1.0	1.0	1.1	1.0	1.0	1.0	1.0	1.0	1.0
1993 peak	ee	1.0	1.0	1.0	1.0	1.0	1.0	1.0	1.0	1.0	1.0
1993 pk+2	ee	1.0	1.0	1.0	1.0	1.0	1.2	1.0	1.0	1.0	1.0
1994 peak	ee	1.0	1.0	1.0	1.0	1.0	1.0	1.0	1.0	1.0	1.0
1995 pk−2	ee	1.0	1.0	1.0	1.0	1.0	1.0	1.0	1.1	1.0	1.0
1995 peak	ee	1.0	1.0	1.0	1.0	1.0	1.0	1.0	1.0	1.0	1.0
1995 pk+2	ee	1.0	1.0	1.0	1.0	1.0	1.0	1.0	1.0	1.0	1.2
		$\mu\mu$	$\mu\mu$	$\mu\mu$	$\mu\mu$	$\mu\mu$	$\mu\mu$	$\mu\mu$	$\mu\mu$	$\mu\mu$	$\mu\mu$
1990	$\mu\mu$	1.0	0.4	0.4	0.4	0.4	0.4	0.4	0.4	0.4	0.4
1991	$\mu\mu$	0.4	1.0	0.4	0.4	0.4	0.4	0.4	0.4	0.4	0.4
1992	$\mu\mu$	0.4	0.4	0.5	0.4	0.4	0.4	0.4	0.4	0.4	0.4
1993 pk−2	$\mu\mu$	0.4	0.4	0.4	1.1	0.4	0.4	0.4	0.4	0.4	0.4
1993 peak	$\mu\mu$	0.4	0.4	0.4	0.4	0.7	0.4	0.4	0.4	0.4	0.4
1993 pk+2	$\mu\mu$	0.4	0.4	0.4	0.4	0.4	1.0	0.4	0.4	0.4	0.4
1994 peak	$\mu\mu$	0.4	0.4	0.4	0.4	0.4	0.4	0.4	0.4	0.4	0.4
1995 pk−2	$\mu\mu$	0.4	0.4	0.4	0.4	0.4	0.4	0.4	1.2	0.4	0.4
1995 peak	$\mu\mu$	0.4	0.4	0.4	0.4	0.4	0.4	0.4	0.4	0.9	0.4
1995 pk+2	$\mu\mu$	0.4	0.4	0.4	0.4	0.4	0.4	0.4	0.4	0.4	0.9
		$\tau\tau$	$\tau\tau$	$\tau\tau$	$\tau\tau$	$\tau\tau$	$\tau\tau$	$\tau\tau$	$\tau\tau$	$\tau\tau$	$\tau\tau$
1990	$\tau\tau$	3.0	3.0	2.0	1.8	1.2	1.6	1.2	1.8	1.2	1.6
1991	$\tau\tau$	3.0	3.0	2.0	1.8	1.2	1.6	1.2	1.8	1.2	1.6
1992	$\tau\tau$	2.0	2.0	2.0	1.8	1.2	1.6	1.2	1.8	1.2	1.6
1993 pk−2	$\tau\tau$	1.8	1.8	1.8	1.8	1.2	1.6	1.2	1.8	1.2	1.6
1993 peak	$\tau\tau$	1.2	1.2	1.2	1.2	1.2	1.2	1.2	1.2	1.2	1.2
1993 pk+2	$\tau\tau$	1.6	1.6	1.6	1.6	1.2	1.6	1.2	1.6	1.2	1.6
1994 peak	$\tau\tau$	1.2	1.2	1.2	1.2	1.2	1.2	1.2	1.2	1.2	1.2
1995 pk−2	$\tau\tau$	1.8	1.8	1.8	1.8	1.2	1.6	1.2	1.8	1.2	1.6
1995 peak	$\tau\tau$	1.2	1.2	1.2	1.2	1.2	1.2	1.2	1.2	1.2	1.2
1995 pk+2	$\tau\tau$	1.6	1.6	1.6	1.6	1.2	1.6	1.2	1.6	1.2	1.6

Table 25: The signed square-root of the covariance matrix elements for systematic errors in the measurement of the lepton asymmetries. There are no appreciable inter-species correlations in the asymmetry measurements. The entries are the absolute errors in units of 10^{-3}.

Parameter	Interpretation in terms of couplings	Without Lepton Universality	With Lepton Universality	Standard Model Prediction
m_{Z} (GeV)		91.1866 ± 0.0031	91.1861 ± 0.0030	input
Γ_{Z} (GeV)		2.4942 ± 0.0042	2.4940 ± 0.0041	$2.4949^{+0.0021}_{-0.0074}$
σ^0_{h} (nb)		41.505 ± 0.055	41.505 ± 0.055	$41.480^{+0.012}_{-0.011}$
$C^{\mathrm{s}}_{\mathrm{ZZ}}(\mathrm{e^+e^-})$	$(g^2_{\mathrm{Ae}}+g^2_{\mathrm{Ve}})(g^2_{\mathrm{Ae}}+g^2_{\mathrm{Ve}})$	0.06330 ± 0.00031		
$C^{\mathrm{s}}_{\mathrm{ZZ}}(\mu^+\mu^-)$	$(g^2_{\mathrm{Ae}}+g^2_{\mathrm{Ve}})(g^2_{\mathrm{A}\mu}+g^2_{\mathrm{V}\mu})$	0.06359 ± 0.00025		
$C^{\mathrm{s}}_{\mathrm{ZZ}}(\tau^+\tau^-)$	$(g^2_{\mathrm{Ae}}+g^2_{\mathrm{Ve}})(g^2_{\mathrm{A}\tau}+g^2_{\mathrm{V}\tau})$	0.06366 ± 0.00033		
$C^{\mathrm{s}}_{\mathrm{ZZ}}(\ell^+\ell^-)$	$(g^2_{\mathrm{A}\ell}+g^2_{\mathrm{V}\ell})^2$		0.06353 ± 0.00022	$0.06382^{+0.00009}_{-0.00031}$
$C^{\mathrm{a}}_{\mathrm{ZZ}}(\mathrm{e^+e^-})$	$g_{\mathrm{Ae}}g_{\mathrm{Ve}}g_{\mathrm{Ae}}g_{\mathrm{Ve}}$	0.000189 ± 0.000094		
$C^{\mathrm{a}}_{\mathrm{ZZ}}(\mu^+\mu^-)$	$g_{\mathrm{Ae}}g_{\mathrm{Ve}}g_{\mathrm{A}\mu}g_{\mathrm{V}\mu}$	0.000320 ± 0.000049		
$C^{\mathrm{a}}_{\mathrm{ZZ}}(\tau^+\tau^-)$	$g_{\mathrm{Ae}}g_{\mathrm{Ve}}g_{\mathrm{A}\tau}g_{\mathrm{V}\tau}$	0.000293 ± 0.000064		
$C^{\mathrm{a}}_{\mathrm{ZZ}}(\ell^+\ell^-)$	$(g_{\mathrm{A}\ell}g_{\mathrm{V}\ell})^2$		0.000294 ± 0.000036	$0.000336^{+0.000014}_{-0.000039}$
$C^{\mathrm{a}}_{\gamma\mathrm{Z}}(\mathrm{e^+e^-})$	$g_{\mathrm{Ae}}g_{\mathrm{Ae}}$	0.242 ± 0.022		
$C^{\mathrm{a}}_{\gamma\mathrm{Z}}(\mu^+\mu^-)$	$g_{\mathrm{Ae}}g_{\mathrm{A}\mu}$	0.232 ± 0.011		
$C^{\mathrm{a}}_{\gamma\mathrm{Z}}(\tau^+\tau^-)$	$g_{\mathrm{Ae}}g_{\mathrm{A}\tau}$	0.234 ± 0.013		
$C^{\mathrm{a}}_{\gamma\mathrm{Z}}(\ell^+\ell^-)$	$g^2_{\mathrm{A}\ell}$		0.2350 ± 0.0080	$0.25130^{+0.00013}_{-0.00047}$
$C^{\mathrm{s}}_{\gamma\mathrm{Z}}(\mathrm{e^+e^-})$	$g_{\mathrm{Ve}}g_{\mathrm{Ve}}$	-0.0262 ± 0.0139		
$C^{\mathrm{s}}_{\gamma\mathrm{Z}}(\mu^+\mu^-)$	$g_{\mathrm{Ve}}g_{\mathrm{V}\mu}$	-0.0029 ± 0.0093		
$C^{\mathrm{s}}_{\gamma\mathrm{Z}}(\tau^+\tau^-)$	$g_{\mathrm{Ve}}g_{\mathrm{V}\tau}$	-0.0011 ± 0.0106		
$C^{\mathrm{s}}_{\gamma\mathrm{Z}}(\ell^+\ell^-)$	$g^2_{\mathrm{V}\ell}$		-0.0075 ± 0.0064	$0.00134^{+0.00006}_{-0.00015}$
χ^2/d.o.f		146.6 / 188	151.8 / 196	

Table 26: Results of the C-parameter fits to the measured cross-section and lepton asymmetry data with and without imposing lepton universality (7 and 15 parameters). Theory uncertainties, other than those on the t-channel for the electrons and the luminosity, are not included in the errors (see section 11.2.2). In the last column we give the values predicted by the SM assuming the parameter variations given in Equation 25.

Parameters		1	2	3	4	5	6	7	8	9	10	11	12	13	14	15
1	m_{Z}	1.000	.043	.034	−.092	−.008	−.005	−.054	.067	.052	.009	.009	.009	−.088	−.142	−.122
2	Γ_{Z}	.043	1.000	−.354	.572	.710	.542	.003	.024	.017	.000	.049	.043	−.024	.022	.021
3	σ^0_{h}	.034	−.354	1.000	−.098	−.120	−.090	.006	.008	.007	−.004	−.007	−.006	−.011	−.018	−.016
4	$C^{\mathrm{s}}_{\mathrm{ZZ}}(\mathrm{e^+e^-})$	−.092	.572	−.098	1.000	.457	.338	.171	−.007	−.007	−.003	.029	.024	.055	.033	.030
5	$C^{\mathrm{s}}_{\mathrm{ZZ}}(\mu^+\mu^-)$	−.008	.710	−.120	.457	1.000	.413	.009	.032	.014	−.003	.059	.032	−.018	.158	.020
6	$C^{\mathrm{s}}_{\mathrm{ZZ}}(\tau^+\tau^-)$	−.005	.542	−.090	.338	.413	1.000	.005	.014	.027	−.001	.028	.075	−.012	.017	.127
7	$C^{\mathrm{a}}_{\mathrm{ZZ}}(\mathrm{e^+e^-})$	−.054	.003	.006	.171	.009	.005	1.000	−.014	−.011	.080	−.001	−.001	−.004	.010	.008
8	$C^{\mathrm{a}}_{\mathrm{ZZ}}(\mu^+\mu^-)$	.067	.024	.008	−.007	.032	.014	−.014	1.000	.016	.001	.208	.003	−.008	.008	−.010
9	$C^{\mathrm{a}}_{\mathrm{ZZ}}(\tau^+\tau^-)$	.052	.017	.007	−.007	.014	.027	−.011	.016	1.000	.001	.002	.184	−.006	−.009	.008
10	$C^{\mathrm{a}}_{\gamma\mathrm{Z}}(\mathrm{e^+e^-})$	.009	.000	−.004	−.003	−.003	−.001	.080	.001	.001	1.000	.000	.000	.217	−.001	−.001
11	$C^{\mathrm{a}}_{\gamma\mathrm{Z}}(\mu^+\mu^-)$	.009	.049	−.007	.029	.059	.028	−.001	.208	.002	.000	1.000	.002	−.003	−.084	.000
12	$C^{\mathrm{a}}_{\gamma\mathrm{Z}}(\tau^+\tau^-)$	.009	.043	−.006	.024	.032	.075	−.001	.003	.184	.000	.002	1.000	−.002	.000	−.089
13	$C^{\mathrm{s}}_{\gamma\mathrm{Z}}(\mathrm{e^+e^-})$	−.088	−.024	−.011	.055	−.018	−.012	−.004	−.008	−.006	.217	−.003	−.002	1.000	.025	.020
14	$C^{\mathrm{s}}_{\gamma\mathrm{Z}}(\mu^+\mu^-)$	−.142	.022	−.018	.033	.158	.017	.010	.008	−.009	−.001	−.084	.000	.025	1.000	.033
15	$C^{\mathrm{s}}_{\gamma\mathrm{Z}}(\tau^+\tau^-)$	−.122	.021	−.016	.030	.020	.127	.008	−.010	.008	−.001	.000	−.089	.020	.033	1.000

Table 27: Error correlation matrix for the C-parameters in Table 26 which do not assume lepton universality.

Parameters		1	2	3	4	5	6	7
1	$m_{\rm Z}$	1.000	.011	.059	−.052	.064	.004	−.207
2	$\Gamma_{\rm Z}$	.011	1.000	−.353	.796	.028	.064	.025
3	$\sigma^0_{\rm h}$	.059	−.353	1.000	−.135	.009	−.010	−.032
4	$C^{\rm s}_{\rm ZZ}(\ell^+\ell^-)$	−.052	.796	−.135	1.000	.051	.078	.119
5	$C^{\rm a}_{\rm ZZ}(\ell^+\ell^-)$	.064	.028	.009	.051	1.000	.185	.005
6	$C^{\rm a}_{\gamma{\rm Z}}(\ell^+\ell^-)$	.004	.064	−.010	.078	.185	1.000	−.031
7	$C^{\rm s}_{\gamma{\rm Z}}(\ell^+\ell^-)$	−.207	.025	−.032	.119	.005	−.031	1.000

Table 28: Error correlation matrix for the C-parameters in Table 26 which assume lepton universality

	Without lepton universality	With lepton universality	SM prediction
$m_{\rm Z}$ (GeV)	91.1858 ± 0.0030	91.1852 ± 0.0030	input
$\Gamma_{\rm Z}$ (GeV)	2.4948 ± 0.0041	2.4948 ± 0.0041	$2.4949^{+0.0021}_{-0.0074}$
$\sigma^0_{\rm h}$ (nb)	41.501 ± 0.055	41.501 ± 0.055	$41.480^{+0.012}_{-0.011}$
$R_{\rm e}$	20.902 ± 0.084		$20.738^{+0.015}_{-0.023}$
R_μ	20.811 ± 0.058		$20.738^{+0.015}_{-0.023}$
R_τ	20.832 ± 0.091		$20.785^{+0.015}_{-0.023}$
R_ℓ		20.823 ± 0.044	$20.738^{+0.015}_{-0.023}$
$A^{0,{\rm e}}_{\rm FB}$	0.0089 ± 0.0044		
$A^{0,\mu}_{\rm FB}$	0.0159 ± 0.0023		
$A^{0,\tau}_{\rm FB}$	0.0145 ± 0.0030		
$A^{0,\ell}_{\rm FB}$		0.0145 ± 0.0017	$0.0158^{+0.0007}_{-0.0018}$
χ^2/d.o.f.	155.6/ 194	158.3/ 198	

Table 29: Results of fitting the model-independent Z parameters to the measured cross-sections and asymmetries. The theory uncertainties given in Table 33, other than those on the t-channel for the electrons and the luminosity, are not included in the errors. In the last column we give the values calculated in the context of the SM assuming the parameter variations given in Equation 25.

	$m_{\rm Z}$	$\Gamma_{\rm Z}$	$\sigma^0_{\rm h}$	R_ℓ	$A^{0,\ell}_{\rm FB}$
$m_{\rm Z}$	1.00	0.05	0.03	0.04	0.07
$\Gamma_{\rm Z}$	0.05	1.00	−0.35	0.02	−0.01
$\sigma^0_{\rm h}$	0.03	−0.35	1.00	0.29	0.02
R_ℓ	0.04	0.02	0.29	1.00	−0.01
$A^{0,\ell}_{\rm FB}$	0.07	−0.01	0.02	−0.01	1.00

Table 30: Error correlation matrix for the 5 parameter fit assuming lepton universality given in Table 29.

	$m_{\rm Z}$	$\Gamma_{\rm Z}$	$\sigma^0_{\rm h}$	$R_{\rm e}$	R_μ	R_τ	$A^{0,{\rm e}}_{\rm FB}$	$A^{0,\mu}_{\rm FB}$	$A^{0,\tau}_{\rm FB}$
$m_{\rm Z}$	1.00	0.05	0.03	0.11	0.00	0.00	−0.05	0.08	0.06
$\Gamma_{\rm Z}$	0.05	1.00	−0.35	0.01	0.02	0.01	0.00	0.00	0.00
$\sigma^0_{\rm h}$	0.03	−0.35	1.00	0.15	0.22	0.14	0.01	0.01	0.01
$R_{\rm e}$	0.11	0.01	0.15	1.00	0.09	0.04	−0.20	0.03	0.02
R_μ	0.00	0.02	0.22	0.09	1.00	0.06	0.00	0.01	0.00
R_τ	0.00	0.01	0.14	0.04	0.06	1.00	0.00	0.00	0.01
$A^{0,{\rm e}}_{\rm FB}$	−0.05	0.00	0.01	−0.20	0.00	0.00	1.00	−0.02	−0.01
$A^{0,\mu}_{\rm FB}$	0.08	0.00	0.01	0.03	0.01	0.00	−0.02	1.00	0.02
$A^{0,\tau}_{\rm FB}$	0.06	0.00	0.01	0.02	0.00	0.01	−0.01	0.02	1.00

Table 31: Error correlation matrix for the 9 parameter fit without assuming lepton universality given in Table 29.

	$m_{\rm Z}$ (GeV)	1990–2	1993–4	1995
1990–2	91.1851 ± 0.0091	1.00	0.02	0.01
1993–4	91.1870 ± 0.0046	0.02	1.00	0.09
1995	91.1851 ± 0.0039	0.01	0.09	1.00

Table 32: Results of the model-independent Z parameters fit with independent $m_{\rm Z}$ for the three main data-taking phases, 1990–2, 1993–4 and 1995. The correlations are given in columns 3–5.

Parameter	Error sources					
	statis-	included systematics				addtl.
	tics	selection	lumi	t-chan.	$E_{\rm beam}$	theory
$m_{\rm Z}$ (GeV)	0.0023	0.0001	0.0003	0.0001	0.0018	0.0003
$\Gamma_{\rm Z}$ (GeV)	0.0036	0.0010	0.0007	0.0000	0.0013	0.0002
$\sigma^0_{\rm h}$ (nb)	0.031	0.033	0.029	0.0000	0.011	0.008
$R_{\rm e}$	0.067	0.040	0.009	0.027	0.014	0.004
R_μ	0.050	0.027	0.008	0.000	0.000	0.004
R_τ	0.055	0.071	0.010	0.000	0.000	0.004
$A^{0,{\rm e}}_{\rm FB}$	0.0038	0.0016	0.0000	0.0018	0.0004	0.0001
$A^{0,\mu}_{\rm FB}$	0.0022	0.0004	0.0000	0.0000	0.0003	0.0001
$A^{0,\tau}_{\rm FB}$	0.0026	0.0014	0.0000	0.0000	0.0003	0.0001
R_ℓ	0.034	0.027	0.008	0.005	0.003	0.004
$A^{0,\ell}_{\rm FB}$	0.0015	0.0006	0.0000	0.0003	0.0002	0.0001
σ^0_ℓ (nb)	0.0032	0.0021	0.0018	0.0005	0.0004	0.0005
$\Gamma_{\rm had}$ (MeV)	2.8	1.8	0.7	0.3	0.8	0.3
$\Gamma_{\ell\ell}$ (MeV)	0.12	0.05	0.03	0.01	0.04	0.01
$\Gamma_{\rm inv}$ (MeV)	1.9	1.6	0.7	0.2	0.5	0.3
$\Gamma_{\rm inv}/\Gamma_{\ell\ell}$	0.017	0.018	0.010	0.002	0.004	0.003
α_s	0.0035	0.0026	0.0026	0.0008	0.0006	
$\log_{10}(m_{\rm H}/{\rm GeV})$	0.41	0.06	0.13	0.05	0.07	

Table 33: Contribution of the various error sources to the uncertainty in the direct and derived Z resonance parameters. "Statistics" include the event counting and luminosity point-to-point statistical errors; "selection" are the systematic errors associated with the event selection; "lumi" errors contain the experimental systematic uncertainties and the theoretical error of the luminosity cross-section; "t-channel" are the theoretical uncertainties of the t-channel correction for $\rm e^+e^- \to e^+e^-$; "$E_{\rm beam}$" includes the uncertainties in the LEP centre-of-mass energy and centre-of-mass energy spread; "addtl. theory" gives the uncertainties related to the determination of the fit parameters from the measured cross-sections and asymmetries which are **not** included in the tables.

	Without lepton universality	With lepton universality	Standard Model prediction
$\Gamma_{\rm inv}$(MeV)	494.4 ± 4.2	498.1 ± 2.6	$501.64^{+0.26}_{-0.93}$
$\Gamma_{\rm ee}$(MeV)	83.66 ± 0.20		$83.977^{+0.058}_{-0.206}$
$\Gamma_{\mu\mu}$(MeV)	84.03 ± 0.30		$83.976^{+0.058}_{-0.206}$
$\Gamma_{\tau\tau}$(MeV)	83.94 ± 0.41		$83.786^{+0.058}_{-0.206}$
$\Gamma_{\ell\ell}$(MeV)		83.82 ± 0.15	$83.977^{+0.058}_{-0.206}$
$\Gamma_{\rm had}$(MeV)	1748.8 ± 4.6	1745.4 ± 3.5	$1741.5^{+1.8}_{-5.9}$

Table 34: Z partial decay widths obtained from a parameter transformation from the fitted model-independent Z parameters given in Table 29. In the last column we give the values of the widths calculated in the context of the SM assuming the parameter variations given in Equation 25.

	$\Gamma_{\rm inv}$	$\Gamma_{\rm ee}$	$\Gamma_{\mu\mu}$	$\Gamma_{\tau\tau}$	$\Gamma_{\rm had}$
$\Gamma_{\rm inv}$	1.00	0.81	−0.40	−0.35	−0.63
$\Gamma_{\rm ee}$	0.81	1.00	−0.19	−0.15	−0.25
$\Gamma_{\mu\mu}$	−0.40	−0.19	1.00	0.33	0.64
$\Gamma_{\tau\tau}$	−0.35	−0.15	0.33	1.00	0.47
$\Gamma_{\rm had}$	−0.63	−0.25	0.64	0.47	1.00

Table 35: Error correlation matrix for the measurements of the partial widths, without assuming lepton universality, presented in Table 34.

	$\Gamma_{\rm inv}$	$\Gamma_{\ell\ell}$	$\Gamma_{\rm had}$
$\Gamma_{\rm inv}$	1.00	0.60	−0.27
$\Gamma_{\ell\ell}$	0.60	1.00	0.36
$\Gamma_{\rm had}$	−0.27	0.36	1.00

Table 36: Error correlation matrix for the measurements of the partial widths, assuming lepton universality, presented in Table 34.

	$\Gamma^{\rm exp} - \Gamma^{\rm SM}$ (MeV)		errors (MeV)		$\Gamma_{95}^{\rm new}$ (MeV)	
$m_{\rm H}$(GeV)	150	1000			150	1000
$\Gamma_{\rm Z}$	−0.1	7.1	±4.1	±2.1	9.0	14.8
$\Gamma_{\rm inv}$	−3.5	−2.6	±2.6	±0.2	3.4	3.7
$\Gamma_{\rm had}$	3.9	9.6	±3.5	±1.9	10.8	16.2
$\Gamma_{\ell\ell}$	−0.15	0.05	±0.15	±0.05	0.22	0.34
$\Gamma_{\rm ee}$	−0.31	−0.11	±0.20	±0.05	0.26	0.35
$\Gamma_{\mu\mu}$	0.05	0.25	±0.30	±0.05	0.63	0.78
$\Gamma_{\tau\tau}$	0.16	0.36	±0.41	±0.05	0.93	1.08

Table 37: Upper limits for total and partial Z widths. The second column gives the difference between the measured width and the expected width in the SM for $m_{\rm H} = 150$ GeV, and the third column for $m_{\rm H} = 1000$ GeV. These two results share the same errors, which are given in the fourth column. The first error is experimental and the second error reflects parametric uncertainties in the SM input parameters $\alpha_{\rm s}$, $m_{\rm t}$ and $\Delta\alpha_{\rm had}^{(5)}$ as specified in Equation 25. The last two columns show the corresponding upper limits (one-sided Bayesian limits at 95 % C.L.) for new contributions, beyond the SM. For $\Gamma_{\ell\ell}$, $\Gamma_{\rm inv}$ and $\Gamma_{\rm had}$ the experimental results with lepton universality imposed have been used. Both experimental and theoretical uncertainties are correlated between the different widths, therefore the limits cannot be used simultaneously.

	Without lepton universality	With lepton universality	SM prediction
$\mathcal{A}_{\rm e}$	$0.109^{+0.025}_{-0.032}$		
$\mathcal{A}_{\mu}$	$0.194^{+0.086}_{-0.044}$		
$\mathcal{A}_{\tau}$	$0.177^{+0.083}_{-0.047}$		
$\mathcal{A}_{\ell}$		$0.1392^{+0.0078}_{-0.0082}$	$0.1450^{+0.0030}_{-0.0084}$

Table 38: The leptonic coupling parameters obtained from a parameter transformation from the model-independent Z parameters given in Table 29. In the last column we give the value of the parameter calculated in the context of the SM assuming the parameter variations given in Equation 25.

	$\mathcal{A}_{\rm e}$	$\mathcal{A}_{\mu}$	$\mathcal{A}_{\tau}$
$\mathcal{A}_{\rm e}$	1.000	-0.869	-0.777
$\mathcal{A}_{\mu}$	-0.869	1.000	0.681
$\mathcal{A}_{\tau}$	-0.777	0.681	1.000

Table 39: Error correlation matrix for the measurements of the leptonic coupling parameters, presented in Table 38.

	Without lepton universality	With lepton universality	Standard Model prediction
$g_{\rm Ae}$	$-0.5009^{+0.0007}_{-0.0007}$		
$g_{\rm A\mu}$	$-0.5004^{+0.0026}_{-0.0013}$		
$g_{\rm A\tau}$	$-0.5011^{+0.0024}_{-0.0016}$		
$g_{\rm A\ell}$		$-0.50095^{+0.00046}_{-0.00046}$	$-0.50130^{+0.00047}_{-0.00013}$
$g_{\rm Ve}$	$-0.027^{+0.008}_{-0.006}$		
$g_{\rm V\mu}$	$-0.049^{+0.011}_{-0.022}$		
$g_{\rm V\tau}$	$-0.045^{+0.012}_{-0.021}$		
$g_{\rm V\ell}$		$-0.0350^{+0.0021}_{-0.0020}$	$-0.0365^{+0.0022}_{-0.0008}$

Table 40: Axial-vector and vector couplings obtained from a parameter transformation from the standard LEP parameter set given in Table 29. In the last column we give the values of the couplings calculated in the context of the SM assuming the parameter variations given in Equation 25.

	$g_{\rm Ae}$	$g_{\rm A\mu}$	$g_{\rm A\tau}$	$g_{\rm Ve}$	$g_{\rm V\mu}$	$g_{\rm V\tau}$
$g_{\rm Ae}$	1.00	-0.37	-0.29	-0.41	0.34	0.31
$g_{\rm A\mu}$	-0.37	1.00	0.49	0.70	-0.83	-0.54
$g_{\rm A\tau}$	-0.29	0.49	1.00	0.52	-0.45	-0.70
$g_{\rm Ve}$	-0.41	0.70	0.52	1.00	-0.87	-0.77
$g_{\rm V\mu}$	0.34	-0.83	-0.45	-0.87	1.00	0.68
$g_{\rm V\tau}$	0.31	-0.54	-0.70	-0.77	0.68	1.00

Table 41: Error correlation matrix for the measurements of the axial vector and vector couplings, without assuming lepton universality, presented in Table 40.

Observable	$\alpha_{\rm s}$
R_ℓ	$0.132 \pm 0.007^{+0.003}_{-0.001}$
$\Gamma_{\rm Z}$	$0.119 \pm 0.008^{+0.017}_{-0.004}$
$\sigma^0_{\rm h}$	$0.114 \pm 0.010^{+0.002}_{-0.001}$
σ^0_ℓ	$0.127 \pm 0.005^{+0.003}_{-0.001}$

Table 42: Determination of $\alpha_{\rm s}$ from the Z resonance parameters. The central value is obtained with the SM parameters $m_{\rm t}$, $m_{\rm H}$ and $\Delta\alpha^{(5)}_{\rm had}$ as specified in Equation 25. The second error reflects the effect on $\alpha_{\rm s}$ when these are varied within the given ranges. In all cases an additional uncertainty of ± 0.002 arises from QCD uncertainties on $\Gamma_{\rm had}$, and must be included.

	OPAL Z resonance measurements alone	external $m_{\rm t} = (174.3 \pm 5.1)$GeV	external $m_{\rm t} = (174.3 \pm 5.1)$GeV $\alpha_{\rm s} = 0.1184 \pm 0.0031$
$m_{\rm Z}$ (GeV)	91.1851±0.0030	91.1851±0.0030	91.1852±0.0030
$m_{\rm t}$ (GeV)	$162 \pm 15^{+25}_{-5}$	174.3±5.1	173.4±5.1
$\Delta\alpha^{(5)}_{\rm had}$ ($\times 10^2$)	$2.803 \pm 0.064^{-0.003}_{+0.001}$	2.802±0.065	2.800±0.064
$\alpha_{\rm s}(m^2_{\rm Z})$	$0.125 \pm 0.005^{+0.004}_{-0.001}$	0.127±0.005	0.121±0.003
$\log_{10}(m_{\rm H}/{\rm GeV})$	–	$2.59^{+0.46}_{-0.55}$	$2.28^{+0.44}_{-0.89}$
$m_{\rm H}$ (GeV)	150 (fixed)	390^{+750}_{-280}	190^{+335}_{-165}
χ^2/d.o.f.	159.7/200	159.7/200	161.7/201

Table 43: Results of the full SM fit to the measured cross-sections and asymmetries. In the second column $m_{\rm H}$ is fixed to 150 GeV. The second errors show the variation for $m_{\rm H} = 90$ GeV *(lower)* and $m_{\rm H} = 1000$ GeV *(upper)*. In the remaining columns $m_{\rm H}$ is determined from the data, with additional external constraints, as indicated. In all cases the electromagnetic coupling constant $\Delta\alpha^{(5)}_{\rm had}$ was used as additional fit parameter with the constraint given in Equation 25.

	$\Delta\sigma$(pb)
$\sigma^{\rm ee}_{\rm F}$(pk −)	1.28
$\sigma^{\rm ee}_{\rm F}$(pk 0)	1.12
$\sigma^{\rm ee}_{\rm F}$(pk +)	1.20
$\sigma^{\rm ee}_{\rm B}$(pk −)	0.32
$\sigma^{\rm ee}_{\rm B}$(pk 0)	0.32
$\sigma^{\rm ee}_{\rm B}$(pk +)	0.32

Table 44: Uncertainties in the forward ($\sigma^{\rm ee}_{\rm F}$) and backward ($\sigma^{\rm ee}_{\rm B}$) electron cross-section for t-channel plus s-t interference diagrams. The designations (pk −), (pk 0), and (pk +) refer to the energy points respectively below, at and above the Z resonance, where the peak region is taken to lie within ±0.9 GeV of $m_{\rm Z}$.

Parameter	fitting $j^{\rm tot}_{\rm had}$	fixing $j^{\rm tot}_{\rm had}$	SM Prediction
$m_{\rm Z}$ (GeV)	91.1901 ± 0.0115	91.1866 ± 0.0031	input
$\Gamma_{\rm Z}$ (GeV)	2.4936 ± 0.0047	2.4943 ± 0.0041	$2.4949^{+0.0021}_{-0.0074}$
$r^{\rm tot}_{\rm had}$	2.962 ± 0.010	2.963 ± 0.009	$2.9627^{+0.0051}_{-0.0173}$
$j^{\rm tot}_{\rm had}$	0.01 ± 0.650		$0.2181^{+0.0048}_{-0.0139}$
$r^{\rm tot}_{\rm e}$	0.14122 ± 0.00085	0.14138 ± 0.00069	
$r^{\rm tot}_{\mu}$	0.14205 ± 0.00061	0.14212 ± 0.00056	$0.14260^{+0.00020}_{-0.00070}$
$r^{\rm tot}_{\tau}$	0.14221 ± 0.00078	0.14229 ± 0.00074	
$j^{\rm tot}_{\rm e}$	-0.085 ± 0.052	-0.076 ± 0.044	
$j^{\rm tot}_{\mu}$	-0.013 ± 0.042	-0.003 ± 0.030	$0.0043^{+0.0002}_{-0.0005}$
$j^{\rm tot}_{\tau}$	-0.007 ± 0.045	0.003 ± 0.034	
$r^{\rm fb}_{\rm e}$	0.00134 ± 0.00086	0.00140 ± 0.00084	
$r^{\rm fb}_{\mu}$	0.00265 ± 0.00046	0.00261 ± 0.00044	$0.00300^{+0.00013}_{-0.00035}$
$r^{\rm fb}_{\tau}$	0.00238 ± 0.00059	0.00234 ± 0.00057	
$j^{\rm fb}_{\rm e}$	0.763 ± 0.070	0.763 ± 0.070	
$j^{\rm fb}_{\mu}$	0.732 ± 0.036	0.732 ± 0.036	$0.7985^{+0.0007}_{-0.0016}$
$j^{\rm fb}_{\tau}$	0.740 ± 0.042	0.740 ± 0.042	
χ^2/d.o.f.	146.6 / 187	146.7 / 188	

Table 45: Results of the 16 and 15 parameter S-Matrix fits to the measured cross-section and lepton asymmetry data. The uncertainties on the LEP energy are included in the errors quoted. In the last column we give the predictions of the SM assuming the parameters and variations given in Table 25.

Parameters		1	2	3	4	5	6	7	8	9	10	11	12	13	14	15	16
1	m_{Z}	1.000	−.441	−.428	−.964	−.578	−.357	−.281	−.537	−.709	−.658	−.252	.295	.237	.024	.002	.007
2	Γ_{Z}	−.441	1.000	.934	.466	.684	.757	.595	.232	.344	.320	.116	−.117	−.096	−.011	.043	.035
3	$r_{\mathrm{had}}^{\mathrm{tot}}$	−.428	.934	1.000	.457	.679	.755	.594	.222	.333	.310	.117	−.110	−.090	−.013	.043	.036
4	$j_{\mathrm{had}}^{\mathrm{tot}}$	−.964	.466	.457	1.000	.585	.377	.296	.536	.708	.657	.247	−.289	−.232	−.023	.000	−.005
5	$r_{\mathrm{e}}^{\mathrm{tot}}$	−.578	.684	.679	.585	1.000	.561	.433	.338	.431	.400	.277	−.175	−.141	−.027	.024	.017
6	r_{μ}^{tot}	−.357	.757	.755	.377	.561	1.000	.475	.186	.359	.259	.098	−.079	−.075	−.011	.059	.028
7	r_{τ}^{tot}	−.281	.595	.594	.296	.433	.475	1.000	.147	.218	.277	.076	−.073	−.043	−.008	.027	.074
8	$j_{\mathrm{e}}^{\mathrm{tot}}$	−.537	.232	.222	.536	.338	.186	.147	1.000	.395	.365	.130	−.161	−.129	.189	−.002	−.004
9	j_{μ}^{tot}	−.709	.344	.333	.708	.431	.359	.218	.395	1.000	.482	.181	−.190	−.170	−.017	−.041	−.003
10	j_{τ}^{tot}	−.658	.320	.310	.657	.400	.259	.277	.365	.482	1.000	.168	−.197	−.138	−.016	.000	−.051
11	$r_{\mathrm{e}}^{\mathrm{fb}}$	−.252	.116	.117	.247	.277	.098	.076	.130	.181	.168	1.000	−.084	−.068	.054	−.001	−.002
12	r_{μ}^{fb}	.295	−.117	−.110	−.289	−.175	−.079	−.073	−.161	−.190	−.197	−.084	1.000	.082	.008	.181	.004
13	r_{τ}^{fb}	.237	−.096	−.090	−.232	−.141	−.075	−.043	−.129	−.170	−.138	−.068	.082	1.000	.006	.002	.162
14	$j_{\mathrm{e}}^{\mathrm{fb}}$	.024	−.011	−.013	−.023	−.027	−.011	−.008	.189	−.017	−.016	.054	.008	.006	1.000	.000	.000
15	j_{μ}^{fb}	.002	.043	.043	.000	.024	.059	.027	−.002	−.041	.000	−.001	.181	.002	.000	1.000	.002
16	j_{τ}^{fb}	.007	.035	.036	−.005	.017	.028	.074	−.004	−.003	−.051	−.002	.004	.162	.000	.002	1.000

Table 46: Error correlation matrix for the S-Matrix fit in Table 45 without assuming lepton universality, and without fixing $j_{\mathrm{had}}^{\mathrm{tot}}$, which controls the γZ interference in the hadron channel.

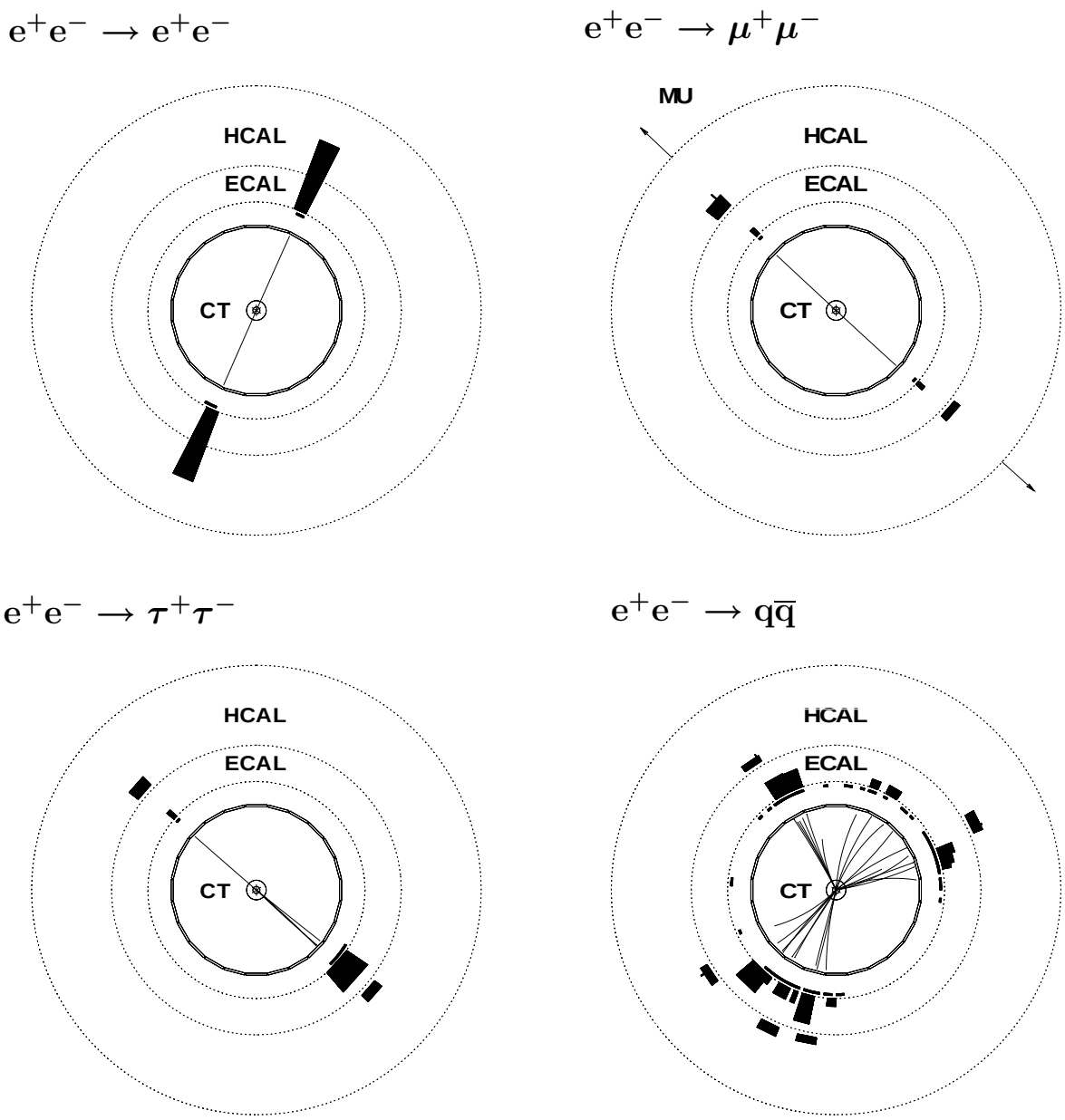

55284507736

Figure 1: Typical examples for the four event categories. These views of the four final states measured in this analysis all show the detector projected along the beam axis, parallel to the magnetic field generated by the solenoid located between CT and ECAL. The approximately radial lines within the volume of the central tracker (CT) represent the reconstructed tracks of inonising particles. The dark trapezoids in the volumes of the electromagnetic calorimeter (ECAL) and hadronic calorimeter (HCAL) represent corresponding observed energy deposits. The arrows within the volume of the multiple-layer muon chambers (MU) represent reconstructed track segments of penetrating particles.

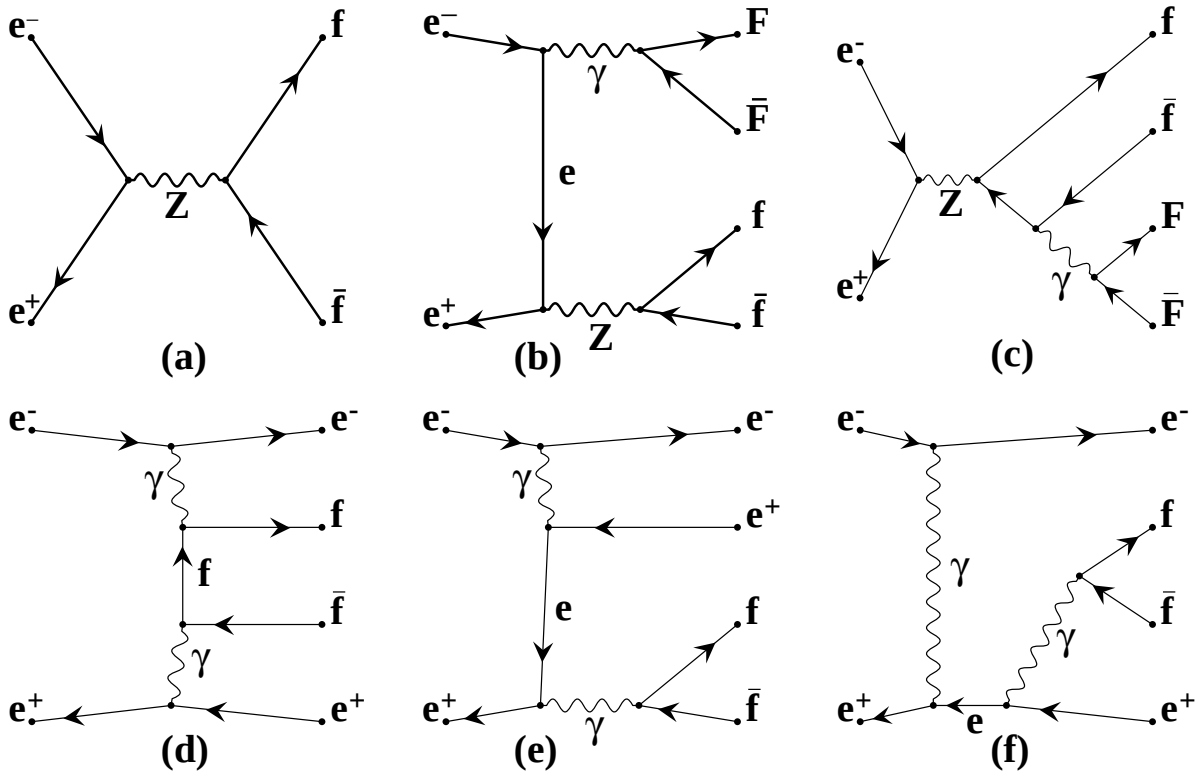

Figure 2: Two- and four-fermion diagrams.
(a) The basic fermion-pair s-channel diagram which is responsible for almost all of the $f\bar{f}$ signal.
(b) Radiative correction to (a) with a fermion pair $F\overline{F}$ in the initial state. Treated as signal.
(c) Radiative correction to (a) with a fermion pair $F\overline{F}$ in the final state. Treated as signal.
(d) Multiperipheral (two-photon) diagram. Treated as background.
(e) Initial-state pair production in the t-channel, treated as background except for $e^+e^- \to e^+e^-$.
(f) Final-state pair production in the t-channel, treated as background except for $e^+e^- \to e^+e^-$.
Only the dominant boson is indicated. Additional contributions arise by substituting Z and γ.

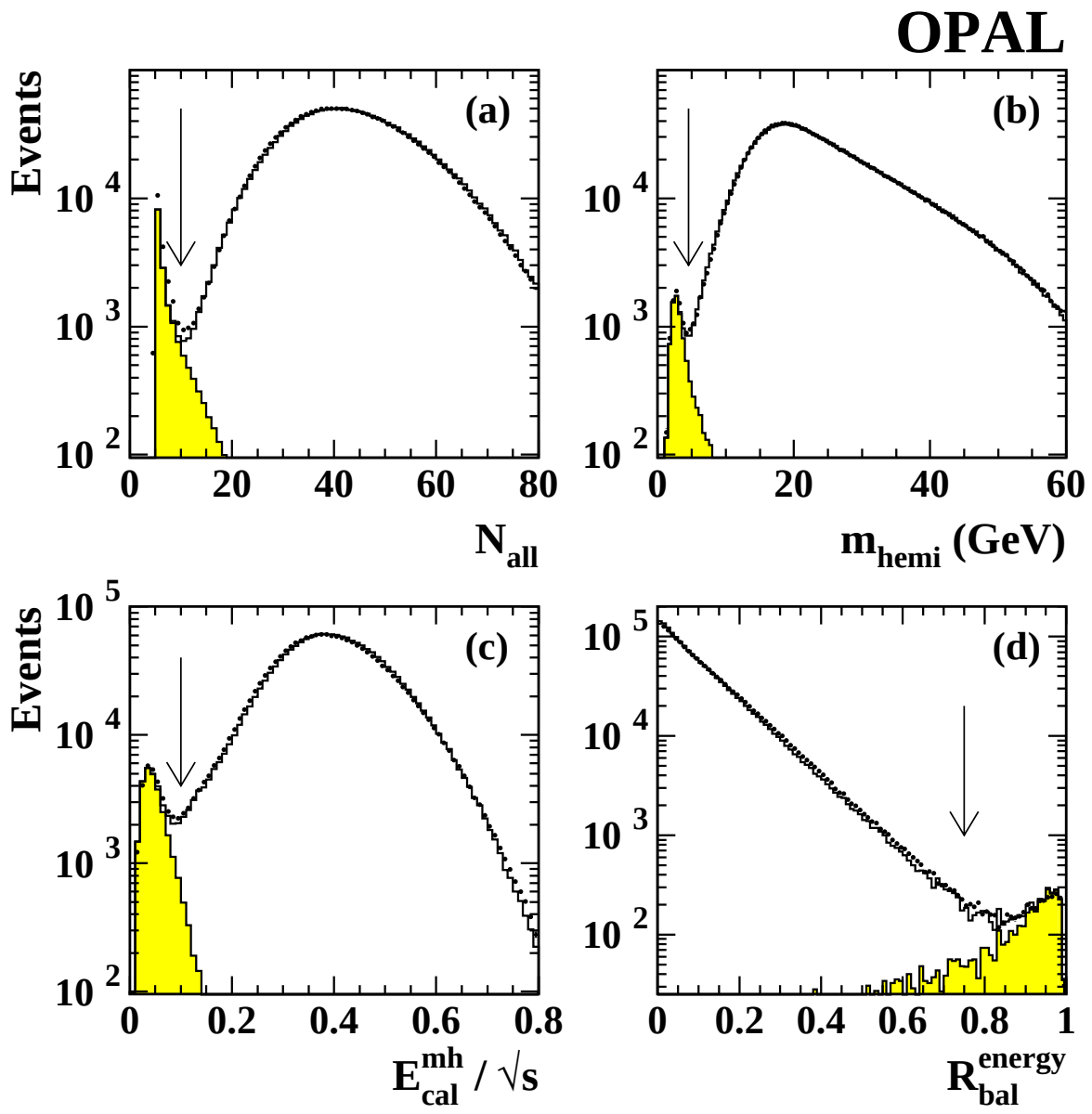

Figure 3: The $e^+e^- \to q\overline{q}$ event selection. A comparison of the cut variables between data and Monte Carlo simulation: (a) the total multiplicity, $N_{\rm all}$, (b) the hemisphere invariant mass sum, $m_{\rm hemi}$, (c) the visible energy, $E^{\rm mh}_{\rm cal}/\sqrt{s}$, (d) the energy imbalance along the beam direction, $R^{\rm energy}_{\rm bal}$. The points are the data and the open histograms the $e^+e^- \to q\overline{q}$ Monte Carlo simulation. The shaded histograms show the background Monte Carlo prediction which is dominated in the case of (a) and (b) by $e^+e^- \to \ell^+\ell^-$ and in the case of (c) and (d) by $e^+e^- \to e^+e^-f\overline{f}$. The cuts are indicated by the arrows. In each case events are plotted only if they pass all the other selection cuts.

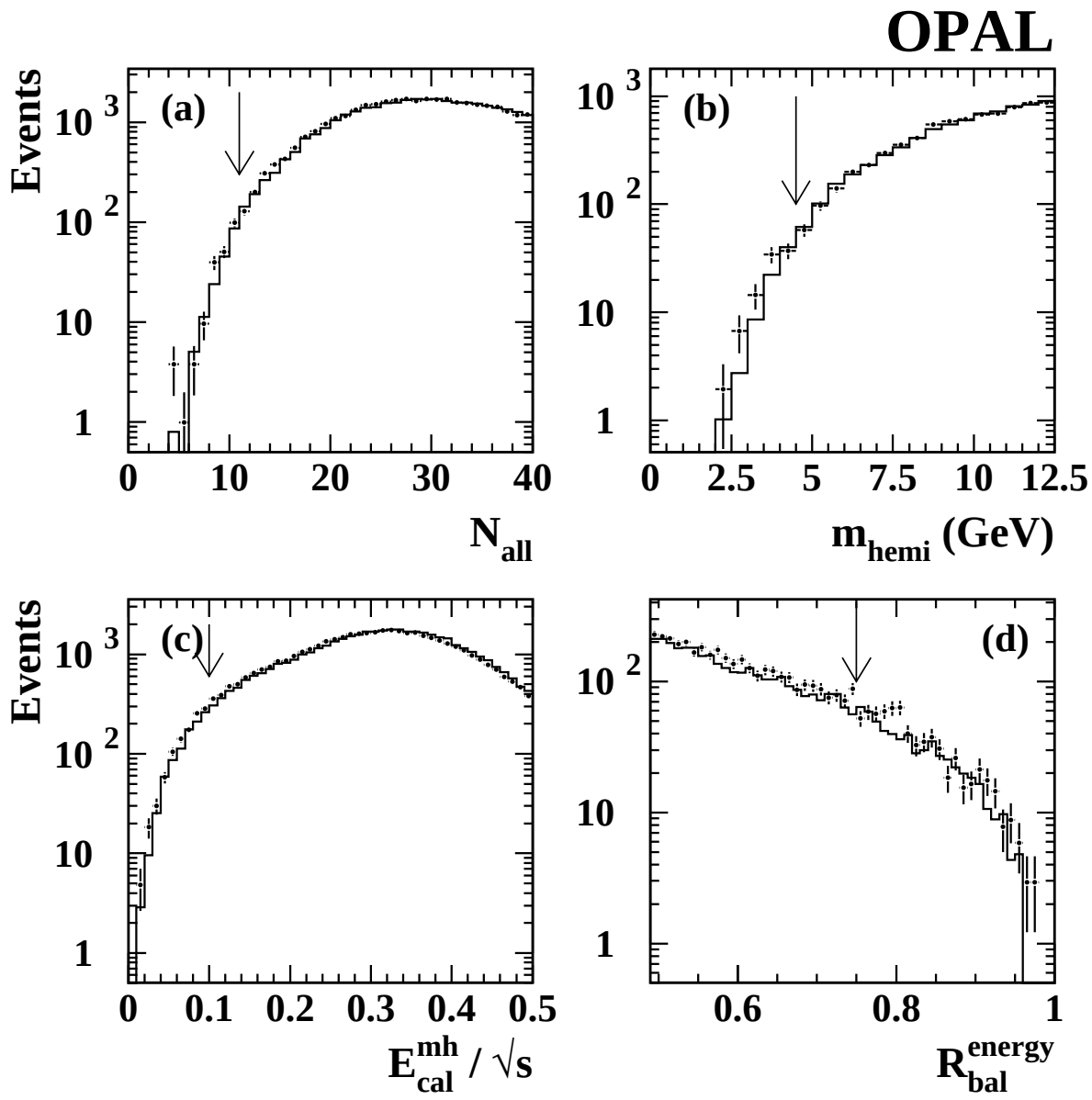

Figure 4: Distributions of the emulated cut variables for $e^+e^- \to q\overline{q}$ events at small angles to the x-axis, which have been processed by the acceptance hole emulation program, as described in the text. The data (points) and the JETSET Monte Carlo events (histogram) are compared. For these plots events are required to pass the standard $e^+e^- \to q\overline{q}$ selection before the hole emulation.

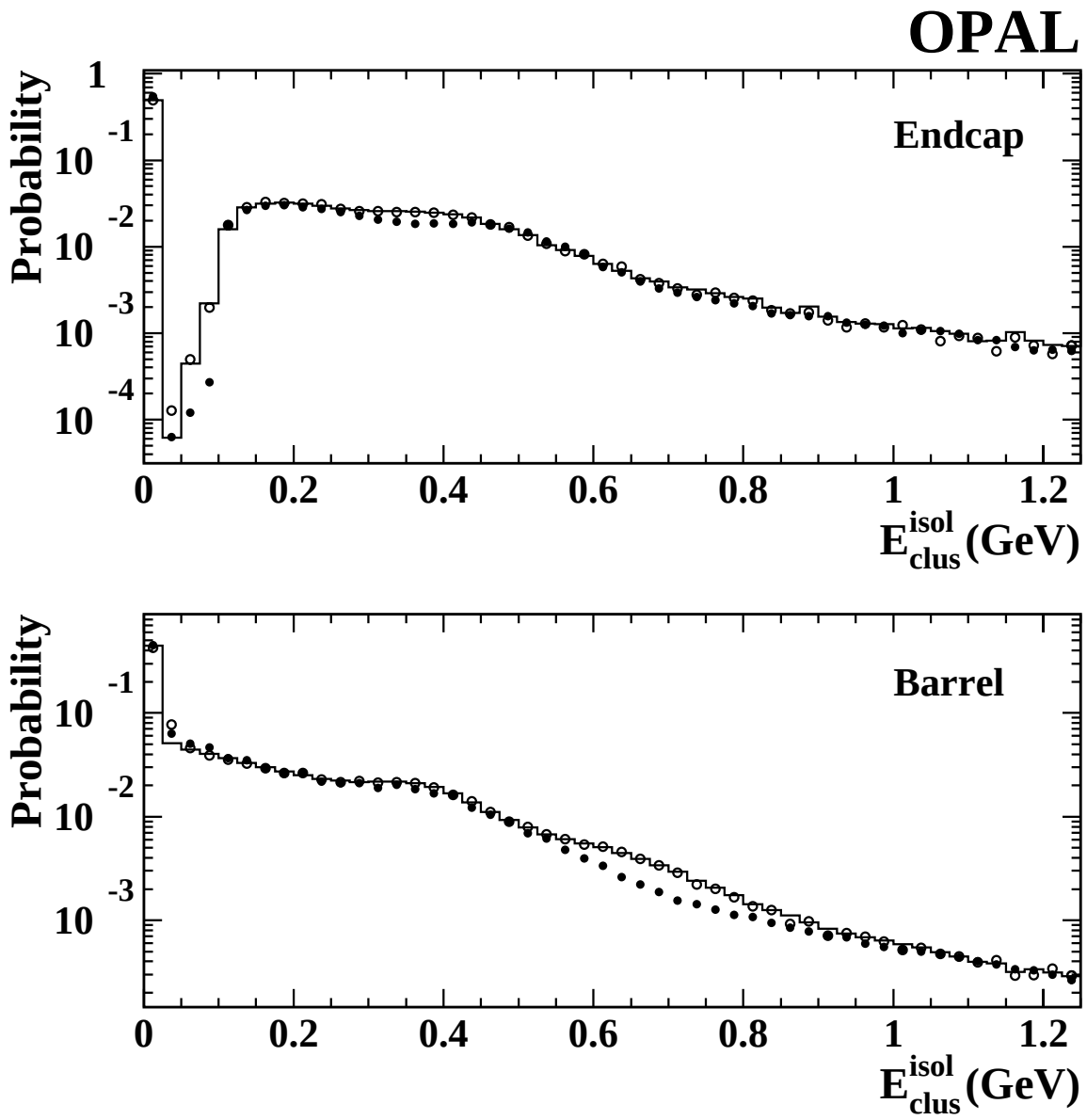

Figure 5: Detector simulation study for the $e^+e^- \to q\overline{q}$ selection. The plots show the energy spectra (normalised to the number of tracks) for single ECAL clusters near isolated tracks for data (histogram), for the standard Monte Carlo simulation (closed circles) and for the corrected Monte Carlo simulation (open circles). The upper plot is for tracks pointing into the endcaps of the electromagnetic calorimeter. The lower plot is for tracks pointing into the barrel region. Both plots are summed over all momenta. A clear improvement in the modelling of the distributions can be seen after correction.

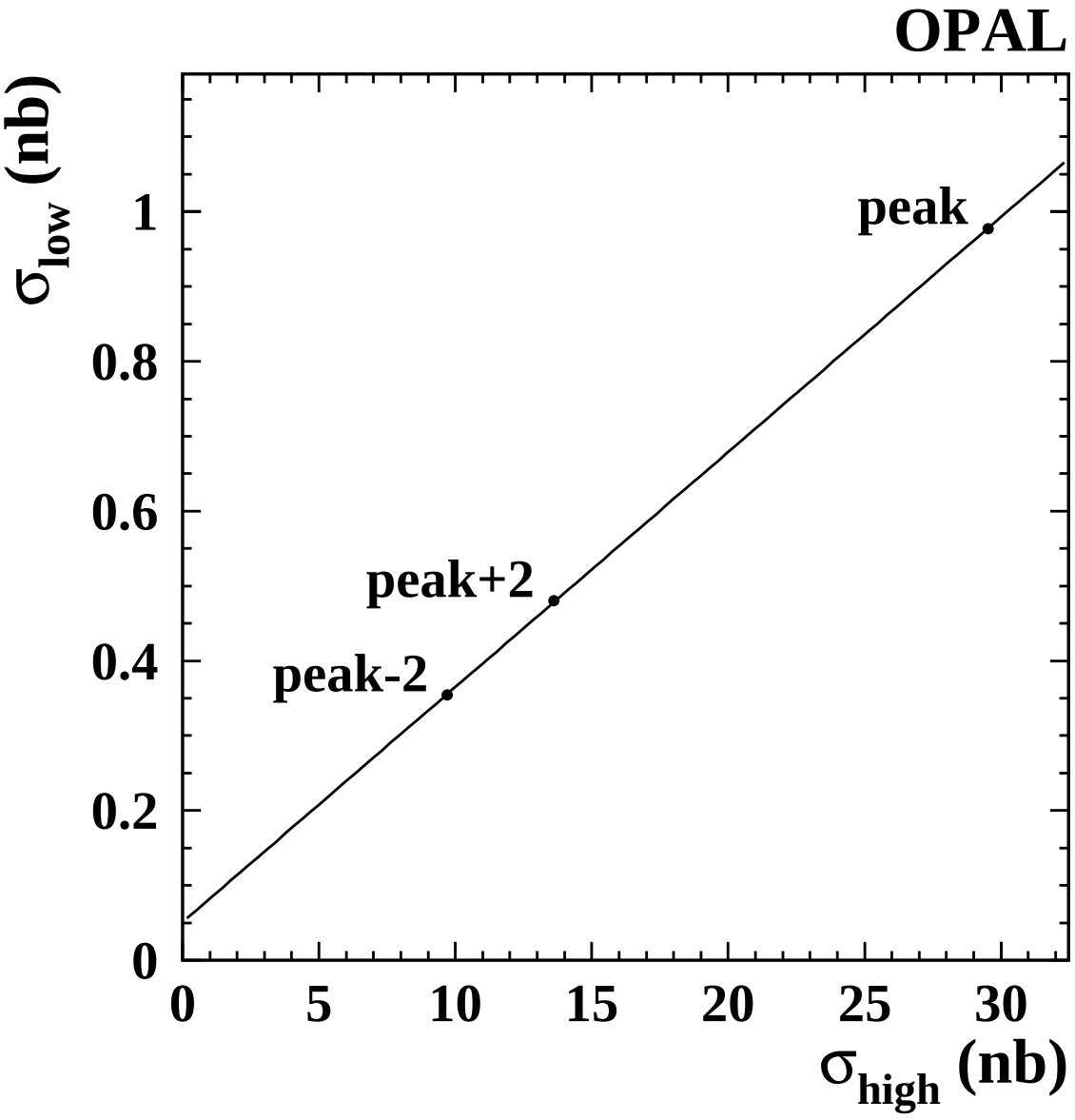

Figure 6: The non-resonant background evaluation for the $e^+e^- \to q\overline{q}$ selection. The plot shows the cross-section for events having a low visible energy, $0.10 < E_{\rm cal}^{\rm mh}/\sqrt{s} < 0.18$, or a large energy imbalance along the beam direction, $0.50 < R_{\rm bal}^{\rm energy} < 0.75$, ($\sigma_{\rm low}$) versus the cross-section for events having a high $E_{\rm cal}^{\rm mh}/\sqrt{s}$ (> 0.18) and a small $R_{\rm bal}^{\rm energy}$ (< 0.50) ($\sigma_{\rm high}$). The intercept of the fitted straight line yields the non-resonant background estimate. The distributions for $E_{\rm cal}^{\rm mh}/\sqrt{s}$ and $R_{\rm bal}^{\rm energy}$ are shown in Figure 3 (c) and (d), respectively.

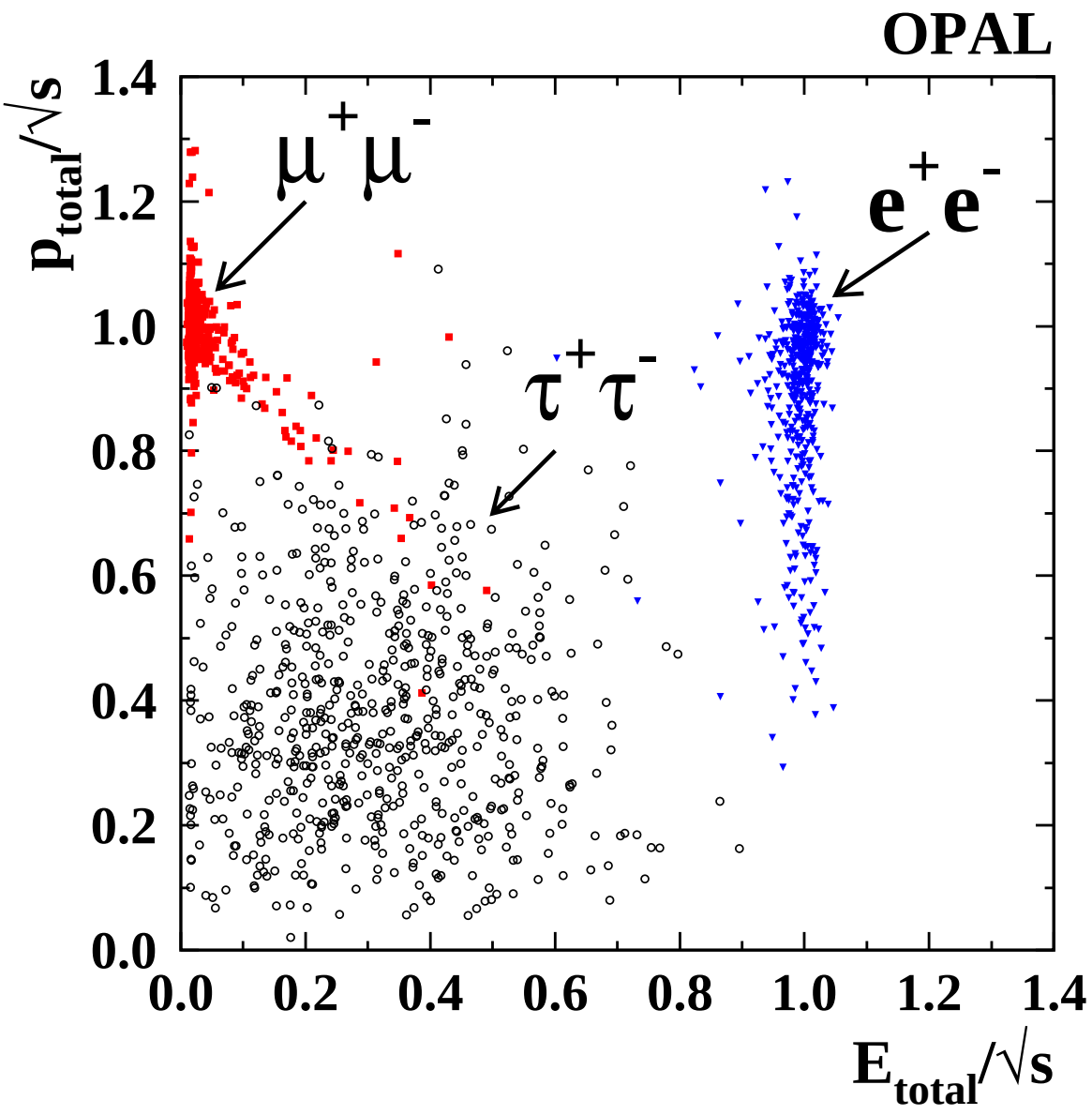

Figure 7: The separation of Monte Carlo $e^+e^- \to \ell^+\ell^-$ events using the energy deposited in the electromagnetic calorimeter summed over all clusters, $E_{\rm total}$ versus the scalar sum of the momenta of the reconstructed tracks in the event, $p_{\rm total}$. Both quantities are scaled to the centre-of-mass energy $\sqrt{s}$. The triangles show $e^+e^- \to e^+e^-$ events, the solid squares show $e^+e^- \to \mu^+\mu^-$ events and the open circles show $e^+e^- \to \tau^+\tau^-$ events.

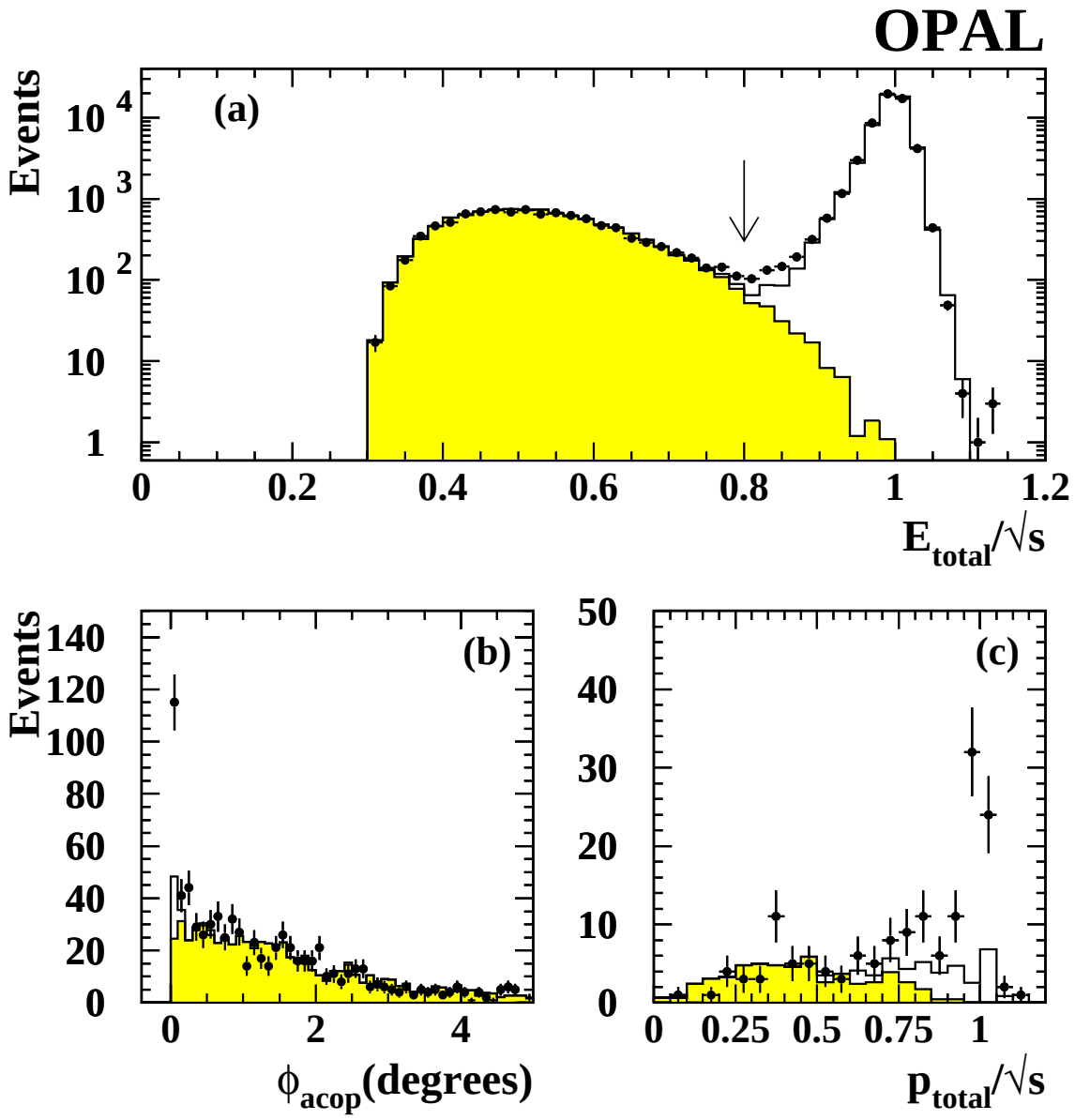

Figure 8: The $e^+e^- \to e^+e^-$ event selection.
(a) Distribution of the sum of electromagnetic energy, $E_{\rm total}/\sqrt{s}$, after all the other cuts have been applied, in the angular range $|\cos\theta_{e^-}| < 0.70$. The arrow indicates the selection cut used.
(b) Distribution of the acoplanarity angle of e^- and e^+ tracks for events satisfying $0.7 < E_{\rm total}/\sqrt{s} < 0.8$.
(c) Distribution of the scalar sum of the track momenta, $p_{\rm total}/\sqrt{s}$, for the events satisfying $0.7 < E_{\rm total}/\sqrt{s} < 0.8$ and $\phi_{\rm acop} < 0.2°$. In each case the points are the on-peak data, the open histogram shows the Monte Carlo expectation and the shaded histogram shows the contribution from background processes.

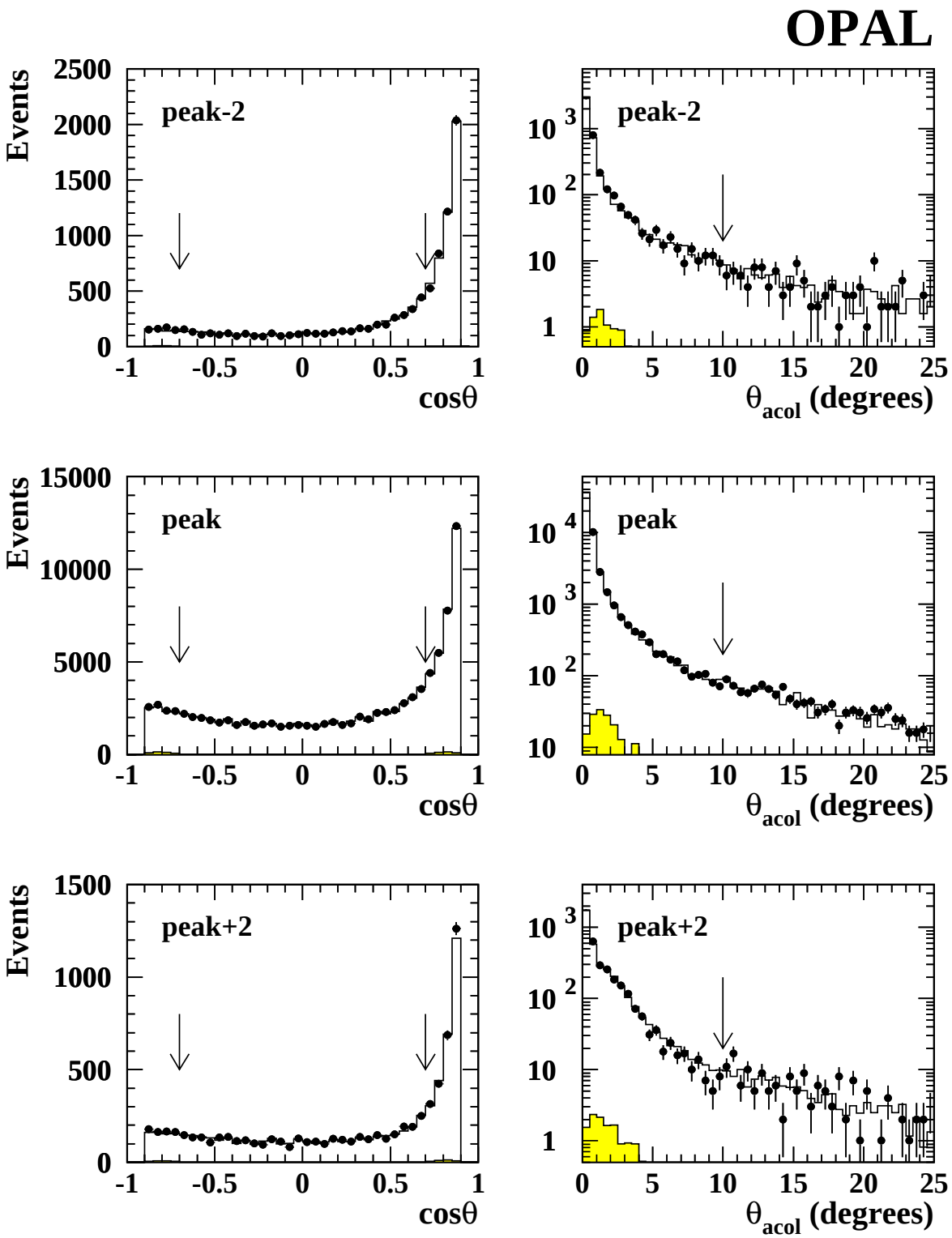

Figure 9: The $e^+e^- \to e^+e^-$ event acceptance. Angular distributions and acollinearity distributions from data samples at three different centre-of-mass energies. In each case the points are the data, the open histogram shows the Monte Carlo expectation and the shaded histogram shows the contribution from background processes. The arrows indicate the acceptance cuts used.

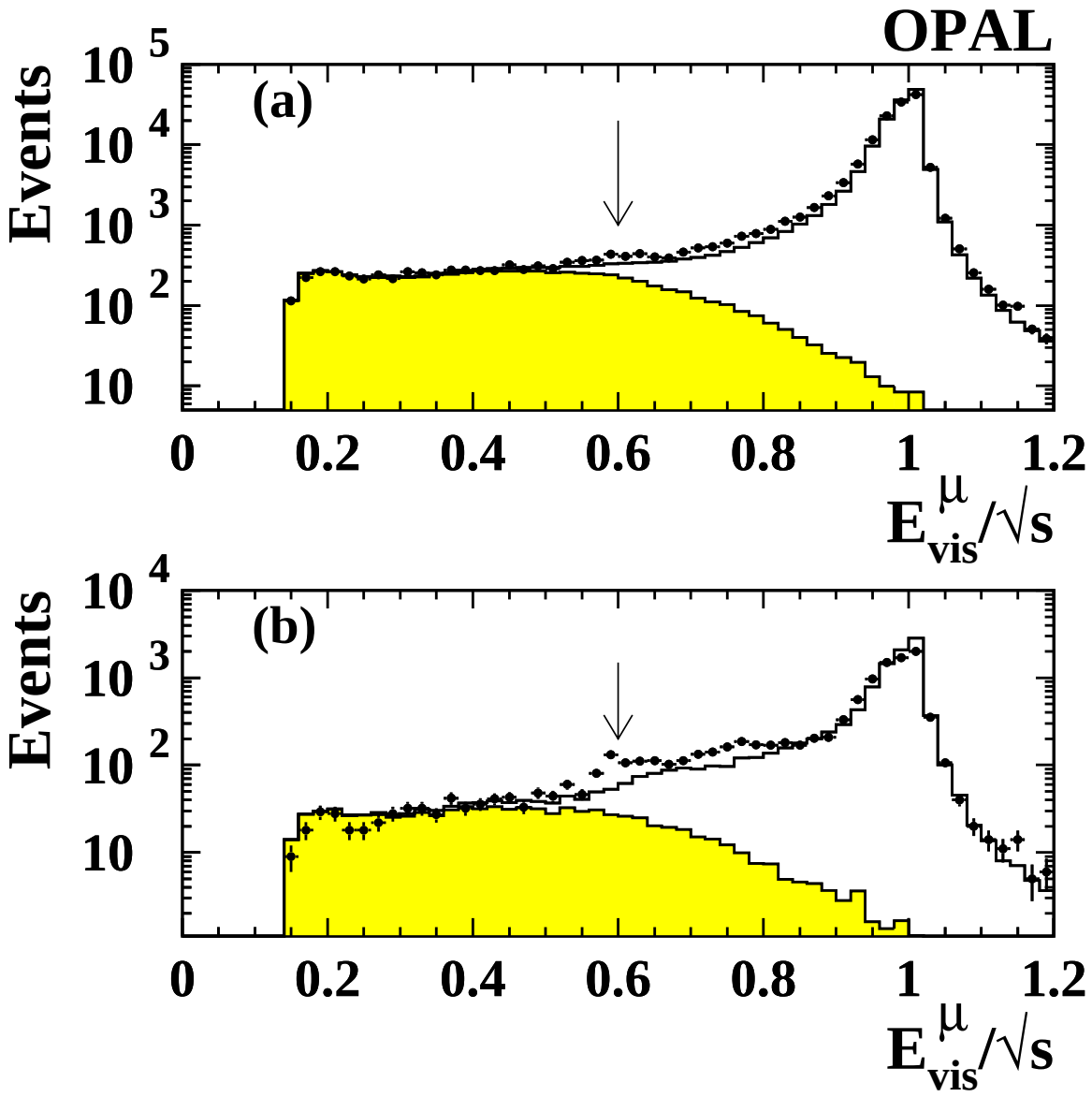

Figure 10: Distribution of $E^{\mu}_{\rm vis}$ for events passing all of the $e^+e^- \to \mu^+\mu^-$ selection cuts with the exception of $E^{\mu}_{\rm vis} > 0.6\sqrt{s}$. The 1993–1995 data are shown by the points and the histograms indicate the Monte Carlo expectation. The shaded histograms represent the background (mainly $e^+e^- \to \tau^+\tau^-$). Figure (a) gives the distribution for all events, while (b) shows those events with tracks within 0.5° of the anode wire planes of the central tracking chamber.

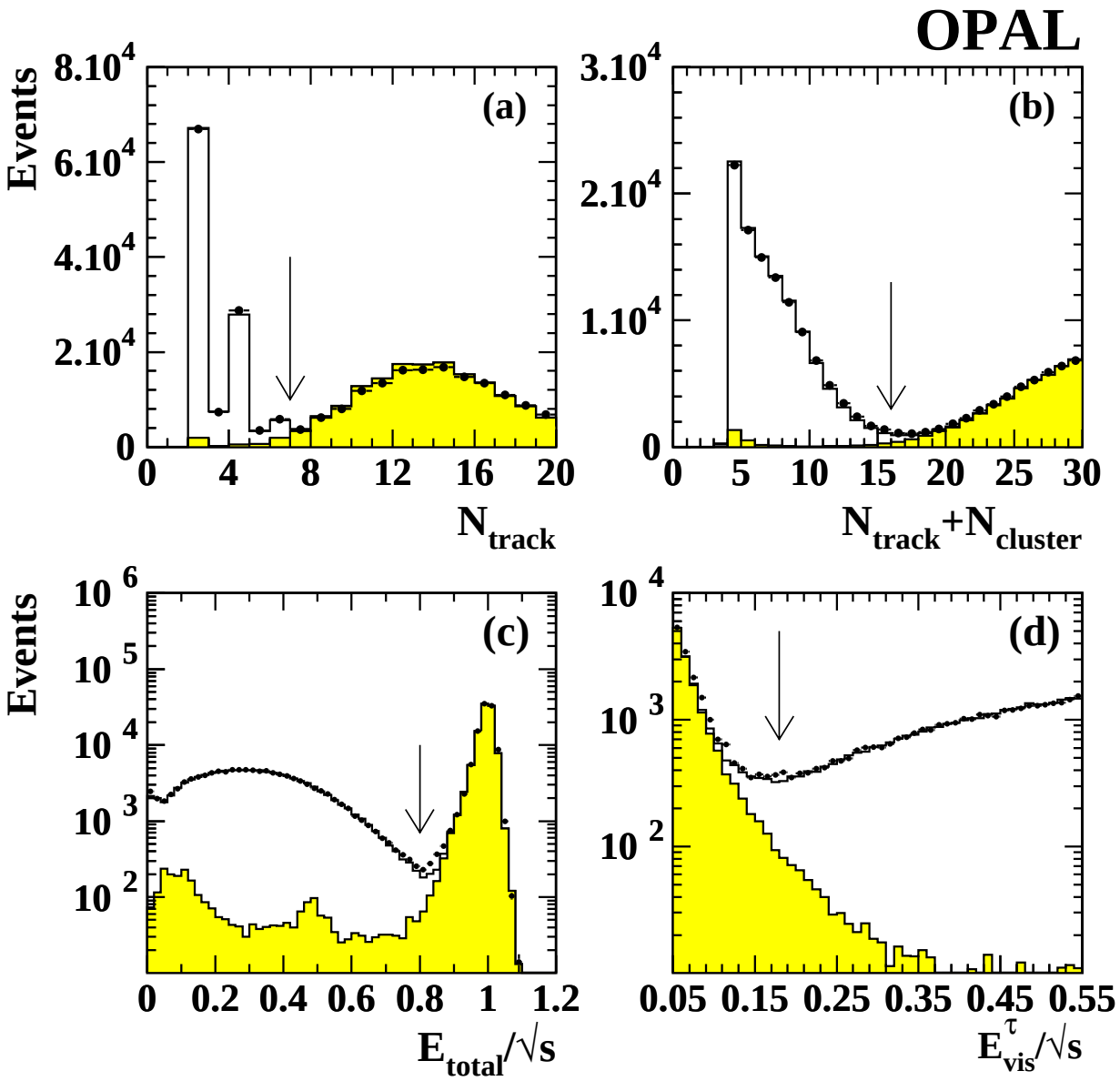

Figure 11: Cuts used in the $e^+e^- \to \tau^+\tau^-$ event selection. Distributions of (a) and (b) the charged and total multiplicity, $N_{\rm track}$ and $N_{\rm track}+N_{\rm cluster}$ used to reject background from $e^+e^- \to q\overline{q}$, (c) $E_{\rm total}$ for events with $|\cos\theta_\tau| < 0.7$ showing the cut used to reject the background from $e^+e^- \to e^+e^-$ in this barrel region of the detector and (d) $E^\tau_{\rm vis}/\sqrt{s}$ showing the cut used to reject two-photon interaction events. In all cases all other selection cuts have been applied. The points represent the 1993–1995 data (on-peak and off-peak), the histograms show the Monte Carlo expectation and the shaded histograms indicate the background component, predominantly $e^+e^- \to q\overline{q}$ in (a) and (b), $e^+e^- \to e^+e^-$ in (c) and $e^+e^- \to e^+e^-\ell^+\ell^-$ in (d). The cuts are indicated by the arrows.

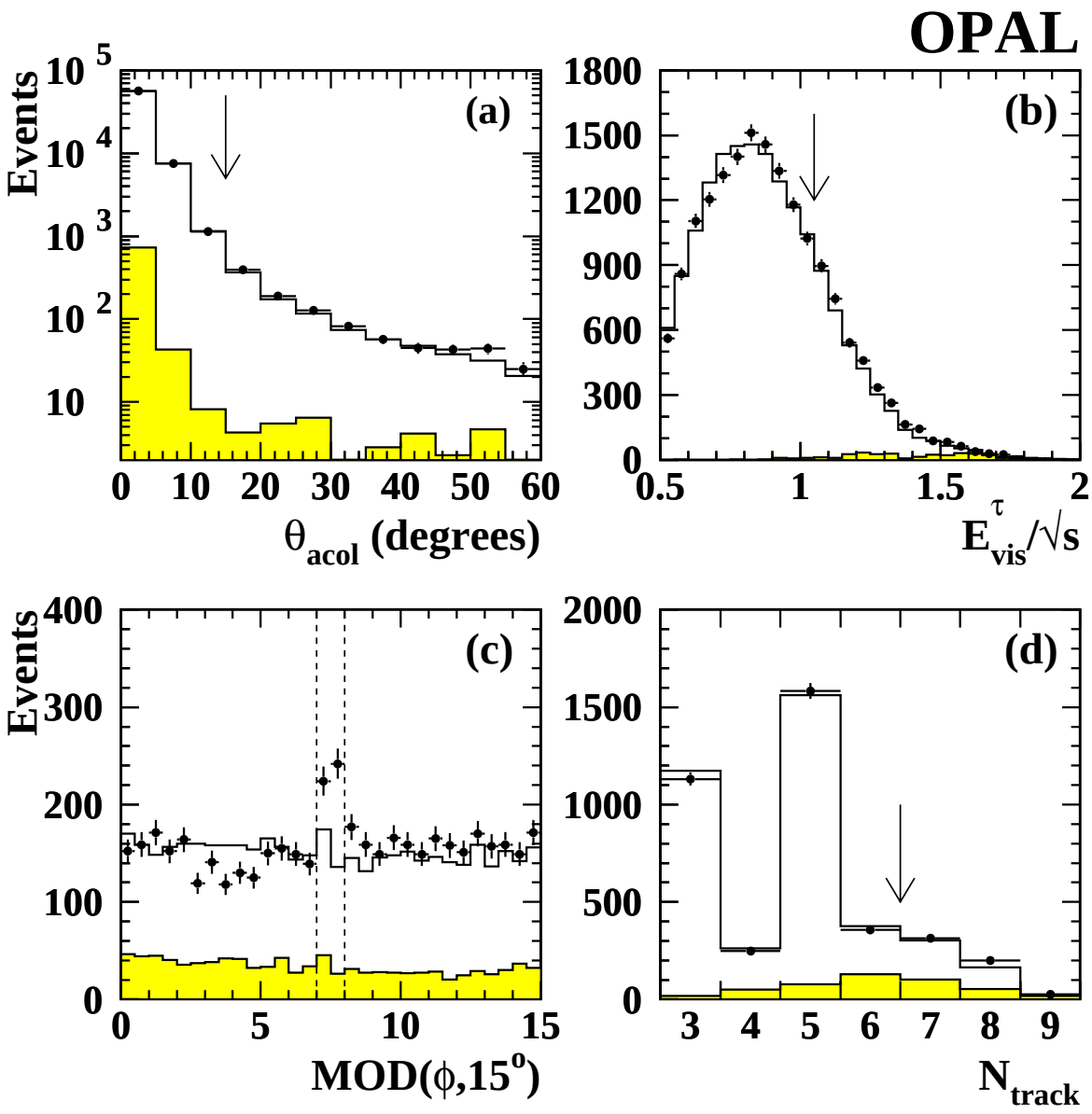

Figure 12: Systematic checks of the $e^+e^- \to \tau^+\tau^-$ event selection.
Each plot corresponds to one of the control samples used to check the efficiency and background of the $e^+e^- \to \tau^+\tau^-$ event selection. Plot a) corresponds to the sample used to assess the effect of the acollinearity cut, b) corresponds to the check of the inefficiency due to the cut on $E^{\tau}_{\rm vis}$ in the region $|\cos\theta_\tau| > 0.7$, c) shows the excess of $e^+e^- \to \mu^+\mu^-$ background events in the region of the jet chamber anode planes, and d) shows the distribution of $N_{\rm track}$ for the control sample used to assess the $e^+e^- \to q\overline{q}$ background. In all plots the data are shown by the points, the total Monte Carlo expectations are shown by the histograms and the contributions from events other than $e^+e^- \to \tau^+\tau^-$ are shown by the shaded histograms. Details are given in the text.

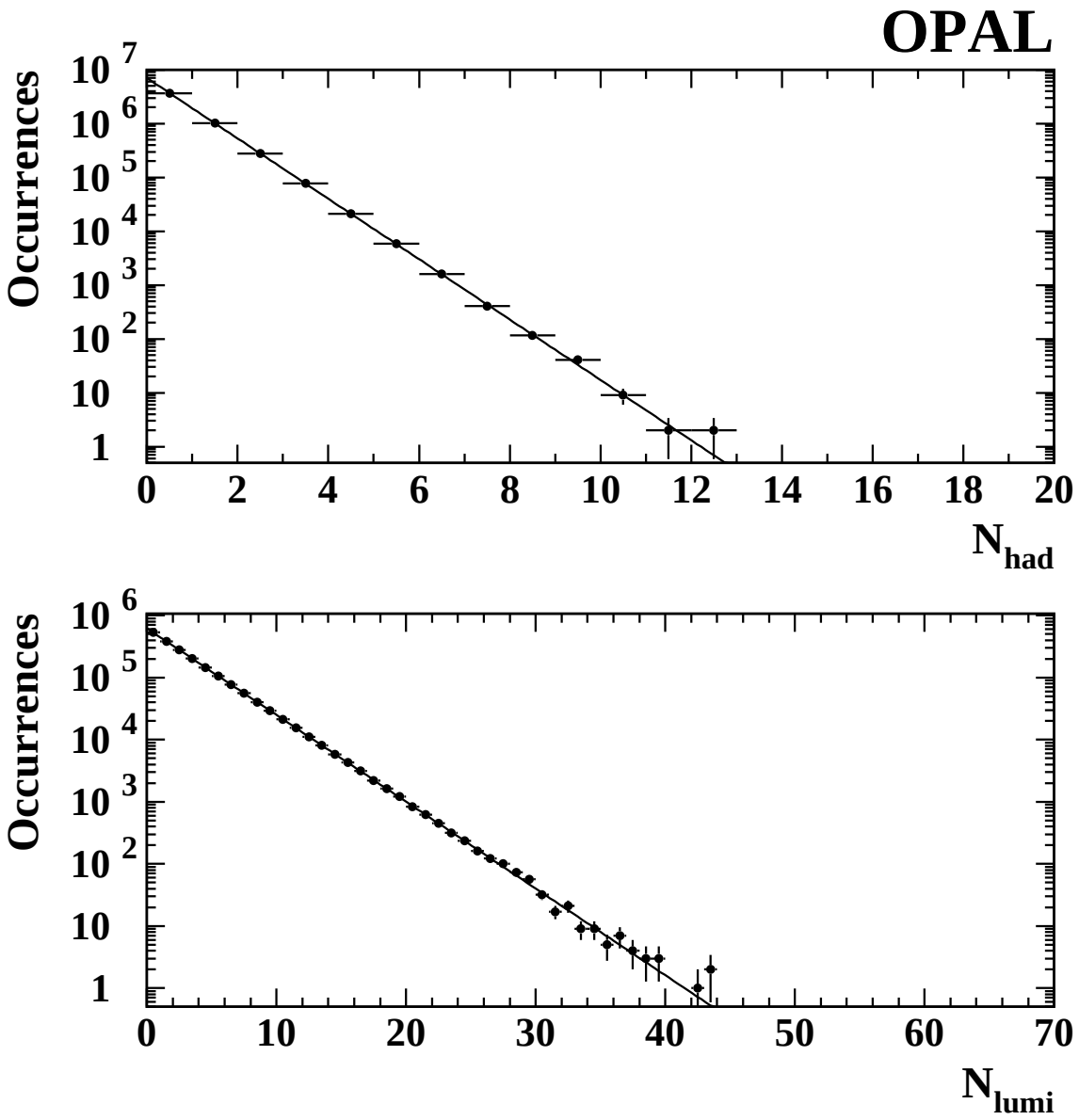

Figure 13: The distribution of the number of events of type (a) observed between adjacent events of type (b) forms a sensitive test for the constancy of the a/b rate ratio. When the ratio truly remains constant, the resulting distribution is a pure exponential, indicated by the line, whose logarithmic slope depends on the event type ratio. The upper plot shows the number of $e^+e^- \to q\overline{q}$ events observed between adjacent luminosity events in the 1993–1995 peak data. The lower plot shows the reverse: the number of luminosity events observed between adjacent $e^+e^- \to q\overline{q}$ events. The tails of these distributions are particularly sensitive to any interruption in the experimental sensitivity to events of type (b), at the level of a few minutes in the sample of about six months of livetime shown. There were no overflows in either of these distributions.

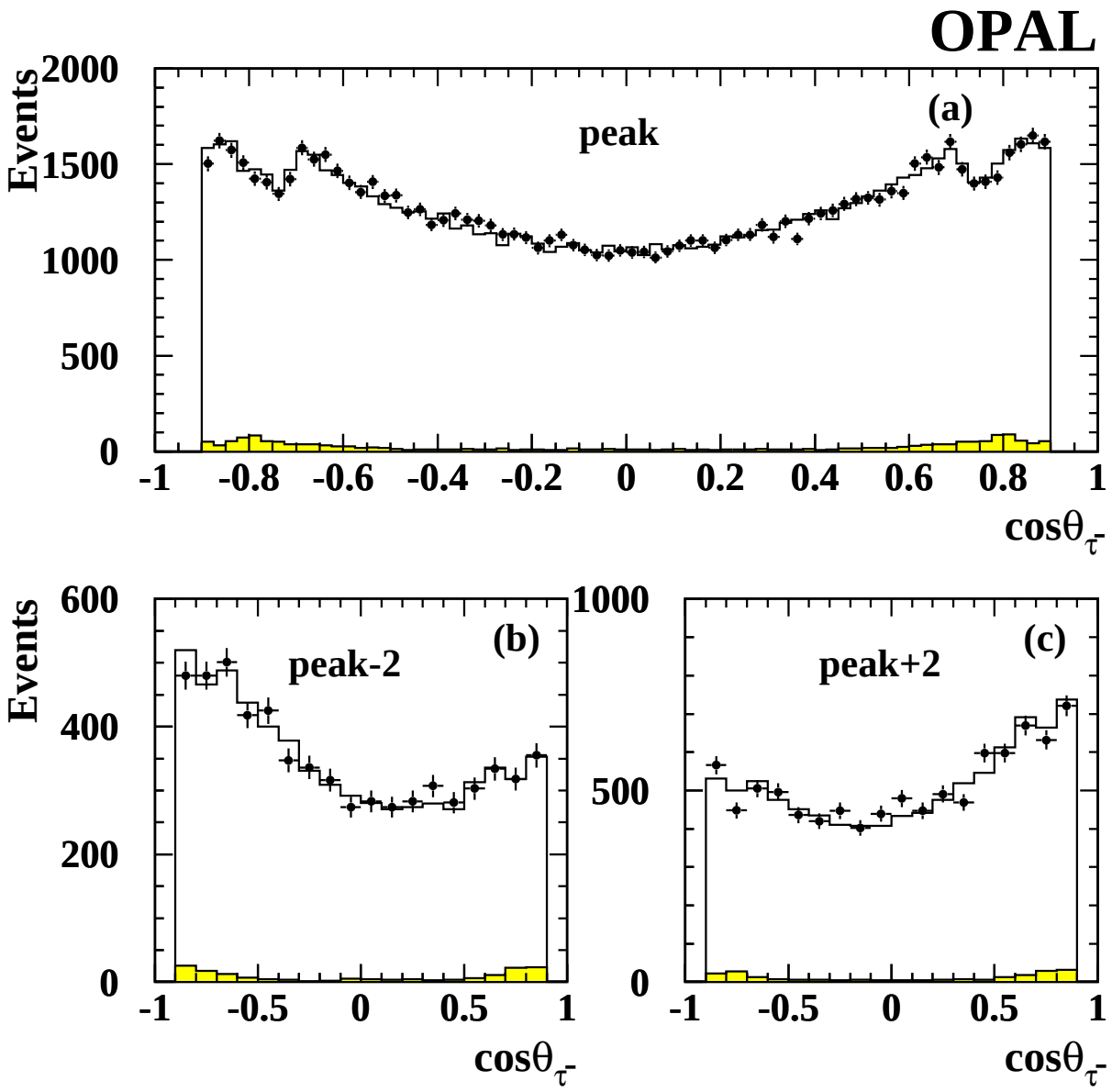

Figure 14: The $e^+e^- \to \tau^+\tau^-$ distribution of polar angle. Distributions of $\cos\theta_{\tau^-}$ for the combined 1993–1995 data (points) separated into peak−2, peak and peak+2 energy points. For these plots $|\cos\theta_{\tau^-}|$ is determined from the average of the polar angles of the positive and negative τ cones determined using tracks and electromagnetic clusters. The additional cuts used for the asymmetry analysis have been applied. The Monte Carlo expectation is shown by the histogram and the background contribution is shown as the shaded component.

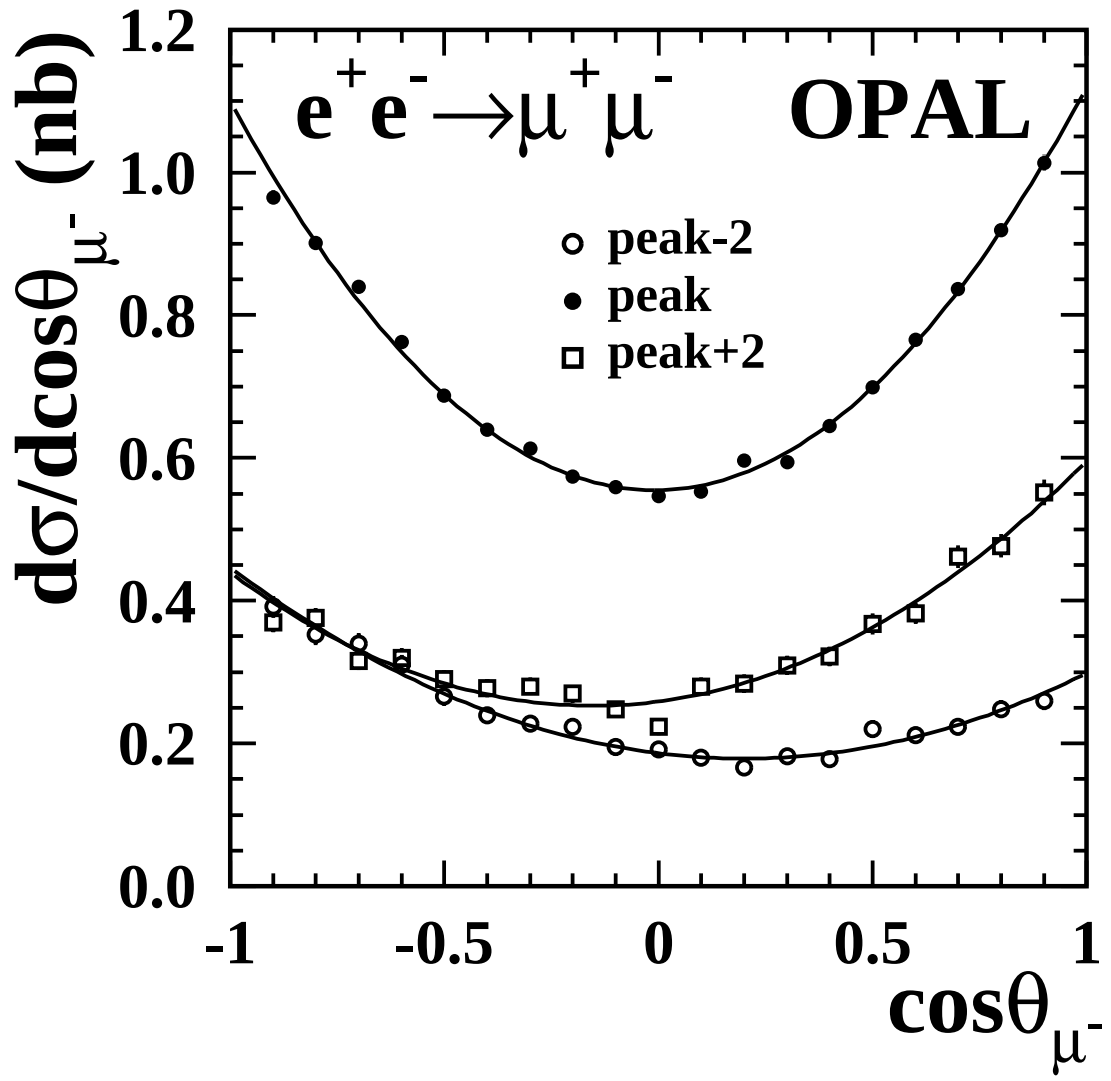

Figure 15: Observed differential cross-sections as a function of $\cos\theta$ for the process $e^+e^- \to \mu^+\mu^-$ at the three centre-of-mass energies in the 1993–1995 data. Corrections have been applied for inefficiency and background. Only statistical errors are shown, bin-by-bin systematic uncertainties are not included. The curves correspond to fits to a simple parametrisation of the form $a(1+\cos^2\theta)+b\cos\theta$.

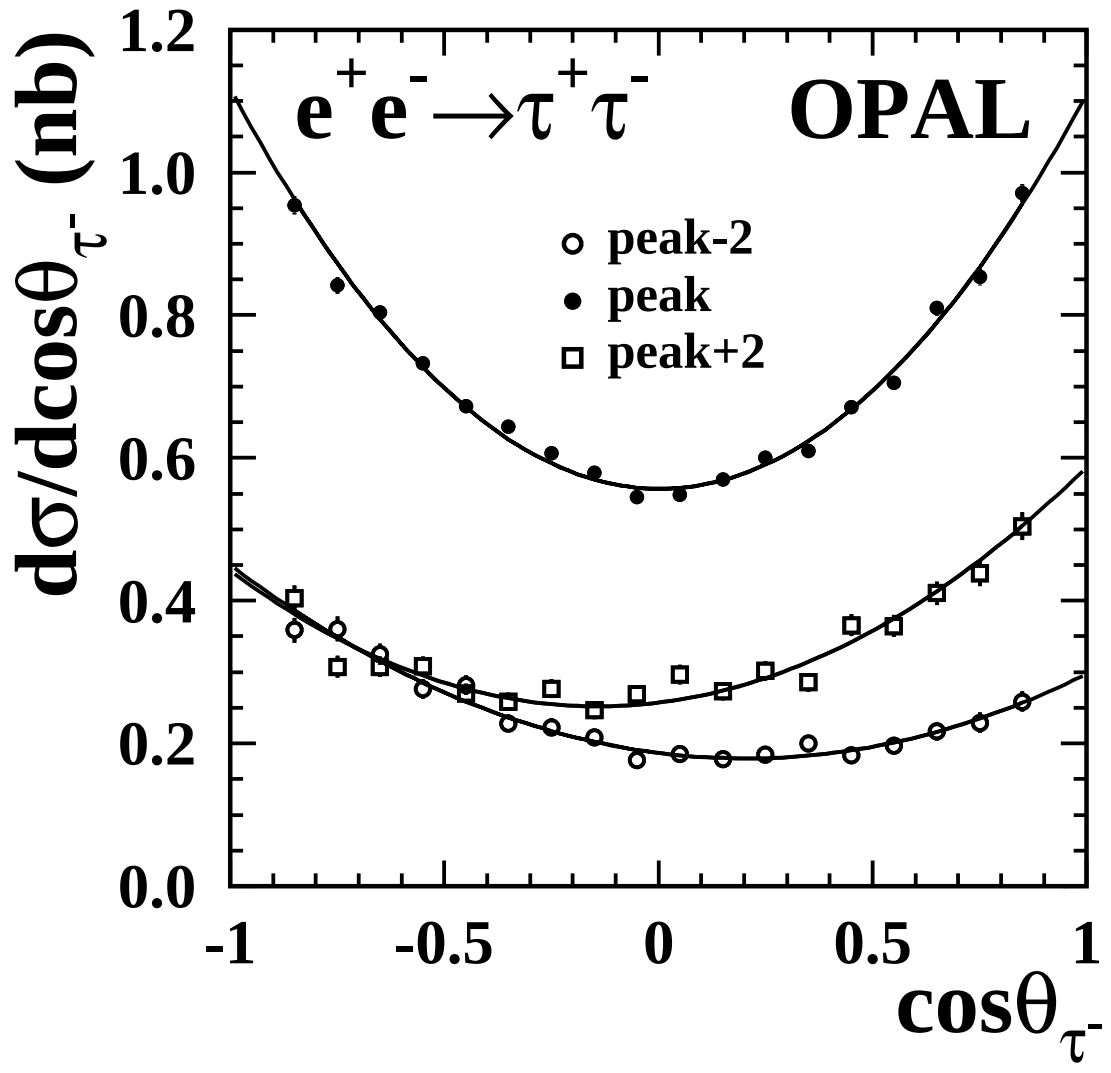

Figure 16: Observed differential cross-sections as a function of $\cos\theta$ for the process $e^+e^- \to \tau^+\tau^-$ at the three centre-of-mass energies in the 1993–1995 data. Corrections have been applied for inefficiency and background. Only statistical errors are shown, bin-by-bin systematic uncertainties are not included. The curves correspond to fits to a simple parametrisation of the form $a(1+\cos^2\theta)+b\cos\theta$.

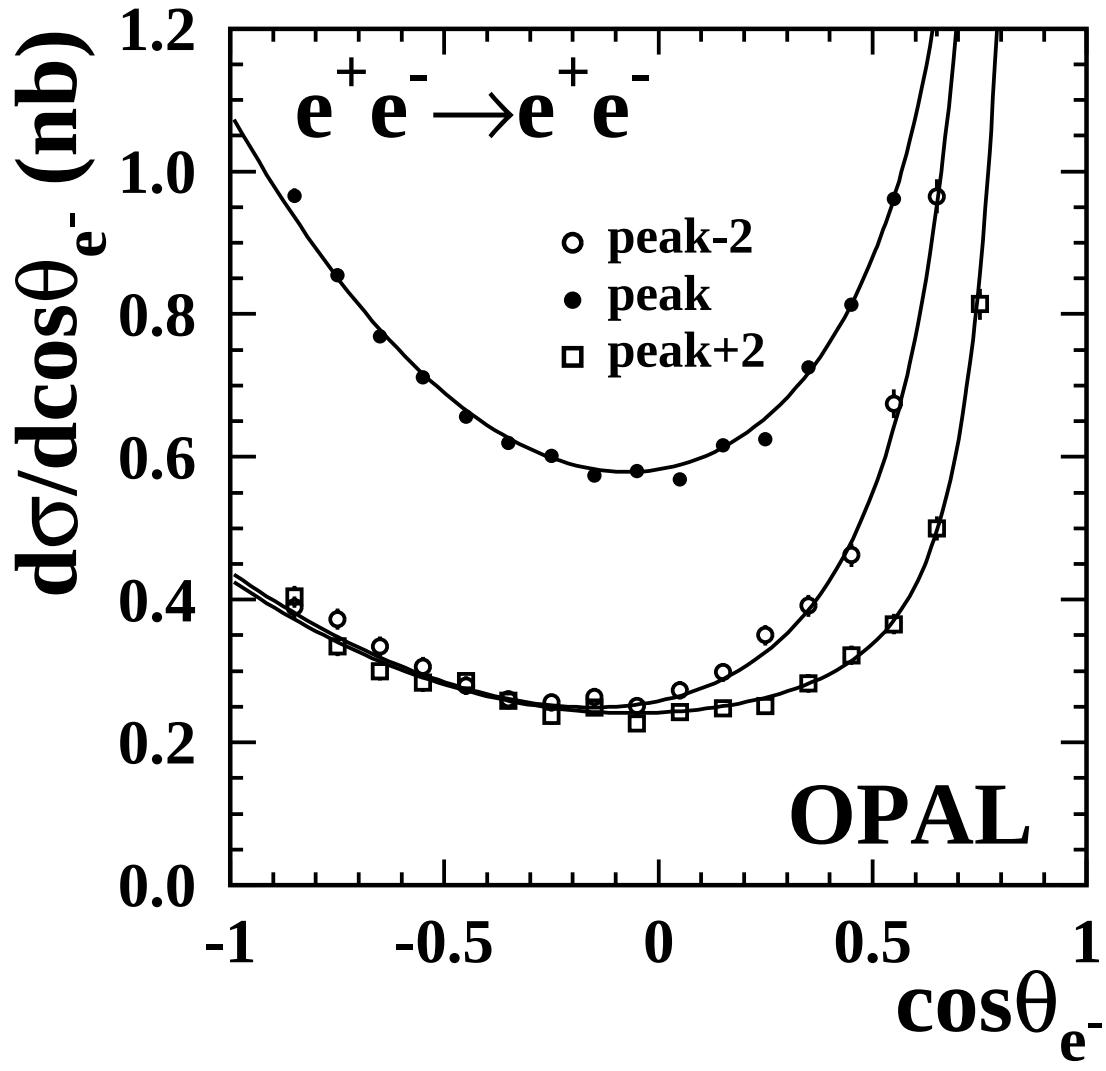

Figure 17: Observed differential cross-sections as a function of $\cos\theta$ for the process $e^+e^- \to e^+e^-$ at the three centre-of-mass energies in the 1993–1995 data. Corrections have been applied for inefficiency and background. Only statistical errors are shown, bin-by-bin systematic uncertainties are not included. The curves show the predictions of ALIBABA.

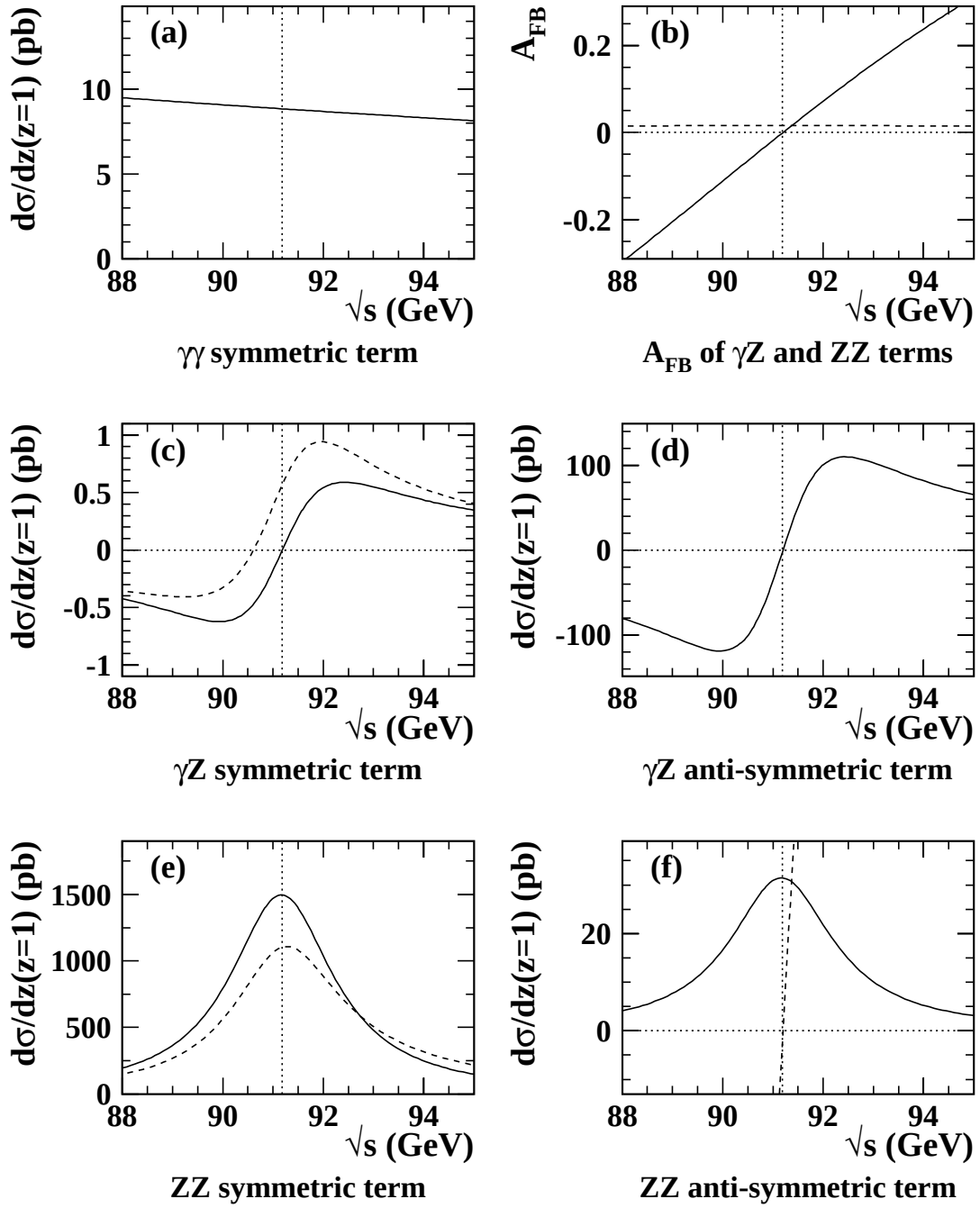

Figure 18: The contribution at tree level of the five terms of equation 8 (solid lines) to the differential cross-section of $e^+e^- \to \mu^+\mu^-$ $(d\sigma\,/\,dz\,(z=1),\ z \equiv \cos\theta$, in (pb)) as a function of $\sqrt{s}$. Plots (a), (c) and (e) give the symmetric terms from γ, γ/Z and Z exchange respectively; (d) and (f) the antisymmetric γ/Z and Z exchange terms. The dashed line in (c) demonstrates the effect when the imaginary parts of the couplings are taken into account. The dashed line in (e) illustrates the profound change of the lineshape due to initial-state radiation. The dashed curve in (f) shows the γ/Z term of (d) superposed to illustrate how rapidly it dominates the more interesting ZZ term as the energy moves away from the peak. (b) shows the forward-backward asymmetry which results from the γ/Z (solid) and ZZ (dashed) terms when the cross-sections are integrated over $-1 < \cos\theta < +1$. The dotted vertical line in each plot indicates $\sqrt{s} = m_{\rm Z}$.

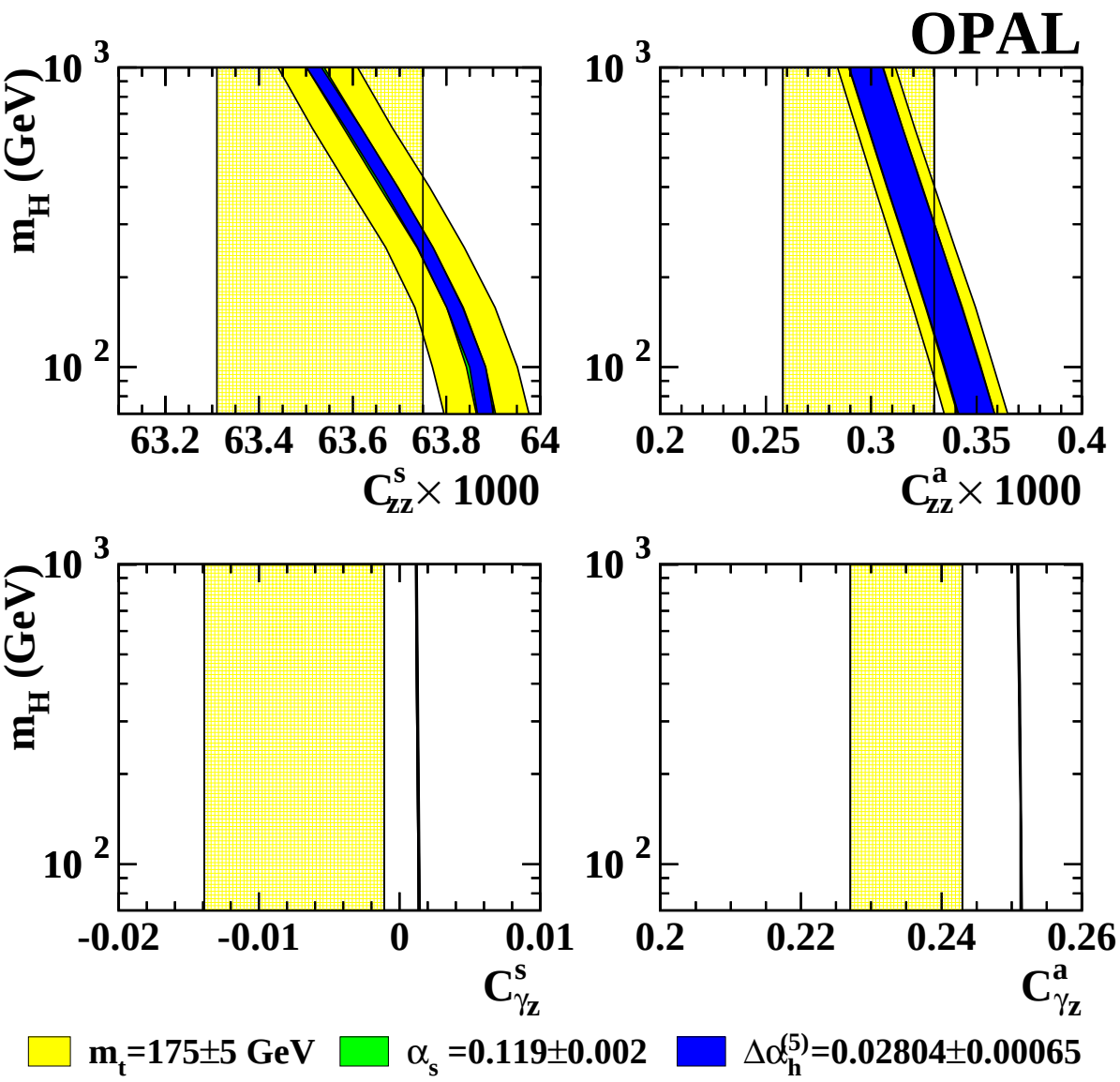

Figure 19: Comparison of the results from the C-parameter fit with the SM prediction as a function of Higgs mass m_{H}. The vertical bands indicate the fit results and their horizontal widths correspond to one standard deviation error intervals. The shaded area shows (linearly) the variation of the SM prediction for m_{t}, α_{s}, and $\Delta\alpha^{(5)}_{\mathrm{had}}$ in the indicated ranges. These parameters are insensitive to α_{s}, and its variation band is therefore invisible.

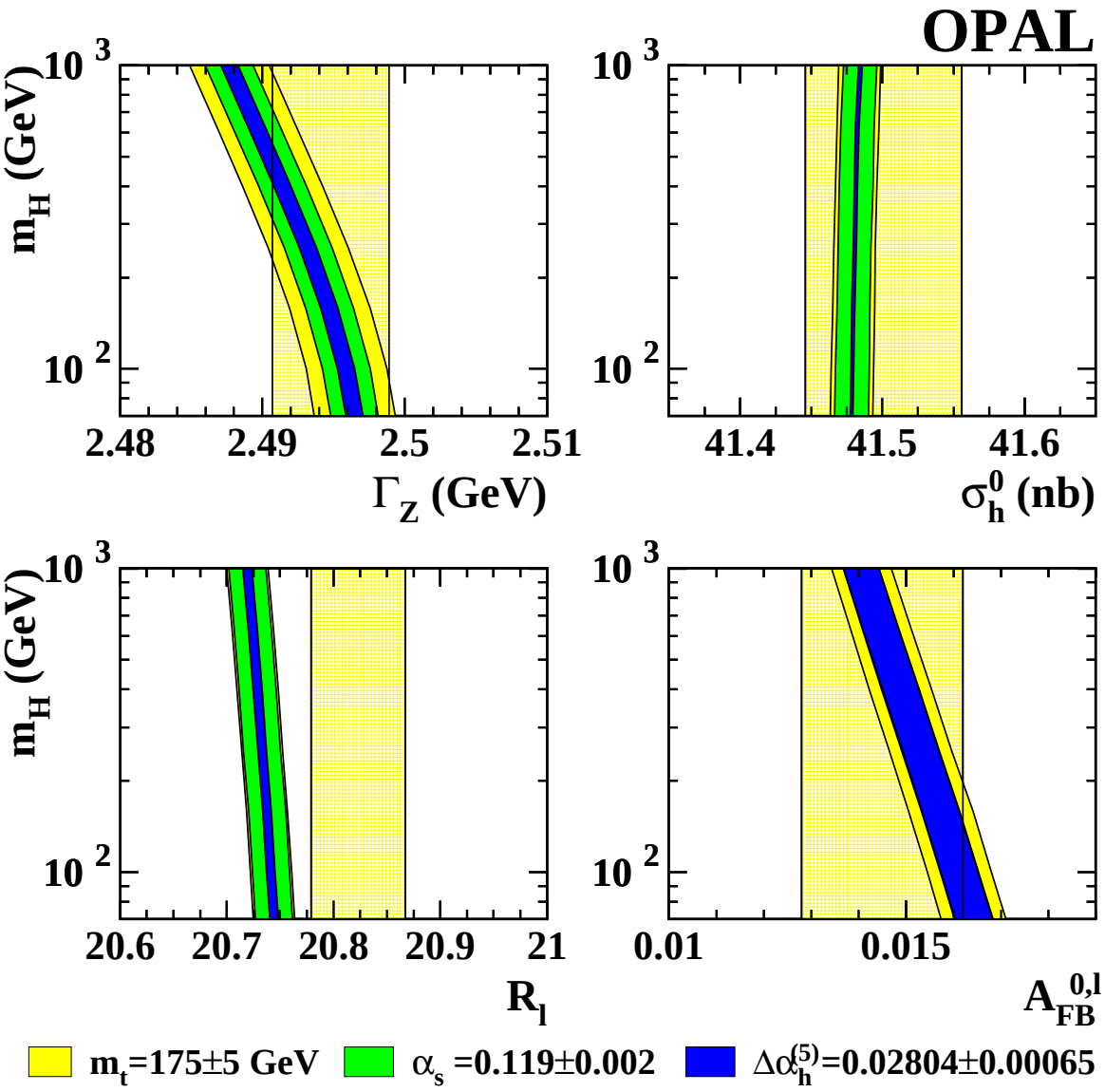

Figure 20: Comparison of the results of the 5-parameter model-independent fit with the SM prediction as a function of Higgs mass m_{H}. The vertical bands indicate the fit results and their horizontal widths correspond to one standard deviation error intervals. The shaded area shows (linearly) the variation of the SM prediction for m_{t}, α_{s}, and $\Delta\alpha^{(5)}_{\mathrm{had}}$ in the indicated ranges.

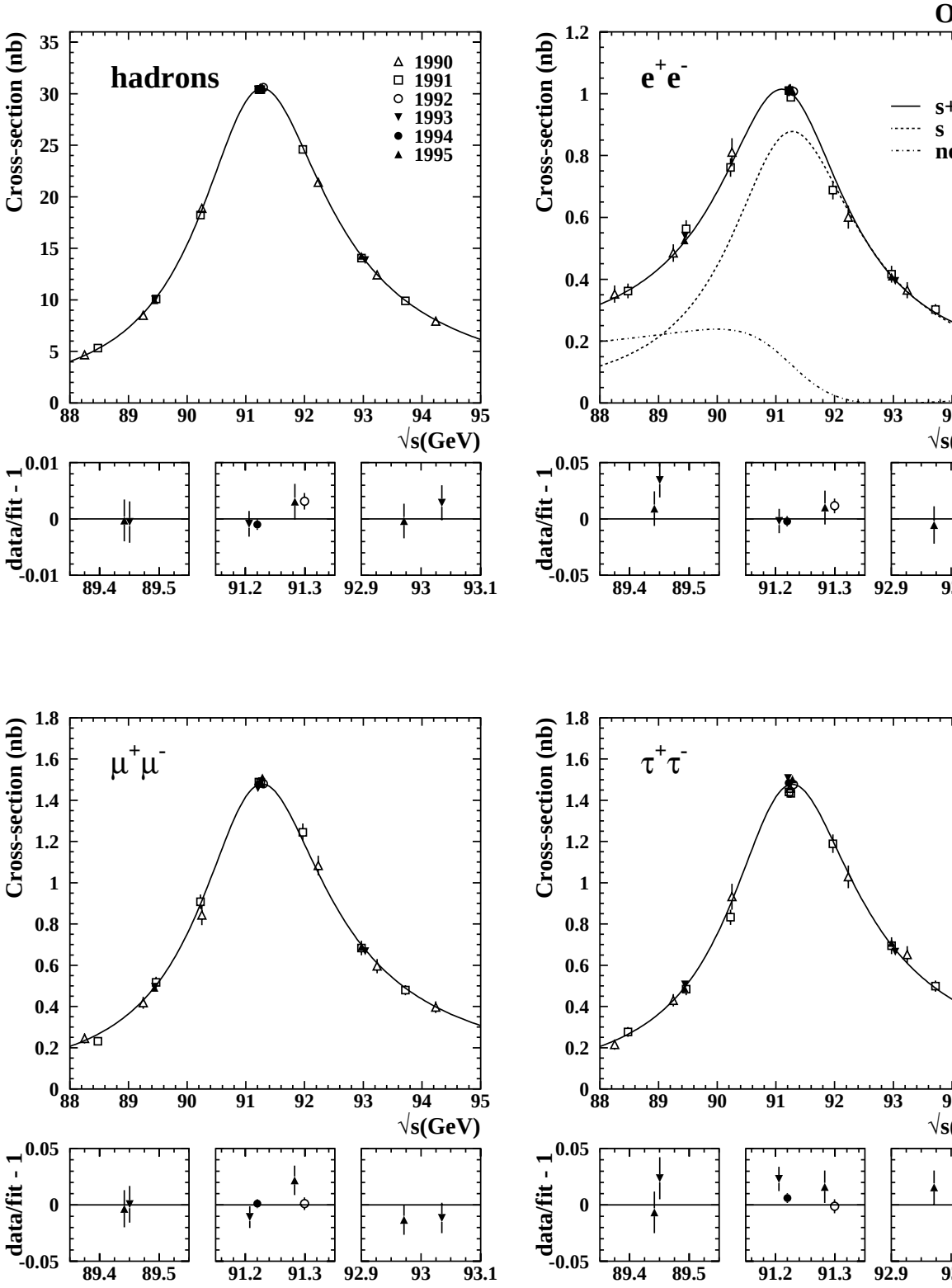

Figure 21: The measured cross-sections for hadronic and leptonic final states as a function of centre-of-mass energy. The errors shown are statistical only. The solid line is the result of the 9-parameter model-independent fit to the combined leptonic and hadronic data (without assuming lepton universality) described in Section 11.2. The lower plots show the residuals to the fit. For the electrons, the dashed curves show the contributions of the pure s-channel, and t-channel plus $s-t$ interference, respectively.

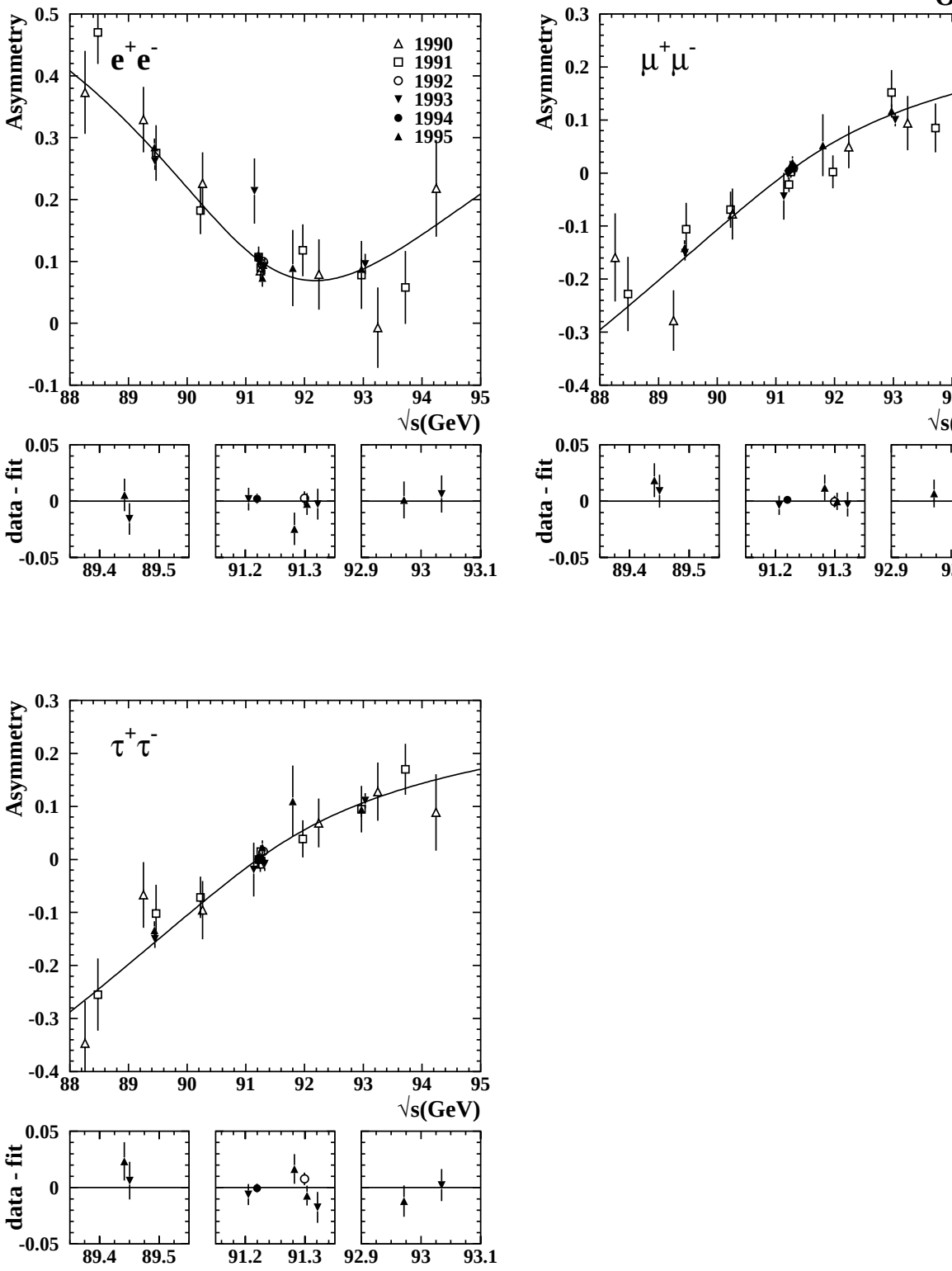

Figure 22: The measured forward-backward asymmetry in leptonic final states as a function of centre-of-mass energy. The errors shown are statistical only. The solid line is the result of the 9-parameter model-independent fit to the combined leptonic and hadronic data (without assuming lepton universality) described in Section 11.2. The lower plots show the residuals to the fit.

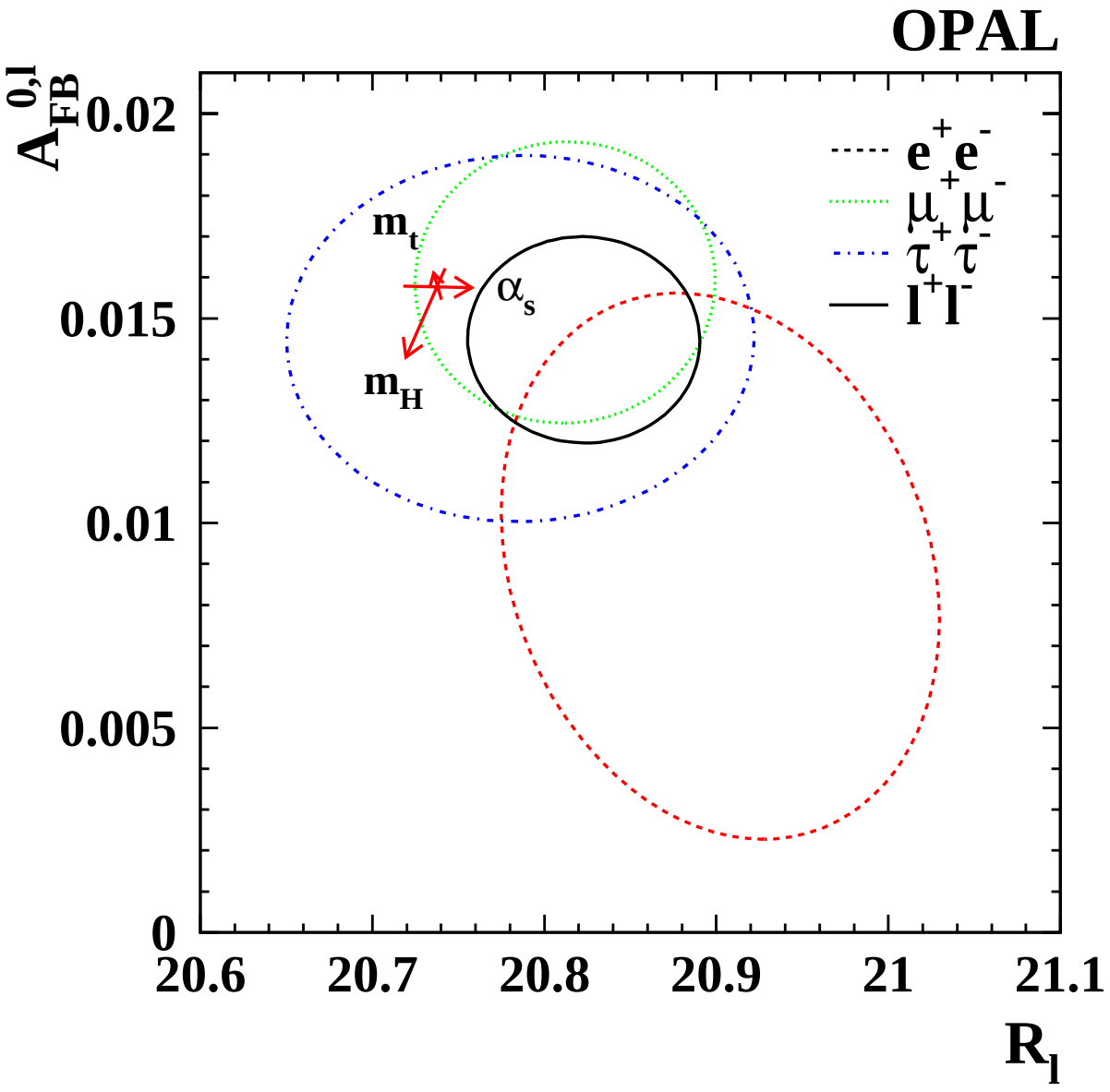

Figure 23: Contours of 68% probability in the $A_{\rm FB}^{0,\ell} - R_\ell$ plane for each of the three lepton species (dotted, dashed). The solid contour results from a fit assuming lepton universality. In this plot, the results for the τ are corrected for the mass effect so that a direct comparison with other lepton species is possible. The SM prediction with $\alpha_{\rm s}$, $m_{\rm t}$, $m_{\rm H}$ and $\Delta\alpha_{\rm had}^{(5)}$ as specified in Equation 25 is also shown as the intersection of the three arrows. The arrows indicate the range of the variation when $\alpha_{\rm s}$, $m_{\rm t}$ and $m_{\rm H}$ are varied within the ranges specified in Equation 25.

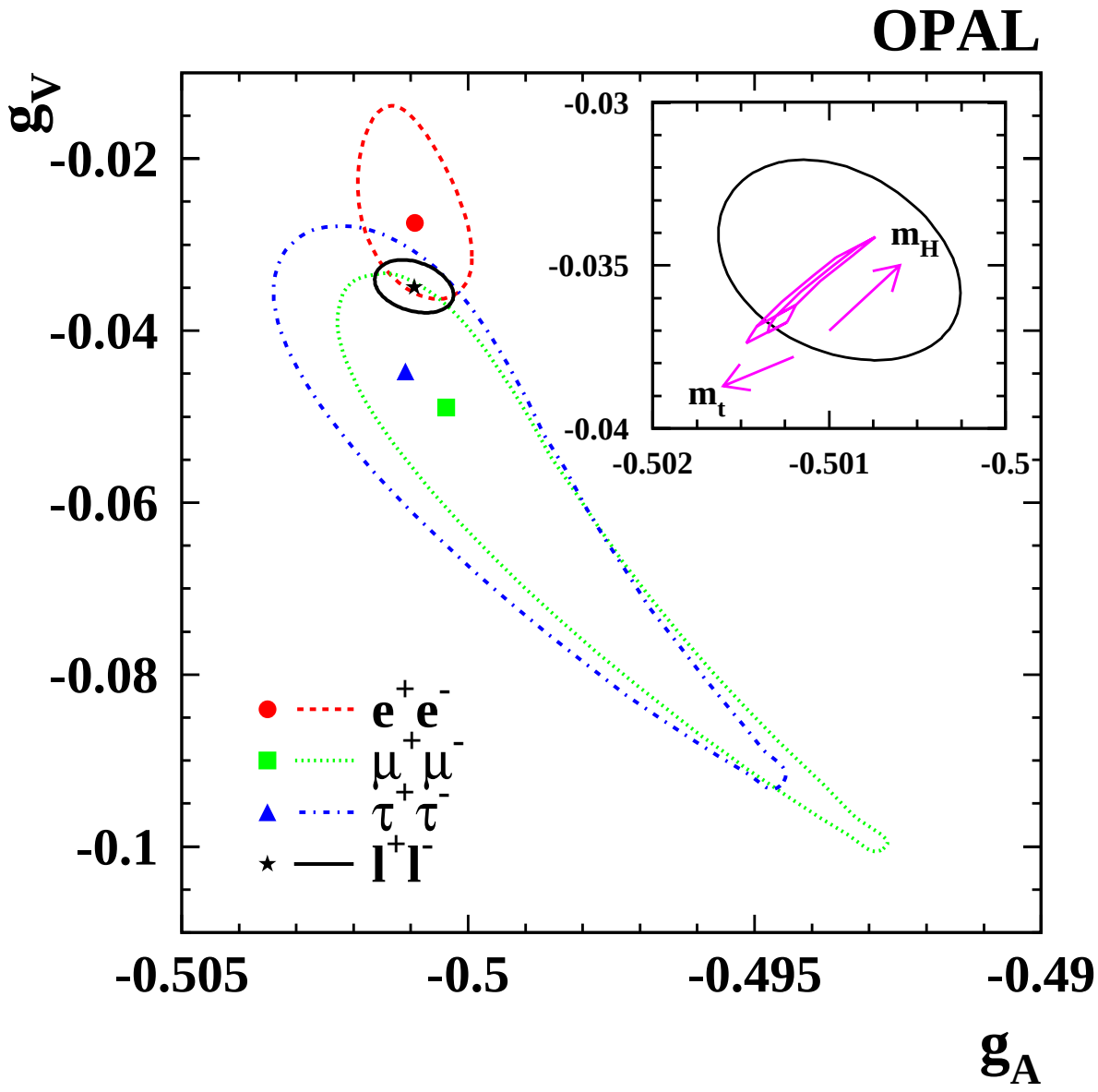

Figure 24: Contours of 68% probability in the $g_{V\ell} - g_{A\ell}$ plane for each of the three lepton species (dotted, dashed). The solid contour results from a fit assuming lepton universality and is also shown enlarged in the inset figure. Here, the band indicates the SM prediction when m_t and m_H are varied as specified in equation 25.

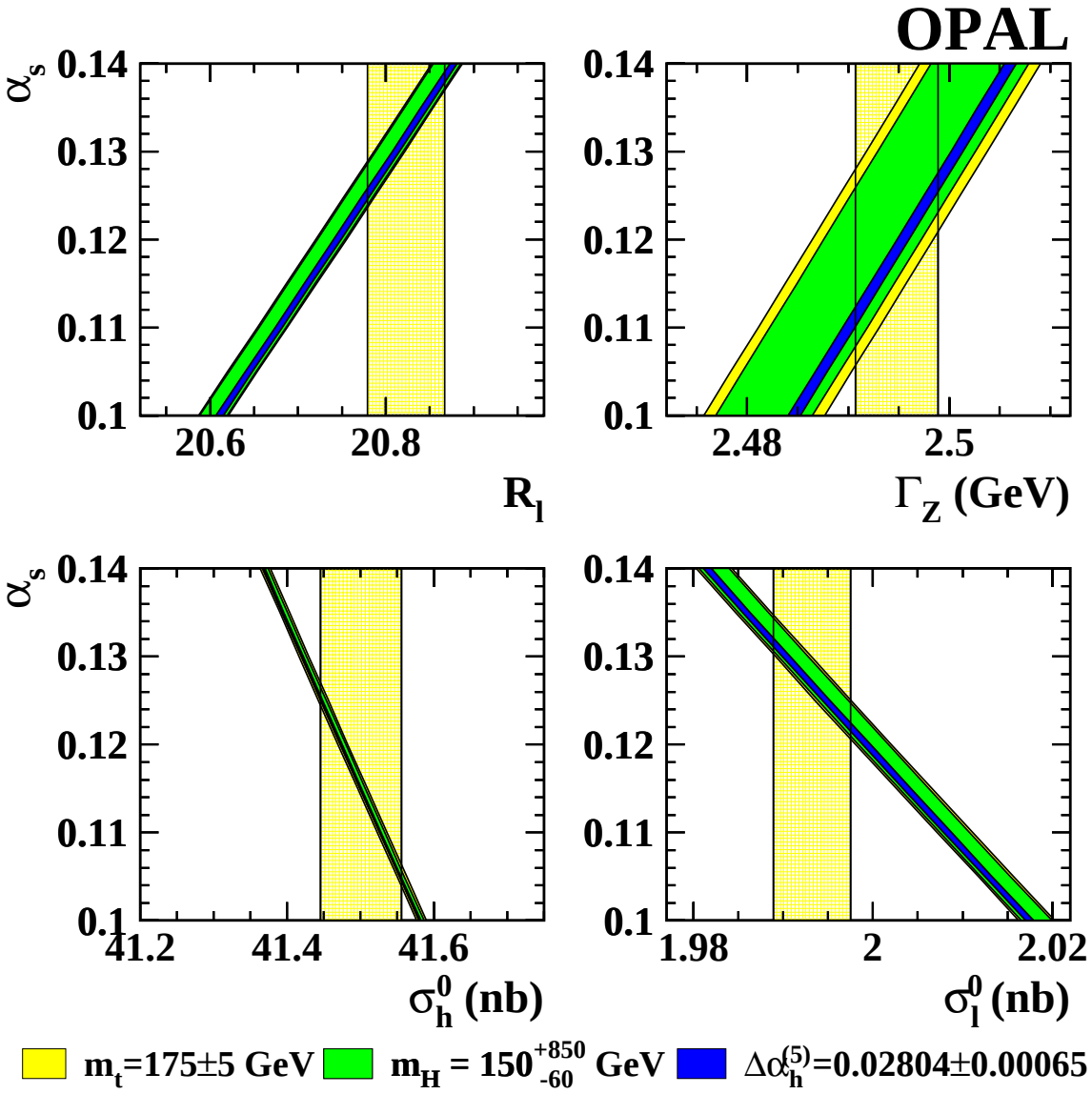

Figure 25: Comparison of Z resonance parameters with the SM prediction as a function of α_s. The vertical bands indicate the fit results and their horizontal widths correspond to one standard deviation error intervals. The hatched area shows (linearly) the variation of the SM prediction when m_t, m_H and $\Delta\alpha^{(5)}_{had}$ are varied as specified in Equation 25 and indicated in the figure.

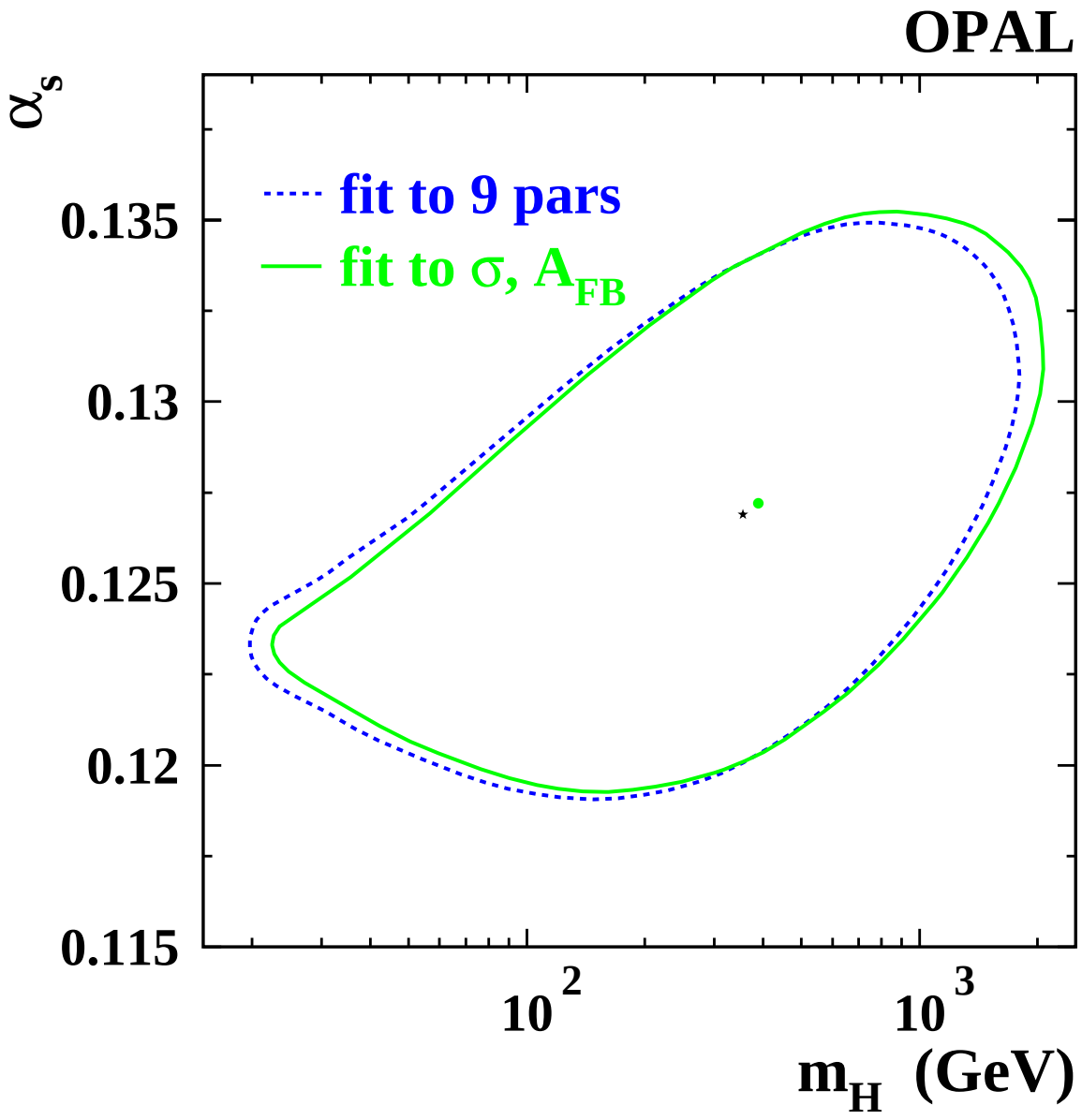

Figure 26: Contours of 68 % probability in the $\alpha_s - m_H$ plane with m_t constrained to 174.3 ± 5.1 GeV [?]. The undashed contour is obtained from the SM fit to cross-sections and asymmetries. For the dashed contour the fit was made on the results of the 9-parameter model-independent fit. The small circle and the star give the central values for the two fits, respectively. In both cases a numerical evaluation of the 68 % C.L. contour was performed which accounts for asymmetric or non-parabolic parameter dependencies (MINUIT contour [?]).